Structural Diagnostics of CFRP Composite Aircraft Components by Ultrasonic Guided Waves and Built-In Piezoelectric Transducers

Los Alamos
NATIONAL LABORATORY
— EST.1943 —

This thesis was accepted by the Department of Structural Engineering, University of California, San Diego, California, in partial fulfillment of the requirements for the degree of Doctor of Philosophy. The text and illustrations are the independent work of the author, and only the front matter has been edited by the IRM-CAS Writing and Editing staff to conform with Department of Energy and Los Alamos National Laboratory publication policies.

National Nuclear Security Administration

Structural Diagnostics of CFRP Composite Aircraft Components by Ultrasonic Guided Waves and Built-In Piezoelectric Transducers

Howard M. Matt*

* University of California San Diego, 9500 Gilman Dr. 0085, La Jolla, California 92093.

Los Alamos
NATIONAL LABORATORY
——— EST.1943 ———

UNIVERSITY OF CALIFORNIA, SAN DIEGO

Structural Diagnostics of CFRP Composite Aircraft Components by Ultrasonic Guided Waves

and Built-In Piezoelectric Transducers

A dissertation submitted in partial satisfaction of the requirements for the degree

Doctor of Philosophy

in

Structural Engineering

by

Howard M. Matt

Committee in Charge:

　　Professor Francesco Lanza di Scalea, Chair
　　Professor Charles Farrar
　　Professor John B. Kosmatka
　　Professor Hidenori Murakami
　　Professor Bhaskar D. Rao

2006

BERKELEY • DAVIS • IRVINE • LOS ANGELES • MERCED • RIVERSIDE • SAN DIEGO • SAN FRANCISCO   SANTA BARBARA • SANTA CRUZ

OFFICE OF GRADUATE STUDIES
(858) 534-3555
FAX: (858) 534-3868

9500 GILMAN DRIVE
LA JOLLA, CALIFORNIA 92093-0003

December 21, 2006

Dr. Howard M. Matt
12904 198th. Avenue E
Summer, WA 98390

Dear Dr. Matt,

I am pleased to note that you have now completed all requirements for the degree of Doctor of Philosophy in Structural Engineering from the Department of Structural Engineering. Your diploma will be forwarded by the Office of the Registrar at a later date.

On behalf of the Graduate Council and the Office of Graduate Studies, I congratulate you on reaching this important milestone in your career.

Sincerely,

Kim E. Barrett
Dean

KB: vc/Doctoral Completed Requirements.doc

cc: Graduate Coordinator in Department of Structural Engineering

DEDICATION

To my family, Vince, Roberta, Sean and Nicole, and my wife to be, Angela for their constant love and encouragement. I love you all.

EPIGRAPH

If a man empties his purse into his head, no man can take it away from him. An investment in knowledge always pays the best interest.

   Benjamin Franklin

TABLE OF CONTENTS

LIST OF SYMBOLS

t	Time
$\boldsymbol{\sigma}$	Stress vector
σ_{ij}	Stress
u_i	Displacement
$\mathbf{U}$	Displacment vector
$\dot{\mathbf{u}}^*$	Complex conjugate of the particle velocity vector
$\mathbf{C}, \mathbf{C}'$	Elastic stiffness matrices
$\mathbf{C}''$	Imaginary part of stiffness matrix
$\widetilde{\mathbf{C}}$	Complex stiffness matrix
$\bar{\mathbf{C}}$	Complex stiffness matrix in global coordinates
$\mathrm{T}_1, \mathrm{T}_2$	Transformation matrices principal material directions
C_{ij}	Elastic constant
$\boldsymbol{\eta}$	Viscosity tensor
ε	Strain vector
ε_{ii}	Normal strain
γ_{ij}	Shear strain
λ_L, μ_L	Lamé constants
Y_i^E	Young's Modulus
G_{ij}	Shear Modulus
ρ	Density of material
ν_{ij}	Poisson's ratio
δ_{ij}	Kronecker delta
$\vec{\nabla}$	Divergance vector
ϕ	Scalar potential
$\vec{\psi}$	Vector potential
c_L	Velocity of bulk longitudinal waves
c_T	Velocity of bulk shear waves
d	Plate half thickness
x, y, z	Cartesian coordinates
i	Imaginary unit
λ	Wavelength
k	Wavenumber
f	Frequency
ω	Angular frequency
$\Phi(z), \Psi(z)$	Standing waves
A_i, B_i	Arbitrary wave amplitudes
r, s	Wave related terms
c	Phase velocity

c_{gr}	Group velocity
l	Length of transducer
b	Width of transducer
t	Thickness of transducer
$\mathbf{D}$	Charge density vector or electric displacement
$\mathbf{e}^{\sigma}$	Dielectric permittivity matrix (measured at constant stress)
$\mathbf{E}$	Electric field vector
$\mathbf{d}$	Piezoelectric charge coefficient matrix
d_{ij}	Piezoelectric charge coefficient
e_{ii}^{σ}	Dielectric permittivity (measured at constant stress)
D_i	Charge density or electric displacement
E_i	Electric field
$[Q]$	Reduced stiffness matrix
Q_{ij}	Reduced stiffness coefficient
V	Transducer voltage
$\overline{V}(\omega)$	Frequency-domain amplitude of transducer to harmonic excitation
∞	Infinity
a	electrode to electrode centerline spacing of MFC (type P1) transducer
g	piezoelectric fiber thickness of MFC (type P1) transducer
w	half width of the electrode of MFC (type P1) transducer
p	unit cells of MFC (type P1) transducer
A_{el}	Active electrode area of transducer
φ	Local potential
$\varphi_{avg.}$	Average potential over electrode area
x'	Direction of wave propagation
y'	Perpendicular direction to wave propagation direction
θ	Angle of wave propagation direction with respect to sensor's lengthwise direction
q, r_R, s_R, R	Rayleigh wave parameters
S_{PZT}	Frequency-independent constant for PZT transducer
$A_{Rayleigh}$	Rayleigh wave amplitude
Re	Real component
$\mathbf{P_V}$	Poynting vector
P_{Vi}	Poynting vector component
$N_{Rayleigh}$	Rayleigh wave normalization factor
$\overline{U}(\omega)$	Frequency-domain response of a linear system subjected to an arbitrary excitation
$\overline{P}(\omega)$	Frequency-domain magnitude of arbitrary excitation
$\varepsilon_{x'x'}^{a}\big|_{z=0}(\omega)$	Amplitude spectrum of the surface strain induced by an arbitrary source at the point of entry into the sensor

$\varepsilon_{x'x'}\big\vert_{z=0}(\omega)$	Amplitude spectrum of the surface strain excited under harmonic conditions
$f(t)$	Time dependant function
T	Time duration of the wave train
n	Number of half cycles of toneburst
$\overline{F}$	Fourier transform of toneburst
E	Arbitrary wave amplitudes for the antisymmetric modes
F	Arbitrary wave amplitudes for the symmetric modes
$A_{antisymm}$	Antisymmetric Lamb wave amplitude
A_{symm}	Symmetric Lamb wave amplitude
N_{Lamb}	Lamb wave normalization factor
A_i	Antisymmetric Lamb wave mode (mode i)
S_i	Symmetric Lamb wave mode (mode i)
$S_{MFC\ P1}$	Frequency-independent parameter for MFC (type P1) transducer
$S_{MFC\ P2}$	Frequency-independent parameter for MFC (type P1) transducer
Φ_S	Strain energy
T_K	Kinetic energy
Ω	Waveguide domain
$\mathbf{L}_x, \mathbf{L}_y, \mathbf{L}_z$	Decomposition matrix
N_{ne}	Shape function
$\mathbf{N}(z)$	Shape function matrix
U_{ine}	Nodal unknown displacements
$\mathbf{q}^{(e)}$	Nodal unknown displacement vector for element
ne	Number of nodes per element
n_{el}	Total number of cross-sectional elements
$\mathbf{m}^{(e)}$	Mass matrix for element e
$\mathbf{U}$	Global vector of unknown nodal displacements
$\mathbf{k}_1^{(e)}, \mathbf{k}_2^{(e)}, \mathbf{k}_3^{(e)}$	Stiffness matrices for element e
$\mathbf{K}_1, \mathbf{K}_2, \mathbf{K}_3$	Assembled global stiffness matrices
$\mathbf{M}$	Assembled global mass matrix
M	Number of total degrees of freedom of the system
V_e	Energy velocity
H	Total waveguide thickness
h	Partial waveguide thickness
$\hat{\mathbf{x}}$	Unit vector
e_{tot}	Total energy density
$\langle e_k \rangle_t$	Time averaged energy for the kinetic component
$\langle e_p \rangle_t$	Time averaged energy for the potential component
α_L	Longitudinal attenuation in a material
α_S	Shear attenuation in a material

RMS	Root mean square
$\psi_{j,n^P}(t)$	Mother wavelet function
W_{j,n^P}	Wavelet coefficients
n^P	Translation parameter
s^P	Scaling parameter
F_C	Mother wavelet central frequency
Δf_j	Bandwidth
Δ	Signal sampling rate
X_{corr}	Cross correlation
$l\tau_0$	Applied actuator pin force
z_ζ	Univariate discordance
x_ζ	Potential outlier
$\bar{x}$	Baseline variable mean
σ_B	Baseline variable standard deviation
D_ς	Mahalanobis squared distance
$\{x\}$	Potential outlier vector
$\{\bar{x}\}$	Mean vector of the baseline data
$[S_{cov}]$	Covariance matrix of the baseline data
S	Broadband sensitivity factor of transducer
$\bar{\varepsilon}_{x'x'}$	Strain magnitude in direction of wave propagation
S_1	Longitudinal (lengthwise) sensitivity factor of a transducer
S_2	Transverse (widthwise) sensitivity factor of a transducer
$\Delta\omega$	Frequency range
$\tilde{S}_1, \tilde{S}_2$	Summation of sensitivity factor over frequency range $\Delta\omega$
n_F	Number of discrete frequency responses
$\tilde{U}$	Total broadband response quantity
β	Angle of rotation of a sensor with respect to global axis x
ϕ	Principal angle of the ultrasonic wave measured from the global axis x and the line intersecting the centroid of a rosette arrangement
K_T	Transverse sensitivity ratio
$[\hat{T}]$	Transformation matrix for piezoelectric sensor
Num	Numerator
Den	Denominator
y_{SOURCE}	Coordinate of damage/impact source along global y axis
x_{SOURCE}	Coordinate of damage/impact source along global x axis

LIST OF FIGURES

LIST OF TABLES

ACKNOWLEDGEMENTS

response of rectangular PZT wafer sensors to ultrasonic stress waves". The dissertation author was the primary investigator and a co-author of this paper.

Another part of chapter 3 will be submitted for publication in *Smart Materials and Structures*, Matt, Howard; Lanza di Scalea, Francesco. 2006. The current running title of this paper is "New method for damage location in complex CFRP structures based upon the use of piezoelectric transducer rosettes". The dissertation author was the primary investigator and author of this paper.

Chapter 4, in part, has been published in the *Proceedings of SPIE's Smart Structures/NDE Conference*, Bartoli, Ivan; Marzani, Allessandro; Matt, Howard; Lanza di Scalea, Francesco; Viola, Erasmo. 2006. The title of this paper is "Modeling wave propagation in damped waveguides of arbitrary cross-section". The dissertation author was a co-author of this paper.

Chapter 5, in part, has been published in the *Journal of Acoustical Society of America*, Matt, Howard; Bartoli, Ivan; Lanza di Scalea, Francesco. 2005. The title of this paper is "Ultrasonic guided wave monitoring of composite wing skin-to-spar bonded joints in aerospace structures". The dissertation author was the primary investigator and author of this paper.

Chapter 6, in part, has been published in the *Journal of Acoustical Society of America*, Matt, Howard; Bartoli, Ivan; Lanza di Scalea, Francesco. 2005. The title of this paper is "Ultrasonic guided wave monitoring of composite wing skin-to-spar bonded joints in aerospace structures". The dissertation author was the primary investigator and author of this paper.

Another part of chapter 6 is in print in the *Journal of Intelligent Material Systems and Structures*, Lanza di Scalea, Francesco; Matt, Howard; Bartoli, Ivan; Coccia, Stefano; Park,

Gyuhae; Farrar, Charles. 2006. The title of this paper is "Health monitoring of UAV wing skin-to-spar joints using guided waves and macro fiber composite tranducers". The dissertation author was the primary investigator and a co-author of this paper.

Chapter 7, in part, will be submitted for publication in the *Journal of Intelligent Material Systems and Structures*, Salamone, Salvatore; Matt, Howard; Rizzo, Piervincenzo; Lanza di Scalea, Francesco. 2006. The current running title of this paper is "The influence of temperature on guided wave based MFC transduction and damage detection". The dissertation author was a co-author of this paper.

Chapter 10, in part, will be submitted for publication in *Smart Materials and Structures*, Matt, Howard; Lanza di Scalea, Francesco. 2006. The current running title of this paper is "New method for damage location in complex CFRP structures based upon the use of piezoelectric transducer rosettes". The dissertation author was the primary investigator and author of this paper.

VITA

2001	Bachelor of Science, University of Washington
2002 – 2004	Research Assistant, University of California, San Diego
2004	Master of Science, University of California, San Diego
2004 – 2006	Research Assistant, University of California, San Diego
2006	Doctor of Philosophy, University of California, San Diego

PUBLICATIONS

<u>JOURNALS</u>

1. Salvatore Salamone, Howard Matt, Francesco Lanza di Scalea and Piervincenzo Rizzo. (2006). "The influence of temperature on guided wave based MFC transduction and damage detection," *to be submitted to Journal of Intelligent Materials and Structures.*

2. Howard Matt and Francesco Lanza di Scalea. (2006). "New method for damage location in complex CFRP structures based upon the use of piezoelectric transducer rosettes," *to be submitted to Smart Materials and Structures*.

3. Francesco Lanza di Scalea, Howard Matt and Ivan Bartoli. (2006). "Fundamental response of rectangular PZT wafer sensors to ultrasonic stress waves," *Journal of the Acoustical Soiceity of America, (in print).*

4. Francesco Lanza di Scalea, Howard Matt, Ivan Bartoli, Stefano Coccia, Gyuhae Park, and Charles Farrar. (2006). "Health monitoring of UAV wing skin-to-spar joints using guided waves and macro fiber composite transducers," *Journal of Intelligent Materials And Structures*, (*in print*).

5. André Filiatrault and Howard Matt. (2006). "Seismic response of high voltage transformer-bushing systems," *ASCE Journal of Structural Engineering* **132**(2), pp. 287-295.

6. André Filiatrault and Howard Matt. (2005). "Experimental seismic response of high voltage transformer-bushing systems," *Earthquake Spectra* **21**(4), pp. 1009-1026.

7. Howard Matt, Ivan Bartoli, and Francesco Lanza di Scalea. (2005). "Ultrasonic guided wave monitoring of composite wing skin-to-spar bonded joints in aerospace structures," *Journal of the Acoustical Society of America* **118**(4), pp. 2240-2252.

CONFERENCE PROCEEDINGS

1. Howard Matt, Ivan Bartoli, Salvatore Salamone, Francesco Lanza di Scalea and Piervincenzo Rizzo. (2007). "Enhanced passive and active damage detection by directional guided-wave piezocomposite transducers," *submitted to SPIE's Smart Structures/NDE Conference*, San Diego, CA, Mar. 18th-22nd.

2. Francesco Lanza di Scalea, Piervincenzo Rizzo, Howard Matt, Ivan Bartoli, Stefano Coccia, Gyuhae Park, Charles Farrar, Alessandro Marzani, Erasmo Viola, Giovanni Pascale, Salvatore Salamone, Mario Di Paola, and Antonella Pirrotta. (2006). "Health monitoring of civil and aerospace structural components by guided ultrasonic waves," *Proceedings of 4th World Conference on Structural Control and Monitoring,* San Diego, CA, July 11th-13th.

3. Howard Matt, Ivan Bartoli, Stefano Coccia, Francesco Lanza di Scalea, Gyuhae Park, and Charles Farrar. (2006). "Automated damage detection in UAV wing skin-to-spar joints based on outlier analysis of guided wave energy ," *Proceedings of 3rd European Workshop on Structural Health Monitoring*, Granada, Spain, July 5th-7th.

4. Francesco Lanza di Scalea, Howard Matt, Ivan Bartoli, Ankit Srivastava, Gyuhae Park, and Charles Farrar. (2006). "The fundamental response of piezoelectric guided-wave sensors and applications to damage and impact location," Proceedings of *3rd European Workshop on Structural Health Monitoring*, Granada, Spain, July 5th-7th.

5. Piervincenzo Rizzo, Howard Matt, Stefano Coccia, Francesco Lanza di Scalea, Ivan Bartoli, Alessandro Marzani, Erasmo Viola. (2006). "Guided ultrasonic waves for the inspection of structural components," *Proceedings of GIMC*, Bologna, Italy, June 26th-28th.

6. Howard Matt, Ivan Bartoli, Stefano Coccia, Francesco Lanza di Scalea, John Kosmatka, Gyuhae Park, and Charles Farrar. (2006). "Ultrasonic guided wave monitoring of composite bonded joints using macro fiber composite transducers," *Proceedings of SPIE's Smart Structures/NDE Conference*, San Diego, CA, Feb. 26th-Mar. 2nd, **6174**.

7. Ivan Bartoli, Alessandro Marzani, Howard Matt, Francesco Lanza di Scalea and Erasmo Viola. (2006). "Modeling wave propagation in damped waveguides of arbitrary cross-section," *Proceedings of SPIE's Smart Structures/NDE Conference*, San Diego, CA, Feb. 26th-Mar. 2nd, **6177**.

8. Howard Matt, Ivan Bartoli, Stefano Coccia, Francesco Lanza di Scalea, John Kosmatka, Gyuhae Park, and Charles Farrar. (2006) "Guided wave interrogation of composite bonded joints using MFC sensors," *Proceedings of 24th International Modal Analysis Conference*, St. Louis, MO, Jan. 30th-Feb.3rd.

9. Ivan Bartoli, Allessandro Marzani, Howard Matt, Francesco Lanza di Scalea, and Erasmo Viola. (2006). "Modeling guided wave propagation for structural health

monitoring applications," *Proceedings of 24th International Modal Analysis Conference*, St. Louis, MO, Jan. 30th-Feb.3rd.

10. Howard Matt, Ivan Bartoli, Stefano Coccia, Francesco Lanza di Scalea, John Kosmatka, Gyuhae Park, and Charles Farrar. (2005). "Built-in guided-wave diagnostic system for the wing skin-to-spar bond in unmanned aerial vehicles," *Proceedings of 5th International Workshop on Structural Health Monitoring, Stanford*, CA, Sept. 12th - 14th, pp. 453-461.

11. Howard Matt, Ivan Bartoli, Francesco Lanza di Scalea, Alessandro Marzani, Stefano Coccia, Joseph Oliver, John Kosmatka, Piervincenzo Rizzo, and Gaetano Restivo. (2005). "A guided-wave system for monitoring the wing skin-to-spar bond in unmanned aerial vehicles," *Proceedings of SPIE's Smart Structures/NDE Conference*, San Diego, CA, Mar. 7th-10th, **5765,** pp. 758-768.

12. Howard Matt, Alessandro Marzani, Gaetano Restivo, Joseph Oliver, Francesco Lanza di Scalea, John Kosmatka, Hoon Sohn, Gyuhae Park, and Charles Farrar. (2005). "A guided-wave monitoring system for the wing skin-to-spar bond in unmanned aerial vehicles," *Proceedings of 23rd International Modal Analysis Conference*, Orlando, FL, Jan. 30th-Feb.3rd.

13. Howard Matt and André Filiatrault. (2003). "A numerical study on the dynamic amplification of high voltage transformers," *Proceedings of TCLEE Sixth U.S. Conference and Workshop on Lifeline Earthquake Engineering*, Long Beach, CA, Aug. 10-13th.

TECHNICAL PUBLICATIONS

1. Howard Matt and André Filiatrault. (2004). "Seismic qualification requirements for transformer-bushing systems," *PEER Lifelines Report SSRP – 2003/12*, May.

2. Ho Jung Lee, Howard Matt, Terri Norton, Nikolaos Politis, and Jale Tezcan. "Tri-Center Review on Post Earthquake Reconnaissance, 2002 Molise Earthquake Field Mission 2003: Italy," MCEER Bulletin, 2003.

ABSTRACT OF THE DISSERTATION

Structural Diagnostics of CFRP Composite Aircraft Components by Ultrasonic Guided Waves

and Built-In Piezoelectric Transducers

by

Howard M. Matt

Doctor of Philosophy in Structural Engineering

University of California, San Diego, 2006

Professor Francesco Lanza di Scalea, Chair

To monitor in-flight damage and reduce life-cycle costs associated with CFRP composite aircraft, an autonomous built-in structural health monitoring (SHM) system is preferred over conventional maintenance routines and schedules. This thesis investigates the use of ultrasonic guided waves and piezoelectric transducers for the identification and localization of damage/defects occurring within critical components of CFRP composite aircraft wings, mainly the wing skin-to-spar joints.

The guided wave approach for structural diagnostics was demonstrated by the dual application of active and passive monitoring techniques. For active interrogation, the guided wave propagation problem was initially studied numerically by a semi-analytical finite element method, which accounts for viscoelastic damping, in order to identify ideal mode-frequency combinations sensitive to damage occurring within CFRP bonded joints. Active guided wave tests across three representative wing skin-to-spar joints at ambient temperature were then conducted using attached Macro Fiber Composite (MFC) transducers. Results from these experiments demonstrate the importance of intelligent feature extraction for improving the sensitivity to damage.

To address the widely neglected effects of temperature on guided wave base damage identification, analytical and experimental analyses were performed to characterize the influence of temperature on guided wave signal features. In addition, statistically-robust detection of simulated damage in a CFRP bonded joint was successfully achieved under changing temperature conditions through a dimensionally-low, multivariate statistical outlier analysis.

The response of piezoceramic patches and MFC transducers to ultrasonic Rayleigh and Lamb wave fields was analytically derived and experimentally validated. This theory is useful for designing sensors which possess optimal sensitivity toward a given mode-frequency combination or for predicting the frequency dependent directivity patterns in a transducer's response. Based upon this theory, a novel approach was developed for passive damage and impact location in anisotropic or geometrically complex systems. The detection and location of simulated "active" damage or impacts was experimentally demonstrated on a scaled CFRP honeycomb sandwich wing skin using this technique.

Chapter 1

Introduction

All civil, mechanical and aerospace structures are subject to damage as a result of fatigue, overloading conditions, material degradation through environmental effects, and unanticipated discrete events such as impacts or seismic events. Damage compromises the ability of the structure to perform its primary functions. Therefore, to ensure performance standards, extend the operational lifespan and maintain life-safety, many structural systems undergo routine inspections and maintenance. Common non-destructive evaluation (NDE) methods for evaluating the integrity of a structural component include the use of Eddy currents, acoustic emission, ultrasonic inspection, radiography, thermography or just basic visual inspection [1]. Depending upon the structural system, the cost associated with systematic time-based NDE inspection and maintenance can be substantial relative to the total life-cycle costs of the system. For commercial and military aircraft, it is estimated that 27% of the average life cycle costs are related to inspection and repair [2]. In addition, there is a corresponding opportunity cost associated with the loss in operational availability during maintenance.

Within the aircraft industry in particular, maintenance procedures are dependant upon the design methodology adopted for the vehicle components. The two dominant design methodologies are safe-life and damage tolerant [1]. For safe-life design, the operational lifespan of structural components is estimated through a statistical analysis. Inspection is not necessary for this methodology since the components are simply replaced prior to its specified design life. As a result, safe-life design is the least economical. Currently, many aircraft are designed according to the damage tolerant methodology. In this approach, models are used to predict the emergence of damage in various components under specified loading conditions.

Based upon these models, NDE inspection and preventive maintenance is performed at frequent time intervals to identify incipient damage and to prevent critical damage growth. An effort is currently being made to implement a newer condition based design methodology. In this case, maintenance is only performed when the system has undergone damage beyond a tolerable level.

Ideally, routinely scheduled inspection would be replaced by the integration of a built-in structural health monitoring (SHM) system that can perform continuous on-line diagnostics as well as prognostics. The objective for the diagnostics is to perform damage identification while the prognostics allows for an estimation of the remaining useful life of the system. Condition based maintenance, based upon an SHM philosophy, is the most economical option. Ideally, an SHM system will increase the operational availability, extend the lifespan of an aircraft, enhance life-safety and dramatically reduce life-cycle costs. It is estimated that a savings of 40% on inspection time and 20% on inspection/maintenance costs could result from the implementation of a properly designed SHM system [1].

The function of an SHM system is to collect periodically sampled dynamic response measurements of the structure using an integrated network of strategically placed transducers [3]. From these measurements, extracted damage sensitive features are then either used to solve a forward or inverse problem with system models or applied in statistical pattern recognition algorithms in order to evaluate the structural condition of the system.

One of the primary objectives of an SHM system is damage identification. Damage identification can be organized into a hierarchical pattern as follows [4]:

Level 1 (Damage Detection): Recognition that damage exists within the structure

Level 2 (Localization): Identification of the geometric position of damage

Level 3 (Classification): Classification of damage type when multiple damage scenarios exist

Level 4 (Assessment): Quantification of damage extent

Level 5 (Prediction): Estimation of residual life of the structure

1.1   General SHM Paradigm

Damage identification in accordance with an SHM paradigm involves progressive stages.   According to Sohn *et al.* [3] and Worden and Dulieu-Barton [4], this sequential process includes operational evaluation, data acquisition, signal processing, feature extraction and statistical pattern processing (Fig. 1.1).

Operational Evaluation: Define SHM objectives and system parameters

Data Acquisition: Collect system response measurements

Signal Processing: Cleanse, denoise and transform data

Feature Extraction: Quantify and collect damage sensitive variables

Statistical Pattern Processing: Characterize condition of system
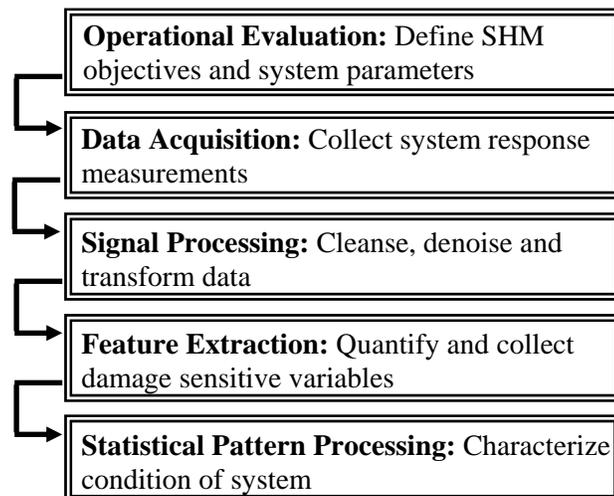
Fig. 1.1. Flowchart of SHM based damage identification process.

The operational evaluation entails the appraisal of economic and life safety motives for the SHM system, definition of damage within the structure, determination of the operational and environmental conditions under which the structure is subjected and how this may affect the ability for data acquisition.

Prior to data acquisition, the type, quantity and placement of transducers must be defined by taking into consideration the adopted damage features and statistical pattern

process.   Following these decisions, data acquisition involves the collection of the dynamic response measurements in the system.

Signal processing, which includes data cleansing, denoising and data transformation, is paramount in the damage identification procedure. Common methods of data cleansing and denoising include digital or analog filters, signal averaging and more recently, the use of the discrete wavelet transform.

Feature extraction consists of quantifying and collecting damage sensitive variables. For enhanced damage identification reliability, it is necessary to carefully select features that allow for maximum sensitivity to the particular damage of interest while also ensuring that their sensitivity to operational and environmental variability is minimal.   Due to likely stringent memory and processing limitations of on-board applications, features should be dimensionally low and computationally simple.

The final stage in damage identification is statistical pattern processing. This involves the application of algorithms that evaluate an observed feature vector in order to assign a corresponding condition of the structure to that vector.   The algorithms used for pattern processing fall within two distinct classes, namely supervised learning (SL) and unsupervised learning (UL). In SL, a set of training data with associated damage classes are determined through the use of structural models or experimental data. With this data, the algorithm can either assign a group classification or perform regression analysis to associate a new data set to the correct defect class within some statistical confidence. Application of SL techniques such as neural networks or support vector machines to SHM damage diagnostics can be found in Zapico *et al.* 2001 and McNamara *et al.* 2004 [5,6]. In UL, the algorithm only needs to indicate whether the observation is part of normal operating conditions, or is an anomaly due to damage. This approach greatly simplifies the diagnostics because there is no need for

collecting damaged data sets. However, relative to SL approaches, less damage information is attained. Several papers by Worden, Manson and others demonstrate the use of a popular UL approach, based upon outlier analyses, for damage detection in various structural systems [7-10]. Regardless of the statistical pattern process, it is important to recognize that the features characterizing the undamaged conditions of the structure are non-stationary as a result of environmental and operational variability. Therefore, to maximize the reliability of the damage identification procedure, the proper selection of damage features and the statistical pattern process must consider the structural application, damage type of interest, extent of damage information required to meet the SHM objectives, as well as the environmental and operational parameters of the system.

1.2   Global vs. Local SHM Approaches

An overwhelming number of SHM-based diagnostic methods have been proposed for damage identification. SHM diagnostic methods can be generally classified as either a global or local.

Global approaches are based upon relatively low frequency vibration measurements of the structure. Data acquisition can be done passively by relying upon the natural operational vibrations for source excitation or actively by forced vibration of the structure. The structural response is measured at discrete locations in terms of acceleration through the use of accelerometers, or strain by employing conventional foil gages, piezoelectric transducers or fiber Bragg gratings in some instances. Damage identification is typically achieved by the extraction of modal parameters such as resonant frequencies [11], modal damping [12], and mode shapes [13], followed by a forward or inverse solution to models of the system. Model based methods [11-13] fall within the category of supervised learning because the models

offer information on both undamaged and damaged conditions of the structure. The system is often modeled analytically for fairly simple structures or numerically using a finite element (FE) analysis for more complex structures. The forward problem involves the solution of the modal features from the input of a given damage type/location. An iterative process is pursued whereby multiple model solutions are compared with the actual measured change in modal parameters until an agreement is found. The inverse problem consists of computing the damage parameters by inputting the measured modal response characteristics into the model [14]. The solution is found by solving the constrained optimization problem to correlate model parameters, such as stiffness, with the modal parameters determined experimentally. Both methods of solution can result in as high as level 4 damage identification; depending upon the sophistication of the model. However, in order for model-based methods to work, there must be confidence that the baseline model accurately predicts the system response and can account for variability in operational and environmental conditions.

Model accuracy is essential for model based vibration-based methods. However, the use of a model is not required for low frequency vibration-based methods. Instead, a comparison of the vibration characteristics of the structure between damaged and undamaged baseline conditions of the structure can be directly assessed. This approach falls within the UL classification, thereby only yielding an indication of damage. Successful model independent vibration based methods have been demonstrated by comparing transmittance functions and resonant frequencies for undamaged and damaged structural conditions [15,16].

All global methods consider low frequency excitation, generally less than 50 KHz. As a result, they are inherently only sensitive to fairly large levels of damage. To detect smaller levels of damage, local SHM diagnostic methods can be utilized. These methods consider high frequency excitation; typically within the range of 10 kHz to 500 kHz. Consequently,

local SHM methods are capable of measuring more localized responses within the structure at the expense of requiring a more densely arranged sensing system. A wide range of local damage identification methods exist. For active diagnostics, excitation of the system occurs through the use of an actuating source such as a piezoelectric device. Conversely, passive diagnostics rely on excitation sources occurring from the quasi-static loading conditions or damage itself, i.e. impact or acoustic emission. Both methods of local system diagnostics have associated advantages and disadvantages. The most common active techniques are based upon the measurement of electro-mechanical impedance or the use ultrasonic guided waves [17-19]. With few exceptions, active methods require the measurement and storage of a vast amount of baseline information and often require a fairly dense array of transducers. However, active methods control the excitation characteristics within the system. Therefore, they possess the capability to customize the excitation in order to achieve greater sensitivity to specific defect types.

Local passive methods for damage identification can alleviate complications associated with the requirement of dense sensor arrays, large storage of baseline feature measurements, complex signal processing and statistical pattern process algorithms. The most common passive approaches use piezoelectric transducers to monitor impacts or acoustic emissions generated from internal material damage [20,21]. These methods thereby rely on measurements of propagating waves within the structure. In this scenario, damage detection is straight forward. Measurements above a specified threshold are assumed to correspond to the onset of damage. Damage localization can be evaluated through the use of simple triangulation algorithms. Otherwise, higher levels of damage identification can be achieved by incorporating neural networks or dynamic models. Damage identification through triangulation and neural networks or dynamic models corresponds to UL and SL statistical

pattern processes, respectively. A disadvantage of passive approaches is the requirement of continuous system monitoring, since it is generally not known when damage may occur. In addition, each of the passive methods discussed show difficulty in accurate damage identification for large scale complex structures which may be anisotropic, non-prismatic sandwich type systems connected to stiffening elements.

The emphasis of this thesis is placed upon the use of integrated piezoelectric transducers and guided ultrasonic waves for performing on-line structural diagnostics in both active and passive modes. Specifically, this thesis extends the current state of knowledge in active guided wave approaches to consider bonded Carbon Fiber Reinforced Polymer (CFRP) composite wing sections under changing environmental conditions. Semi-analytical finite element models were used to model the guided wave response in the various systems of interest. These models assisted in the selection of ideal guided wave features for experimental damage identification. In addition, analytical models characterizing the response of rectangular piezoelectric transducers to guided ultrasonic waves were derived. These models lead to the development of a new *in-situ* method for enhanced passive damage detection and location within non-prismatic, orthotropic structural elements. Guided wave damage identification was demonstrated on simulated CFRP wing skin-to-spar joints of Unmanned Aerial Vehicles (UAVs). The proof of principle tests will be useful when attempting to monitor an actual aircraft under realistic operational conditions.

The following sections of chapter 1 will discuss in a more comprehensive manner the variety of applied and proposed methods for fault detection in CFRP composite structures according to localized response measurements. In particular, emphasis will be placed upon damage identification studies for CFRP composite systems based upon the use of guided ultrasonic waves. This review will be followed by a discussion on the unique contributions of

this thesis to the field of guided-wave-based SHM diagnostics. Finally, chapter 1 will be concluded with an overview of the thesis structure.

1.3   Definition of Damage in CFRP Composite Components

Damage can be defined as changes in the material, geometry or connectivity of the system that adversely affect its current or future performance [3]. Although defects exist within any engineering material at the microscopic level, it is generally accounted for in the initial design of the structure, such as through the appropriate designation of material yield strength. As a result, the system can still perform according to the optimal design specifications. Contrarily, damage results in system performance below idealized conditions. Common damage sources include fatigue, overloading conditions, material degradation through environmental effects, and unanticipated discrete events such as impacts or seismic events.

Carbon fiber reinforced polymer (CFRP) composites are becoming widely used within the aerospace industry due to its very high specific strength and stiffness properties. However, FRP composites are also quite susceptible to various forms of damage. Common damage modes within FRP composites include matrix cracking, delamination, and fiber breakage [22]. For composite laminates, delamination is a major concern since this can significantly reduce the load carrying capacity of the laminate. Unlike metallic structures which are homogenous and have the ability to dissipate energy through yielding, composite structures are relatively brittle and exhibit weak interfacial strength between laminae. As a consequence, even low-velocity impacts on FRP composites can introduce significant delamination that is not visible from the surface.

Sandwich structures are commonly used in the aerospace industry because they tend to increase the energy absorption capabilities and bending stiffness without compromising the weight advantages of composites. In addition to the laminate damage described above, damage mechanisms in sandwich panels include core-face sheet debonding and core crushing [23]. The debonding between core and face sheet is a more prominent damage source for the reason that it can be induced by transverse loading conditions, such as low-velocity impact.

Although the damage mechanisms described above may be the primary concern for many applications, they do not necessarily constitute the most critical type of damage that can occur in a composite structure. For many structural systems, the connection joints of individual load bearing members are critical regions for maintaining overall structural integrity. In CFRP composite joints, the connection is often epoxy bonded as opposed to bolted to prevent the introduction of stress concentrations. Adhesively bonded composite joints can be found in some private all-composite aircraft, stiffened composite panels of the Airbus aircrafts and the wing skin-to-spar joint of Unmanned Aerial Vehicles (UAVs) [24]. Damage that can occur in adhesive bonded joints includes disbonds, porosity, poor bond adhesion, and reduced cohesive strength of the adhesive (Fig. 1.2) [25]. Disbonds have a more likelihood of occurring during service while porosity, poor adhesion, and reduced cohesive strength are generally a consequence of the manufacturing process. Disbonding due to overloading conditions is likely to result in a kissing bond scenario. For this disbond type, the surfaces are touching. Therefore, shear stress transfer is greatly reduced across the bondline while normal stress continuity is maintained. The existence of disbonds in the wing skin-to-spar joint diminishes the torsional rigidity of the aircraft's wing, compromising both performance and safety.
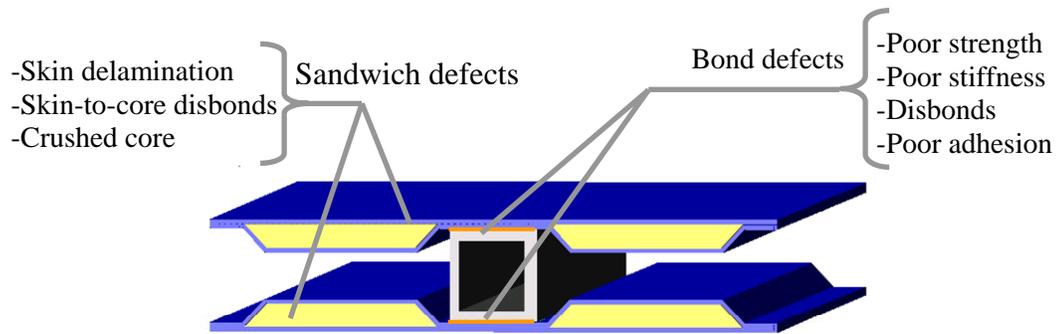
Fig. 1.2. Possible damage scenarios in CFRP adhesive joints found in aircraft structures.

Damage detection in CFRP composites presents more difficulty than metallic structures due to its mechanical anisotropy and heterogeneous composition. Damage generally occurs beneath the material surface and the brittle nature of high strength CFRP composites can lead to sudden failure mechanisms. Current NDE methods are often unreliable or impractical for inspection of large scale composite structures. Therefore, an SHM philosophy for damage identification is particularly well suited for aircraft comprised mainly of CFRP components, such as many UAVs. The following sections will initially discuss through thickness ultrasonic NDE techniques, followed by several applied and proposed methods for SHM damage identification in CFRP components based upon local response measurements.

1.4 Through Thickness Ultrasonic Methods for Inspecting Adhesive Bonds

A large number of ultrasonic inspection methods exist for the monitoring of bonded joints. Traditional ultrasonic NDE methods consist of generating and receiving bulk waves with conventional ultrasonic transducers either in a pulse-echo or pitch-catch mode across the joint [26]. The actuated and received waves can be done at normal or oblique-incidence as shown in Fig. 1.3.

NORMAL-INCIDENT
PULSE ECHO

NORMAL-INCIDENT
THROUGH TRANSMISSION

OBLIQUE-INCIDENT
PITCH-CATCH

actuator/receiver

actuator

actuator   receiver

(a)

(b)   receiver

(c)

adhesive bondline
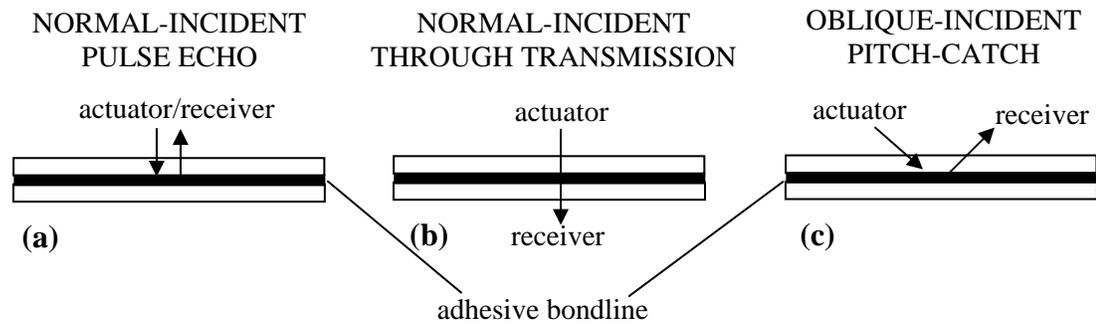
Fig. 1.3. Traditional ultrasonic NDE testing in (a) Normal-incident pulse echo (b) normal-incident through transmission and (c) oblique-incident pitch-catch modes.

Frequencies typically used during ultrasonic testing lie within the range of 0.1-20 MHz. Gross defects such as cracks, porosity, disbonds or voids cause a significant change in acoustic impedance occurring within the joint. Therefore, these damage sources can easily be detected by analyzing changes in either the reflected wave amplitude for normal incident pulse-echo and oblique incident tests or through transmitted wave amplitude for through transmission tests. Reflected bulk ultrasonic waves at oblique incidence are generally regarded to be more sensitive to bond conditions than normal incident waves [25]. A thorough theoretical analysis for this approach was presented by Rokhlin and Wang [27], where predicted reflection coefficients were shown to be sensitive to slip boundary conditions within the joint, i.e. continuity of normal stress with vanishing shear stress across the bondline.

Although effective for disbonds and voids, traditional ultrasonic test methods are generally ineffective in detecting changes in adhesive stiffness or strength. To measure such parameters, spectroscopy methods have been successfully employed. Ultrasonic spectroscopy measures the through-thickness longitudinal resonances of the multilayered joint structure [25]. The Fokker Bond Tester MK II, which uses relatively low frequency spectroscopic measurements (50-500 kHz), has been employed in aerospace applications for the detection of

voids and disbonds. This instrument can also estimate the cohesive strength in low strength joints (less than 1-2 GN/m^3) by correlating it to the measured specific stiffness, which is defined as the ratio of adhesive modulus to adhesive thickness [28]. For high-strength joints (2-3×10^4 GN/m^3 or greater), the Fokker Bond Tester MK II gives unreliable results in strength estimation due to its inability to accurately measure the specific stiffness. To improve the measurement capability of adhesive strength in high-strength joints, ultrasonic spectroscopy methods using typical frequencies in the range of 1-10 Mhz have been employed. Studies by Guyott and Cawley used normal-incidence ultrasonic spectroscopy testing to determine the modulus and thickness of the bond layer for high strength joints [28,29].

The previously described NDE methods for monitoring bonded joints are extremely localized and cannot be implemented within an SHM strategy. However, impedance and guided wave-based ultrasonic methods provide a greater damage detection range and lend themselves to built-in monitoring systems. The background and applicability of these two methods for monitoring CFRP components will described in the following sections.

1.5   Impedance-based Methods for SHM of CFRP Components

Electro-mechanical impedance-based methods of damage identification have generated considerable interest in the academic community over the past decade. This approach typically utilizes piezoelectric patches that act as collocated actuators/sensors. Piezoelectric devices have the ability to convert mechanical energy into electrical energy and *vice versa*. In the direct piezoelectric effect, mechanical strain induces an electrical charge. For the converse piezoelectric effect, the application of an electric field induces mechanical strain within the transducer.

The attached or embedded self-sensing piezoelectric actuators are used to simultaneously excite the structure harmonically and indirectly measure its mechanical impedance, $Z(\omega)$ (Fig. 1.4). The ability to evaluate the structures impedance is made possible by the fact that the electrical impedance of the piezoelectric transducer is a combined function of its mechanical impedance as well as that of the host structure. Electrical impedance is analogous to electrical resistance but specifically defined for alternating currents, therefore it is evaluated by taking the ratio of the input voltage and measured output current from the transducer [17]. Mechanical impedance is the ratio of applied force to the structure and resulting particle velocity.

IMPEDANCE METHOD
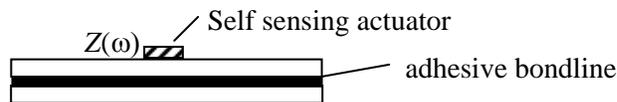
Fig. 1.4. Illustration of mechanical impedance, $Z(\omega)$ measurements within a bonded joint.

Changes in the mechanical properties of a structure will alter its mechanical impedance. Therefore, damage detection is accomplished by monitoring deviations in the real and imaginary part of the piezoelectric transducer's electrical impedance. Damage is identified by comparing features of the impedance spectrum evaluated at an unknown state with that acquired under undamaged baseline conditions. Impedance methods thereby fall within the classification of UL. The frequency of excitation is generally done within the range of 30-400 kHz, much higher than global vibration based methods [17]. As a consequence, impedance based methods are effective at identifying minor structural changes within the structure. However, the coverage area of this approach is generally limited to a small region surrounding the attached transducer. According to multiple studies, the sensing radius of a single PZT (Pb(Zr-Ti)O3) transducer on composite structures is around .4 m [17]. This can

vary greatly depending upon the material and geometric properties of the PZT and host structure as well as the frequencies ranges selected for damage detection.

Several studies have demonstrated the application of electro-mechanical impedance based methods for SHM damage identification in bonded composite repair patches. Chaudhry *et al.* [30] successfully identified minor debonding near the edge of the repair patch by observing changes in the electrical impedance of the PZT transducer. Excitation occurred within the frequency range of 1 kHz to 40 kHz. Crack growth under cyclic loading and progressive debonding resulted in clear shifts in the resonant frequencies of the structure. Results from the imaginary part of the impedance measurements also indicated changes in the corresponding phase-angles. Koh *et al.* [31] simulated disbonds between the repair patch and substrate structure by inserting Teflon release film of varying sizes near the patch edge. The electrical impedance was measured over two frequency ranges (0.4 kHz to 1 kHz and 1 kHz to 25 kHz) and for PZT transducers attached directly over the disbond and on the aluminum substrate. The relative reduction in impedance was generally consistent with the disbond area. As expected, the PZT mounted directly over the disbond was most sensitive to the simulated damage. Xu and Liu [32] developed a model of infinitesimal length springs to characterize the bond between composite repair patches and the host structure. These models were utilized to evaluate changes in the electrical admittance (inverse of impedance) of a bonded PZT transducer due to variation in the spring stiffness representing the repair patch bond. It was proposed that a quantitative determination of the bond integrity could be evaluated by minimizing the difference between the model predicted and experimentally measured admittance.

Raju *et al.* [33] also employed an impedance based monitoring approach to detect delamination and cracking within composite reinforced masonry walls. During monotonic

loading of the system, changes in the magnitude of the analyzed impedance spectrum clearly identified incipient damage growth within the structure prior to any physical indication of damage.

Electro-mechanical impedance based damage detection on CFRP composite laminates was investigated by Pohl *et al.* [34]. Delamination due to impacts was shown to influence the real part of the impedance magnitude and resonant peaks within the spectrum above 1 kHz. Changes within the resonant peaks, corresponding to eigenmodes of the structure, were more pronounced than the broad reduction in impedance magnitude. Finite element analyses corroborated these experimental results. Notable changes in the impedance response were also observed due to changes in the operational parameters such as loading conditions, integrity of the electrical contacts and aging effects. Bois and Hochard [35] also utilized impedance measurements and a beam model based upon laminate theory, which accounts for the piezoelectric constitutive laws, in order to investigate delamination damage. Damage was qualitatively identified by an increase in magnitude and observed shifts in the resonant peaks of the impedance spectrum.

Although impedance methods have demonstrated sensitivity toward changes in the structure due to damage, there are several issues which must be addressed in order for this method to be suitable for performing SHM diagnostics in realistic structures. The impedance features used for damage detection are often sensitive to variation in humidity, temperature and loading conditions. Therefore, intelligent feature extraction and robust pattern recognition algorithms must be incorporated into the approach. This is yet to be studied extensively. The majority of studies using an impedance approach require the use of bulky, and expensive impedance analyzers. For onboard applications, a simplified method of obtaining impedance

signatures is needed. The addressed studies also reveal the limitation of impedance methods for far-field damage detection.

1.6 Ultrasonic Guided Wave Methods for SHM of CFRP Components

Guided waves result from the constructive interference of bulk longitudinal and shear waves propagating within a confined geometry such as a railhead, wing skin, or pipeline. An illustration of the guided wave phenomenon, thought of as the superposition of bulk longitudinal and shear waves, is shown in figure 1.5. To satisfy the boundary conditions at each interface, mode conversion into to both longitudinal and shear waves occurs due to an incoming bulk wave. With enough propagation distance, the large number of mode converted bulk waves result in bulk wave resonances, otherwise known as guided waves.

L: Longitudinal wave
S: Shear wave
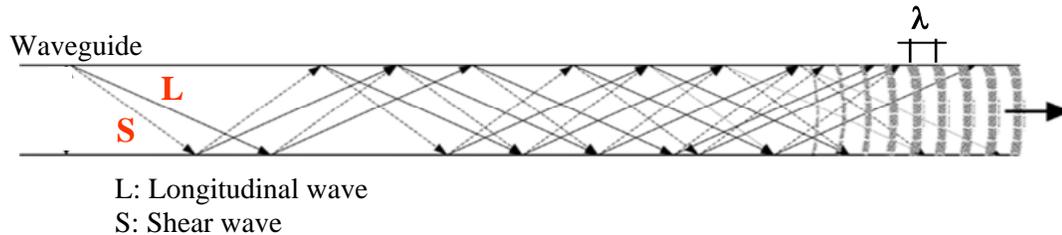
Fig. 1.5. Guided waves propagating within a confined geometry.

Most structural elements of aerospace vehicles are natural waveguides, thereby lending themselves to ultrasonic guided wave based SHM methods. The guided wave method can be an effective diagnostic tool due to its capability of long-range inspection as well as its flexibility in selecting sensitive mode-frequency combinations. In addition, through the use of built-in actuators and sensors, the guided wave approach is complementary to the development of integrated systems for continuous on-line diagnostics as opposed to regularly-scheduled NDT maintenance. The difficulties associated with the use of guided waves for

SHM include their dispersive nature (wave velocity is frequency dependant) and the existence of multiple modes propagating simultaneously.

For SHM applications, guided wave actuation is conducted using relatively inexpensive, unobtrusive, piezoelectric ceramics such as PZT (Pb(Zr-Ti)O3) or piezoelectric composites like the MFC (Macro Fiber Composite) or AFC (Active Fiber Composite) transducers. Sensing of guided waves can be achieved by similar piezoelectric transducers in addition to fiber optic sensors and piezoelectric films such as PVDF (poly(vinylidene fluoride)).

Feature extraction occurs within the ultrasonic regime. As a result guided wave methods are effective at identifying small localized damage while being relatively insensitive to in-service loading conditions occurring from static loads and low frequency vibrations within the structure.

Researchers have studied a vast number of approaches for SHM based damage identification in CFRP composite systems using guided ultrasonic waves. The majority of research has focused upon damage sources such as delamination, low velocity impact and disbonds in sandwich and stiffened CFRP structures. In general, each method can be categorized as either active interrogation, i.e. actuation and sensing within the system or passive monitoring, i.e. "listening" for impact/damage signatures. For an active diagnostic approach, the selection of specific mode-frequency combinations allows for enhanced sensitivity to a wide variety of damage types. Passive diagnostic methods can monitor relatively large areas for impacts or incipient/progressive internal damage.

Most recently, the majority of research has focused upon active methods because they do not require continuous system monitoring and enable more control of the wave characteristics and dynamics within the system. The most common features employed for

damage detection are related to wave energy or shape. Quantification of these features can be done within the time [36-39], frequency [40,41] and joint-time frequency domain [42-46] of reflected [19,47], diffracted [18,48] and through transmitted guided waves [21,49].

For structures with plate-like geometry, the location and extension of damage can be estimated with a fairly dense array of transducers by observing the intersected region of multiple actuator-receiver damaged paths [50,51]. A more sophisticated approach to damage localization is based upon time delay measurements of diffracted waves [18,52,53]. In this approach, the wavespeed is estimated and an elliptical function which characterizes possible damage locations is generated from each received waveform. Optimization routines are then utilized to triangulate the damage location as well as estimate the damage extension.

With few exceptions such as those based upon time reversal acoustics [54,55], active methods require the measurement and storage of baseline features and often require a fairly dense array of transducers. In addition, the dispersive nature of guided waves and their complex interaction with defects necessitate extensive signal processing and knowledge of the wave behavior. Variation in the environmental conditions and gradual aging of structural components may significantly alter baseline features of the pristine state, further complicating accurate damage identification. For this reason, intelligent feature extraction and the use of robust statistical pattern recognition algorithms is necessary for active SHM diagnostic methods.

Passive monitoring techniques can alleviate complications associated with the requirement of dense sensor arrays, large storage of baseline feature measurements, complex signal processing and robust pattern recognition routines. Current guided wave methods for passive damage detection will be discussed in section 1.8.

1.7   Other Methods for SHM of CFRP Components

Damage identification has been achieved using alternative methods to through-thickness ultrasonics, impedance and ultrasonic guided wave based approaches. In particular, quasi-static strain measurements have been used to for damage identification of bolted CFRP wing skin-to-spar joints [56] and disbonds occurring at bonded composite repair patches [57] and T-joints [58]. Strain measurements for quasi-static loading can be acquired using FBG sensors or conventional copper foil strain gages. Gupta *et al.* [56] used a neural network pattern recognition scheme to identify simulated damage. Jones and Galea [57] and Li *et al.* [58] adopted a UL approach using spatial strain gradient features to detect and locate damage.

Impact damage identification in CFRP composites has also been demonstrated by measuring changes in the electrical resistance across a composite panel [59]. Both strain based and electrical resistance methods of damage identification are extremely localized. As a result, these approaches are only practical for the monitoring of known damage critical regions of the structure.

As discussed, each particular SHM method for damage identification has associated advantages and limitations. Therefore combined methods have recently gained interest within the research community. Lemistre and Balageas [60] demonstrated a hybrid electromagnetic guided wave approach to identify damage within a CFRP plate. Features extracted from the electric field demonstrated sensitivity to simulated lighting strikes and local burning of the CFRP plate while guided wave features proved to be more sensitive to mechanical damage such as impacts. Combined methods of electric impedance/guided wave and electrical impedance/global vibration have also been employed for SHM based damage identification in composite systems [61-62].

1.8   Extension of Knowledge in Guided Wave SHM Theory and Application

The most significant original contributions of this thesis include the following:

1) Theoretical study of wave propagation in adhesively bonded CFRP joints (SAFE analyses);

2) Experimental application of guided waves for SHM of CFRP composite-to-composite bonded joints;

3) Application of outlier analyses for discrimination between joint damage and large temperature variations;

4) Analytical and experimental response characterization of piezoceramic (PZT) and MFC transducers to ultrasonic guided waves;

5) Theoretical and experimental quantification of temperature effects on guided wave measurements;

6) MFC rosette method for damage/impact localization in anisotropic or geometrically complex structures.

A summary of these research aspects are shown in Fig. 1.6. The subsequent sections will describe in more detail the original contributions of this thesis to the theory and application of guided wave based SHM. This will be prefaced by a partial review of documented research in each respective sub-topic.

Fig. 1.6. Original contributions of research to guided wave SHM.
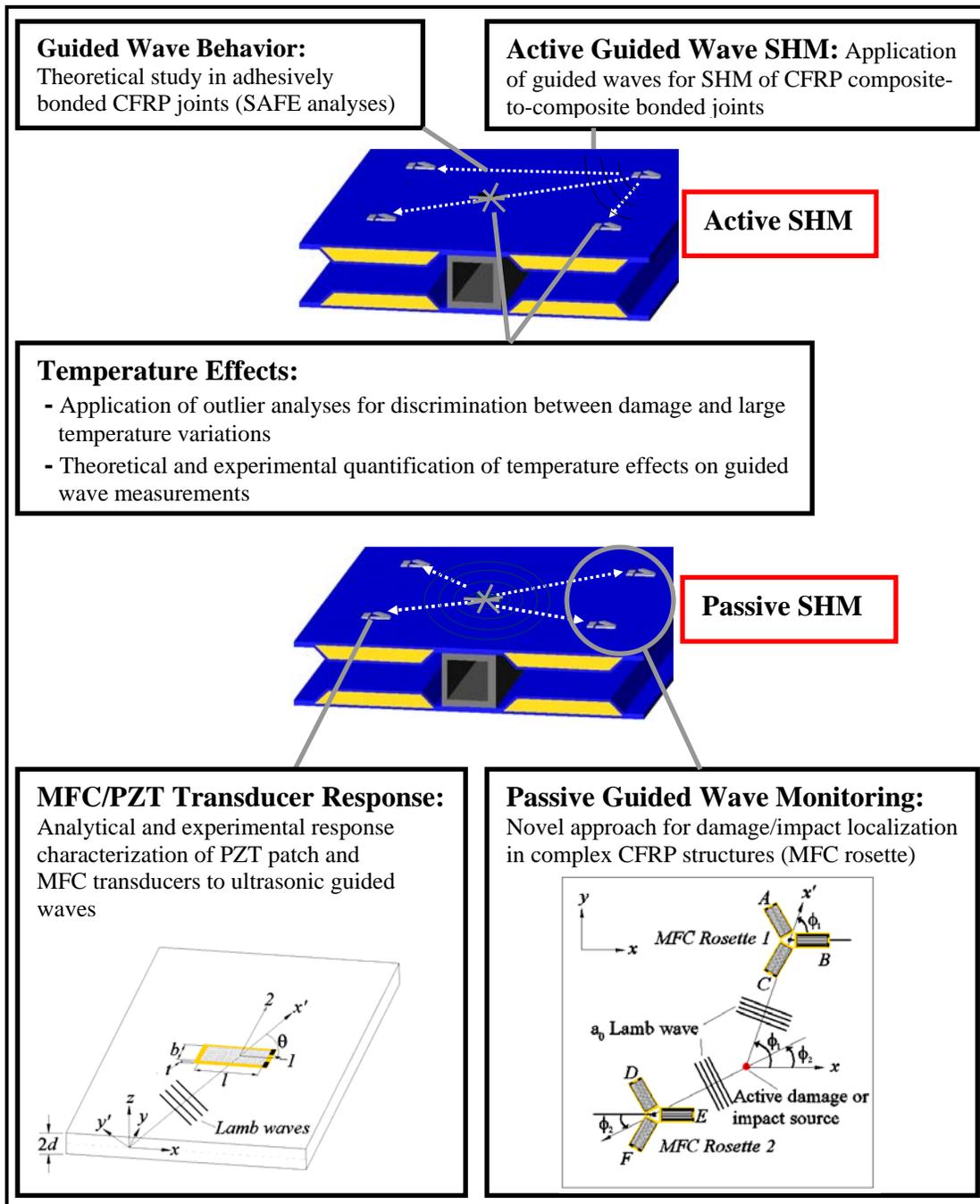
1.8.1   SAFE Analysis of Guided Waves in Viscoelastic Media

Exact solutions of guided wave propagation generally do not generally exist when modeling a large number of layers such as composite laminates and that of waveguides with arbitrary cross-section. Furthermore, when complex wavenumbers are part of the solution such as in the case of leaky and/or damped waveguides, exact methods require iterative bi-dimensional root searching algorithms that may miss some of the solutions [63]. As an alternative, the Semi-Analytical Finite Element (SAFE) approach has emerged as a promising technique to model such systems.

When modeling the entire waveguide, a Finite Element Method (FEM) requires three-dimensional discretization. However, the SAFE approach uses a finite element discretization of the waveguide cross-section only, while the displacements along the wave propagation direction are described by harmonic exponential functions. This concept is illustrated in Fig. 1.7. Numerically, the three-dimensional model of the waveguide is thus reduced to a bi-dimensional one, resulting in considerable computational savings.

Displacement field described as:
$$\mathbf{u}(x, y, z, \mathrm{t}) = \mathbf{U}(y, z)e^{i(kx-\omega \mathrm{t})}$$

$e^{i(kx-\omega \mathrm{t})}$

2-D discretization over the domain Ω
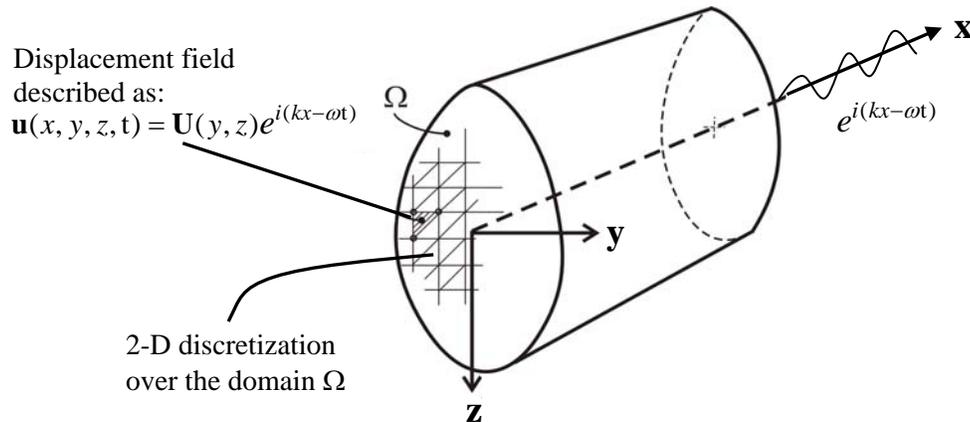
Fig. 1.7. Concept of SAFE model.

A SAFE model of waveguides having an arbitrary cross section was developed by Alaami in 1973 [64]. In this study, dispersive solutions were obtained for the propagative

modes only (i.e. real wavenumbers only). The same technique was used by Dong to study free vibration and standing waves in orthotropic circular cylinders [65] and to calculate both propagative modes and nonpropagative or evanescent modes (complex wavenumbers) in laminated orthotropic cylinders [66,67]. While the evanescent modes do not transport any energy along the structure, they are important from a theoretical viewpoint to satisfy the boundary conditions.   More recently, SAFE methods capable of only obtaining the propagative solutions were applied to wedges [68], rods and rails [69,70]. An approximation of the method in [69,70] was also implemented in a standard finite element package by imposing a cyclic axial symmetry condition [71]. Studies by Dong and Huang [72] and Mukdadi *et al.* [73] employed SAFE methods for analyzing laminated composite waveguides.

SAFE was also used in Kohl *et al.* [74] to perform an analysis of propagating and edge vibrations of anisotropic composite cylinders. More recently the approach was adopted to characterize the wave properties in a functionally graded cylinder considering a linear variation of the material properties in the thickness direction [75].

The focus of previous SAFE works was upon obtaining propagative and evanescent modes in undamped waveguides. However, for SHM applications on high-loss materials such as viscoelastic fiber-reinforced polymer composites, the inclusion of material damping within the model may be desired. One very recent work which demonstrates a SAFE application to damped, viscoelastic composite laminates is found in Shorter [76]. In this study, a damping loss factor was estimated indirectly from the power dissipated by the wave. The formulation therefore still does not allow for the calculation of the true frequency-dependant wave attenuation.

Within this thesis, a SAFE method, which accounts for material damping, was adopted for modeling guided wave dispersive solutions in CFRP laminates and bonded joints.

Damping was accounted for by incorporating a complex stiffness matrix for the material. Therefore the appropriate energy velocity, rather than the conventional group velocity, was calculated along with the frequency-dependent attenuation of the guided waves. The ability to compute wave attenuation was particularly useful for identifying ideal mode-frequency combinations which show preferential sensitivity toward damage sources in bonded CFRP joints.

1.8.2 Ultrasonic Guided Wave Monitoring of Bonded Joints

There are two approaches traditionally used for guided wave inspection of bonds. In the first approach, the waves are both generated and detected in the bonded region ("within the bond" testing configuration). In the second approach, the waves are generated in the adherend on one side of the bond and received across the bond ("across the bond" testing configuration). The main difference of the second approach is the occurrence of mode conversion when the wave enters and leaves the bond due to the transition from the single adherend geometry to the bonded assembly geometry, and viceversa. Several previous studies used the "within the bond" configuration to relate wave amplitude, velocity and frequency to the elastic properties of the adhesive layer [77-89]. Recent applications of the "within the bond" configuration have also examined the possibility of inspecting the bond between a composite skin and a core in sandwich aerospace panels [90,91]. The "across the bond" configurations was also used successfully for the inspection of lap-shear joints, tear strap-to-skin joints, and bonded patch repairs for damaged aircraft panels [92-99].

These previous studies provided a great deal of knowledge on the behavior and defect sensitivity of various guided wave modes propagating in adhesively-bonded joints. However, none of these works examined the case of composite-to-composite bonded joints, such as

those found in wing skin-to-spar bonds of UAVs. In addition, the majority of previous works were not focused on built-in structural monitoring systems. The preferred application of built-in guided wave sensing arrays has been the detection of delamination and impact damage in FRP aerospace panels, rather than the condition monitoring of bonds [18,42,43,52,100-104].

Only a couple of known studies exist on active guided wave SHM of bonded CFRP composites [38,105]. Both of these works focused primarily on disbonds occurring between CFRP repair patches and the concrete substrate.

This thesis extends active ultrasonic guided wave methods to the structural health monitoring of composite-to-composite bonded joints. MFC transducers were employed since they are better candidates for on-board applications than the commonly used piezoceramic elements. The specific bond damage considered includes disbonds and regions where the stiffness of the adhesive is significantly reduced.

1.8.3 SHM Damage Identification in a Variable Temperature Environment

On-board application of an SHM system will require a statistical pattern process capable of robust damage identification accuracy despite large variation in environmental and structural conditions. The range in the environmental and operational state will lead to significant changes in the features used for damage detection. If not accounted for, this effect increases the probability of false damage classification. In acknowledgement of this, several researchers have successfully employed a statistical outlier approach for anomaly detection under varying operational conditions [7,8,106,107]. The study by Surace and Worden [106] considered damage detection in a off shore drilling platform model. Changes in the operational conditions resulted from varying the stored oil mass upon the deck. Manson *et al.* [8] studied the influence of temperature on the outlier approach applied to guided wave

features. Analyses only considered a small range of temperature change, 20 deg. C to 30 deg. C, and did not attempt to differentiate between normal and damaged conditions of the structure. Sohn *et al.* [107] successfully demonstrates a novelty detection approach on low frequency strain data acquired upon a fast surface patrol boat. Statistical variation with the data resulted from differences in the environmental and operational conditions. No measures of the operational and environmental conditions were provided and due to the limited data, this study did not consider known damaged observations during the outlier analyses. The study by Worden *et al.* [7] employed an outlier approach to simulated data of a 2 DOF lumped-mass system. Damage and temperature effects were accounted for in the model by mathematically relating these parameters with the prescribed damping and stiffness of the system. Lee *et al.* [108] utilized guided waves and a principal component analysis in an attempt to distinguish between damage in an aluminum plate and feature changes resulting from temperature variation. The temperature range considered was between 35 deg. C to 70 deg. C. This study concluded that the adopted method was unsuccessful in discriminating between damage and temperature effects. More recently, Michaels and Michaels [109] and Konstantinidis *et al.* [110] studied the effect of temperature on diffused waves propagating in an aluminum plate; however, neither study employed a statistical pattern approach for damage identification. In addition, only small variations in temperature were considered.

This thesis successfully demonstrates a novelty detection approach for automated damage identification within CFRP joints despite large changes in the ambient temperature. Compared with previous studies, both temperature and damage in a CFRP system was considered. Furthermore, damage detection was demonstrated over a very broad temperature range (-40 deg. C to 60 deg. C), which is typical of grounded and or operational aircraft conditions. Discrimination between normal operating conditions and damaged conditions was

accomplished through a dimensionally-low multivariate outlier analysis. As opposed to the approach suggested by Worden *et al.* [7], only two baseline measurements corresponding to above and below ambient temperature were required to achieve positive detection of the damage states.

1.8.4   Response of MFC and PZT Transducers to Ultrasonic Waves

With the advent of on-board SHM systems based on ultrasonic waves, piezoelectric transducers are being increasingly used due to their low-cost, low-profile, and ease of integration within the structure. The fundamental electro-mechanical behavior of piezoelectric transducers is well understood [111-114], and the transducer-structure interaction has been previously addressed for applications involving Lamb waves. One of the earliest works was conducted by Monkhouse *et al.* [115] on piezoelectric polymer films for Lamb wave transduction. The authors extended the use of piezoelectric films with interdigitated electrodes, previously exploited for generating narrowband surface acoustic waves, to the actuation of Lamb waves. Moulin *et al.* [116] utilized a hybrid method (finite element and normal mode expansion) to solve for the Lamb wave response resulting from surface-mounted and embedded piezoelectric actuators in CFRP laminates. Lin and Yuan [117] analytically derived the voltage response of a piezoceramic sensor attached to a plate and subjected to narrowband (toneburst) excitation originating from a piezoceramic actuator. In this study Mindlin plate theory was used to examine the fundamental antisymmetric A_0 mode below the cut-off frequencies of higher-order modes. Giurgiutiu [114] analytically derived and experimentally validated the Lamb wave tuning capability of attached piezoceramic actuators for both the fundamental symmetric, S_0, and antisymmetric, A_0, mode. He found that the preferential excitement of specific mode-frequency combinations occurs according to the

relation between the Lamb wavelength (or wavenumber) and the dimension of the actuator (wavelength tuning). Giurgiutiu's closed form solution for the actuator-generated waves assumes harmonic excitation and was obtained by coupling a pin-force shear stress at the plate's surface (two concentrated in-plane forces at either end of the transducer) with the theoretical Rayleigh-Lamb displacement and strain fields.

Building on the above work, Raghavan and Cesnik [118] used 3-D linear elasticity to obtain the general solution for S_0 and A_0 circularly-crested waves excited by a circular piezoceramic actuator. The pin-force shear stress excitation was, again, assumed to predict displacement and strain fields generated in the plate. The solution was derived for both harmonic excitation and narrowband (toneburst) excitation. This study also examined the voltage response of piezoceramic *sensors* subjected to harmonic Lamb wave fields generated by either rectangular piezo-actuators (plane wave fields) or circular piezo-actuators (circularly-crested wave fields). One important conclusion was that wavelength tuning conditions do not necessarily govern the response of piezo-sensors. Rather, the general theoretical trend is a monotonic increase in the output voltage with decreasing sensor dimension as a result of averaging the wave strain field over the sensor gage length.

It should be noted that the difference in response between a piezo-actuator and a piezo-sensor, indeed, does not contradict elastodynamic reciprocity conditions. The pin-force applied by a finite-size actuator will generally excite multiple modes of the structure. Based on reciprocity, the response of the same finite-size sensor to an excitation consisting of the same, multiple modes would be equivalent to the response of the actuator. This equivalence is being recently used in baseline-free damage detection based on time-reversal acoustics using pitch-catch actuator-sensor pairs. However, the response of a sensor to a single incoming mode cannot be immediately recovered from the pin-force actuation solution on the basis of

reciprocity.

Greve *et al.* [119] and Nieuwenhuis *et al.* [120] compared Giurgiutiu's theoretical models for S_0 and A_0 harmonic excitation by a piezo-actuator to finite element simulations of narrowband (toneburst) excitation. Their model showed slight shifts in the frequencies at which wavelength tuning occurs compared to the theoretical harmonic case. This work also examined the response of piezo-sensors to the piezo-actuated fields under narrowband excitation. It was confirmed that the response of the piezo-sensor to Lamb waves cannot be predicted by the pin-force piezo-actuator model.

The majority of the works reviewed above have covered the response of monolithic piezoelectric sensors to piezo-generated wave fields. It is of interest to examine the fundamental response of a piezo-sensor to an incoming arbitrary wave field. This knowledge is relevant, for example, to passive-only structural monitoring (e.g. acoustic emission testing) and, also, to active monitoring when the piezo-actuated wave changes dispersive properties prior to reaching the piezo-sensor. The latter case, for example, can occur through mode conversions caused by scattering at small discontinuities or simply by changes in the waveguide thickness.

In an extension to the above studies, this thesis examines the fundamental response of surface-mounted, monolithic piezoelectric sensors subjected to harmonic, broadband and narrowband wave fields under plane wave hypotheses. The study first considered the case of Rayleigh surface waves and subsequently that of Lamb waves. The response of Macro Fiber Composite (MFC) transducers to broadband plate waves was also derived. The sensor voltage response was derived by coupling the direct piezoelectric effect to the wave strain field that is averaged over the effective electrode area. Analytical expressions are obtained for the general case of waves propagating at oblique incidence relative to the rectangular sensor orientation.

The predictions are compared to experimental data for the broadband excitation cases on aluminum and both aluminum and CFRP composite plates for the PZT and MFC transducers, respectively.

1.8.5   Temperature Effects on Guided Wave Signals

Very few published works exist on the effect of temperature upon guided wave signals acquired by piezoelectric transducers. Michaels and Michaels [109] experimentally examined disparity in multiple features extracted from diffused signals as a result of temperature variation between 5 deg. C to 40 deg. C. Konstantinidis *et al.* [110] compared the variation in wave amplitude for specific regions of a diffused signal. These regions of the signal included coherent noise, the first arrival of the fundamental S_0 and A_0 modes and edge reflections. The change in wave amplitude was identified experimentally for temperature variation between 22 deg. C to 32 deg. C. Simulations were also run to identify changes in the amplitude of the A_0 wavepacket resulting from deviation in plate thickness, propagation distance, and Young's modulus of the aluminum plate. Lee *et al.* [108] merely observed the effects of temperature on guided wave signals, but did not consider their origin.

This thesis addresses in detail the effect of temperature on the guided wave signals acquired by piezoelectric transducers. The influence of temperature on the mechanical, electrical and thermal properties of each layer in the transducer-structure system were used as a basis for justifying known variations in guided wave signals as a function of temperature. Theoretical and experimental analyses were performed to validate the qualitatively described effects.

1.8.6 Passive Damage/Impact Detection and Location in Complex CFRP Systems

Researchers have studied a vast number of approaches to obtain level 2 diagnostics (damage detection and location) of CFRP composite systems using guided ultrasonic waves.   An unsupervised approach based upon triangulation of impacts or acoustic emissions has been extended to anisotropic composite plates. This was achieved by utilizing genetic algorithms to perform optimization routines [121] or assumptions of constant wavespeed [122]. Triangulation methods in composites have their limitations as well. These include the types of damage it is capable of detecting, as well as the associated increase in complexity and corresponding decrease in accuracy for complex structures which may be highly anisotropic, non-prismatic sandwich type systems connected to stiffening elements. For such systems, error in triangulation based methods results from the large variation in wavespeed as a function of propagation path.

Specifically for impact monitoring, supervised learning methods based upon the use of neural networks [123] and dynamic models [124] have been employed with success for more complex composite systems. However, neural networks require an extensive number of training observations while dynamic models must be uniquely and accurately developed for a particular system, making both approaches difficult to implement in full scale structures.

This thesis introduces a novel approach for damage detection and location within complex composite systems that does not require the direct use of optimization routines, training data or models. Ideally, this technique could be adopted for both active and passive diagnostics. The method employed MFC transducers arranged in a rosette configuration. The rectangular geometry of these transducers was exploited such that response characteristics

exhibit predictable directivity behavior. When positioned in a rosette arrangement, the guided wave source location was deduced without requiring knowledge of the wavespeed.

A similar fiber optic rosette approach was demonstrated in the past for guided waves diffracted from defects [125]. This approach however cannot be done in a passive manner and requires the use of optimization routines and successive measurements as a result of the multiplexed optical fiber. The only other known use of a transducer rosette concept for guided wave applications was done using piezoelectric transducers in a conventional active mode in order to better control the actuated wave characteristics. In this study, simulated damage location and severity was predicted through the dual application of a dynamic plate model and supervised neural network [126].

For the proposed method, damage location can be resolved due to diffracted signals, impacts or acoustic signals emitted under overstrained structural conditions. This thesis emphasizes the use of MFC rosettes for passive damage detection and location for the latter two cases. The development of MFC rosette theory was based upon the derived response characteristics and directivity behavior of MFC transducers to broadband ultrasonic Lamb waves. This theory enables the direction of incoming elastic waves to be evaluated. Finally, the application of this concept was demonstrated for the detection and location of simulated damage on an aluminum plate, composite plate, and a scaled CFRP honeycomb wing skin specimen.

1.9   Thesis Overview

The emphasis of this thesis is placed upon the use of integrated piezoelectric transducers and guided ultrasonic waves for performing on-line structural diagnostics. Specifically, this thesis extends the current state of knowledge in active guided wave

approaches to consider bonded carbon fiber reinforced polymer (CFRP) composite wing sections under changing environmental conditions.

Semi-analytical finite element models are used to model the guided wave response in the various systems of interest. These models assisted in the selection of ideal guided wave features for experimental damage identification. In addition, analytical models are derived which characterize the response of rectangular piezoelectric transducers used strictly in a passive mode for the detection of guided ultrasonic waves. Results from these models lead to the development of a new *in-situ* method for enhanced passive damage detection and location within anisotropic or geometrically-complex structural elements.

Chapter 2 gives an overview of guided wave solutions in isotropic and anisotropic multi-layer structures. The response of rectangular PZT and MFC transducers to ultrasonic Rayleigh and Lamb waves is discussed in chapter 3. The expressions describing the theoretical transducer responses were validated through simple experimental tests. Chapter 4 introduces the theoretical framework for SAFE modeling of guided waves. Practical application of the SAFE solutions for damage identification is also discussed. The SAFE model results are presented in chapter 5 for CFRP plate-to-spar bonded joints. Chapter 6 discusses an experimental study of active guided wave damage identification on two CFRP plate-to-spar bonded joints. Chapter 7 extends these results for a specimen subjected to a widely varying temperature environment. The effects of temperature on guided wave signals and an overview on novelty detection by means of an outlier analysis are also included. Chapter 8 presents the SAFE model results for a scaled representation of a UAV wing skin-to-spar joint. This is followed in chapter 9 by the experimental results for active guided wave damage identification for this particular specimen at ambient temperature. The final chapter introduces a novel approach for damage detection and location upon a scaled honeycomb

sandwich wing skin through the use of MFC rosettes. Initially, the theory for MFC rosette based damage detection is developed. Experimental application of this concept was demonstrated for the detection and location of simulated damage on an aluminum plate, a composite plate, and a scaled CFRP honeycomb wing skin specimen.

Finally, the thesis concludes with a brief discussion on the key results of this research, potential complications in the outlined methods for application to real aircraft structures, and research topics requiring further study.

Chapter 2

Overview of Guided Wave Solutions

2.1 Guided Waves in Single Isotropic Elastic Layer

Prior to deriving the guided wave solutions in a bounded isotropic layer, it is important to understand wave propagation in an unbounded medium. According to Newton's second law, the equations of motion of a three-dimensional body (neglecting body forces) are described as [127]:

$$\frac{\partial \sigma_x}{\partial x} + \frac{\partial \sigma_{xy}}{\partial y} + \frac{\partial \sigma_{xz}}{\partial z} = \rho \frac{\partial^2 u_1}{\partial t^2}$$

$$\frac{\partial \sigma_y}{\partial y} + \frac{\partial \sigma_{xy}}{\partial x} + \frac{\partial \sigma_{yz}}{\partial z} = \rho \frac{\partial^2 u_2}{\partial t^2} \tag{2.1}$$

$$\frac{\partial \sigma_z}{\partial z} + \frac{\partial \sigma_{yz}}{\partial y} + \frac{\partial \sigma_{xz}}{\partial x} = \rho \frac{\partial^2 u_3}{\partial t^2}$$

where ρ is the density of the material and u_1, u_2 and u_3 corresponds to the displacement along the x, y and z cartesian coordinates. These equations hold regardless of the stress-strain behavior of the medium. The generalized form of Hooke's law relating stress and strain in elastic material is:

$$\begin{Bmatrix} \sigma_{xx} \\ \sigma_{yy} \\ \sigma_{zz} \\ \sigma_{yz} \\ \sigma_{zx} \\ \sigma_{xy} \end{Bmatrix} = \begin{bmatrix} C_{11} & C_{12} & C_{13} & C_{14} & C_{15} & C_{16} \\ C_{12} & C_{22} & C_{23} & C_{24} & C_{25} & C_{26} \\ C_{13} & C_{23} & C_{33} & C_{34} & C_{35} & C_{36} \\ C_{14} & C_{24} & C_{34} & C_{44} & C_{45} & C_{46} \\ C_{15} & C_{25} & C_{35} & C_{45} & C_{55} & C_{56} \\ C_{16} & C_{26} & C_{36} & C_{46} & C_{56} & C_{66} \end{bmatrix} \begin{Bmatrix} \varepsilon_{xx} \\ \varepsilon_{yy} \\ \varepsilon_{zz} \\ \gamma_{yz} \\ \gamma_{zx} \\ \gamma_{xy} \end{Bmatrix} \tag{2.2}$$

where C_{ij} represent the elastic constants of the material. For a material which is anisotropic, 21 independent elastic constants exist. For an isotropic solid, the number of independent elastic constants reduces to two, denoted as Lamé's constants λ_L and μ_L. The Lamé constants are directly related to the Young's modulus, Y^E and Poisson' ratio, ν of the material. The stress-strain relation for an isotropic medium can thereby be represented in tensor form as:

$$\sigma_{ij} = \lambda_L \delta_{ij} \varepsilon_{kk} + 2\mu_L \varepsilon_{ij} \tag{2.3}$$

where δ_{ij} is the Kronecker delta and $\varepsilon_{kk} = \varepsilon_{xx} + \varepsilon_{yy} + \varepsilon_{zz}$ is the dilatation. Substitution of the stress-strain relation into the equations of motion described by eq. (2.1) leads to Navier's equation of motion for an isotropic, elastic medium:

$$(\lambda_L + \mu_L)\vec{\nabla}(\vec{\nabla} \bullet \vec{u}) + \mu \nabla^2 \vec{u} = \rho \frac{\partial^2 \vec{u}}{\partial t^2} \tag{2.4}$$

In Navier's equation, $\vec{u}$ is the displacement vector, and $\vec{\nabla}$ represents the divergence vector and the operator $\nabla^2 = \frac{\partial^2}{\partial x^2} + \frac{\partial^2}{\partial y^2} + \frac{\partial^2}{\partial z^2}$. Based upon Clebsch theorem, the displacement $\vec{u}$ can be decomposed into dilatation and rotation using the scalar and vector potentials ϕ and $\vec{\psi}$ such that:

$$\vec{u} = \vec{\nabla}\phi + \vec{\nabla} \times \vec{\psi} \qquad \text{with} \qquad \vec{\nabla} \bullet \vec{\psi} = 0 \tag{2.5}$$

Plugging the displacement vector into Navier's equation results in the following expression:

$$\vec{\nabla}\left[(\lambda_L + 2\mu_L)\nabla^2\phi - \rho\frac{\partial^2\phi}{\partial t^2}\right] + \vec{\nabla} \times \left[\mu_L\nabla^2\vec{\psi} - \rho\frac{\partial^2\vec{\psi}}{\partial t^2}\right] = 0 \tag{2.6}$$

This equation is satisfied if either the scalar or vector potential vanishes, resulting in two decoupled wave equations:

$$c_L^2 \nabla^2 \phi = \frac{\partial^2 \phi}{\partial t^2}, \qquad c_T^2 \nabla^2 \vec{\psi} = \frac{\partial^2 \vec{\psi}}{\partial t^2}, \tag{2.7}$$

where:

$$c_L = \left(\frac{\lambda_L + 2\mu_L}{\rho} \right)^{1/2}, \qquad c_T = \left(\frac{\mu_L}{\rho} \right)^{1/2} \tag{2.8}$$

Therefore, two types of bulk waves exist; namely dilatation waves traveling with a constant speed of c_L and rotational waves traveling at a constant speed of c_T.

Now let us consider wave propagation in a bounded isotropic, elastic plate with thickness $2d$ as shown in Fig. 2.1.
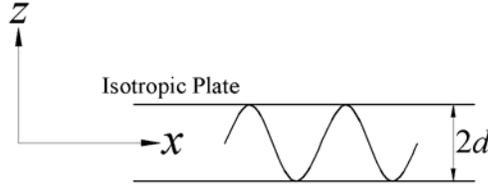
Fig. 2.1. Guided wave propagation within a thin isotropic plate

Displacement u_z and the z axis corresponds to the through thickness direction and the displacement u_x and the x axes corresponds to the direction of propagation. The coordinate $z=0$ is taken to be at the mid-plane of the plate. It is assumed that plane strain conditions exist such that the out of plane displacement $u_y = 0$ and $\frac{\partial}{\partial y} = 0$. From eq. (2.5), the displacement is expressed as [128]:

$$\begin{aligned} u_x &= \frac{\partial \phi}{\partial x} + \frac{\partial \psi}{\partial z} \\ u_z &= \frac{\partial \phi}{\partial y} - \frac{\partial \psi}{\partial z} \end{aligned} \tag{2.9}$$

For simplicity, the subscript y has been omitted from ψ in eq. (2.9). Plugging in the expressions for u_x and u_z into Navier's equation, we obtain the two partial differential wave equations for which plane strain is two-dimensional:

$$\frac{\partial^2 \phi}{\partial x^2} + \frac{\partial^2 \phi}{\partial z^2} = \frac{1}{c_L^2} \frac{\partial^2 \phi}{\partial t^2}$$
$$\frac{\partial^2 \psi}{\partial x^2} + \frac{\partial^2 \psi}{\partial z^2} = \frac{1}{c_T^2} \frac{\partial^2 \psi}{\partial t^2}$$

(2.10)

The general solution for ϕ and ψ are expressed as:

$$\phi = \Phi(z)\exp[i(kx - \omega t)]$$
$$\psi = \Psi(z)\exp[i(kx - \omega t)]$$

(2.11)

where $\Phi(z)$ and $\Psi(z)$ is an expression that represents standing waves in the z direction and the $\exp[i(kx - \omega t)]$ term represents a propagating wave in the x direction. The terms k and ω represent the spatial distribution and temporal frequency of the wave, otherwise known as wavenumber and angular frequency respectively. The wavenumber is related to the wavelength by $k=2\pi/\lambda$. Now plugging in eq. (2.11) into the two partial differential wave equations, the wave equations reduce to two ordinary differential equations such that the solution, with r and s imaginary, leads to two complex exponential expressions for $\Phi(z)$ and $\Psi(z)$, which can be simplified as:

$$\Phi(z) = A_1 \sin(rz) + A_2 \cos(rz)$$
$$\Psi(z) = B_1 \sin(sz) + B_2 \cos(sz)$$

(2.12)

where A_1, A_2, B_1 and B_2 are the wave amplitudes. The terms r and s are represented as:

$$r = \left(\frac{\omega^2}{c_L^2} - k^2 \right)^{1/2}$$
$$s = \left(\frac{\omega^2}{c_T^2} - k^2 \right)^{1/2}$$

(2.13)

Using the wave equation solutions in eq. (2.11), the displacements and stresses can be evaluated from eqs. (2.3) and (2.9) respectively as:

$$u_x = [ik\Phi + \frac{d\Psi}{dz}]\exp[i(kx - \omega t)]$$

$$u_z = [\frac{d\Phi}{dz} - ik\Psi]\exp[i(kx - \omega t)]$$

$$\sigma_{xz} = [\mu(2ik\frac{d\Phi}{dz} + k^2\Psi + \frac{d^2\Psi}{dz^2})]\exp[i(kx - \omega t)]$$

$$\sigma_{zz} = [\lambda(-k^2\Phi + \frac{d^2\Phi}{dz^2}) + 2\mu(\frac{d^2\Phi}{dz^2} - ik\frac{d\Psi}{dz})]\exp[i(kx - \omega t)]$$

(2.14)

where $\Phi(z)$ and $\Psi(z)$ are defined in eq. (2.12). From eq. 2.14 it can be seen that the displacement components can be written in terms of elementary functions. For the displacement in the x direction, the motion is symmetric (antisymmetric) with respect to the mid-plane, if u_x contains cosines (sines). The displacement in the z direction is symmetric (antisymmetric) if u_z contains sines (cosines) [128]. The modes of wave propagation can thus be split into symmetric and antisymmetric solutions. Therefore for symmetric and antisymmetric modes:

$$\Phi(h) = A_2 \cos(rz)$$
$$\Psi(h) = B_1 \sin(sz)$$
Symmetric (2.15)

$$\Phi(h) = A_1 \sin(rz)$$
$$\Psi(h) = B_2 \cos(sz)$$
Antisymmetric (2.16)

where the expression relating frequency ω to the wavenumber k is obtained by utilization of the boundary conditions. For free boundaries, we thus impose at $z = \pm d$ that $\sigma_{xz} = \sigma_{zz} = 0$.

For the symmetric modes, application of these boundary conditions yields a system of two homogeneous equations for the constants A_2 and B_1. Similarly for the antisymmetric modes, we obtain two homogeneous equations for the constants A_1 and B_2. Since the systems

are homogeneous, we take the determinant of each system to obtain the simplified expressions

which relate ω and k. These expressions are shown as:

$$\frac{\tan(sd)}{\tan(rd)} = -\frac{4k^2 rs}{(s^2 - k^2)^2} \qquad\qquad \textbf{Symmetric modes} \qquad\qquad (2.17)$$

$$\frac{\tan(sd)}{\tan(rd)} = -\frac{(s^2 - k^2)^2}{4k^2 rs} \qquad\qquad \textbf{Antisymmetric modes} \qquad\qquad (2.18)$$

These are the commonly found expressions for the Rayleigh-Lamb frequency equations. An

infinite number of eigensolutions exist for eqs. (2.17) and (2.18), thereby an infinite number of

guided wave modes exist. Each eigenvalue corresponds to a particular angular frequency and

mode of propagation, namely symmetric or antisymmetric. At low frequencies, only two

propagating modes exist corresponding to the fundamental symmetric mode, S_0 and

antisymmetric mode, A_0. For each eigenvalue, a corresponding set of eigencoefficients also

exist: $\left(A_2, B_1\right)$ and $\left(A_1, B_2\right)$ for the symmetric and antisymmetric case respectively. These

coefficients can be used in eq. (2.14) to evaluate the Lamb mode shapes across the plate depth.

The Lamb wave speeds are also a function of the frequency and are given as $c = \omega/k$ where c

denotes the phase velocity for a particular mode. As a result, Lamb waves are dispersive. The

speed at which the guided wave packet (or envelope) travels is known as the group velocity

and is evaluated as $c_{gr} = \partial\omega/\partial k$. The guided wave dispersion solutions for a particular system

are most commonly represented through (phase velocity) vs. (frequency×thickness) and

(group velocity) vs. (frequency×thickness) plots.

2.2 Analytical Solutions to Guided Waves in Flat Multilayer Anisotropic Systems

Wave propagation equations in an isotropic media consisting of an arbitrary number of flat layers were initiated by Thomas [129]. This approach, referred to as the Transfer Matrix Method, is based upon the superposition of bulk waves. The displacements and stresses in any location of a particular layer are related to the four bulk wave amplitudes according the field matrix. The coefficients of the field matrix are a function of the through thickness position in the layer, density, bulk wave velocities, frequency and wavenumber. By imposing continuity of stress and strain at each layer interface, the boundary conditions at the first layer are related to the boundary conditions at the last interface by multiplying the field matrices for each layer [63]. The guided wave solutions are then obtained by applying the appropriate external boundary conditions and solving the characteristic equation.

More recently, the extension of transfer matrix method has been extended to multilayered anisotropic media [130,131]. In this case, the matrix assembly and solution procedure is the same; however the field matrix is more considerably more complex due to the coupling between wave propagation in different directions. The viscoelastic material behavior was accounted for in the Transfer Matrix Method by Hosten [132] and Hosten and Caistaings [131]. This is achieved by prescribing a complex stiffness matrix for each layer where the imaginary part of the stiffness matrix represents the material viscosity. The wave displacement therefore contains a complex wavenumber where the real part describes the wave propagation and the imaginary part defines the exponential decay of the wave or attenuation.

Solving multiple layer systems by means of the transfer matrix method requires numerical implementation. When considering high frequencies or thick layers, a loss in the numerical precision occurs, resulting in undesirable solution error. To circumvent this,

Knopoff [133] proposed the use of a global matrix formulation to describe the entire system instead of the use of individual field matrices. The advantage of the Global Matrix Method is that it does not have instabilities at large (thickness×frequency) values; however, the global matrix describing the entire system may be large. As a result, finding the solution may be relatively slow. For the Global Matrix Method, multi-layer viscoelastic layers which are anisotropic can also be modeled. In its general form, the global matrix results in $6(n\text{-}1)$ equations, where n represents the number of layers. These equations are assembled, in sets of six, in order to satisfy the boundary conditions at each interface, i.e. continuity of stress and displacement. The final assembly results in $6(n\text{-}1)$ equations and $6n$ unknowns corresponding to the incoming and reflected longitudinal and shear wave amplitudes in each layer of the system. Therefore, solution of system requires 6 known wave amplitudes. For ultrasonic applications, it is convenient to prescribe the incoming wave amplitudes from each half space above and below the multilayer plate. For the guided wave modal solution, the incoming waves are zero, resulting in a homogeneous set of equations. At this stage, the global matrix can be reformulated depending upon the properties of the half-space and contact conditions at the interfaces. The wavenumber-frequency relation for the guided wave modes are then found by solving the characteristic equation of the system. A much more thorough review of both the Transfer Matrix Method and Global Matrix Method is given by Lowe [63].

Approximate guided wave solutions for flat multilayer anisotropic systems have been developed according to laminated plate theories [134,135]. For this approach, through thickness plate displacement is generally represented by a linear combination of unknown functions multiplied by a time harmonic exponential. The wavenumber-frequency relation for flexural and extensional modes is obtained by solving the dynamic equations of motion for the plate.

The use of laminated plate theories are not valid for describing the dispersive solutions of guided wave modes at frequencies at which the wavelengths are comparable to the plate thickness [136]. Exact solutions based upon the superposition of bulk waves do not generally exist when modeling a very large number of layers such as thick composite laminates and that of waveguides with arbitrary cross-section. In addition, when complex wavenumbers are part of the solution such as in the case of leaky and/or damped waveguides, exact methods, require iterative bi-dimensional root searching algorithms that may miss some of the solutions [63]. To model such systems, the Semi-Analytical Finite Element (SAFE) approach has emerged as a promising technique. The theory of the SAFE method is discussed in Chapter 4. The following chapter discusses the response characteristics of piezoelectric transducers to ultrasonic Rayleigh and Lamb waves.

Chapter 3

Response of Rectangular Piezoceramic Patch and MFC Transducers to Ultrasonic Rayleigh and Lamb Waves

This section examines the fundamental response of surface-mounted, rectangular piezoelectric sensors (both piezoceramic and piezocomposite) subjected to harmonic, broadband and narrowband wave fields under plane wave hypotheses. The chapter first treats the case of Rayleigh surface waves and subsequently that of Lamb waves in isotropic media. The sensor voltage response was derived by coupling the direct piezoelectric effect to the wave strain field that is averaged over the sensor's effective electrode area. Analytical expressions are obtained for the general case of waves propagating at oblique incidence relative to the rectangular sensor. The predictions are compared to experimental data for the broadband excitation cases.

3.1   Piezoelectric Transducers Used for Guided Wave Applications

With the advent of on-board structural health monitoring systems based on ultrasonic guided waves, piezoelectric transducer patches are being increasingly used due to their low-cost, low-profile, and ease of integration within the structure. Piezoelectric transducers can be used as sensors or actuators. Actuation relies upon the converse effect, in which an applied voltage across the polarization direction induces strain in the material. When used in sensing applications, the direct effect results in an induced electric charge on the electrodes or electric field in the material due to applied strain. The most common piezoelectric materials used for guided wave transduction are piezoceramics (e.g., $Pb(Zr\text{-}Ti)O_3$ – PZT), piezopolymers (e.g.,

(poly(vinylidene fluoride)) – PVDFs) and piezocomposites (e.g. Active Fiber Composites – AFC and Macro Fiber Composites – MFC).

Monolithic PZT patches are frequently used in SHM based guided wave studies; however their brittle nature may be detrimental for on-board applications. PVDF transducers bring the advantages of durability and flexibility when compared to PZT transducers. These particular transducers have a reduced electro-mechanical coupling efficiency which requires increased actuation power in generation and heavy amplification in detection. The fact that PVDFs work best in the high-frequency range (500 kHz – 4 MHz) poses some limitations in terms of increased wave attenuation. Finally, the large temperature dependency of the PVDF coupling efficiency is another aspect of concern.

AFC and the MFC transducers are more recently being used in an effort to couple the electro-mechanical efficiency of PZTs with the flexibility of PVDFs. The two common MFC transducers are referred to as (type P1) and (type P2). Both MFC transducers are made of very thin, rectrangular piezoceramic fibers that are unidirectionally aligned and sandwiched between two sets of electrode patterns printed on a polyimide film (Fig. 3.1) [137].
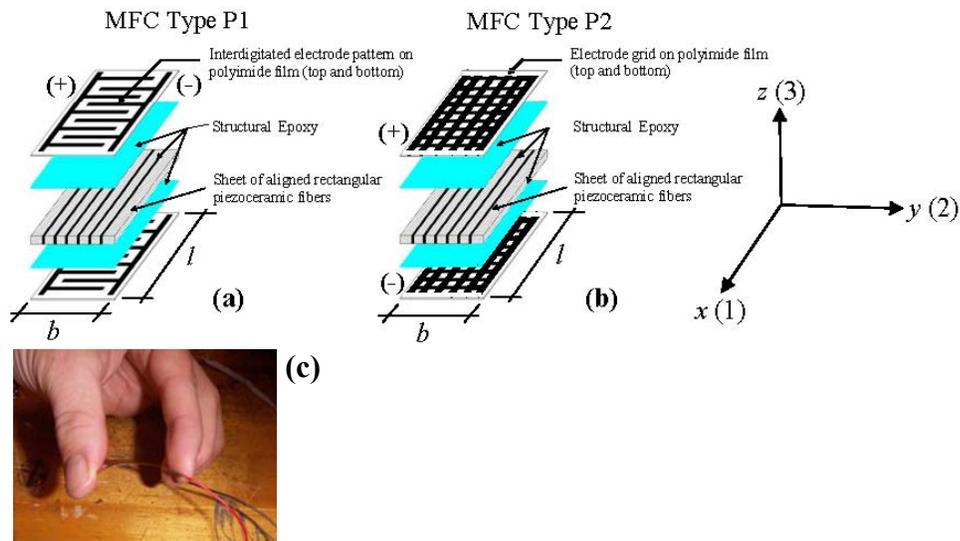
Fig 3.1. Schematic of Macro Fiber Composite transducer (a) type P1 (b) type P2. (c) Flexing of MFC type P1 transducer

AFC and MFC (type P1) transducers have inter-digitated electrodes which provide an electric field that exploits the large, in-plane (1-1) electro-mechanical coupling [138]. AFC transducers have been used for guided wave transduction in the low hundreds of kHz range [139,140]. MFC transducers have been primarily utilized for structural control and vibration suppression [137,141,142], and, in select cases, as guided wave transducers [44,143]. The main advantage of MFCs over AFCs is the reduced manufacturing cost. The circular AFC fibers are manufactured through a very costly extrusion process, as opposed to the rectangular fibers of MFCs which are cut from monolithic piezoceramic wafers.

The transducers considered in this chapter are piezoceramic transducers and both types of MFC transducers (i.e. type P1 and type P2). As opposed to the inter-digitated electrode arrangement for (type P1), the MFC (type P2) transducers have electrode grids of opposite polarization on each face (Fig. 3.1(b)). Therefore, both piezoceramic and MFC (type P2) transducers operate according to the d_{31}/d_{32} electro-mechanical coupling mechanism [137]. All of the aforementioned transducers are mostly sensitive to in-plane normal strains as a result of their geometry.

3.2 Strain Sensitivity of Rectangular Piezoelectric Transducers

3.2.1 PZT Transducers

The piezoelectric constitutive equations are described as [144]:

$$\mathbf{D} = \mathbf{e}^{\sigma}\mathbf{E} + \mathbf{d}\,\boldsymbol{\sigma} \qquad\qquad \text{(direct effect)} \qquad\qquad (3.1a)$$

$$\boldsymbol{\sigma} = -\left(\mathbf{dC}\right)^{T}\mathbf{E} + \mathbf{C}\boldsymbol{\varepsilon} \qquad\qquad \text{(converse effect)} \qquad\qquad (3.1b)$$

where in eq. (3.1a), $\mathbf{D}$ is the charge density vector (3×1), $\mathbf{e}^{\sigma}$ is the dielectric permittivity matrix (3×3) measured at zero stress, $\mathbf{E}$ is the electric field vector (3×1), $\mathbf{d}$ is the piezoelectric coefficient matrix (3×6), and $\boldsymbol{\sigma}$ is the stress vector (6×1). In eq. (3.1b), $\mathbf{C}$ is

the elastic stiffness matrix (6×6) measured at zero electric field, ε is the strain vector (6×1), while the superscript ^{T} indicates transposed matrix.

Consider a thin, rectangular piezoceramic sensor with length l, width b, and thickness t along directions *1*, *2* and *3*, respectively, Fig. 3.2.
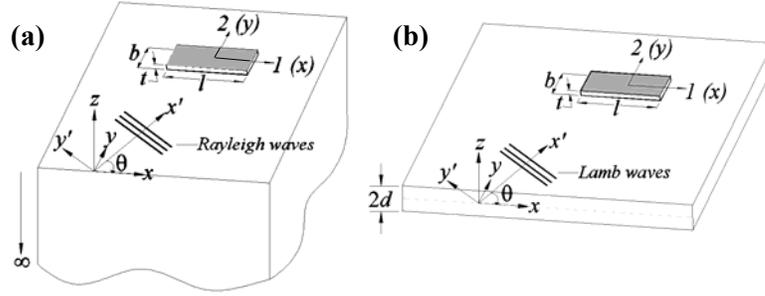
Fig. 3.2. A rectangular piezoelectric sensor and its interaction with (a) Rayleigh waves and (b) Lamb waves in general oblique incidence.

The piezoelectric element can be considered as transversely isotropic where the plane of isotropy corresponds to the (1, 2) plane. The electrical poling is assumed to be along the transducer's thickness direction, *3*. Consequently, under plane stress conditions ($\sigma_{33} = \sigma_{23} = \sigma_{13} = 0$), and after simplification and substitution of eq. (3.1b) into eq. (3.1a) the direct effect of the piezoelectric transducer reduces to [145]:

$$D_3 = \begin{bmatrix} d_{31} & d_{32} & 0 \end{bmatrix} \begin{bmatrix} Q_{11} & Q_{12} & 0 \\ Q_{12} & Q_{22} & 0 \\ 0 & 0 & Q_{66} \end{bmatrix} \left(\begin{bmatrix} \varepsilon_{11} \\ \varepsilon_{22} \\ \gamma_{12} \end{bmatrix} - E_3 \begin{bmatrix} d_{31} \\ d_{32} \\ 0 \end{bmatrix} \right) + e_{33}^{\sigma} E_3 \tag{3.2}$$

where d_{31} and d_{32} are the piezoelectric constants with units (m/V), e_{33}^{σ} is the dielectric permittivity with units (Farad/m) and ε_{11}, ε_{22}, γ_{12} are the strain components in the sensor. In the case of monolithic piezoceramic elements ($d_{31} = d_{32}$), and the reduced stiffness matrix, $[Q]$ can be written as:

$$[Q] = \begin{bmatrix} \dfrac{Y^E}{1-v^2} & \dfrac{vY^E}{1-v^2} & 0 \\[2mm] \dfrac{vY^E}{1-v^2} & \dfrac{Y^E}{1-v^2} & 0 \\[2mm] 0 & 0 & \dfrac{Y^E}{2(1+v)} \end{bmatrix} \tag{3.3}$$

where Y^E and v are the Young's modulus and Poisson's ratio of the piezoelectric transducer in the plane of isotropy. Expanding eq. (3.2), the expression describing the charge density becomes:

$$D_3 = d_{31}(Q_{11} + Q_{12})(\varepsilon_{11} + \varepsilon_{22}) - \left[2d_{31}^2(Q_{11} + Q_{12}) - e_{33}^\sigma \right] E_3 \tag{3.4}$$

Considering the electrical boundary conditions of the piezoelectric patch to be an open circuit, the total charge $\iint D_3 \mathrm{dxdy} = 0$ [146]. Under such conditions, the transducer voltage can be described as:

$$V = -\frac{\iiint E_3 \mathrm{dxdydz}}{lb} \tag{3.5}$$

After integration of the charge density over the electrode area and employing eq. (3.5), the voltage response is found to be:

$$V = \frac{d_{31}(Q_{11} + Q_{12})t \iint (\varepsilon_{11} + \varepsilon_{22}) \mathrm{dxdy}}{lb \left[e_{33}^\sigma - 2d_{31}^2(Q_{11} + Q_{12}) \right]} \tag{3.6}$$

Note that eq. (3.6) assumes that the in plane normal strains are constant through the transducer's thickness. This assumption was verified for static cases in Wang and Meguid [147].

Substitution of the reduced stiffness matrix given in eq. (3.3) into eq. (3.6) results in the following expression for the voltage generated by the piezoelectric patch as a function of the two in-plane strain components:

$$V = \frac{d_{31}Y^E t \iint (\varepsilon_{11} + \varepsilon_{22}) \mathrm{d}x\mathrm{d}y}{lb\left[e_{33}^{\sigma}(1-v) - 2Y^E d_{31}^2\right]} \tag{3.7}$$

The above equation is the voltage response of a monolithic piezoceramic strain sensor with poling along its thickness, and considering open circuit, plane stress conditions.

3.2.2 MFC (Type P1) Transducers

Consider a thin rectangular MFC transducer (type P1) acting as a sensor and having an effective length l, width b, and thickness t along body coordinates 1, 2 and 3, respectively (Fig. 3.1(a)). The effective length and width of the transducer corresponds to the active PZT area between the upper and lower electrode arrangements. The type P1 MFC is classified as a generally orthotropic laminate [145]. However, if we presume that the MFC transducers are much thinner than that of the substrate and small transverse displacements occur, the entire MFC can be approximated as a single fiber reinforced lamina where the fibers are PZT-5A material, and the reinforcing matrix is epoxy [148].

The direct piezoelectric effect occurs along the (1) direction due to the poling and interdigitated electrode pattern. Now let us consider the charge density occurring within a 2-D unit cell of the MFC transducer as shown in Fig. 3.3. In this analysis, the origin of the z-axis was chosen to correspond to the mid-height of the piezoceramic fiber. The 2-D unit cell cross section is constant along the effective width b of the transducer. The electrode to electrode centerline spacing and the piezoelectric fiber thickness are denoted as a and g, respectively. The half width of the electrode is defined as w. The entire MFC transducer contains p unit cells along the length of the transducer.
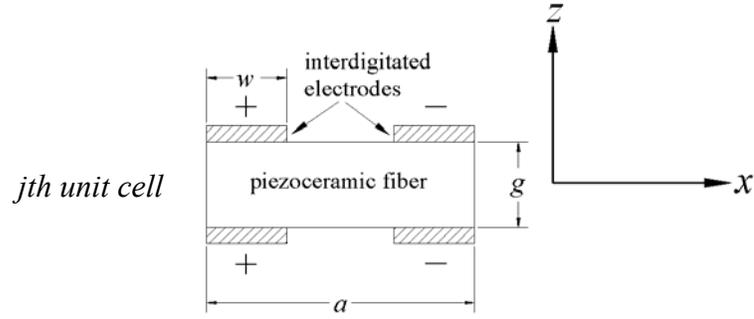
Fig. 3.3. 2-dimensional unit cell of MFC (type P1) transducer.

Imposing plane stress conditions, the constitutive relation of the *j*th MFC unit cell, which is poled along the fiber axis and used as a sensor (direct piezoelectric effect) becomes [140]:

$$D_1^j = \begin{bmatrix} d_{11} & d_{12} & 0 \end{bmatrix} \begin{bmatrix} Q_{11} & Q_{12} & 0 \\ Q_{12} & Q_{22} & 0 \\ 0 & 0 & Q_{66} \end{bmatrix} \left(\begin{bmatrix} \varepsilon_{11} \\ \varepsilon_{22} \\ \gamma_{12} \end{bmatrix} - E_1^j \begin{bmatrix} d_{31} \\ d_{32} \\ 0 \end{bmatrix} \right) + e_{11}^\sigma E_1^j \tag{3.8}$$

where e_{11}^σ, D_1^j and E_1^j is the dielectric permittivity, the charge density and electric field respectively for the *j*th unit cell. The terms d_{11} and d_{12} are the piezoelectric constants for the MFC (type P1) transducer. It is presumed in the following analysis that the in-plane normal strains are constant through the thickness of the piezoceramic fibers. The matrix $[Q]$ represents the reduced stiffness matrix of the MFC unit cell and can be written as:

$$[Q] = \begin{bmatrix} \dfrac{Y_1^E}{1-v_{21}v_{12}} & \dfrac{v_{12}Y_2^E}{1-v_{21}v_{12}} & 0 \\ \dfrac{v_{12}Y_2^E}{1-v_{21}v_{12}} & \dfrac{Y_2^E}{1-v_{21}v_{12}} & 0 \\ 0 & 0 & G_{12} \end{bmatrix} \tag{3.9}$$

where Y_1^E and Y_2^E are the Young's modulus of the MFC transducer along the 1 and 2 body coordinates and v_{12} and v_{21} are the respective Poisson's ratios. G_{12} represents the in-plane

shear modulus of the MFC transducer. Expanding eq. (3.8), the expression describing the charge density of the unit cell becomes:

$$D_1^j = (d_{11}Q_{11} + d_{12}Q_{12})\varepsilon_{11} + (d_{11}Q_{12} + d_{12}Q_{22})\varepsilon_{22}$$
$$- \left[d_{11}^2 Q_{11} + 2d_{11}d_{12}Q_{12} + d_{12}^2 Q_{22} - e_{11}^\sigma \right] E_1^j \tag{3.10}$$

The total charge over the active MFC electrode area is:

$$\iint D_1 dA_{el} = \sum_{j=1}^{p} \int_0^b \left[\int_{(j-1)a}^{(j-1)a+w} D_1^j dx + \int_{ja-w}^{ja} D_1^j dx \right] dy = \sum_{j=1}^{p} \int_0^b \left[\int_{(j-1)a}^{ja} D_1^j dx - \int_{(j-1)a+w}^{ja-w} D_1^j dx \right] dy \tag{3.11}$$

The active electrode area A_{el} is equivalent to $(2w)bp$ for an MFC (type P1) transducer. Because no electrode is present between the length $(j-1)a + w$ and $ja - w$, the charge density vanishes and the second integral in eq. 3.11 becomes zero. Therefore eq. 3.11 reduces to:

$$\iint D_1 dA_{el} = \sum_{j=1}^{p} \int_0^b \int_{(j-1)a}^{ja} D_1^j dxdy = \int_0^b \int_0^l D_1^j dxdy \tag{3.12}$$

Considering the electrical boundary conditions of the MFC sensor to be an open circuit, the total charge over the active MFC electrode area is $\iint D_1 dA_{el}$ [146]. The local potential in a unit cell at either surface of the piezoceramic fiber, ($z = \pm g/2$) can be evaluated by integrating the electric field over the unit cell length a. The local potential in the unit cell is expressed as:

$$\varphi^j(x,y) = - \int_{(j-1)a}^{ja} E_1^j(x,y)dx \tag{3.13}$$

The average potential at the electrodes for the entire MFC should therefore be:

$$V = \varphi_{avg.} = \frac{\int_0^b \left(\sum_{i=1}^{p} \phi^j(x,y) \right) dy}{A_{el}} = -\frac{\sum_{i=1}^{p} \int_0^b \int_{(j-1)a}^{ja} E_1^i(x,y)dxdy}{(2w)bp} = -\frac{\int_0^b \int_0^l E_1^j(x,y)dxdy}{(2w)bp} \tag{3.14}$$

After integration of the charge density over the electrode area (eq. 3.12) and plugging this expression into eq. (3.14), the voltage response is found to be:

$$V = \frac{\int_0^b \int_0^l \left[(d_{11}Q_{11} + d_{12}Q_{12})\varepsilon_{11} + (d_{11}Q_{12} + d_{12}Q_{22})\varepsilon_{22} \right] dxdy}{(2w)bp\left[e_{11}^\sigma - \left(d_{11}^2 Q_{11} + 2d_{11}d_{12}Q_{12} + d_{12}^2 Q_{22} \right) \right]} \tag{3.15}$$

Substitution of the reduced stiffness matrix given in eq. (3.9) into eq. (3.15) results in the following expression of the voltage generated by the MFC sensor as a function of the two in-plane strain components:

$$V = \frac{\int_0^b \int_0^l \left[\left(d_{11}Y_1^E + d_{12}v_{12}Y_2^E \right)\varepsilon_{11} + \left(d_{11}v_{12}Y_2^E + d_{12}Y_2^E \right)\varepsilon_{22} \right] dxdy}{(2w)bp\left[\left(1 - v_{21}v_{12} \right)e_{11}^\sigma - \left(d_{11}^2 Y_1^E + 2d_{11}d_{12}v_{12}Y_2^E + d_{12}^2 Y_2^E \right) \right]} \tag{3.16}$$

The above expression is the voltage response of a type P1 MFC sensor assumed to behave as a single lamina and considering plane stress conditions.

3.2.3 MFC (Type P2) Transducers

Consider a thin rectangular MFC transducer (type P2) acting as a sensor and having an effective length l, width b, and thickness t along body coordinates 1, 2 and 3, respectively (Fig. 3.1(b)). Similar to the formulation for the (type P1) transducer, the entire MFC (type P2) transducer is approximated as a single orthotropic lamina. The reduced stiffness matrix, $[Q]$ of the MFC transducer is thereby described by eq. (3.9) where the appropriate elastic constant for the MFC (type P2) transducer are utilized. The electro-mechanical behavior of the MFC (type P2) transducer is similar to that of the monolithic piezoceramic transducer. Therefore, by applying the same formulation as that described in section 3.2.1, the voltage generated by the MFC (type P2) sensor as a function of the two in-plane strain components is [149]:

$$V = \frac{t\int_0^b \int_0^l \left[\left(d_{31}Y_1^E + d_{32}v_{12}Y_2^E \right)\varepsilon_{11} + \left(d_{31}v_{12}Y_2^E + d_{32}Y_2^E \right)\varepsilon_{22} \right] dxdy}{lb\left[\left(1 - v_{21}v_{12} \right)e_{33}^\sigma - \left(d_{31}^2 Y_1^E + 2d_{31}d_{32}v_{12}Y_2^E + d_{32}^2 Y_2^E \right) \right]} \tag{3.17}$$

where the effective electrode area for the MFC (type P2) transducer is approximated as *lb*. The above expression is the voltage response of a type P2 MFC strain sensor assumed to behave as a single lamina and considering plane stress conditions.

The sensor response of piezoceramic and MFC transducers to Rayleigh and Lamb ultrasonic waves are examined in the following sections by considering the appropriate strain fields in eqs. (3.7), (3.16) and (3.17). It is presumed in this analysis that the presence of the sensor does not significantly alter the strain field of the incident wave. In addition, the dynamic strain ratio between the induced strain within the transducer and the surface strain of the host structure is presumed to be unity over the sensor area. This assumption is valid for structures much stiffer than the piezoelectric transducer and transducers with large length to thickness aspect ratios [150]. The predicted responses for the piezoceramic and MFC (type P2) transducers are compared to experimental data for the broadband excitation cases.

3.3   Response of Rectangular Piezoceramic (PZT) Transducers to Rayleigh Waves

3.3.1   Harmonic Rayleigh Excitation

Consider a rectangular PZT sensor bonded to the surface of an isotropic elastic medium and subjected to a harmonic surface (Rayleigh) plane wave. In general, the wave propagates along a direction *x'* inclined at an angle θ from the sensor's lengthwise direction *x*, Fig. 3.2(a). In order to calculate the sensor voltage response from eq. (3.7), the surface strain components along the wave propagation axes (*x'*, *y'*) must be rotated to the sensor geometrical axes (*x*, *y*). For plane waves ($\varepsilon_{y'y'} = 0$), the following strain invariant can be written:

$$\varepsilon_{xx} + \varepsilon_{yy} = \varepsilon_{x'x'} + \varepsilon_{y'y'} = \varepsilon_{x'x'} \tag{3.18}$$

where the Rayleigh surface strain $\varepsilon_{x'x'}$ can be written as [151]:

$$\varepsilon_{x'x'}|_{z=0} = -\frac{ik^2 B}{2q}(q - 2s_R r_R)e^{i(kx'-\omega t)} \tag{3.19}$$

where k is the wavenumber, B is the arbitrary amplitude of the wave, and

$q = 2 - (c/c_T)^2$, $r_R = \sqrt{1 - (c/c_L)^2}$, $s_R = \sqrt{1 - (c/c_T)^2}$. Ignoring shear lag, and thus assuming

a very thin and stiff adhesive layer [152], the sensor experiences the same strain as the

structure, thus $(\varepsilon_{11} + \varepsilon_{22}) = (\varepsilon_{xx} + \varepsilon_{yy})|_{z=0}$. Substituting eq. (3.19) into eq. (3.7) yields the

following voltage response:

$$V = -\frac{d_{31} Y^E t i k^2 B (q - 2s_R r_R) \iint e^{i(kx'-\omega t)} dx dy}{2qlb\left[e_{33}^\sigma(1-v) - 2Y^E d_{31}^2\right]} \tag{3.20}$$

Using the variable transformation $x' = x\cos\theta + y\sin\theta$, evaluating the integral in y over the

sensor width [–b/2, b/2], and considering the integration limits of x over the sensor length [-

l/2, l/2], the previous expression can be written as:

$$V = -\frac{S_{PZT} k B R \int_{-l/2}^{l/2} e^{i(kx\cos\theta - \omega t)}\left(e^{i\frac{kb\sin\theta}{2}} - e^{-i\frac{kb\sin\theta}{2}}\right) dx}{lb\sin\theta} \tag{3.21}$$

where S_{PZT} and R are frequency-independent constants defined as:

$$\begin{cases} S_{PZT} = \dfrac{d_{31} Y^E t}{\left[e_{33}^\sigma(1-v) - 2Y^E d_{31}^2\right]} \\ R = \dfrac{(q - 2s_R r_R)}{2q} \end{cases} \tag{3.22}$$

Using Euler's and prosthaphaeresis formulae in eq. (3.21), the sensor voltage response to a

harmonic Rayleigh wave can be simplified to:

$$V = -i\overline{V}e^{-i\omega t} \tag{3.23}$$

where the amplitude is:

$$\overline{V} = \frac{S_{PZT} \, A_{Rayleigh}}{lb \sin\theta \cos\theta} \sin\left(\frac{kb \sin\theta}{2}\right) \sin\left(\frac{kl \cos\theta}{2}\right) \qquad \text{(oblique incidence)} \qquad (3.24)$$

The term $A_{Rayleigh} = 4BR$ is related to the Rayleigh wave amplitude.

When the wave propagation direction, x', is parallel to the sensor's lengthwise direction, x, the incidence angle, θ, is equal to zero. In this case, since $\lim_{\alpha \to 0}(\sin\alpha)/\alpha = 1$, eq. (3.24) simplifies to the following result, expressed in terms of either the wavenumber, k, or the wavelength, λ:

$$\overline{V} = \overline{V}\Big|_{\theta \to 0} = \frac{S_{PZT} \, A_{Rayleigh} \, k}{2l} \sin\left(\frac{kl}{2}\right) = \frac{S_{PZT} \, A_{Rayleigh} \, \pi}{\lambda l} \sin\left(\frac{\pi l}{\lambda}\right) \qquad \text{(parallel incidence)} \qquad (3.25)$$

Eq. (3.25) shows that the response to a given wavenumber (or wavelength) will be influenced by the dimension of the sensor parallel to the wave propagation direction. From the sinusoidal term, the response will be large at $\lambda = 2l/(2n-1)$ for $n = 1, 2, 3\ldots$ corresponding to sensor lengths equal to an odd multiple of half the wavelength. This behavior is referred to as wavelength tuning. Contrarily to what was concluded for piezoelectric actuators [114], these conditions do not necessarily correspond to local maxima of the response due to the presence of the factor $(S_{PZT} \, A_{Rayleigh} \, \pi / \lambda l)$. The response will be zero at $\lambda = l/n$ for $n = 1, 2, 3\ldots$ corresponding to sensor lengths equal to an integer multiple of the wavelength. Furthermore, from the term l in the denominator of the multiplication factor, the response will increase with decreasing sensor length.

Through the factor $A_{Rayleigh}$, eqs. (3.24)-(3.25) contain the arbitrary amplitude of the wave, B. Therefore, a normalization is required in order to compare the sensor response to different wavelengths/frequencies of the incoming field. One approach is to normalize the response by the power flow carried by the wave. The following normalization factor was considered for the Rayleigh response:

$$N_{Rayleigh} = \sqrt{\int_{-\infty}^{0} \mathrm{P_{Vx'}}\, dz} \qquad (3.26)$$

where $\mathrm{P_{Vx'}}$ is the x'-component of the wave Poynting vector which, in turn, is calculated from the relevant stress components and particle velocities as:

$$\mathrm{P_{Vx'}} = -\frac{1}{2}\mathrm{Re}\left[\sigma_{x'x'}\left(\frac{\partial u_{x'}}{\partial t}\right)^{*} + \sigma_{x'z}\left(\frac{\partial u_{z}}{\partial t}\right)^{*} \right] \qquad (3.27)$$

where Re indicates real part, and * indicates complex conjugate.

For Rayleigh waves propagating in steel (c_L = 5.9 mm/μs, c_T = 3.2 mm/μs, c = 2.99 mm/μsec), the normalized surface strain ($\varepsilon_{x'x'}|_{z=0} / N_{Rayleigh}$) is shown in Fig. 3.4 as a function of frequency. The resulting nonlinear trend indicates that, with increasing frequency, the square root of the power flow increases faster than the surface strain.
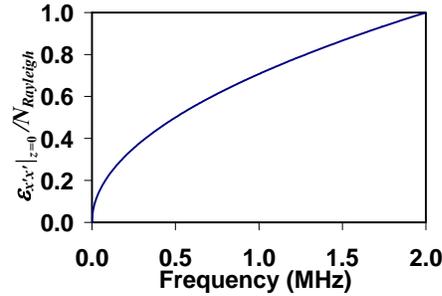
Fig. 3.4 Surface strain of a Rayleigh wave in steel normalized by the wave power flow through the solid at various frequencies.

The normalized voltage response to harmonic Rayleigh waves propagating along the lengthwise direction of the sensor, $\overline{V} / N_{Rayleigh}$ calculated from eqs. (3.25)-(3.26), is plotted in Fig. 3.5(a) for the following sensor dimensions: l = 12.7 mm (0.5 in) , l = 6.35 mm (0.25 in) and l = 3.17 mm (0.125 in). The limit case of l = 0 (point sensor) is also shown. As discussed above, the response is large at frequencies where the sensor length is equal to an odd multiple of half the wavelength; the response is, instead, zero at frequencies where the sensor length is

equal to an integer multiple of the wavelength. This result is further emphasized in Fig. 3.5(b) where the non-dimensional ratio of the Rayleigh wavelength to sensor length is plotted for the 6.35mm-long sensor. Notice that the first two local maxima of the response at $f = 0.25$ MHz and 0.75 MHz, circled in Fig. 3.4, are slightly shifted from the conditions $\lambda = 2l/(2n-1)$. The shift is due to the factor $(S_{PZT} A_{Rayleigh} \pi / \lambda l)$ in eq. (3.25) and to the frequency dependence of $N_{Rayleigh}$. Fig. 3.5(a) shows that the magnitude of the local response maxima for a given sensor length decreases with increasing frequency. The figure also confirms that the response to a given wave frequency increases with decreasing sensor length, as a result of the term l in the denominator of eq. (3.25).

The limit case of the point sensor ($l = 0$) results in a larger response than any of the finite-length sensors. The point-sensor response also identically matches the normalized surface strain shown in Fig. 3.5, confirming the "ideal strain sensor" behavior where smearing effects due to strain averaging over the sensor length are not present.
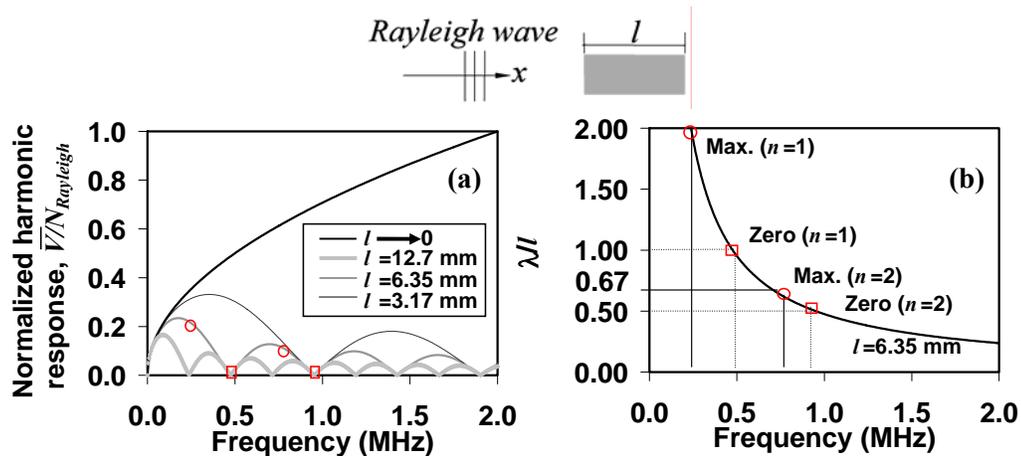
Fig. 3.5 (a) Normalized voltage response of sensor subjected to parallel incident harmonic Rayleigh wave for varying sensor lengths; (b) ratio of Rayleigh wavelength to sensor length of 6.35 mm.

3.3.2 Arbitrary Excitation

The harmonic Rayleigh wave excitation assumed in eqs. (3.24)-(3.25) is of theoretical interest. However, harmonic excitation will seldom occur in a practical structural health monitoring application where the wave fields will likely be either broadband (e.g. an acoustic emission detection) or narrowband (e.g. a pitch-catch testing configuration).

The amplitude $\overline{U} = \overline{U}(\omega)$ of the frequency-domain response of a linear system subjected to an arbitrary excitation can be calculated from the product of the frequency-domain response of the system to harmonic excitation, $\overline{V} = \overline{V}(\omega)$, and the amplitude of the Fourier transform of the excitation, $\overline{P} = \overline{P}(\omega)$ [153]:

$$\overline{U} = \overline{V} \times \overline{P} \tag{3.28}$$

In turn, the sensor excitation can be expressed in terms of the amplitude spectrum of the surface strain induced by the arbitrary source at the point of entry into the sensor, $\varepsilon^a_{x'x'}\big|_{z=0}(\omega)$, in the following manner:

$$\overline{P} = \frac{\varepsilon^a_{x'x'}\big|_{z=0}}{\varepsilon_{x'x'}\big|_{z=0}} \tag{3.29}$$

where $\varepsilon_{x'x'}\big|_{z=0}(\omega)$ is the amplitude spectrum of the surface strain excited under harmonic conditions, and the dependence of all terms on ω is implicit. The sensor response to arbitrary excitation can be thus calculated as:

$$\overline{U} = \overline{V} \times \frac{\varepsilon^a_{x'x'}\big|_{z=0}}{\varepsilon_{x'x'}\big|_{z=0}} \tag{3.30}$$

The following two sections address the response to broadband and narrowband Rayleigh wave fields, respectively.

3.3.3   Broadband Rayleigh Excitation

3.3.3.1 Semi-Analytical Analysis

The harmonic surface strain field at a point is equivalent to the sensor response to harmonic excitation from eq. (3.24) when the sensor length l and width b are taken to be 0 (point sensor). In order to transform voltage into strain, the point-wise response must be further divided by the term S_{PZT} which contains the piezoelectric constant of the sensor. Thus the arbitrary excitation spectrum can be written as:

$$\overline{P} = \frac{\varepsilon_{x'x'}^{a}\big|_{z=0}}{\varepsilon_{x'x'}\big|_{z=0}} = \frac{\varepsilon_{x'x'}^{a}\big|_{z=0}}{\lim\limits_{l,b\to 0} \overline{V}/S_{PZT}} = \varepsilon_{x'x'}^{a}\big|_{z=0}\,\frac{\lambda^{2}}{A_{Rayleigh}\,\pi^{2}} \tag{3.31}$$

Substituting eqs. (3.24) and (3.31) into eq. (3.28), the response of the sensor to broadband Rayleigh wave excitation is [154]:

$$\overline{U} = \frac{S_{PZT}\,\lambda^{2}\varepsilon_{x'x'}^{a}\big|_{z=0}}{\pi^{2}lb\sin\theta\cos\theta}\sin\left(\frac{\pi b\sin\theta}{\lambda}\right)\sin\left(\frac{\pi l\cos\theta}{\lambda}\right) \tag{3.32}$$

This expression shows that the response to broadband waves follows a similar wavelength tuning behavior as the response to harmonic waves, with appropriate scaling factors. For example, the response to parallel incidence will be large for sensor dimensions equal to an odd multiple of half the wavelength, and it will be zero for sensor dimensions equal to an integer multiple of the wavelength.

In this analysis, the surface strain spectrum $\varepsilon_{x'x'}^{a}\big|_{z=0}(\omega)$ in eq. (3.32) was obtained through a conventional, 2-D Finite Element Analysis (FEA) of a broadband Rayleigh wave generation. The total sensor response $\overline{U}$ was thus predicted by a semi-analytical analysis.

The FEA used ABAQUS Explicit to discretize a steel block ($c_{L} = 5.9$ mm/μs, $c_{T} = 3.2$ mm/μs, density $\rho = 7700$ kg/m^{3}), 250 mm (9.8 in) in length and 50 mm (1.98 in) in thickness [155]. The block was assumed infinitely wide to reflect plain strain conditions. The

excitation was a half-sinusoid forcing function (0.24 μsec in duration), with a nearly uniform energy spectrum in the DC - 2 MHz frequency range of interest, applied to a surface node and directed along the thickness direction to simulate an ablative laser source. Material damping effects were neglected. The block's material, dimensions, and excitation-detection distance were equivalent to what was used in the experimental tests to be discussed in the next section. The discretization used 4-node, bilinear plane strain quadrilateral elements with two degrees of freedom per node. Element sizes are typically conditioned by the minimum wavelength, λ_{min}, as determined by the highest frequency of interest [156,157]. The largest element dimension was chosen equal to $\lambda_{min}/10$. The integration time step was set to $\Delta t = 0.01$ μsec.

3.3.3.2 Experimental Analysis

Experimental tests were conducted on a 250 mm × 250 mm × 50 mm (9.8 in × 9.8 in × 1.98 in) steel block upon which a rectangular PZT patch of dimensions 6.35 mm × 3.17 mm × 0.5 mm (0.25 in × 0.125 in × 0.02 in) was bonded using a thin layer of instant adhesive. A 12-nsec pulse from an Nd:YAG Q-switched laser was focused to a line on the block's surface to generate broadband Rayleigh waves in the ablative regime. The block's orientation was varied such that the waves propagated at various angles relative to the sensor's geometrical axes. Signal acquisition was performed by a National Instruments PXI-1010 unit running under LabVIEW software which recorded the first Rayleigh wave arrivals and subsequently performed the Fast-Fourier Transform in the DC - 2 MHz range.

The results for wave propagation directions inclined at $\theta = 0°$, 30º, 60º, and 90º from the lengthwise direction of the sensor are shown in Fig. 3.6. Each response spectrum was normalized by the peak response of a commercial acoustic emission transducer bonded next to the PZT so as to eliminate the effects of the laser shot-to-shot variations. The corresponding

responses calculated theoretically from eq. (3.32) are also shown for comparison. The amplitude of the response increases with decreasing sensor dimension along the wave propagation direction, and it is thus smallest for the 0º incidence (6.35 mm length) in Fig. 3.6(a), and largest for the 90º incidence (3.17 mm length) in Fig. 3.6(d). There is a reasonably good agreement between experiment and theory regarding the position of the local maxima and minima of the response according to wavelength tuning. The relative amplitude of the response also compares relatively well between theory and experiment. The strongest discrepancies are seen above 1 MHz, where the theory overestimates the experimental response for the 0º and the 90º incidence, while it underestimates the experimental response for the 60º incidence. These differences could result from either wave attenuation losses or shear lag effects, both of which were neglected in the theory. Another potential source of discrepancy is the finite thickness of the transducer which may modify the incoming strain field due to local changes in mass and stiffness of the waveguide.
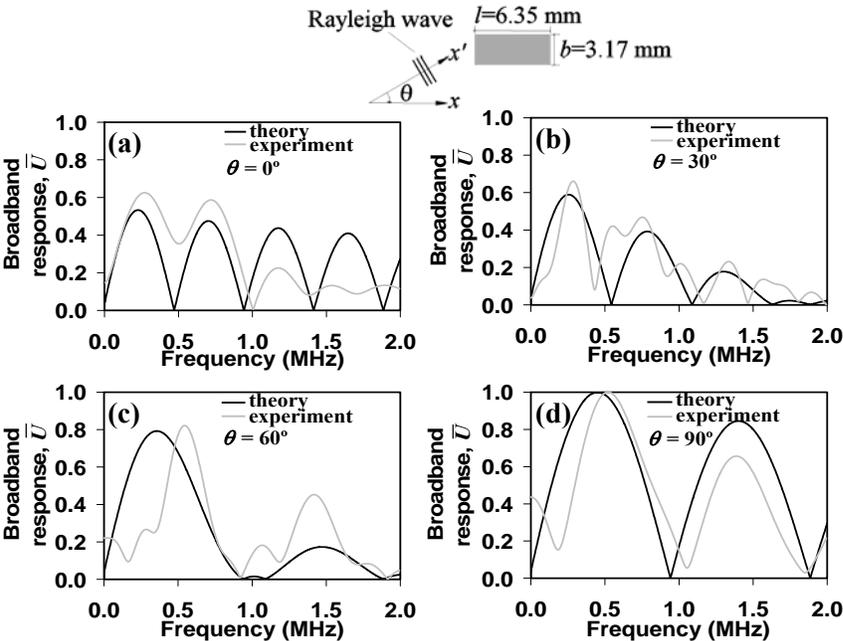
Fig. 3.6 Experimental and theoretical frequency response of 6.35mm × 3.17mm rectangular piezoelectric sensor to broadband Rayleigh waves propagating at (a) 0 deg, (b) 30 deg, (c) 60 deg, and (d) 90 deg from the lengthwise sensor dimension.

3.3.4   Narrowband Rayleigh Excitation

The specific case of narrowband excitation examined is that of a toneburst wave field which may be excited by an actuator in a pitch-catch testing configuration. Only parallel incidence ($\theta = 0^\circ$) was considered in this analysis. The extension to oblique incidence is a relatively straight forward matter. An unmodulated toneburst of unit amplitude in the time domain, $f(t)$, can be expressed as:

$$f(t) = \begin{cases} \sin \omega_0 t & \text{for } |t| < T/2 \\ 0 & \text{for } |t| > T/2 \end{cases} \tag{3.33}$$

where ω_0 is the central frequency and T is the time duration of the wave train.

The Fourier transform amplitude of the fixed time window toneburst of central frequency ω_0 can be expressed as [158]:

$$\overline{F} = \left[\frac{\sin 2n\pi\left(\dfrac{\omega}{\omega_0}+1\right)}{(\omega+\omega_0)} - \frac{\sin 2n\pi\left(\dfrac{\omega}{\omega_0}-1\right)}{(\omega-\omega_0)} \right] \tag{3.26}$$

where n is number of half cycles within the time window. Assuming that this quantity corresponds directly to the surface strain $\varepsilon^a_{x'x'}\big|_{z=0}$, the amplitude spectrum of the sensor excitation from eq. (3.32) becomes:

$$\overline{P} = \frac{\varepsilon^a_{x'x'}\big|_{z=0}}{\varepsilon_{x'x'}\big|_{z=0}} = \frac{\overline{F}}{\lim\limits_{l,b\to 0} \overline{V}/S_{PZT}} = \overline{F}\frac{\lambda^2}{A_{Rayleigh}\,\pi^2} \tag{3.35}$$

Substituting eqs. (3.25) and (3.35) into eq. (3.28), the response amplitude of the piezoelectric sensor to a toneburst Rayleigh wave excitation of unit amplitude and center frequency ω_0 is:

$$\overline{U} = \left[\frac{\sin 2n\pi\left(\dfrac{2\pi c}{\lambda\omega_0}+1\right)}{\left(\dfrac{2\pi c}{\lambda}+\omega_0\right)} - \frac{\sin 2n\pi\left(\dfrac{2\pi c}{\lambda\omega_0}-1\right)}{\left(\dfrac{2\pi c}{\lambda}-\omega_0\right)} \right] \frac{S_{PZT}\,\lambda}{\pi l}\sin\left(\frac{\pi l}{\lambda}\right) \tag{3.36}$$

where the wavelength λ has been used instead of the frequency ω in the square brackets for consistency with the other terms in the expression.

It is clear from this equation that the response is dependent on both the toneburst center frequency, ω_0, and the harmonic wavelength tuning term, $\sin(\pi l/\lambda)$. Results from eq. (3.36) are shown in Figs. 3.7(a), 3.7(b) and 3.7(c) for a sensor length $l = 6.35$ mm, and assuming steel ($c = 2.99$ mm/μsec) as the test material. Three different center frequencies for the excitation toneburst were chosen for these plots. Two of them coincided with a large value (f_{max}) and the first zero value (f_{min}) of the harmonic sensor response (where f_{max} corresponds to $\lambda = 2l$, and f_{min} corresponds to $\lambda = l$ from wavelength tuning). The third center frequency was chosen to coincide with an intermediate value (f_{int}) of the harmonic sensor response. From Fig. 3.5, these frequency values were: $f_{max} = 0.24$ MHz, $f_{int} = 0.35$ MHz and $f_{min} = 0.47$ MHz for $l = 6.35$ mm. The expected conclusion from Fig. 3.7 is that the response increases when the excitation toneburst frequency approaches the favorable sensor length-to-wavelength ratio. Notice also that a non-negligible response is obtained in Fig. 3.7(c) for toneburst frequencies corresponding to zero harmonic response as a result of the finite bandwidth and the side lobes of the toneburst spectrum. The same results are plotted for a smaller sensor ($l = 3.17$ mm) in Figs. 3.7(d), 3.7(e) and 3.7(f), considering the corresponding $f_{max} = 0.48$ MHz, $f_{int} = 0.72$ MHz and $f_{min} = 0.95$ MHz as toneburst center frequencies.
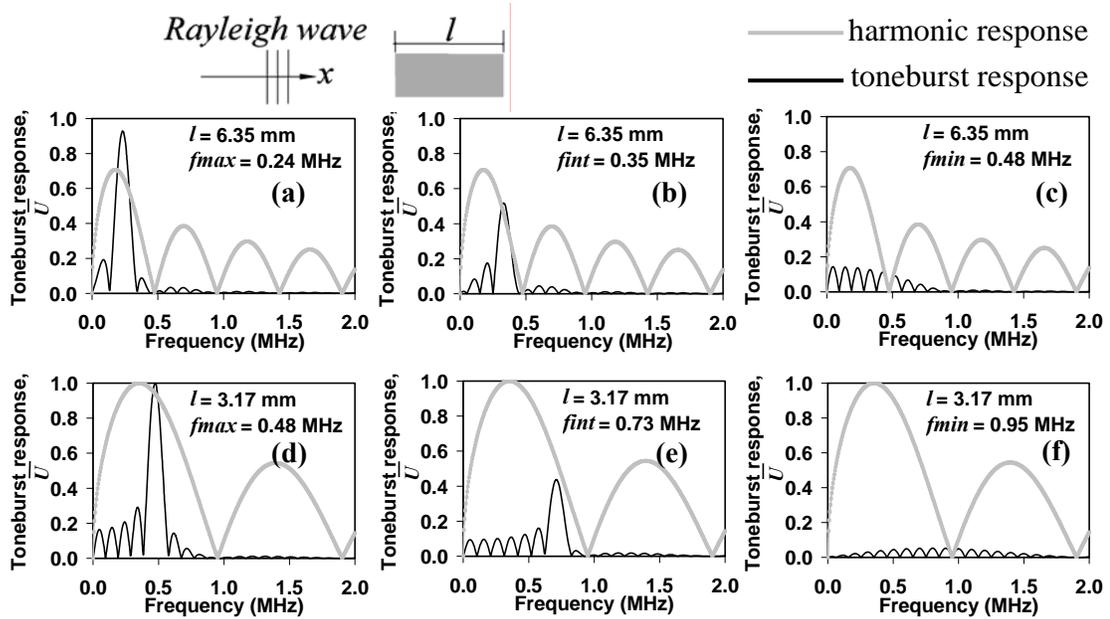
Fig. 3.7 Frequency response of piezoelectric sensor to a narrowband (toneburst) Rayleigh wave centered at frequencies corresponding to a large (a), an intermediate (b), and a zero (c) harmonic response for sensor length $l = 6.35$ mm. (d), (e), (f), same as above for sensor length $l = 3.17$ mm. Harmonic responses in gray lines.

3.4 Response of Rectangular Piezoceramic (PZT) Transducers to Lamb Waves

3.4.1 Harmonic Lamb Excitation

Consider a rectangular piezoelectric sensor bonded to the upper surface of an isotropic plate of thickness $2d$ and subjected to a harmonic strain field associated to Lamb waves propagating in the plane (x', z) along direction x', Fig. 3.2(b). As for the Rayleigh wave case, the wave propagation direction x' forms an angle θ with the lengthwise direction of the sensor. The origin of the thickness coordinate, $z = 0$, is at the mid-plane of the plate. For plane waves ($\varepsilon_{y'y'} = 0$) the only strain relevant to the surface-mounted sensor is the in-plane component in the wave propagation direction given by [159]:

$$\varepsilon_{x'x'}\Big|_{z=d} = i\,k^2 E\left(\tanh rd - \frac{2rs}{k^2 + s^2}\cdot\tanh sd\right)e^{i\left(kx' - \omega t - \frac{\pi}{2}\right)} \qquad \text{(antisymmetric modes)} \qquad (3.37)$$

and

$$\varepsilon_{x'x'}\Big|_{z=d} = i\,k^2 F\left(\coth rd - \frac{2rs}{k^2 + s^2}\cdot\coth sd\right)e^{i\left(kx' - \omega t - \frac{\pi}{2}\right)} \qquad \text{(symmetric modes)} \qquad (3.38)$$

where E and F are the two arbitrary wave amplitudes for the antisymmetric and symmetric

modes, respectively and $r = \sqrt{k^2 - (\omega/c_L)^2}$, $s = \sqrt{k^2 - (\omega/c_T)^2}$.

The voltage response to harmonic Lamb waves can be obtained by substituting eqs.

(3.37) or (3.38) in eq. (3.7). For the antisymmetric modes, this substitution results in:

$$V = \frac{d_{31}Y^E t\,ik^2 E}{e_{33}^\sigma lb(1-\nu)}\left(\tanh rd - \frac{2rs}{k^2 + s^2}\cdot\tanh sd\right)\iint e^{i\left(kx' - \omega t - \frac{\pi}{2}\right)}dxdy \qquad (3.39)$$

Following the same steps of the Rayleigh wave case, eq. (3.39) can be simplified to:

$$V = i\,\overline{V}\,e^{-i\left(\omega t + \frac{\pi}{2}\right)} \qquad (3.40)$$

where the amplitude $\overline{V}$ of the sensor response to harmonic, antisymmetric or symmetric Lamb

waves is:

$$\overline{V}_{antisymm,symm} = \frac{S_{PZT}\,A_{antisymm,symm}}{lb\sin\theta\cos\theta}\sin\left(\frac{kb\sin\theta}{2}\right)\sin\left(\frac{kl\cos\theta}{2}\right) \qquad \text{(oblique incidence)} \qquad (3.41)$$

Where the terms $A_{antisymm} = 4E\left(\tanh rd - \dfrac{2rs}{k^2 + s^2}\cdot\tanh sd\right)$ and

$A_{symm} = 4F\left(\coth rd - \dfrac{2rs}{k^2 + s^2}\cdot\coth sd\right)$ are related to the Lamb wave fields. Comparing eq.

(3.41) with eq. (3.24), it can be seen that the Lamb and Rayleigh wave responses are formally

equivalent, with the difference being contained in the terms $A_{Rayleigh}$, $A_{antisymm}$ and

A_{symm} which define the specific wave fields. For parallel incidence ($\theta = 0$), eq. (3.33)

simplifies to:

$$\overline{V}_{antisymm,symm} = \overline{V}\Big|_{\theta \to 0} = \frac{S_{PZT}\,A_{antisymm,symm}\,k}{2l}\sin\left(\frac{kl}{2}\right) = \frac{S_{PZT}\,A_{antisymm,symm}\,\pi}{\lambda l}\sin\left(\frac{\pi l}{\lambda}\right)$$

<div align="right">(parallel incidence)   (3.42)</div>

where the results are expressed in terms of either wavenumbers or wavelengths.

The sinusoidal terms in eq. (3.42) follow the same wavelength tuning behavior as for the Rayleigh wave case. The response will also generally increase with decreasing sensor length due to the presence of the term l in the denominator of the expressions. Again, this may only be observed experimentally for constant transducer length to thickness aspect ratios.

In order to eliminate the arbitrary terms E and F implicitly present in eqs. (3.41)-(3.42), the response can be normalized by the Lamb wave power flow

$$N_{Lamb} = \sqrt{\int_{-d}^{+d} P_{Vx'}\,dz}$$

<div align="right">(3.43)</div>

Plots of the normalized strain at the top surface of the plate, $\varepsilon_{x'x'}\big|_{z=d}/N_{Lamb}$, are shown in Figs. 3.8(a) and 3.8(b) for the fundamental A_0 and S_0 modes, respectively. The plate is assumed 2.38 mm (0.09 in) thick and made of aluminum ($c_L = 6.3$ mm/μs, $c_T = 3.1$ mm/μs, $\rho = 2700$ kg/m^3).

In the case of A_0, Fig. 3.8(a), the normalized surface strain rapidly decreases from an asymptotically large value at extremely low frequencies to a relatively constant value over the remaining frequency range.
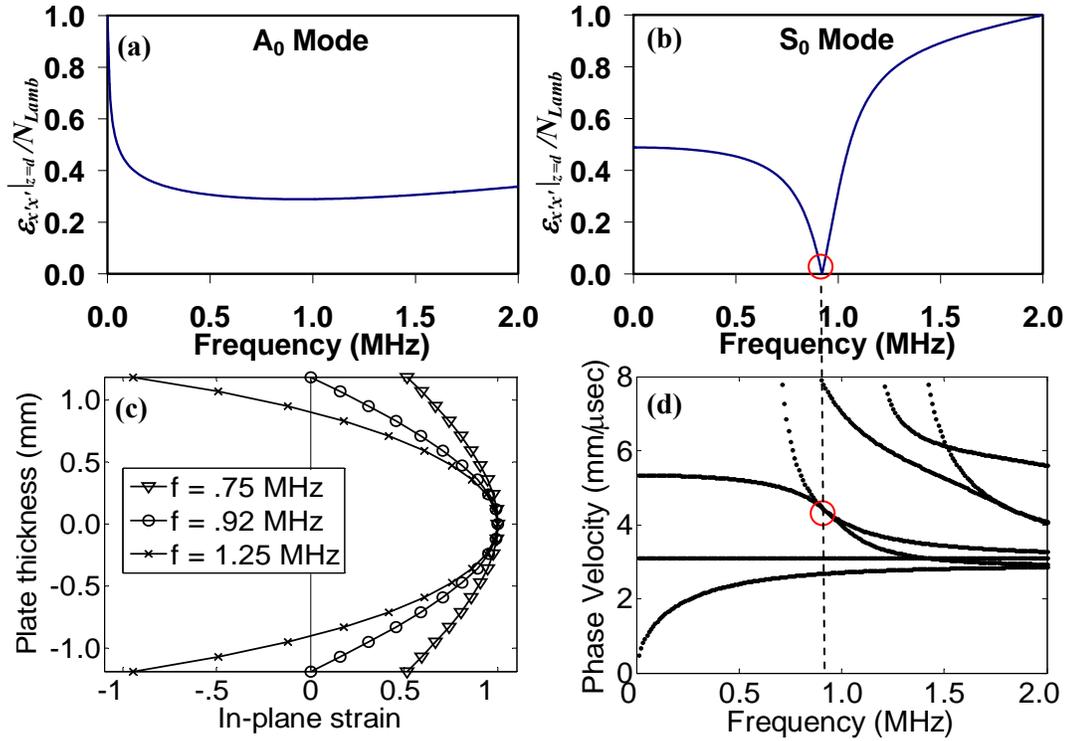
Fig. 3.8 In-plane surface strain of (a) A_0 Lamb wave and (b) S_0 Lamb wave in 2.38-mm thick aluminum plate normalized by the wave power flow through the plate at various frequencies; (c) progression of cross-sectional mode shapes of in-plane strains for S_0 at various frequencies; (d) phase velocity dispersion curves for the subject plate.

In the case of S_0, Fig. 3.8(b), two distinct trends exist: normalized strain values decrease with frequency for the first half of the frequency range, and increase with frequency for the second half of the frequency range. Separating these regions, a specific frequency (0.92 MHz) exists at which the normalized surface strain is zero. The 0.92 MHz value is the transition point between positive and negative strains at the plate's surface. The behavior can be seen in Fig. 3.8(c) showing the $\varepsilon_{x'x'}$ cross-sectional mode shapes of S_0 as the frequency changes from 0.75 MHz, to 0.92 MHz and then 1.25 MHz. In addition, this pivotal frequency occurs at the point of intersection between S_0 and the first-order shear horizontal mode, SH_1, as shown in the phase velocity dispersion curves of Fig. 3.8(d). It can be seen that the pivotal frequency is also a point of inflection of the S_0 dispersion curve. These conditions apply to

isotropic plates of any thickness. In practice, the zero-strain pivotal frequency can be useful, for example, to exclusively detect (or excite) the A_0 mode by eliminating the influence of the S_0 mode.

The normalized voltage response $\overline{V}/N_{Lamb}$ calculated from eq. (3.42) is plotted in Figs. 3.9(a) and 3.9(b) for harmonic A_0 and S_0 waves, respectively, propagating in the 2.38mm thick aluminum plate. The sensor dimensions in the wave propagation direction are the same as those considered for the Rayleigh response in Fig. 3.5: l = 12.7 mm, 6.35 mm and 3.17 mm, in addition to l = 0 (point sensor). It is clear from Fig. 3.7 that the sensor response to Lamb waves is considerably different from that to Rayleigh waves.
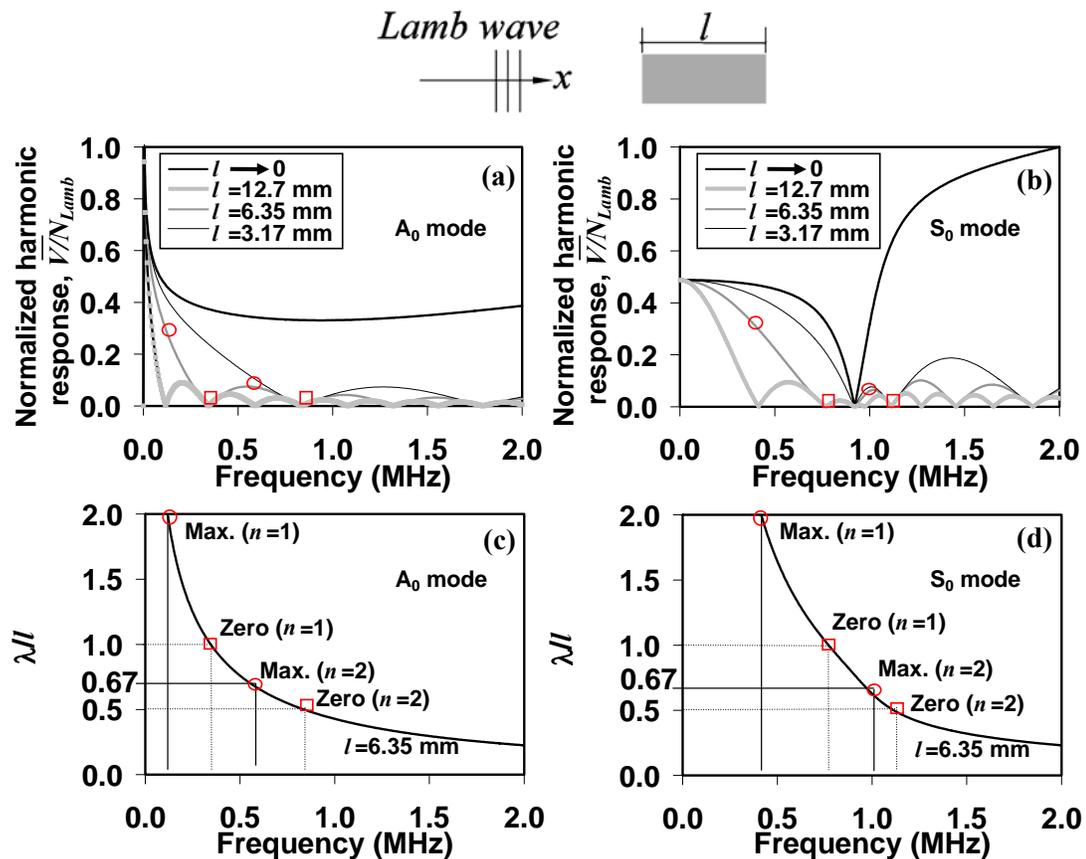
Fig. 3.9 Normalized voltage response of sensor subjected to parallel incident harmonic A_0 Lamb wave (a) and S_0 Lamb wave (b) for varying sensor lengths. Ratio of wavelength to sensor length of 6.35 mm for A_0 (c) and for S_0 (d).

For the A_0 mode, Fig. 3.9(a), the response asymptotically increases at extremely low frequencies. The response is generally smaller at higher frequencies, where it is primarily controlled by the wavelength tuning effect depending upon the ratio of Lamb wavelength to sensor dimension, λ / l. This ratio is plotted in Fig. 3.9(c) for A_0 and $l = 6.35$ mm. As for the Rayleigh wave, the local maxima are slightly shifted from the $\lambda = 2l/(2n-1)$ conditions due to the terms multiplying the sinusoidal function in eq. (3.42). Notice that the first local maximum point ($\lambda = 2l$) is overshadowed by the large response at the low frequencies. Zero response is obtained at sensor lengths equal to an integer multiple of the wavelength ($\lambda = l / n$). The amplitude of the A_0 response generally decreases with increasing frequency (for a given sensor length) and, instead, increases with decreasing sensor length (for a given frequency). The largest response is always obtained from the ideal point sensor ($l = 0$), which also matches identically the normalized, in-plane strain at the plate's surface in Fig. 3.8(a). Finally, the responses of the finite-size sensors converge to that of the point sensor at extremely low frequencies, where $\lambda \gg l$ and thus the exact strain solution at a point is retrieved.

The response to the S_0 mode is shown in Fig. 3.9(b). The asymptotic behavior at the low frequencies of the A_0 response is not present in the S_0 response, which is consistent with the surface strain plot in Fig. 3.8(b). The wavelength tuning effect is also apparent in the S_0 response as confirmed by the λ / l plot in Fig. 3.9(d) for the 6.35mm-long sensor. The zero response seen at $f = 0.92$ MHz, however, is not determined by wavelength tuning; it is rather the result of the vanishing surface in-plane strain as discussed in Fig. 3.8. Consequently, the zero response at the pivotal frequency applies regardless of the dimensions of the sensor. This behavior will always occur for any isotropic plate at the point of inflection of the S_0 dispersion curve, as discussed earlier. The response to frequencies around the pivotal value is also affected by the phenomenon. For example, notice that above 0.92 MHz the response does not

follow the usual trend of decreasing amplitude with increasing frequency (for a given sensor length). As in the previous cases, the S_0 response to a given frequency increases with decreasing sensor length, with the point sensor ($l = 0$) always yielding the largest response.

3.4.2   Arbitrary Excitation

Eq. (3.28) can be used to find the sensor response to an arbitrary, single mode Lamb wave excitation based on the harmonic response and the frequency content of the excitation. The same two cases examined for the Rayleigh waves, broadband and narrowband (toneburst) excitation, are considered for the Lamb waves in the following sections.

3.4.3   Broadband Lamb Excitation

3.4.3.1 Semi-Analytical Analysis

The term $\overline{P}$ in eq. (3.28) should represent the amplitude spectrum of the Lamb wave entering the sensor, as generated by a broadband excitation of the plate. As for the Rayleigh wave case, the surface strain spectrum $\varepsilon_{x'x'}^{a}\big|_{z=d}$ in the expression for $\overline{P}$ of eq. (3.29) was obtained through an FEA analysis of a plate subjected to broadband excitation. The harmonic response term $\overline{V}$ in eq. (3.28) was, instead, derived analytically from eq. (3.41). Thus the total sensor response $\overline{U}$ to broadband Lamb wave excitation was predicted semi-analytically.

The plate studied by the FEA ABAQUS Explicit simulations was aluminum ($c_L = 6.3$ mm/μs, $c_T = 3.1$ mm/μs, $\rho = 2700$ kg/m^3), 2.38 mm (0.09 in) in thickness and 400 mm (15.7 in) in length [155]. The discretization used 4-node, bilinear plane strain quadrilateral elements with two degrees of freedom per node. Material damping effects were neglected. The spatial resolution criterion was $\lambda_{min}/10$, and the integration time step was $\Delta t = 0.01$ μsec.

The simulated excitation used the half-sinusoid forcing function of 0.24 μsec in duration. Two distinct analyses were performed in order to preferably excite the fundamental antisymmetric (A_0) or the symmetric (S_0) mode. For the A_0 excitation, an out-of-plane force was applied to the surface node in one of the plate's free ends. For the S_0 excitation, an in-plane force was applied to the mid-thickness node of the plate's free end. These conditions replicated the excitation conditions adopted in the experimental tests that follow. Consistent with the positions of the PZT sensors used in the experiment, the detection points were located at 40 mm (1.57 in) from the antisymmetric excitation, and at 109 mm (4.3 in) from the symmetric excitation. The calculated in-plane strains at the surface of the plate, $\varepsilon_{x'x'}^{a}\big|_{z=d}$, are shown in Figs. 3.10(a) and 3.10(b) for the antisymmetric and the symmetric excitation, respectively. The strain amplitude is normalized to the relative maximum in the plots.

One complication is that multiple Lamb modes are generated by practical plate excitations including the ones considered in this study. Single-mode excitation can only be achieved if pure cross-sectional mode shapes are induced. This is generally difficult to do, particularly over a wide frequency range such as the DC – 2 MHz range considered here. Because the harmonic response of the sensor to a single mode is known, it is important to identify and separate its contribution from that of the other modes when possible. For this purpose, Continuous Wavelet Transform (CWT) spectrograms, shown in Figs. 3.10(c) and 3.10(d), were calculated from the strain time histories. The CWT analysis decomposes the signals in both time and frequency, providing useful information regarding the guided wave energy captured in the signals. A complex Morlet mother wavelet (center frequency equal to 5, bandwidth parameter equal to 2) was used. The theoretical arrival times of the relevant modes from Rayleigh-Lamb theory are indicated as solid lines. It can be seen from the spectrograms that A_0 and S_0 are exclusively excited only below the cut-off frequencies of A_1

($\sim$ 0.7 MHz) and S_1 ($\sim$ 1.2 MHz), respectively.

In order to compute the sensor excitation spectrum, $\overline{P}$, the Fast-Fourier Transform (FFT) amplitude of the strain signals was calculated and is shown in Figs. 3.10(e) and 3.10(f) for the antisymmetric and the symmetric cases, respectively. Based on the CWT scalograms, prior to FFT processing appropriate time gates were applied to the strain time histories to isolate the contribution of the zero-order modes. For the antisymmetric excitation, Fig. 3.10(c), a time gate of 5 μsec – 90 μsec was employed to capture the A_0 contribution in the frequency ranges 0 MHz – 0.65 MHz and 0.75 MHz – 2 MHz. Between these frequency ranges, from 0.65 MHz to 0.75 MHz, a separate time gate of 0 μsec – 20 μsec was applied in order to separate A_0 from A_1. For the symmetric excitation, Fig. 3.10(d), the S_0 contribution was calculated using a time gate of 0 μsec – 80 μsec in the frequency range 0 MHz – 1.17 MHz, and a separate gate of 40 μsec – 70 μsec in the range 1.17 MHz – 2 MHz. These gates, however, could not fully isolate the contribution of S_0 from that of S_1 at around 1.25 MHz due to their equivalent group velocities. As a result, the spike in the symmetric spectrum of Fig. 3.10(f) at around 1.25 MHz reflects the contribution of S_1. Despite this interference, the sensor response $\overline{U}$ was evaluated by only considering the harmonic response to S_0. Although a more accurate representation should consider the superimposition of each modal contribution, this simplification was deemed sufficient given the dominant contribution of the zero-order modes and the time gates applied to limit the role of higher-modes.
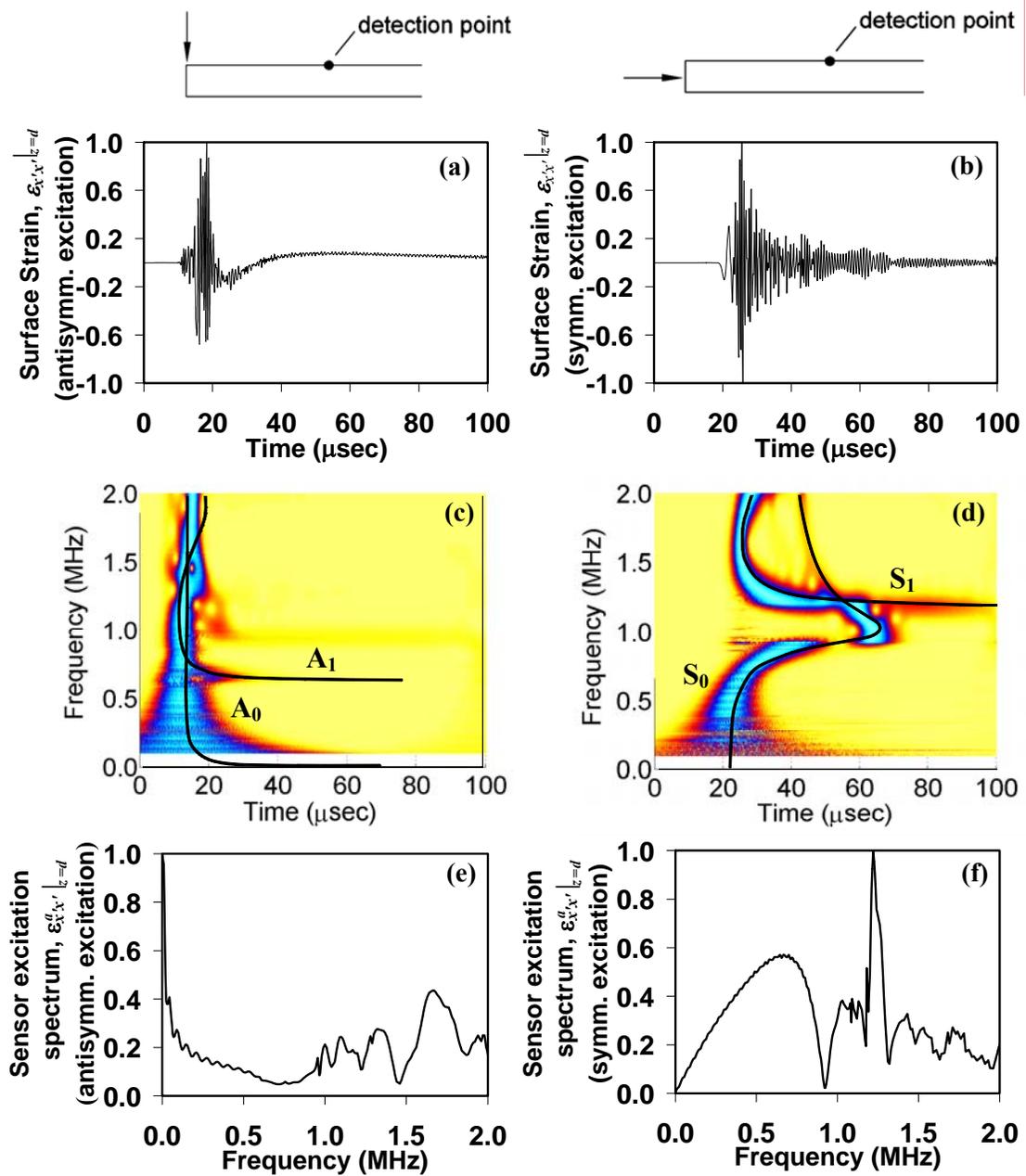
Fig. 3.10 FEA time histories of the in-plane surface strain in a plate generated by broadband antisymmetric (a) and symmetric (b) excitation. Wavelet Transform spectrograms of antisymmetric (c) and symmetric (d) responses. Sensor excitation spectra for symmetric (e) and antisymmetric (f) excitations.

3.4.3.2 Experimental Analysis

Experimental tests were conducted on a 216 mm × 172 mm × 2.38 mm (8.5 in × 6.7 in × 0.09 in) aluminum plate upon which a PZT sensor of dimensions 6.35 mm × 3.17 mm × 0.5 mm (0.25 in × 0.125 in ×0.02 in) was bonded using a thin layer of instant adhesive. The same Nd:YAG laser used for the Rayleigh wave tests was employed to generate the broadband Lamb waves in the plate in the slightly ablative regime. For the antisymmetric excitation, the laser pulse was applied normal to the plate surface at 40 mm from the sensor. For the symmetric excitation, the laser pulse was applied at the plate's free edge at 109 mm from the sensor. Results were collected for waves propagating at angles $\theta = 0°$ and $\theta = 90°$ from the lengthwise direction of the sensor. The sensor readings were processed through the CWT, gated in time to isolate the fundamental Lamb modes when possible, and then processed by the FFT.

Fig. 3.11 compares the voltage time histories measured by the sensor to the $\varepsilon_{x'x'}^{a}\big|_{z=d}$ surface strain computed by the FEA simulation and averaged over the sensor area. The two results should coincide if the simulation represented exactly the experimental conditions. The wave incidence angle is $\theta = 0°$. The plots in Figs. 3.11(a) and 3.11(b) correspond to the antisymmetric and the symmetric excitations, respectively. In both cases, the earlier portion (< 30 μsec) of the measurements is in good agreement with the averaged strain from the FEA. Beyond 30 μsec, the agreement is poorer primarily due to the reflections from the plate edges that are not present in the simulation, and also due to slightly different contributions of the higher-order modes.

The CWT spectrograms of the experimental results are shown in Figs. 3.11(c) and 3.11(d), again with the theoretical Rayleigh-Lamb solutions for the visible modes. It can be seen that an S_0 contribution appears in the antisymmetric excitation, Fig. 3.11(c). Similarly,

A_0 and A_1 contributions appear in the symmetric excitation, Fig. 3.11(d). An edge reflection can also be seen at around 50 µsec for the antisymmetric excitation.
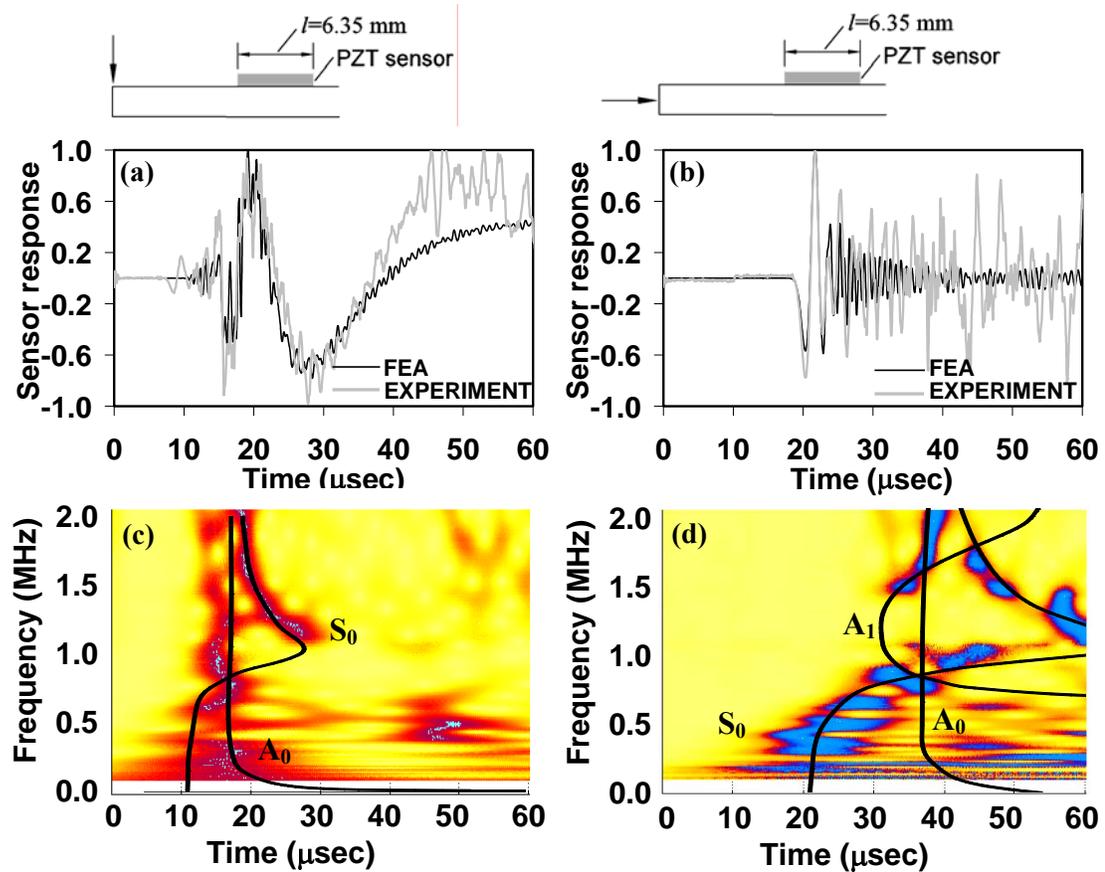
Fig. 3.11 Comparison between experiment and FEA of sensor response to broadband antisymmetric (a) and symmetric (b) excitation of a plate. Wavelet Transform spectrograms of antisymmetric (c) and symmetric (d) responses.

The experimental voltage responses of the sensor to broadband excitation are shown as grey lines in Fig. 3.12 for the wave incidence angles $\theta = 0°$ and $\theta = 90°$. Superimposed as dark lines are the sensor responses, $\overline{U}$, calculated from the semi-analytical analysis through eq. (3.28). The response to antisymmetric excitation, Figs. 3.12(a) and 3.12(b), is dominated by the asymptotically large amplitude at DC. The wavelength tuning condition of zero response, $\lambda = l$, can be observed in both the $\theta = 0°$ incidence at $f = 0.37$ MHz, and in the $\theta =$

90º incidence at f = 0.8 MHz.

As for the response to symmetric excitation, Figs. 3.12(c) and 3.12(d), local maxima are found at around 0.5 MHz for both incidence angles. This large response is due to the substantial S_0 contribution seen in Fig. 3.10(f), rather than to any wavelength tuning phenomena. Notice also that the magnitude of the response is generally larger for the perpendicular incidence (where the sensor dimension along the wave propagation direction, 3.17 mm, is small), consistent with the harmonic response of Fig. 3.9(b). The zero response seen in both Figs. 3.12(c) and 3.12(d) at 0.9 MHz is the pivotal point at which the S_0 in-plane strain at the surface vanishes (Fig. 3.8). Most of the other frequency values with zero response correspond to the wavelength tuning points $\lambda = l / n$. Once more, the spike at 1.25 MHz is due to the contribution of the S_1 mode.
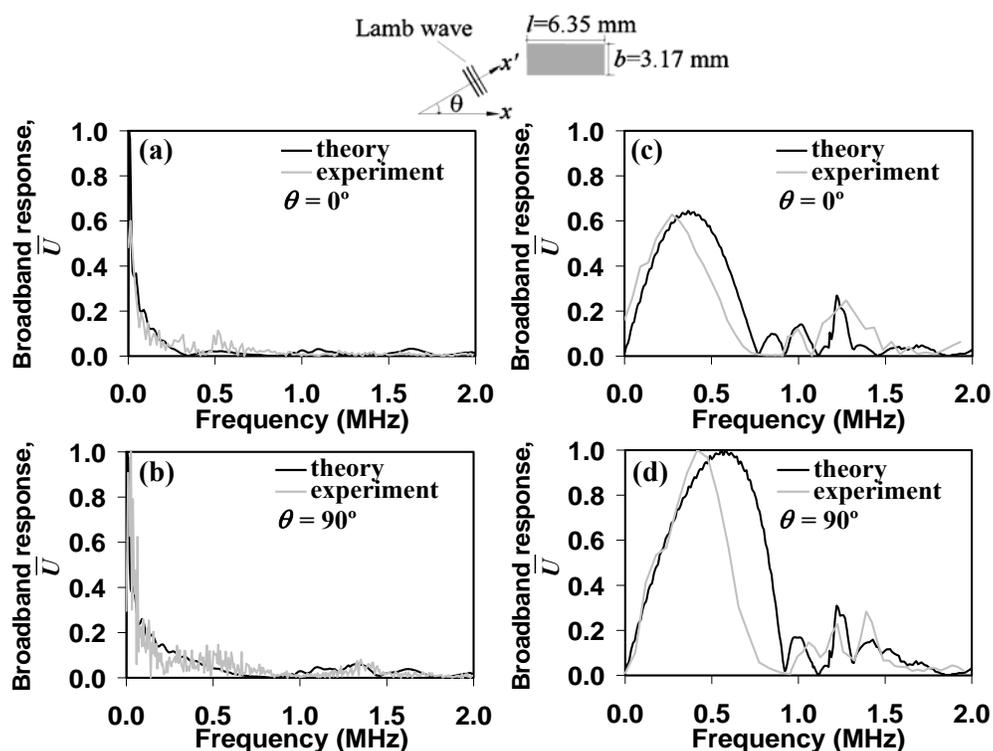
Fig. 3.12 Experimental and theoretical frequency response of 6.35mm × 3.17mm rectangular piezoelectric sensor to broadband antisymmetric (a, b) and symmetric (c, d) Lamb waves propagating at 0 deg (a, c) and 90 deg (b, d) from the lengthwise sensor dimension.

Because of the difficulty in generating a pure mode in practical broadband Lamb wave tests, the exact sensor excitation will depend on the geometrical and the physical properties of the plate, as well as the distance between the excitation and the detection points. The good agreement between experiment and theory shown in Fig. 3.12 suggests that a semi-analytical approach of the type used in this study could be used to reasonably predict the sensor response to broadband Lamb waves in other cases.

A more complete picture of the effect of the wave incidence angle is given in Fig. 3.13, where the response is calculated for $\theta = 0º$, $30º$, $60º$ and $90º$ for broadband antisymmetric Lamb excitation, Fig. 3.13(a), and symmetric Lamb excitation, Fig. 3.13(b). These results represent $\overline{U}$ in eq. (3.20) calculated from the semi-analytical analysis. The plots for $\theta = 0º$ and $90º$ coincide with those of Fig. 3.12. As expected, the results indicate an increase in response magnitude with decreasing sensor dimension along the wave propagation direction (i.e. increasing θ). Wavelength tuning effects are also visible. Notice again the pivotal, zero-response frequency of 0.9 MHz in the symmetric responses of Fig. 3.13(b) that occurs at all incidence angles.
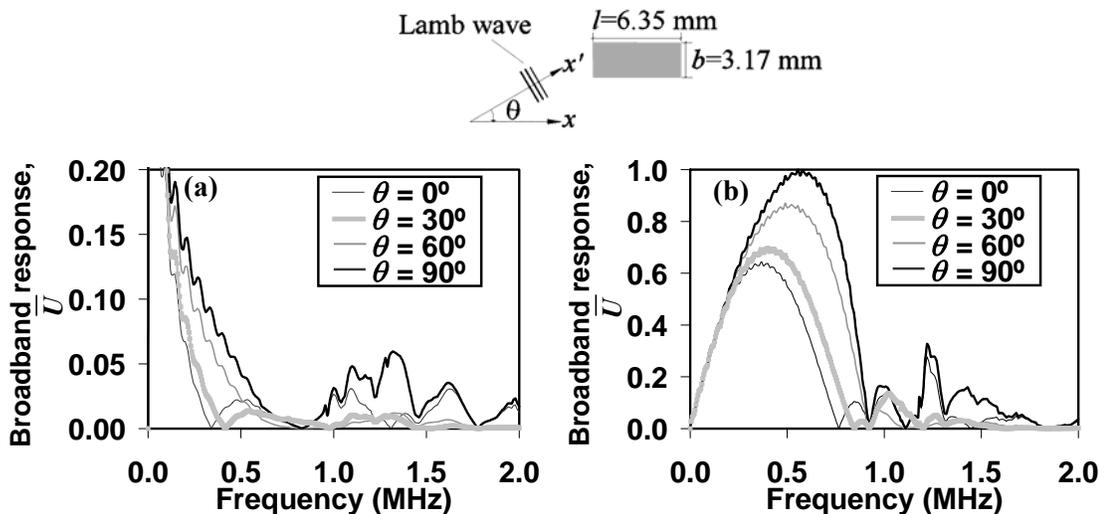
Fig. 3.13 Theoretical frequency response of rectangular sensor to broadband antisymmetric (a) and symmetric (b) Lamb wave excitation as a function of the wave incidence angle.

3.4.4   Narrowband Lamb Excitation

The same toneburst excitation examined for the Rayleigh wave is considered for the Lamb wave case. Eq. (3.28) is, again, used to calculate the sensor response as $\overline{\overline{U}} = \overline{V} \times \overline{P}$. For parallel incidence ($\theta = 0°$), the harmonic response $\overline{V}$ is given by eq. (3.42). The excitation spectrum $\overline{P}$ is given by eq. (3.35) with the substitution of $A_{Rayleigh}$ with $A_{antisymm}$ or A_{symm} for the antisymmetric and symmetric cases, respectively.   The total sensor response can thus be written as:

$$\overline{\overline{U}} = \left[\frac{\sin 2n\pi \left(\dfrac{2\pi c}{\lambda \omega_0} + 1 \right)}{\left(\dfrac{2\pi c}{\lambda} + \omega_0 \right)} - \frac{\sin 2n\pi \left(\dfrac{2\pi c}{\lambda \omega_0} - 1 \right)}{\left(\dfrac{2\pi c}{\lambda} - \omega_0 \right)} \right] \frac{S_{PZT} \lambda}{\pi l} \sin\left(\frac{\pi l}{\lambda} \right) \tag{3.44}$$

where the wavelength λ is explicitly indicated, and c is the phase velocity of the given Lamb mode. The above expression is formally identical to that obtained for the narrowband Rayleigh response in eq. (3.36). Also, the expression applies to both antisymmetric and symmetric Lamb waves. The individual response spectra, however, will be different because the velocity and the wavelength at each frequency in eqs. (3.36) or (3.44) will depend on the particular wave (Rayleigh, antisymmetric Lamb or symmetric Lamb mode).

Results from eq. (3.44) are plotted in Fig. 3.14 for sensor lengths $l = 6.35$ mm and 3.17 mm subjected to a narrowband antisymmetric excitation in the 2.38mm thick aluminum plate. As for the Rayleigh wave case, the three different center frequencies for the tonebust correspond to a large value (f_{max} at $\lambda = 2l$), an intermediate value (f_{int}), and the first zero value (f_{min} at $\lambda = l$) of the sensor's response to harmonic A_0. These frequencies are: $f_{max}= 0.11$ MHz, $f_{int}= 0.21$ MHz, $f_{min}= 0.34$ MHz for the 6.35-mm sensor; $f_{max}= 0.34$ MHz, $f_{int}= 0.55$ MHz, $f_{min}= 0.83$ MHz for the 3.17-mm sensor. Large responses are obtained when the toneburst center

frequency corresponds to the favorable wavelength tuning condition. The non-negligible outputs at zero harmonic response, f_{min}, is a consequence of the finite bandwidth of the toneburst and its associated side lobes. Similar results, not shown here, can be found for the symmetric excitation.
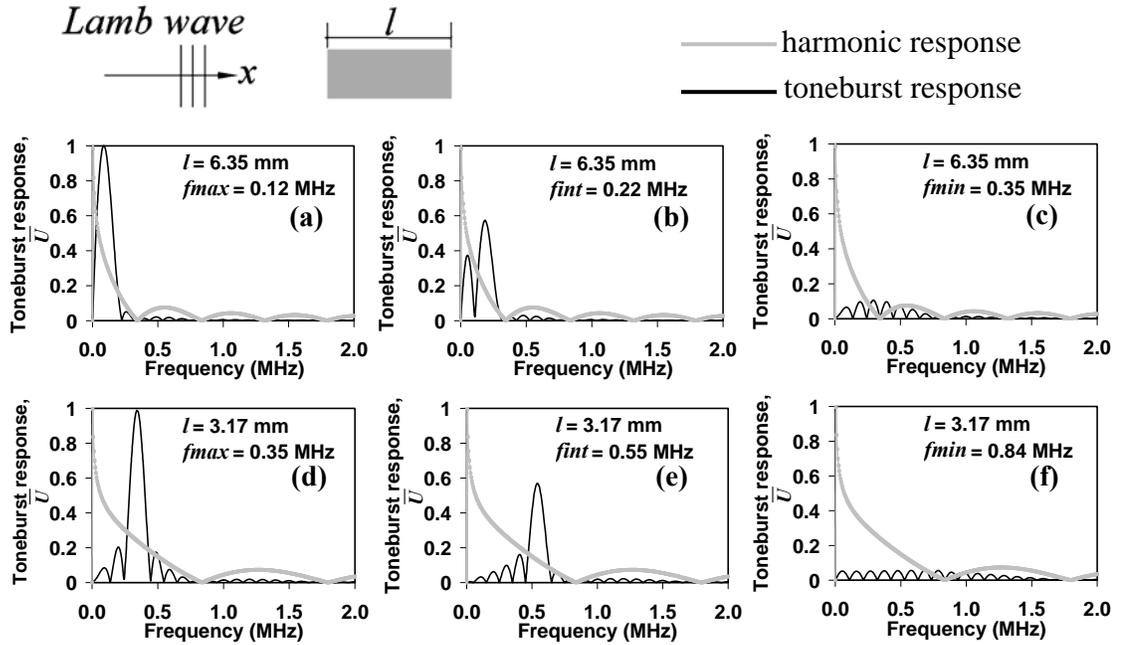
Fig. 3.14 Frequency response of piezoelectric sensor to narrowband (toneburst) antisymmetric A_0 Lamb wave centered at frequencies corresponding to a large (a), an intermediate (b), and a zero (c) harmonic response for sensor length $l = 6.35$ mm. (d), (e), (f), same as above for sensor length $l = 3.17$ mm. Harmonic responses in gray lines.

3.5   Response of MFC Transducers to Lamb Waves

3.5.1   Harmonic Lamb Excitation

Consider a rectangular MFC (type P1 or type P2) sensor bonded to the upper surface of an isotropic plate of thickness $2d$ and subjected to a harmonic strain field associated to plane Lamb waves propagating in the plane (x', z) along direction x' (Fig. 3.15).
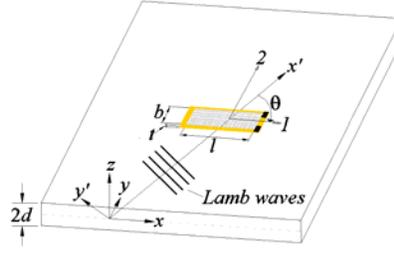
Fig. 3.15. Rectangular MFC sensor and its interaction with Lamb waves in general oblique incidence.

The wave propagation direction x' forms an angle θ with the lengthwise direction of the sensor. As dictated by eqs. (3.24) and (3.25), the MFC transducer is considered to respond to only in-plane normal strains. The in-plane Lamb wave strain $\varepsilon_{x'x'}$ can be transformed along the lengthwise and widthwise axes of the MFC transducer using the following strain transformation:

$$
\begin{aligned}
\varepsilon_{11} &= \varepsilon_{x'x'} \cos^2 \theta \\
\varepsilon_{22} &= \varepsilon_{x'x'} \sin^2 \theta
\end{aligned}
\tag{3.45}
$$

Ignoring shear lag effects, the MFC voltage expressions given in eqs. (3.24) and (3.25) therefore become:

$$
V = \frac{\displaystyle\int_0^b \int_0^l \left[\left(d_{11} Y_1^E + d_{12} \nu_{12} Y_2^E \right) \varepsilon_{x'x'} \cos^2 \theta + \left(d_{11} \nu_{12} Y_2^E + d_{12} Y_2^E \right) \varepsilon_{x'x'} \sin^2 \theta \right] dxdy}{(2w)bp\left[\left(1 - \nu_{21} \nu_{12} \right) e_{11}^\sigma - \left(d_{11}^2 Y_1^E + 2 d_{11} d_{12} \nu_{12} Y_2^E + d_{32}^2 Y_2^E \right) \right]}
$$

$$
\text{(MFC type P1) (3.46a)}
$$

$$
V = \frac{t\displaystyle\int_0^b \int_0^l \left[\left(d_{31} Y_1^E + d_{32} \nu_{12} Y_2^E \right) \varepsilon_{x'x'} \cos^2 \theta + \left(d_{31} \nu_{12} Y_2^E + d_{32} Y_2^E \right) \varepsilon_{x'x'} \sin^2 \theta \right] dxdy}{lb\left[\left(1 - \nu_{21} \nu_{12} \right) e_{33}^\sigma - \left(d_{31}^2 Y_1^E + 2 d_{31} d_{32} \nu_{12} Y_2^E + d_{32}^2 Y_2^E \right) \right]}
$$

$$
\text{(MFC type P2) (3.46b)}
$$

Following the same procedure outlined in section 3.4.1 yields the following expressions for the harmonic MFC voltage response magnitudes [148,149]:

$$\overline{V}_{antisymm,symm} = \frac{S_{MFC\ P1}\ A_{antisymm,symm}}{(2w)bp\sin\theta\cos\theta}\sin\left(\frac{kb\sin\theta}{2}\right)\sin\left(\frac{kl\cos\theta}{2}\right) \qquad \text{(MFC type P1) (3.47b)}$$

$$\overline{V}_{antisymm,symm} = \frac{S_{MFC\ P2}\ A_{antisymm,symm}}{lb\sin\theta\cos\theta}\sin\left(\frac{kb\sin\theta}{2}\right)\sin\left(\frac{kl\cos\theta}{2}\right) \qquad \text{(MFC type P2) (3.47b)}$$

Note that the MFC voltage response to Lamb wave excitation is nearly identical to that of a monolithic PZT transducer described in eq. (3.41) with exception of the frequency independent terms $S_{MFC\ P1}$, $S_{MFC\ P2}$ and the effective electrode area $(2w)bp$ in the case of the MFC (type P1) transducer. Unlike the case of the monolithic transducer, the terms $S_{MFC\ P1}$ and $S_{MFC\ P2}$ are dependant upon the incident angle (due to the anisotropy of the MFC device) and are described according to the following expressions:

$$S_{MFC\ P1} = \frac{\left[\left(d_{11}Y_1^E + d_{12}\nu_{12}Y_2^E\right)\cos^2\theta + \left(d_{11}\nu_{12}Y_2^E + d_{12}Y_2^E\right)\sin^2\theta\right]}{\left[\left(1-\nu_{21}\nu_{12}\right)e_{11}^\sigma - \left(d_{11}^2Y_1^E + 2d_{11}d_{32}\nu_{12}Y_2^E + d_{12}^2Y_2^E\right)\right]} \qquad \text{(MFC type P1) (3.48a)}$$

$$S_{MFC\ P2} = \frac{t\left[\left(d_{31}Y_1^E + d_{32}\nu_{12}Y_2^E\right)\cos^2\theta + \left(d_{31}\nu_{12}Y_2^E + d_{32}Y_2^E\right)\sin^2\theta\right]}{\left[\left(1-\nu_{21}\nu_{12}\right)e_{33}^\sigma - \left(d_{31}^2Y_1^E + 2d_{31}d_{32}\nu_{12}Y_2^E + d_{32}^2Y_2^E\right)\right]} \qquad \text{(MFC type P1) (3.48b)}$$

3.5.2 Broadband Lamb Excitation

3.5.2.1 Analytical Analysis

For consistency with the experimental tests, only the MFC (type P2) transducer was considered in the analytical analysis. Following the same formulation as outlined in section 3.3.2 and 3.3.3.1, the response magnitude of the MFC (type P2) sensor to an oblique incident broadband Lamb wave excitation is:

$$\overline{U} = \frac{S_{MFC\ P2}\ \lambda^2 \varepsilon_{x'x'}^a\big|_{z=0}}{\pi^2 lb\sin\theta\cos\theta}\sin\left(\frac{\pi b\sin\theta}{\lambda}\right)\sin\left(\frac{\pi l\cos\theta}{\lambda}\right) \qquad (3.49)$$

where $\varepsilon_{x'x'}^{a}\big|_{z=0}(\omega)$ is the amplitude spectrum of the surface strain induced by the arbitrary source at the point of entry into the sensor. It is important to note that this expression is only valid for characterizing the response to a single mode. For multimode excitation, the broadband response could be found by the summation of terms on the r.h.s of eq. (3.49) where each term corresponds to a particular mode and each modal contribution is captured by $\varepsilon_{x'x'}^{a}\big|_{z=0}(\omega)$.

3.5.2.2 Experimental Analysis

Experimental tests were conducted on a $1.22\times1.22\text{m}^2$ aluminum and $[0/\pm45]_{2s}$ CFRP plate with dimensions $.33\times.33\text{m}^2$ in order to evaluate the response of the MFC (type P2) transducer to a broadband source. An MFC transducer was permanently bonded to the surface of each specimen. The active piezoelectric dimensions of the MFC transducer are 12.2mm $\times$ 25.5mm. For the CFRP specimen, the transducer were bonded such that the widthwise dimension ran parallel with the 0º fiber axis.

For the following tests, broadband excitation was simulated by performing pencil lead breaks (Hsu-Neilsen source) normal to the plate surface. This out-of-plane excitation initiated a predominant zero order flexural wave and is similar in nature to delamination and impact sources [122]. Excitation was induced at locations which produced wavefronts at incident angles of 0º, 45º, and 90º with respect to widthwise axis of the transducer. The distance between source and receiver was maintained at 76.2 mm. Each signal was acquired using a National Instruments PXI unit coupled with Labview for performing frequency analysis of the received waveforms.

The theoretical and experimentally measured frequency response of the MFC transducers is shown in Fig. 3.16 for each test specimen. Plots (a) and (d), (b) and (e) and (c)

and (f) correspond to incident angles of 0°, 45°, and 90°, respectively. The theoretical response (gray series) was computed according to eq. (3.49) where the wavenumbers k for the zero order antisymmetric mode were extracted from the dispersion solutions of the system by means of a semi-analytical finite element analysis (SAFE). Description of the SAFE method will be given in chapter 4. The width b and length l variables represent the active electrode dimensions of the transducer and θ corresponds to the incident angle of the wavefront. Because the excitation was broadband in nature, the amplitude spectrum of the surface strain induced by the source, $\varepsilon_{x'x'}^{a}\big|_{z=0}$ was approximated as unity over the entire frequency range of interest. Values for the piezoelectric and elastic constants used in the evaluation of the theoretical response are summarized in table 1 [142]. To compare the theoretical and experimental frequency response, the maximum of the response spectra for each angle was normalized to a value of 1.

Table 3.1. Piezoelectric and elastic constants for the MFC (type P2) transducer adopted in theoretical response evaluation.

Y_1^E (GPa)	Y_2^E (GPa)	d_{31} (pC/N)	d_{32} (pC/N)	v_{12}	v_{21}	e_{33}^{σ} (nF/m)
16	30	-370	-370	0.17	0.31	16.37
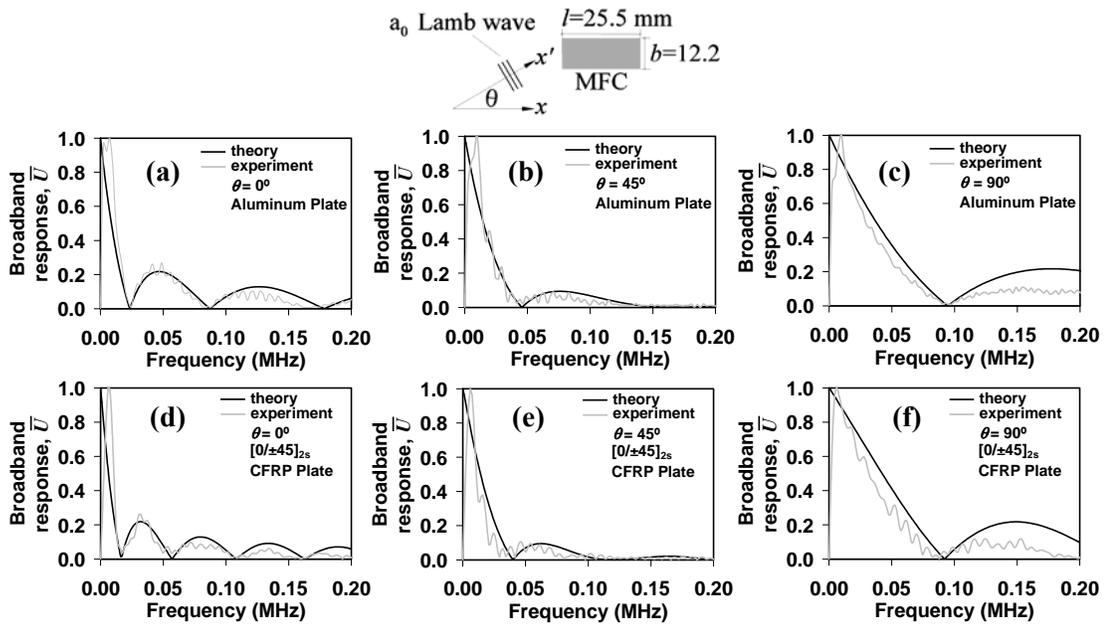
Fig. 3.16 Experimental and theoretical frequency response of 12.2mm $\times$ 25.5mm MFC sensor bonded to aluminum plate and subjected to broadband Lamb waves propagating at (a) 0º, (b) 45º, and (c) 90º from lengthwise sensor dimension. (d), (e), and (f) Same but for $[0/\pm45]_{2s}$ CFRP plate.

It can be observed that the broadband response magnitude is a maximum at low frequencies. This is a consequence of the very large wavelengths, whereby the transducer behaves as an ideal point sensor. At higher frequencies, the response is governed by wavelength-sensor dimension tuning effects; formalized in the two sine terms in eq. (3.49). Comparison of the experimentally measured and theoretically predicted frequency response behavior on the aluminum and the CFRP plate show very good agreement both in relative amplitude and spectral shape. Slightly larger discrepancy exists between experiment and theory for the composite plate case. However, it is important to note that the oblique incident broadband MFC response defined in eq. (3.49) was derived for isotropic systems. For anisotropic laminated systems, the analytical expression for Lamb wave strain (eq. (3.37)) is no longer valid. Instead, the Lamb wave solution is much more complex and closed form

solutions for the Lamb wave strain in terms of a single arbitrary wave amplitude are not available.

3.6   Conclusions

The majority of the studies detailing piezoelectric transducer-wave interaction have only considered piezo-generated wave fields. In an extension to the these studies, this chapter examined the fundamental response of surface-mounted, piezoceramic (PZT) and piezocomposite (MFC) sensors subjected to harmonic, broadband and narrowband wave fields under plane wave hypotheses. The problem was studied by coupling the essential behavior of each sensor as a strain integrator to the strain field associated to a particular wave type.

For parallel incidence, the solutions contained the wavelength tuning term, $\sin(\pi l/\lambda)$, where l is the dimension of the transducer along the direction of incidence. This term predicts local maxima in the response for sensor dimensions equal to an odd multiple of half the wavelength, and zeroes in the response for sensor dimensions equal to an integer multiple of the wavelength. However, the presence of other terms related to the wave strain field smears the wavelength tuning effect by shifting the position of the local maxima and controlling the relative magnitude of these maxima. The additional terms also produce interesting phenomena not related to wavelength tuning, such as an asymptotically large response to A_0 Lamb modes at low frequencies, and an identically zero response to S_0 Lamb modes at the point of inflection of their phase velocity dispersion curve. The response was shown to generally increase with decreasing sensor dimensions. The point sensor (zero dimension) resulted in the largest response, identically matching the wave strain field spectrum and thus confirming the "ideal sensor" behavior.

A slight discrepancy was observed between the theoretical and experimental

broadband frequency response characteristics of the piezoceramic transducers. However, better agreement between theory and experiment in both aluminum and composite substrates was achieved when considering the MFC (type P2) transducer. The larger discrepancy in theory for the piezoceramic transducer is most likely a consequence of its larger thickness and stiffness compared with the MFC transducer. As a result, the assumptions that the induced strain within the transducer and the surface strain of the host structure are equal as well as that the in-plane normal strain is constant throughout the transducer's thickness produced greater error in the predicted response [150]. Minor error between theory and experiment for both transducer pairs was also a result of approximated surface strain values, $\varepsilon_{x'x'}^{a}\big|_{z=0}$ used to evaluate the theoretical response behavior.

From this study, it was acknowledged that the derived sensor response characteristics resulted in a predictable directivity behavior for rectangular transducers. Therefore, in addition to extending the work of previous investigations, the results from this chapter were utilized to develop a new passive damage detection approach for complex composite systems. This approach is discussed in detail in chapter 10. Derived expressions for the MFC (type P1) transducer voltage response are employed in chapter 7 to evaluate the theoretical effects of temperature on the transducer response behavior.

Acknowledgement

Another part of chapter 3 will be submitted for possible publication in *Smart Materials and Structures*, Matt, Howard; Lanza di Scalea, Francesco. 2006. The current running title of this paper is "New method for damage location in complex CFRP structures based upon the use of piezoelectric transducer rosettes". The dissertation author was the primary investigator and author of this paper.

Chapter 4

Semi-Analytical Finite Element Models of Guided Waves in Multilayered Plates

4.1   Framework of SAFE Method

4.1.1   Viscoelastic Models for Wave Propagation

A linear viscoelastic model was used in the SAFE formulation in order to model the material damping. Linear viscoelasticity can be modeled by allowing complex components in the material's stiffness matrix as follows:

$$\widetilde{\mathbf{C}} = \mathbf{C}' - i\mathbf{C}'' \tag{4.1}$$

In Eq. (4.1) $\mathbf{C}'$ contains the storage moduli, representing the capacity of the material to store and release energy conservatively, and $\mathbf{C}''$ contains the loss moduli, responsible for the dissipation of energy. In practice, the matrix $\widetilde{\mathbf{C}}$ can be expressed as a combination of the elastic stiffness tensor, $\mathbf{C}'$, and the viscosity tensor $\boldsymbol{\eta}$. The coefficients of the viscosity tensor are typically measured at a single characteristic frequency value.

The hysteretic model, well-established in ultrasonic NDE, was considered in this study to represent material damping. The imaginary component of the stiffness matrix in eq. (4.1) is frequency independent, thus:

$$\widetilde{\mathbf{C}} = \mathbf{C}' - i\boldsymbol{\eta} \tag{4.2}$$

As a consequence, the hysteretic stiffness matrix has to be determined only once for the entire frequency range examined.

4.1.2 Equations of Motion

Guided wave equations of motion are formulated using Hamilton's principle. In general, the non-conservative form of Hamilton's principle, i.e. the generalized Hamilton's principle, should be used to account for energy loss. However, the following analysis adopts a simplified approach that assumes a conservative waveguide. By accounting for viscoelastic materials, the strain energy distribution is complex along with the wavenumbers. Therefore, the energy loss is accounted for by estimating the power dissipated by the section from the imaginary part of the cross-sectional strain energy distribution. This approach is valid if the cross-sectional strain energy distribution of a propagating wave is not significantly modified by increasing levels of damping [160].

The first variation of the Hamiltonian of the waveguide, which vanishes at all material points, is:

$$\delta H = \int_{t_1}^{t_2} \delta \left(\Phi_S - T_K \right) \, dt = 0 \tag{4.3}$$

where Φ_S is the strain energy and T_K is the kinetic energy. The strain energy is given by:

$$\Phi = \frac{1}{2} \int_{V_W} \boldsymbol{\varepsilon}^T \widetilde{\mathbf{C}} \boldsymbol{\varepsilon} \, dV \tag{4.4}$$

where the upper script T means a transpose vector and V_W is the waveguide volume. The kinetic energy is represented as:

$$T = \frac{1}{2} \int_{V_W} \dot{\mathbf{u}}^T \rho \, \dot{\mathbf{u}} dV \tag{4.5}$$

where ρ is the mass density and the dot represents a time derivative. By integrating by parts the firs variation of the Hamiltonian of the waveguide becomes:

$$\int_{t_1}^{t_2} \left[\int_{V_W} \delta \left(\boldsymbol{\varepsilon}^T \right) \widetilde{\mathbf{C}} \boldsymbol{\varepsilon} \, dV_W + \int_{V_W} \delta \left(\mathbf{u}^T \right) \rho \, \ddot{\mathbf{u}} dV_W \right] dt = 0 \tag{4.6}$$

4.1.3   Waveguide Displacement Field

The mathematical model presented here is for the case of a plate-like waveguide immersed in vacuum, as shown in Fig. 4.1(a). The waveguide is an infinitely wide plate that can generally be composed of anisotropic viscoelastic materials as well as orthotropic layers. The wave propagates along direction x with wavenumber k and angular frequency ω. In cartesian coordinates, the displacement, stress and strain field components at each point of the waveguide are expressed by:

$$\mathbf{u} = \begin{bmatrix} u_x & u_y & u_z \end{bmatrix}^T, \quad \boldsymbol{\sigma} = \begin{bmatrix} \sigma_x & \sigma_y & \sigma_z & \sigma_{yz} & \sigma_{xz} & \sigma_{xy} \end{bmatrix}^T, \quad \boldsymbol{\varepsilon} = \begin{bmatrix} \varepsilon_x & \varepsilon_y & \varepsilon_z & \gamma_{yz} & \gamma_{xz} & \gamma_{xy} \end{bmatrix}^T \tag{4.7}$$

The strain-displacement relationships can be written in matrix form as:

$$\boldsymbol{\varepsilon} = \left[\mathbf{L}_x \frac{\partial}{\partial x} + \mathbf{L}_y \frac{\partial}{\partial y} + \mathbf{L}_z \frac{\partial}{\partial z} \right] \mathbf{u} \tag{4.8}$$

where

$$\mathbf{L}_x = \begin{bmatrix} 1 & 0 & 0 \\ 0 & 0 & 0 \\ 0 & 0 & 0 \\ 0 & 0 & 0 \\ 0 & 0 & 1 \\ 0 & 1 & 0 \end{bmatrix}, \quad \mathbf{L}_y = \begin{bmatrix} 0 & 0 & 0 \\ 0 & 1 & 0 \\ 0 & 0 & 0 \\ 0 & 0 & 1 \\ 0 & 0 & 0 \\ 1 & 0 & 0 \end{bmatrix}, \quad \mathbf{L}_z = \begin{bmatrix} 0 & 0 & 0 \\ 0 & 0 & 0 \\ 0 & 0 & 1 \\ 0 & 1 & 0 \\ 1 & 0 & 0 \\ 0 & 0 & 0 \end{bmatrix} \tag{4.9}$$

The displacement field is assumed to be harmonic along the propagation direction, x, and spatial functions are used to describe its amplitude along the cross-sectional axis z:

$$\mathbf{u}(x,y,z,\mathrm{t}) = \begin{bmatrix} u_x(x,z,\mathrm{t}) \\ u_y(x,z,\mathrm{t}) \\ u_z(x,z,\mathrm{t}) \end{bmatrix} = \begin{bmatrix} u_x(z) \\ u_y(z) \\ u_z(z) \end{bmatrix} e^{i(kx-\omega \mathrm{t})} \tag{4.10}$$

where $i=sqrt(-1)$ is the imaginary unit.
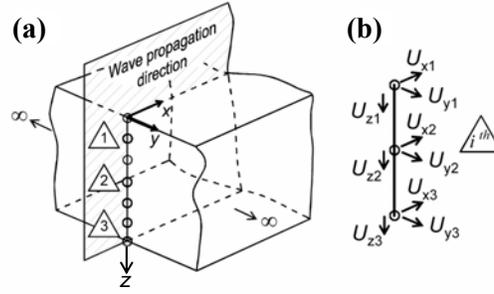
Fig. 4.1. (a) Discretization of an infinite plate and (b) degrees of freedom of the mono-dimensional three-node element.

4.1.4 Semi-Analytical Finite Element Method

The plate section is discretized in the thickness direction, z, by a set of one-dimensional finite elements with quadratic shape functions and three nodes, with three degrees of freedom per node. The displacement vector can be approximated over the element domain in terms of the shape functions, $N_{ne}(z)$, and the nodal unknown displacements, (U_{xne}, U_{yne}, U_{zne}) in the x, y and z directions (Fig. 4.1):

$$\mathbf{u}^{(e)}(x,y,z,\text{t}) = \begin{bmatrix} \sum\limits_{ne=1}^{3} N_{ne}(z)U_{xne} \\ \sum\limits_{ne=1}^{3} N_{ne}(z)U_{yne} \\ \sum\limits_{ne=1}^{3} N_{ne}(z)U_{zne} \end{bmatrix}^{(e)} e^{i(kx-\omega\text{t})} = \mathbf{N}(z)\mathbf{q}^{(e)}e^{i(kx-\omega\text{t})} \tag{4.11}$$

where:

$$\mathbf{N}(z) = \begin{bmatrix} N_1 & 0 & 0 & N_2 & 0 & 0 & N_3 & 0 & 0 \\ 0 & N_1 & 0 & 0 & N_2 & 0 & 0 & N_3 & 0 \\ 0 & 0 & N_1 & 0 & 0 & N_2 & 0 & 0 & N_3 \end{bmatrix} \tag{4.12}$$

$$\mathbf{q}^{(e)} = \begin{bmatrix} U_{x1} & U_{y1} & U_{z1} & U_{x2} & U_{y2} & U_{z2} & U_{x3} & U_{y3} & U_{z3} \end{bmatrix}^{\text{T}} \tag{4.13}$$

and *ne* denotes the number of nodes per element. The strain vector in the element can be represented as a function of the nodal displacements:

$$\boldsymbol{\varepsilon}^{(e)} = \left[\mathbf{L}_x \frac{\partial}{\partial x} + \mathbf{L}_y \frac{\partial}{\partial y} + \mathbf{L}_z \frac{\partial}{\partial z} \right] \mathbf{N}(z)\mathbf{q}^{(e)} e^{i(kx-\omega t)} = \left(\mathbf{B}_1 + ik\mathbf{B}_2 \right) \mathbf{q}^{(e)} e^{i(kx-\omega t)} \tag{4.14}$$

where $\mathbf{B}_1 = \mathbf{L}_z\mathbf{N}_{,z}$, $\mathbf{B}_2 = \mathbf{L}_x\mathbf{N}$ and $\mathbf{N}_{,z}$ is the derivative of the shape function matrix with respect to the z coordinates. From eq. (4.6), the discrete form of the Hamiltonian function becomes:

$$\int_{t_1}^{t_2} \left\{ \bigcup_{e=1}^{n_{el}} \left[\int_{V_{We}} \delta\left(\boldsymbol{\varepsilon}^{(e)\mathrm{T}}\right) \widetilde{\mathbf{C}}_e \boldsymbol{\varepsilon}^{(e)} \, dV_{We} + \int_{V_{We}} \delta\left(\mathbf{u}^{(e)\mathrm{T}}\right) \rho_e \, \ddot{\mathbf{u}}^{(e)} dV_e \right] \right\} dt = 0 \tag{4.15}$$

where n_{el} is the total number of cross-sectional elements and $\widetilde{\mathbf{C}}_e$ and ρ_e are the element's complex stiffness matrix and mass density, respectively.

The substitution of eq. (4.14) into the strain energy term in eq. (4.15), followed by some algebraic manipulation gives [161]:

$$\int_{V_e} \delta\left(\boldsymbol{\varepsilon}^{(e)\mathrm{T}}\right) \widetilde{\mathbf{C}}_e \boldsymbol{\varepsilon}^{(e)} \, dV_{We} =$$

$$\delta\mathbf{q}^{(e)\mathrm{T}} \int_z \left[\mathbf{B}_1^{\mathrm{T}} \widetilde{\mathbf{C}}_e \mathbf{B}_1 - ik\mathbf{B}_2^{\mathrm{T}} \widetilde{\mathbf{C}}_e \mathbf{B}_1 + ik\mathbf{B}_1^{\mathrm{T}} \widetilde{\mathbf{C}}_e \mathbf{B}_2 + k^2 \mathbf{B}_2^{\mathrm{T}} \widetilde{\mathbf{C}}_e \mathbf{B}_2 \right] dz\mathbf{q}^{(e)} \tag{4.16}$$

The element stiffness matrix can be calculated by integrating over the depth z only. The integration over x reduces to a unity factor due to the complex conjugate terms $exp[\pm i(kx-\omega t)]$. For viscoelastic materials, eq. (4.16) represents the sum of a real component, describing the time-averaged elastic energy in the section, and an imaginary component, related to the time-averaged power dissipated by the section.

Substituting the displacement expressions of eq. (4.11) in the second term of eq. (4.15) that is the element kinetic energy, and simplifying the harmonic terms $exp[\pm i(kx-\omega t)]$, the following can be written:

$$\int_{V_{We}} \delta\left(\mathbf{u}^{(e)\mathrm{T}}\right)\rho_e \ddot{\mathbf{u}}^{(e)} dV_{We} = \iint_{z\ x} \delta\left(\mathbf{u}^{(e)\mathrm{T}}\right)\rho_e \ddot{\mathbf{u}}^{(e)} dxdz = -\omega^2 \delta\mathbf{q}^{(e)\mathrm{T}} \int_z \mathbf{N}^{\mathrm{T}}\rho_e \mathbf{N} dz \mathbf{q}^{(e)} \tag{4.17}$$

Finally substituting Eqs. (4.16)-(4.17) into eq. (4.15) yields:

$$\int_{t_1}^{t_2} \left\{ \bigcup_{e=1}^{n_{el}} \delta\mathbf{q}^{(e)\mathrm{T}} \left[\mathbf{k}_1^{(e)} + ik\mathbf{k}_2^{(e)} + k^2\mathbf{k}_3^{(e)} - \omega^2\mathbf{m}^{(e)} \right] \mathbf{q}^{(e)} \right\} dt = 0 \tag{4.18}$$

where

$$\mathbf{k}_1^{(e)} = \int_z \left[\mathbf{B}_1^{\mathrm{T}}\widetilde{\mathbf{C}}_e\mathbf{B}_1 \right]dz, \quad \mathbf{k}_2^{(e)} = \int_z \left[\mathbf{B}_1^{\mathrm{T}}\widetilde{\mathbf{C}}_e\mathbf{B}_2 - \mathbf{B}_2^{\mathrm{T}}\widetilde{\mathbf{C}}_e\mathbf{B}_1 \right]dz$$

$$\mathbf{k}_3^{(e)} = \int_z \left[\mathbf{B}_2^{\mathrm{T}}\widetilde{\mathbf{C}}_e\mathbf{B}_2 \right]dz, \quad \mathbf{m}^{(e)} = \int_z \mathbf{N}^{\mathrm{T}}\rho_e\mathbf{N} dz \tag{4.19}$$

Applying standard finite element assembling procedures to eq. (4.18) gives:

$$\int_{t_1}^{t_2} \left\{ \delta\mathbf{U}^{\mathrm{T}} \left[\mathbf{K}_1 + ik\mathbf{K}_2 + k^2\mathbf{K}_3 - \omega^2\mathbf{M} \right]\mathbf{U} \right\} dt = 0 \tag{4.20}$$

where $\mathbf{U}$ is the global vector of unknown nodal displacements, and:

$$\mathbf{K}_1 = \bigcup_{e=1}^{n_{el}} \mathbf{k}_1^{(e)}, \quad \mathbf{K}_2 = \bigcup_{e=1}^{n_{el}} \mathbf{k}_2^{(e)}, \quad \mathbf{K}_3 = \bigcup_{e=1}^{n_{el}} \mathbf{k}_3^{(e)}, \quad \mathbf{M} = \bigcup_{e=1}^{n_{el}} \mathbf{m}^{(e)} \tag{4.21}$$

Due to the arbitrarity of $\delta\mathbf{U}$, the following homogeneous general wave equation is finally obtained:

$$\left[\mathbf{K}_1 + ik\mathbf{K}_2 + k^2\mathbf{K}_3 - \omega^2\mathbf{M} \right]_M \mathbf{U} = \mathbf{0} \tag{4.22}$$

where the subscript M is the number of total degrees of freedom of the system. Eq. (4.22) is the dispersion equation. Recasting eq. (4.22) by doubling its algebraic size as:

$$\left[\mathbf{A} - k\mathbf{B} \right]_{2M} \mathbf{Q} = \mathbf{0} \tag{4.23}$$

where:

$$\mathbf{A} = \begin{bmatrix} \mathbf{0} & \mathbf{K}_1 - \omega^2\mathbf{M} \\ \mathbf{K}_1 - \omega^2\mathbf{M} & \mathbf{K}_2 \end{bmatrix}, \quad \mathbf{B} = \begin{bmatrix} \mathbf{K}_1 - \omega^2\mathbf{M} & \mathbf{0} \\ \mathbf{0} & -\mathbf{K}_3 \end{bmatrix}, \quad \mathbf{Q} = \begin{bmatrix} \mathbf{U} \\ k\mathbf{U} \end{bmatrix} \tag{4.24}$$

leads to a first order eigenvalue problem in the wavenumber for a given frequency ω. Solution of the eigenvalue problem yields a complex spectrum of propagative and evanescent modes.

At each frequency ω, $2M$ complex eigenvalues $k_m = k_{Re} + ik_{Im}$, and, consequently, $2M$ complex eigenvectors are obtained. The eigenvectors are the M forward and the corresponding M backforward modes. The m-th eigenvalue k_m represents the m-th wavenumber, and Q_m is the corresponding eigenvector in which the first M components describe the m-th mode shape.

4.2   Dispersive Solutions of Guided Wave Propagation

Once the wavenumbers have been evaluated, for each guided wave mode the *phase velocity* can be determined by $c = \omega/k_{Re}$ and the wave *attenuation*, in Nepers per meter, is given by k_{Im}, where k_{Re} and k_{Im} are the real and imaginary parts of the wavenumber. At a given frequency, ω, a guided wave with attenuation κ Nepers per meter means that the wave amplitude will decay by $e^{-\kappa}$ in one meter. The attenuation of a guided wave, defined as the loss per unit distance traveled, is strictly related to the dissipation of energy and therefore to the loss moduli of the material. For the adopted hysteric damping model, the wave attenuation for non-dispersive waves is a linear function of the frequency [162].

Since the waves are attenuated, the propagation speed does not coincide with the classical group velocity, $c_{gr} = \partial\omega/\partial k$ [163]. In this case the wavenumber is complex. As a result, the differentiation with respect to the real part of the wavenumber leads to non-physical solutions such as infinite velocities at some locations of the dispersion curves. The *energy velocity*, V_e, is the appropriate property for damped media. The definition of the energy velocity can be found in classical textbooks [127]. The expression used in the present work is:

$$V_e = \frac{\dfrac{1}{H}\displaystyle\int_H \mathbf{P_V} \cdot \hat{\mathbf{x}}\,dz}{\dfrac{1}{T_P}\displaystyle\int_{T_P}\left(\dfrac{1}{H}\displaystyle\int_H e_{tot}\,dz\right)d\mathrm{t}} \tag{4.25}$$

Where $\hat{\mathbf{x}}$ is the unit vector along the wave propagation direction, H is the total waveguide thickness, $1/T_P\int(..)d\mathrm{t}$ denotes the time average over one period T_P, e_{tot} is the total energy density (kinetic and potential), and $\mathbf{P_V}$ represents the time averaged Poynting vector (real part only). The time averaged Poynting vector can be calculated as:

$$\mathbf{P_V} = -\frac{1}{2}\mathrm{Re}(\boldsymbol{\sigma}\dot{\mathbf{u}}*) \tag{4.26}$$

where σ is the classical 3×3 stress tensor, and $\dot{\mathbf{u}}*$ is the complex conjugate of the particle velocity vector. The numerator in eq. (4.26) is the average power flow carried by a mode in the wave propagation direction over a unit period of time. The denominator in eq. (4.26) can be evaluated by introducing the expressions of the time averaged energy for the kinetic component, $\langle e_k \rangle_\mathrm{t}$, and the potential component, $\langle e_p \rangle_\mathrm{t}$, following the formulation in Bernard *et al.* [157]:

$$\langle e_k \rangle_\mathrm{t} = \frac{\omega^2}{4}\rho\mathbf{u}^\mathrm{T}\mathbf{u}, \qquad \langle e_p \rangle_\mathrm{t} = \frac{1}{4}\boldsymbol{\varepsilon}^\mathrm{T}\mathbf{C'}\boldsymbol{\varepsilon} \tag{4.27}$$

where the constant 1/4 results from the time integration over the period T_P. Eqs. (4.26) and (4.27) can be evaluated and substituted in eq. (4.25) once the element nodal displacements are calculated from the eigenvalue problem and the displacement and strain fields are reconstructed.

4.3   Conclusions

For guided wave analysis, the SAFE approach requires at most a 2-D discretization of the system; allowing for greater computational efficiency relative to standard FE methods. The SAFE approach also provides the flexibility in finding solutions to systems where exact methods are incapable, such as systems of arbitrary cross-section and laminates containing a large number of layers.

Within this thesis, the SAFE method was adopted for modeling guided wave dispersive solutions in CFRP laminates and bonded joints. Due to the non-negligible damping effects in FRP composites, damping was accounted for in the models by incorporating a complex stiffness matrix for the material. As a result of this, the appropriate energy velocity, rather than the conventional group velocity, was calculated along with the frequency-dependent attenuation of the guided waves. The ability to compute wave attenuation was useful for recognizing mode-coupling regions as well as identifying modes which can propagate long distances with minimal signal loss.

In addition to the wave attenuation, the SAFE models were used to evaluate the frequency dependant guided wave mode velocities, mode shapes, and other useful quantities of guided wave modes that exist for each particular structure of interest. The phase velocity curves provided a simple means for determining the frequency-wavelength relation. As discussed in chapter 3, this information was relevant for determining the optimal response frequencies for transducers of specific dimensions. The computed energy velocity allowed for mode identification during experimental testing. For wave propagation through discretely non-prismatic regions, such as across the wing skin-to-spar joint, mode shapes were useful in predicting the mode conversion behavior that occurs at the boundaries. SAFE solutions enable the evaluation of strain and powerflow distribution throughout the cross-section. This

ability was particularly useful for identifying ideal mode-frequency combinations which show preferential sensitivity toward damage sources in bonded CFRP joints. For all of the above stated reasons, the SAFE analyses performed in this research proved to be highly beneficial in the design of an effective guided wave based damage identification strategy.

Acknowledgement

Chapter 4, in part, has been published in the *Proceedings of SPIE's Smart Structures/NDE Conference*, Bartoli, Ivan; Marzani, Allessandro; Matt, Howard; Lanza di Scalea, Francesco; Viola, Erasmo. 2006. The title of this paper is "Modeling wave propagation in damped waveguides of arbitrary cross-section". The dissertation author was a co-author of this paper.

Chapter 5

SAFE Analysis of CFRP Plate-to-Spar Joints

5.1   Problem Statement

The focus of this thesis is upon damage detection in aircraft wings which are comprised primarily of carbon fiber-reinforced polymer (CFRP) composites. One example of a heavy use of composites is found in Unmanned Aerial Vehicles (UAV's). An illustration showing a partial cross section of a typical UAV wing assembly is shown in Fig. 5.1(a).
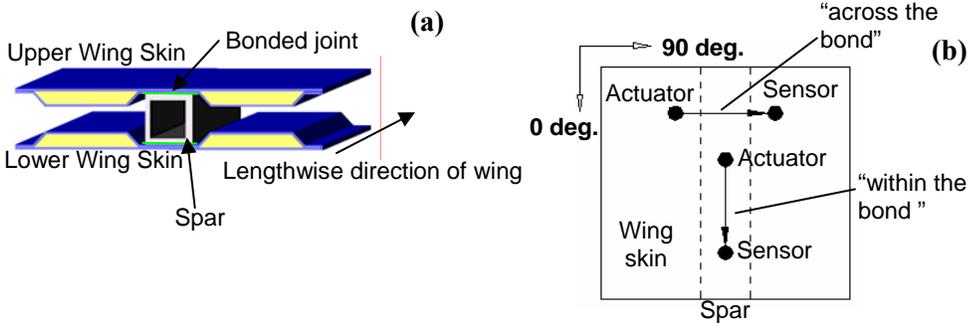
Fig. 5.1. (a) Typical wing skin-to-spar assembly in unmanned aerial vehicles. (b) "Across the bond" and "within bond test" testing configurations.

The wing skin is generally made of a Nomex or aluminum honeycomb core sandwiched between two CFRP laminated composite plates. Each skin is bonded using high strength epoxy adhesive to a tubular composite spar that runs down the length of the wing. The sandwiched skin tapers down in the bonded region, where only the CFRP laminates are bonded to the spar. The adhesively bonded wing skin-to-spar joint is one of the most critical structural components of the aircraft wing. Consequently, in this thesis, the active methods for damage identification were applied to representative wing skin-to-spar assemblies. Damage considered within the joint includes regions with poorly-cured adhesive and disbonded regions. For active guided wave interrogation, the theoretical and experimental tests that are discussed in chapters 5-9 were performed on three representative wing skin-to-spar specimens.

The first two specimens consist of CFRP laminates directly bonded to a woven CFRP square tube. These systems are a sufficiently accurate representation of the wing skin-to-spar joint when the ultrasonic transducers are installed in close proximity to the bonded region. The third specimen is a scaled UAV wing section containing a single CFRP spar. The SAFE analyses for guided waves in the first two specimens are considered in this chapter.

The SAFE models were used to evaluate the frequency dependant guided wave velocities, attenuation, mode shapes, and cross sectional strain profiles within the wing skin-to-spar specimens. For active interrogation, the main guided wave feature used to characterize the joint condition was based upon the strength of transmission. Therefore, the SAFE models were also used to predict the change in strength of transmission as a function of bond state. This was achieved by assessing the poweflow of the identified joint modes responsible for transmitting energy across the joint.

5.2   Model Definition

The two specimens considered for this analysis are identical with exception of their plate layups. These layups consist of a quasi-isotropic $[0/\pm45/90]_S$ and a $[0/\pm45/0]_S$ layup. Both plates consist of eight plies and are bonded to a woven $[0/90]$ tubular spar. The $[0/\pm45/0]_S$ layup is a better representation of most UAVs, where the 0-deg fibers provide flexural rigidity and the ±45-deg fibers provide torsional rigidity to the wing. The quasi-isotropic lay-up was examined as the most simplified model of the UAV wing.

The bond conditions that were examined in this analysis are regions with poorly-cured adhesive and disbonded regions, in addition to regions with properly-cured adhesive. For consistency with experiments, analyses considered guided waves propagating across the joint

and strictly within the joint. The "within the bond" and "across the bond" test configurations are depicted in Fig. 5.1(b).

For the "within the bond" case, Fig. 5.2(a), the only model of interest was the bonded region with the wave propagating along the lengthwise direction of the spar. For the "across the bond" configuration, Fig. 5.2(b), the wing skin model was examined separately in addition to the bonded region with the wave propagating across the spar. In both cases, the bond model assumed a uniform thickness for the spar, neglecting the localized increase in thickness at the bond edges found in the "across the bond" case due to the tubular geometry. This approximation was considered acceptable given that the frequency content of the waves examined was such that their penetration beyond the wall thickness of the spar was negligible. Also, mode conversion effects at the bond edges for the "across the bond" case were predicted based on the similarities between cross-sectional mode shapes of the excitation and the carrier modes found from the models, following the same philosophy adopted in previous works [96,99,127].

The SAFE method was implemented in Matlab$^{©}$ using the PDE toolbox for creating the finite element mesh. The waveguide was modeled as a system of N homogeneous and generally viscoelastic anisotropic layers. As discussed in chapter 4, the dimensions were considered infinite in the width direction, y, perpendicular to the wave propagation direction, x. Thus the wave propagation problem could be studied by simply considering a longitudinal section in the x-z wave propagation plane. The section was discretized in the thickness direction, z, by a set of one-dimensional finite elements with quadratic shape functions and three nodes, with three degrees of freedom per node.
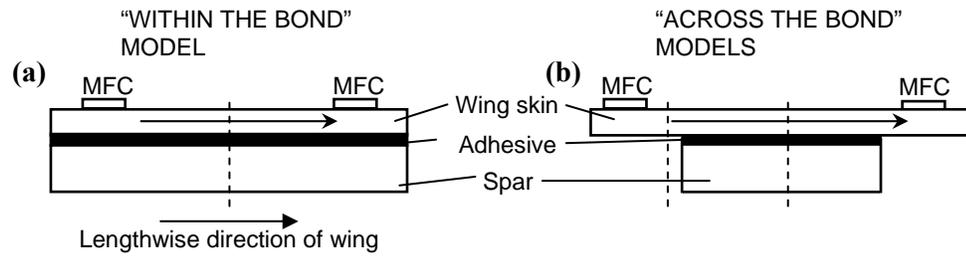
Fig. 5.2. Wave propagation models for (a) "within bond" test configuration, (b) "across bond" test configuration.

Each ply of the CFRP wing skin was modeled as a transversely isotropic layer with the following standard constitutive laws in the global laminate directions (x, y, z):

$$\boldsymbol{\sigma} = \overline{\mathbf{C}}\boldsymbol{\varepsilon} = \mathbf{T}_1^{-1}\widetilde{\mathbf{C}}\mathbf{T}_2\boldsymbol{\varepsilon} \tag{5.1}$$

where $\overline{\mathbf{C}}$ is the complex stiffness matrix in the global directions of the laminate, $\widetilde{\mathbf{C}}$ is the complex stiffness matrix in the principal material directions of the individual ply, $\mathbf{T}_1$ and $\mathbf{T}_2$ are the transformation matrices from the principal material directions to the global laminate directions as defined in Jones [164].

The values of the real components, C_{ij}', and of the imaginary components, C_{ij}'', of the stiffness matrix adopted in the models are shown in Table 5.1. For the eight CFRP layers of the skin, the real components of the stiffness matrix were based upon experimentally determined elastic values of Y_1^E, Y_2^E, G_{12} for T700/ p7263w-15 carbon epoxy prepreg and typical Poisson's ratio values of ν_{12}, ν_{23} for T300/5208 carbon epoxy prepreg. The imaginary components of the stiffness matrix were assumed equal to the values used by Neau *et al.* [165].

Table 5.1. Real and imaginary stiffness coefficients and geometric and physical properties for bonded layers.

Layer	C'_{11} [GPa] (C''_{11}) [GPa]	C'_{12} [GPa] (C''_{12}) [GPa]	C'_{13} [GPa] (C''_{13}) [GPa]	C'_{22} [GPa] (C''_{22}) [GPa]	C'_{23} [GPa] (C''_{23}) [GPa]	C'_{33} [GPa] (C''_{33}) [GPa]	C'_{44} [GPa] (C''_{44}) [GPa]	C'_{55} [GPa] (C''_{55}) [GPa]	C'_{66} [GPa] (C''_{66}) [GPa]	Density [kg/m³]	Thickness [mm]
CFRP Lamina	135 (8.23)*	5.70 (0.65)*	5.70 (0.60)*	14.2 (0.34)*	8.51 (0.25)*	14.2 (0.65)*	2.87 (0.24)*	4.55 (0.28)*	4.55 (0.25)*	1530	0.133
CFRP Spar	88.0 (4.28)	5.45 (0.65)	5.09 (0.425)	88.0 (4.28)	5.09 (0.425)	11.3 (0.65)	4.64 (0.26)	4.64 (0.26)	6.00 (0.25)	1530	5.235
Properly-cured Bond	8.24 (0.39)	4.10 (0.028)	4.10 (0.028)	8.24 (0.39)	4.10 (0.028)	8.24 (0.39)	2.07 (0.18)	2.07 (0.18)	2.07 (0.18)	1421	0.203
Poorly-cured Bond	6.89 (0.19)	4.58 (0.064)	4.58 (0.064)	6.89 (0.19)	4.58 (0.064)	6.89 (0.19)	1.16 (0.066)	1.16 (0.066)	1.16 (0.066)	1465	0.203
Disbond	0.0697 (0.0352)	0.0695 (0.0349)	0.0695 (0.0349)	0.0697 (0.0352)	0.0695 (0.0349)	0.0697 (0.0352)	0.000118 (0.000128)	0.000118 (0.000128)	0.000118 (0.000128)	1421	0.203

* From Neau et al., 2002

The CFRP spar was modeled as one homogenous layer with anisotropic properties equivalent to the multilayer [0/90] structure of T800/924. The real and imaginary components of the stiffness matrix, $\overline{\mathbf{C}}_{eq}$, for the equivalent spar layer were computed by averaging the coefficients of the stiffness matrices of two adjacent layers, $\overline{\mathbf{C}}_0$ and $\overline{\mathbf{C}}_{90}$, obtained from eq. (5.1). These equivalent coefficients were consistent with those obtained from the independent approach of Karunasena *et al.* [166]. The homogeneous equivalent coefficients are accurate when the number of layers is high and the wavelengths are large compared to the individual layer thickness, as was the case for the test spar. The epoxy adhesive was modeled as a viscoelastic isotropic layer. In this case the viscoelastic matrix, $\widetilde{\mathbf{C}}$, depends only on the two elastic constants, Young's modulus, Y^E, and shear modulus, G, that were calculated from the bulk longitudinal and shear wave velocities, $\tilde{c}_L$ and $\tilde{c}_S$. These complex velocities were calculated by the known expressions:

$$\tilde{c}_{L,S} = c_{L,S}\left(1 + i\frac{\alpha_{L,S}}{2\pi}\right)^{-1} \tag{5.2}$$

where $\alpha_{L,S}$ are the longitudinal and shear attenuation in the material, expressed in Nepers per wavelength. The attenuation and elastic constants for the properly-cured epoxy and for the poorly-cured epoxy were obtained through normal-incidence ultrasonic tests on properly-

mixed and poorly-mixed bulk epoxy samples. The poorly-cured epoxy resulted in a 42% degradation of the Young's modulus and a 44% degradation of the shear modulus compared to the properly-cured epoxy. The disbond was simulated in the model by reducing the shear wave velocity (real part) of the properly-cured adhesive by a factor of 100, reducing the longitudinal wave velocity by a factor of 10, and increasing the longitudinal and shear attenuation by a factor of 10. This simulation was considered representative of the Teflon release films used to simulate disbonded conditions in the experimental tests. The properties assumed for the various bond conditions are summarized in Table 1 in terms of stiffness coefficients, and in Table 2 in terms of bulk ultrasonic velocities and attenuations.

Convergence of the dispersion solutions was found satisfactory using one element for each ply in the wing skin, one element for the bond layer, and five elements for the spar. The number of elements was doubled to plot displacement, strain, and power flow cross-sectional shapes.

Table 5.2. Ultrasonic bulk longitudinal and shear velocities and material attenuations for the adhesive layer.

Layer	C_L [m/s]	C_T [m/s]	α_L [Np/λ]	α_T [Np/λ]
Properly-cured [1] Bond	2410	1210	0.149	0.276
Poorly-cured[1] Bond	2170	890	0.089	0.178
Disbond [2]	241	12.1	1.497	2.763

5.3   Dispersion Results for Different Bond States

Phase velocity, energy velocity and attenuation curves were obtained from the SAFE models for the three bond conditions examined (properly-cured bond, poorly-cured bond, and

[1] Values were experimentally measured
[2] Values were predicted

disbonded interface), each under the two testing configurations ("within" and "across" the bon

bond) and the two wing skin lay-ups ($[0/\pm45/90]_S$ and $[0/\pm45/0]_S$).

For the ease of the reader, throughout this thesis the conventional nomenclature of symmetric or antisymmetric character is used for all guided modes. However, the only true symmetric and antisymmetric modes exist when considering just the wing skin plate. The modes in skin-to-spar bond are not truly symmetric nor antisymmetric because the cross-section is not symmetric about its mid-plane. Modes propagating in the single skin plate will be indicated with a lower case, s_i , a_i and sh_i for the symmetric, the antisymmetric, and the shear horizontal modes, respectively. Modes propagating in the bonded region will be indicated with an upper case, S_i, A_i and SH_i. Due to the presence of the ±45 deg plies, the horizontally and vertically polarized partial waves are generally not de-coupled, and thus the dispersion curves presented always include the shear horizontal modes. For the sake of brevity, dispersion results will be shown only for the $[0/\pm45/0]_S$ joint under the "across the bond" test configuration. The complete set of results for all test cases considered will be shown in terms of transmission strengths in Section 5.5.

The results for the $[0/\pm45/0]s$ plate bonded to the spar with the properly-cured adhesive are shown in Fig. 5.3 considering wave propagation in the "across the bond" test configuration. The frequency range shown is DC-300 kHz which corresponds to the operating range of the experimental tests. The four modes of interest here are the zero-order symmetric, S_0, the zero- and first-order antisymmetric, A_0 and A_1, and the zero-order shear horizontal, SH_0. Figs. 5.3(b) and 5.3(c) show that A_1 is propagative only above 135 kHz whereas the other three modes are propagative throughout the frequency range. Although other higher-order modes exist with cut-on frequencies above 135 kHz, Fig. 5.3(b), they are not considered further due to their large attenuation, Fig. 5.3(c).
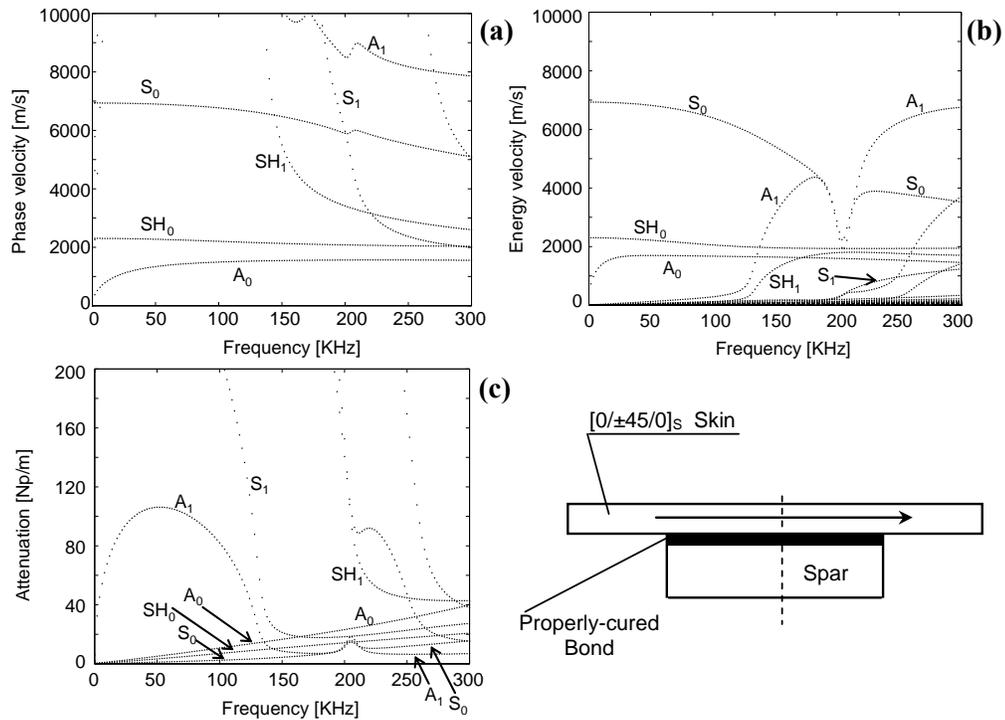
Fig. 5.3. (a) Phase velocity, (b) energy velocity, (c) and attenuation cuves for the [0/±45/0]s skin bonded to the spar with properly cured adhesive ("across the bond" testing configuration).

The two modes with minimum attenuation losses are S_0 below 200 kHz and A_1 above 200 kHz, Fig. 5.3(c). Thus these two modes appear to be preferred candidates for a bond monitoring system within the frequency range examined. Moreover, MFC and PZT transducers used for built-in ultrasonic structural diagnostics are typically operated in either the 1-1 or 3-1 electro-mechanical coupling mode, i.e. to generate and receive in-plane, rather than out-of-plane displacements. The cross-sectional mode shapes presented in the next section indicate that both S_0 and A_1 have substantial in-plane displacements at the skin plate surface, and they are thus coupled very effectively to the built-in piezoelectric transducers. The opposite is true for either A_0 (predominant out-of-plane displacement) or SH_0 (zero in-plane displacement along the wave propagation direction).

A closer look at Fig. 5.3 reveals a mode coupling effect occurring for both S_0 and A_1 at around 200 kHz. Mode coupling is a known phenomenon that can be caused by damping effects present in a single layer [163] or solely by geometrical effects in undamped multilayered structures [90]. In this study mode coupling is due to both viscoelastic damping and multilayer geometrical effects, as seen in Fig. 5.4(a).
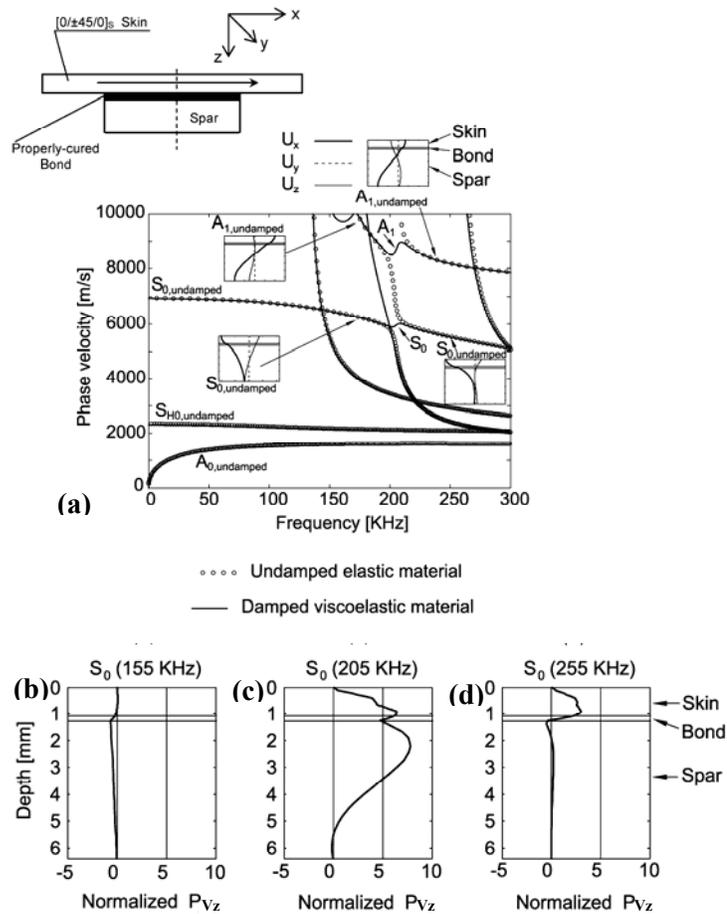
Fig. 5.4. (a) Phase velocity dispersion curves for the $[0/\pm 45/0]_S$ skin-to-spar joint ("across the bond" testing configuration) with damping and without damping. Through-thickness Poynting vector for S_0 at (b) 155 kHz, (c) 205 kHz, and (d) 255 kHz.

In Fig. 5.4(a), the phase velocity results are obtained from the SAFE model of the bonded joint with and without damping losses. The examination of the displacement mode shapes of $S_{0,undamped}$ and $A_{1,undamped}$ reveals that apparently different branches on either side of

the 200 kHz frequency value are indeed the same mode even in the undamped case. In other words, the branches are already coupled in the undamped case although they are not physically connected at 200 kHz. Once damping is included in the model, S_0 and A_1 essentially retrace the corresponding $S_{0,undamped}$ and $A_{1,undamped}$, and connect the branches at the mode coupling points around 200 kHz.

Mode coupling is generally associated to sharp changes in group or energy velocity, increased attenuation, and large transfer of energy across the thickness of the waveguide. The first two phenomena are clearly visible in Figs. 5.3(b) and 5.3(c) for both S_0 and A_1 at around 200 kHz. The third phenomenon is seen in the plots of Figs. 5.4(b), 5.4(c) and 5.4(d), comparing the normalized through-thickness power flow, P_{Vz}, of S_0 at the three frequencies of 155 kHz, 205 kHz and 255 kHz, respectively. At the mode coupling frequency of 205 kHz, Fig. 5.4(c), a large exchange of energy occurs between the top skin and the bottom spar. Contrarily, most of the energy flow occurs within the bottom spar at 155 kHz, Fig. 5.4(b), and within the top skin at 255 kHz, Fig. 5.4(d), with little interlayer flow. Similar Poynting vector results, not shown here, can be found for A_1. The large transfer of energy in the thickness direction is particularly relevant for a bond monitoring system as the one proposed here, that is based on relating bond defects to an increased strength of transmission through the joint. Exciting modes with large energy transfer between adherends, such as S_0 and A_1 at mode coupling frequencies, would clearly be beneficial in this case.

The dispersion curves for the case of the poorly-cured bond, where only the material properties within the thin bond layer were altered according to Table 5.1, did not show any notable change from those of the properly-cured bond. This is because the thickness of the bond layer was very small compared to the thickness of the entire skin-to-spar assembly that

dominates the dispersion. However, substantial changes in the wave power flow between the two cases were predicted, and this will be discussed in detail in the following sections.

As for the disbond case, shown in Figs. 5.5(a), 5.5(b), and 5.5(c), dramatic changes in the phase velocity, energy velocity and attenuation curves are evident. The main observation in this case is the appearance of additional modes that did not exist for either of the two bond cases discussed previously. For most of the frequency range examined, the additional modes of the disbonded joint essentially coincide with the solutions of the single wing skin plate, represented in the plots by the open dots. Therefore, the introduction of a disbond allows for the propagation of two separate types of modes, namely those whose energy is mainly concentrated within the upper plate above the bondline (identified in Fig. 5.5 by $S_{0,plate}$, $A_{0,plate}$, $SH_{0,plate}$, etc.), and those whose energy is mainly concentrated within the spar below the bondline (identified by $S_{0,spar}$, $A_{0,spar}$, $SH_{0,spar}$, etc.). Mode $S_{0,spar}$ of the disbonded joint corresponds to mode S_0 of the properly-cured joint. Similarly, $A_{1,spar}$ corresponds to A_1 of the properly-cured joint. A comparison of Fig. 5.5 to Fig. 5.3 indicates that the behavior of S_0 does not change substantially between the two bond cases. However, the mode coupling for A_1 disappears when a disbond is present. Under the testing conditions used in this study, the predominant carrier of energy through the disbonded joint is $S_{0,plate}$; that should thus be considered the most relevant mode in Fig. 5.5. The dispersion curves of $S_{0,plate}$ in the disbonded joint are virtually coincident to those of the single-plate s_0 mode above 100 kHz. Below this frequency, the mode deviates from the single-plate behavior as more energy leaks through the spar.
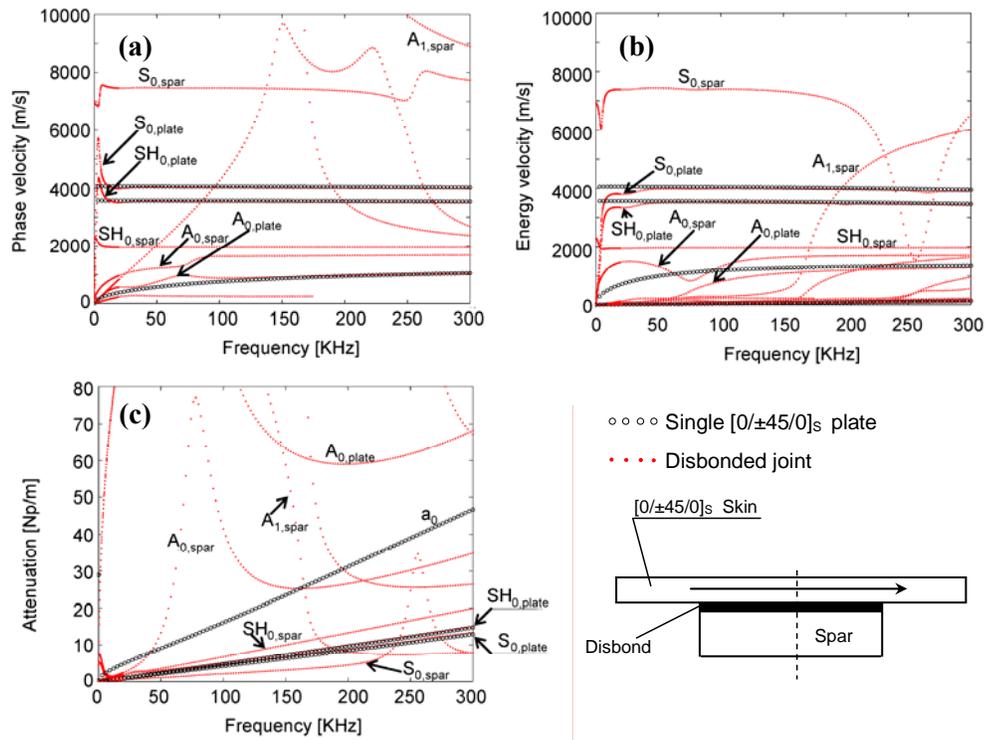
Fig. 5.5. (a) Phase velocity, (b) energy velocity, and (c) attenuation curves for the $[0/\pm45/0]_S$ skin-to-spar joint with a disbonded interface and for the single $[0/\pm45/0]_S$ plate ("across the bond" testing configuration).

5.4   Identification of Carrier Modes

Mode conversion effects as the wave travels through the joints were evaluated on the basis of the similarity between the displacement mode shapes of an incoming mode and those of a carrier mode. Guided wave analyses in the "across the bond" test configuration were based upon initial excitation of the s_0 mode and subsequent mode conversion in the bonded region. Likewise, the analysis for the "within the bond" test configuration was based upon initial excitation of those overlap modes with similar modes shapes to those of the single-plate s_0 mode. These assumptions were consistent with the in-plane (3-1) electro-mechanical coupling characterizing the operation of the piezoelectric transducers employed in the experiments.

Fig. 5.6(a) shows the displacement mode shapes for the $[0/\pm45/0]_S$ skin-to-spar bond tested in the "across the bond" configuration at the mode coupling frequency of 205 kHz. The left-hand plot in this figure shows the incoming s_0 mode in the wing skin. The plots to the right show the four possible carrier modes in the bond, namely S_0, A_0, A_1 and SH_0, considering the properly-cured bond condition. The notation for the displacement components is consistent with the reference system in Fig. 4.1. The dominant displacement for s_0 is the in-plane component in the wave propagation direction, u_x, that thus also dominates the mode conversion process. The u_x displacement is also the dominant component for the S_0 and A_1 carrier modes, and its symmetry within the upper plate in both carrier modes is similar to that of the incoming mode. Conversely, u_x is not dominant for A_0 and it is altogether absent for the shear horizontal SH_0 mode. It is therefore suggested that S_0 and A_1 will act as the primary energy carriers across the joint at this frequency.

Fig. 5.6(b) shows the cross-sectional strain components in the plane of propagation of the wave for the two carrier modes S_0 and A_1 at 205 kHz. To emphasize the bonded region, only the upper portion of composite spar wall is shown. It can be seen that both modes show a concentration of both normal strain, ε_{zz}, and shear strain, γ_{xz}, within the adhesive layer. Thus both modes are suitable candidates for detecting changes in both longitudinal and shear stiffness of the adhesive layer. Between the two modes, it is S_0 that produces the larger concentration of strains at the bondline, suggesting a larger sensitivity to bond conditions. This result will be confirmed by power flow considerations in the next section.

Similar results were found when analyzing the mode shapes in the poorly-cured joint. This is because the changes in the bond stiffness that were considered had little influence on the shapes of the modes, which are dominated by the skin and the spar adherends.
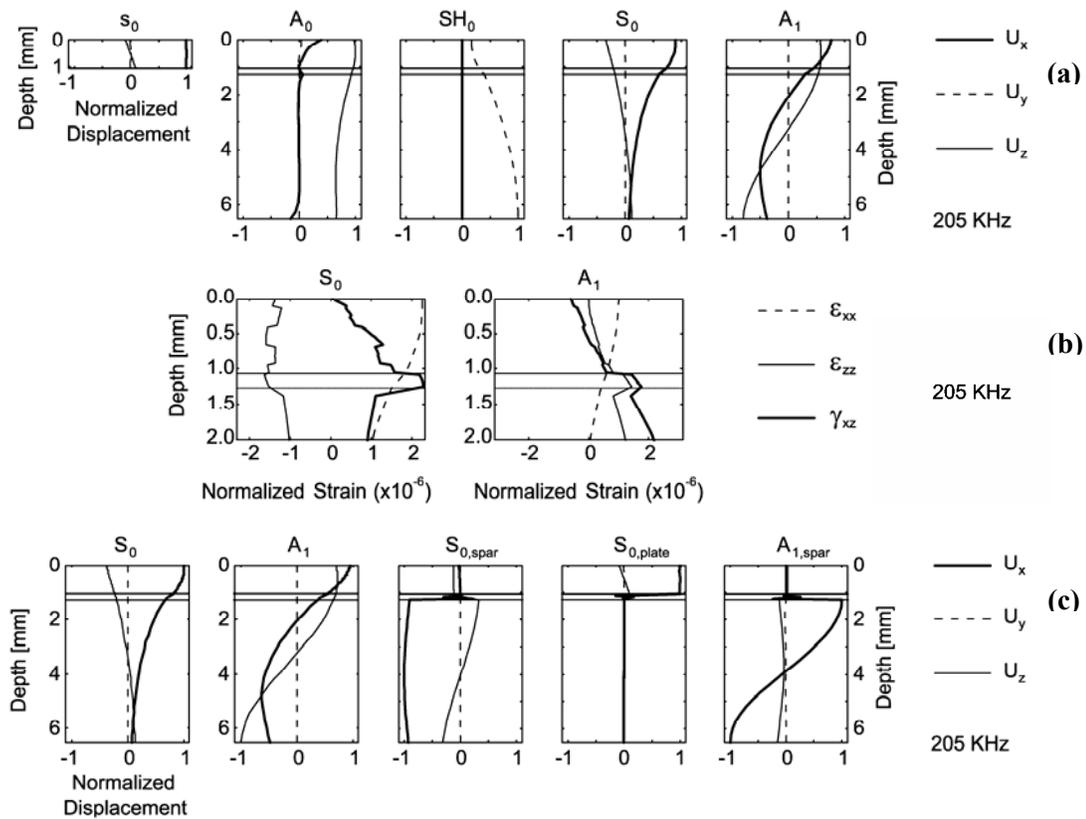
Fig. 5.6. The $[0/\pm45/0]_S$ skin-to-spar joint in the "across the bond" testing configuration: (a) displacement mode shapes at 205 kHz in the properly-cured bond, (b) strain profiles for modes S_0 and A_1 at 205 kHz in the properly-cured bond, (c) displacement mode shapes at 205 kHz in the disbonded joint. Also shown are the corresponding mode shapes for the incoming s_0 mode in the single plate (a) and the S_0 and A_1 modes in the properly-cured joint (c).

The next step is the case of wave propagation across a central disbonded portion of the skin-to-spar joint (again, $[0/\pm45/0]_S$ skin lay-up in the "across the bond" configuration). The s_0 mode is still assumed to be initially excited outside of the bond region. Mode conversion into the S_0 and A_1 modes occurs at the joint boundary. In turn, these two modes will mode convert once they reach the disbond. Fig. 5.6(c) shows the S_0 and A_1 mode shapes for the properly-cured region together with the $S_{0,spar}$, $S_{0,plate}$ and $A_{1,spar}$ mode shapes for the disbonded region at 205 kHz. For $S_{0,spar}$ and $A_{1,spar}$ the largest displacements occur below the bondline in

the spar wall. Conversely, the largest displacements occur in the top plate for $S_{0,plate}$. Since the initial wave excitation is in the top plate, it is expected that the majority of the wave energy will remain confined to this component for short propagation distances. In the experimental setup adopted, the propagation distance to a centralized disbond was less than half of either S_0 or A_1 wavelengths at 205 kHz. Thus it can be assumed that $S_{0,plate}$ is the predominant carrier mode through the disbonded region.

5.5   Strength of Transmission as a Function of Bond State

The change in strength of transmission as a function of bond condition was predicted from the cross-sectional averaged power flow. This quantity was divided by the normalization factor $\left(\int_H \mathbf{P_V} \cdot \hat{\mathbf{x}} dz \right)$ to enable direct comparisons between the various bond conditions and carrier modes. Fig. 5.7 shows the real P_{Vx} component profiles for the $[0/\pm45/0]_S$ skin-to-spar joint probed in the "across the bond" configuration for the different bond conditions. Notice that the discontinuities in the results for the skin layer reflect the different stiffnesses of the individual plies in the wave propagation direction. The properly-cured bond and the poorly-cured bond are compared in the top four plots for the two carrier modes S_0 and A_1. Figs. 5.7(a) and 5.7(b) refer to S_0 propagating at 155 kHz and 205 kHz, respectively. It can be seen that the S_0 strength of transmission is larger in the poor bond as compared to the good bond. This phenomenon manifests itself mainly within the upper plate layer. The power flow profile justifies the commonly identified reduction in "energy leakage" that occurs when guided waves are transmitted across poor adhesive joints. It is also evident in Figs. 5.7(a) and 5.7(b) that the normalized power flow for a given bond condition is larger at 205 kHz than it is at 155 kHz, and the increase in transmission strength with degrading bond conditions is also larger at 205 kHz than it is at 155 kHz. The change in transmission strength between the two bond

conditions in much less pronounced for the A_1 carrier mode shown in Figs. 5.7(c) and 5.7(d). In fact, a slight decrease in transmission strength within the upper plate occurs at 205 kHz as the bond is degraded. It can be further deduced that the S_0 mode would be primarily responsible for the sensitivity to bond stiffness based on transmission measurements. This conclusion is consistent with the cross-sectional strain profiles of Fig. 5.6(b) where S_0 is seen to produce larger strains than A_1 at the bond layer.
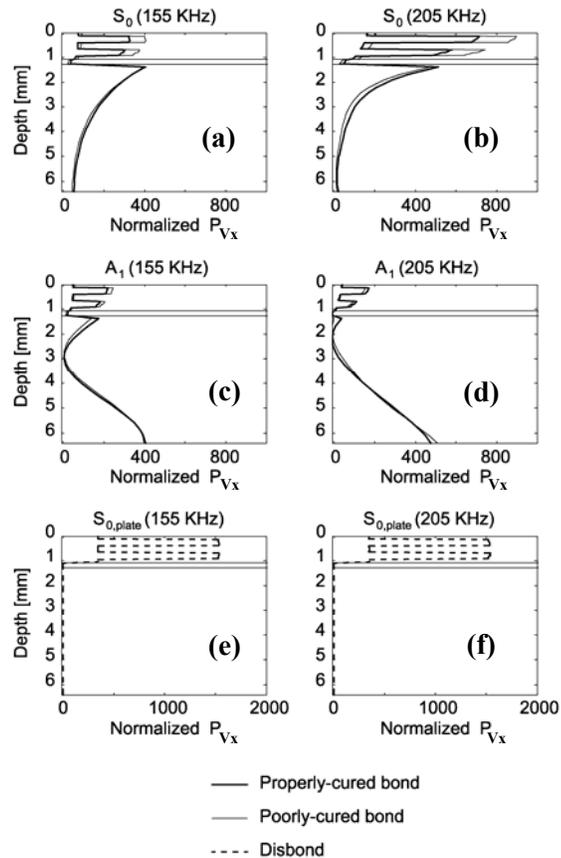
Fig. 5.7. P_{Vx} component of the Poynting vector in the properly-cured bond and in the poorly-cured bond for (a) S_0 at 155 kHz, (b) S_0 at 205 kHz, (c) A_1 at 155 kHz, and (d) A_1 at 205 kHz. Same quantity in the disbonded case for (e) $S_{0,plate}$ at 155 kHz, and (f) $S_{0,plate}$ at 205 kHz.

As for the disbonded case, shown in Figs. 5.7(e) and 5.7(f) for 155 kHz and 205 kHz, the power flow results confirm that $S_{0,plate}$ is completely confined to the top plate. As a result, the strength of transmission should be expected much larger than what seen in either of the

two carrier modes, S_0 or A_1, in the previous two bond conditions. Significant changes in the P_{Vx} component of the Poynting vector in the disbonded case were not observed over the frequency range of interest. In fact, the result at 155 kHz in Fig. 5.7(e) is indistinguishable from the one at 205 kHz in Fig. 5.7(f).

The cross-sectional power flow information was used to predict changes in transmission strength as a function of bond condition over the frequency range 100 kHz – 300 kHz, for both plate lay-ups ($[0/\pm45/0]_S$ and $[0/\pm45/90]_S$) and both testing configurations ("within" and "across" the bond).

Figs. 5.8(a) and 5.8(b) plot the strength of transmission in terms of normalized power flow over the thickness of the upper plate and bond layer. This quantity was calculated by:

$$\overline{P_V} = \frac{\int_h P_{Vx} dz}{\int_H \mathbf{P_V} \cdot \hat{\mathbf{x}} dz} \tag{5.3}$$

where h is the combined thickness of the upper plate and the bond layer. Fig. 5.8(a) compares A_1 and S_0 propagating across the properly-cured and the poorly-cured bonds, for the $[0/\pm45/0]_S$ lay-up. It can be seen that S_0 is the main energy carrier in most of the frequency range, with its transmission strength increasing with degrading adhesive properties. A_1 is seen to have a minor role in the energy transmission and it is also seen less sensitive to the change in bond condition. Also notice that the A_1 contribution is eliminated below the 135 kHz cut-on frequency. The same general behavior can be observed for the other plate lay-up, $[0/\pm45/90]_S$, shown in Fig. 5.8(b). The main difference is this case is the increased transmission strength of A_1 with degrading adhesive properties below 200 kHz.

The sensitivity to bond condition was compared directly by computing the relative differences in transmission strength between the degraded bonds and the properly-cured bond. First, the relative excitability of the individual carrier modes needed to be taken into account

considering the single incoming mode, s_0, for the "across the bond" configuration. An excitation factor for each potential carrier mode was evaluated based on the similarity between the displacement mode shapes of the incoming mode and those of the carrier mode. These displacements were normalized by the factor $\sqrt{\int_H \mathbf{P_V} \cdot \hat{\mathbf{x}} \mathrm{d}z}$ in order to capture their relative magnitude at the various frequencies and for the various modes. The maximum of the cross-correlation function was used as the similarity index. The following Excitation Factor was defined for an i-th carrier mode (CMi) under a single incoming mode (IM):

$$\text{Excitation Factor}_{\mathrm{CM}\,i}(f) = \frac{\sum\limits_{k=x,y,z} \text{Max}\left|u_{k,\mathrm{IM}}(f) \otimes u_{k,\mathrm{CM}i}(f)\right|}{\sum\limits_{i=1}^{N} \sum\limits_{k=x,y,z} \text{Max}\left|u_{k,\mathrm{IM}}(f) \otimes u_{k,\mathrm{CM}i}(f)\right|} \tag{5.4}$$

where $\otimes$ is the cross-correlation operation between the k-th cross-sectional displacement component of the incoming mode, $u_{k,\mathrm{IM}}$, and that of the i-th carrier mode, $u_{k,\mathrm{CM}i}$, computed at the various frequencies and in the upper plate only. In eq. (5.4) the Excitation Factor is normalized by the contribution of all possible N carrier modes existing at the incoming frequency. For the subject tests, the excitability remains dominated by the u_x displacement component overweighing the other components of the incoming s_0 mode. The values of the Excitation Factor for the properly-cured and the poorly-cured bonds varied from 0.28 to 0.83 for S_0 and from 0 to 0.63 for A_1 in the 100 kHz – 300 kHz range. The Excitation Factor for A_0 was significant only below 135 kHz with a maximum value of 0.26. In the disbonded case, the $S_{0,\mathrm{plate}}$ mode was confirmed to be predominantly excited with an Excitation Factor ranging from 0.80 to 0.99 in the same frequency range.

Across Bond
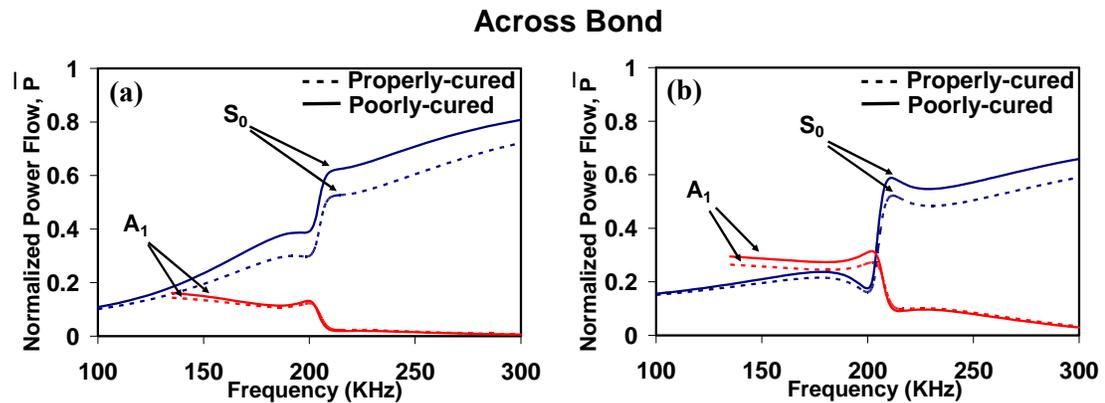
Fig. 5.8. Above spar power flow of S_0 and A_1 for the properly-cured and the poorly-cured skin-to-spar bonds in the "across the bond" testing of (a) the $[0/\pm45/0]_S$ skin and (b) the $[0/\pm45/90]_S$ skin.

Generally, the transmission strength will also be affected by attenuation losses. This effect was only factored explicitly into the contribution of the A_1 mode below 135 kHz where a zero Excitation Factor was assumed to reflect non-propagative conditions (Fig. 5.3). Above 135 kHz, since the attenuation values for A_1 and S_0 were close, the relative weights of eq. (5.4) were considered for the perfectly elastic case without loss of accuracy. The respective Excitation Factors computed in the "across the bond" configuration for S_0, A_0, A_1 and $S_{0,plate}$ were applied to the "within the bond" configuration.

Finally, the excitation-adjusted power flow differences, computed after weighing $\overline{P_V}$ of eq. (5.3) with the respective Excitation Factors, are shown in the plots of Figs. 5.8(c) through 5.8(f). These results were also normalized by the maximum power flow of the properly-cured bond to provide a relative transmission change. This is a consequence of the unique character of the $S_{0,plate}$ mode that carries the incoming s_0 mode energy very efficiently. It should be reminded that the current simulation considers the limit case of a disbond extending for the entire joint width. Clearly, the effect will be much reduced for a localized disbond within a joint as is the case for the experimental tests that follow. Thirdly, comparing

the poorly-cured to the properly-cured bond, an abrupt increase in sensitivity is seen to occur around 200 kHz in all cases. The increase in sensitivity is due to the mode coupling phenomenon discussed earlier, affecting both S_0 and A_1 near this frequency value. The increased energy transfer through the thickness of the waveguide at the mode coupling frequencies is the physical basis for the abrupt increase in sensitivity.
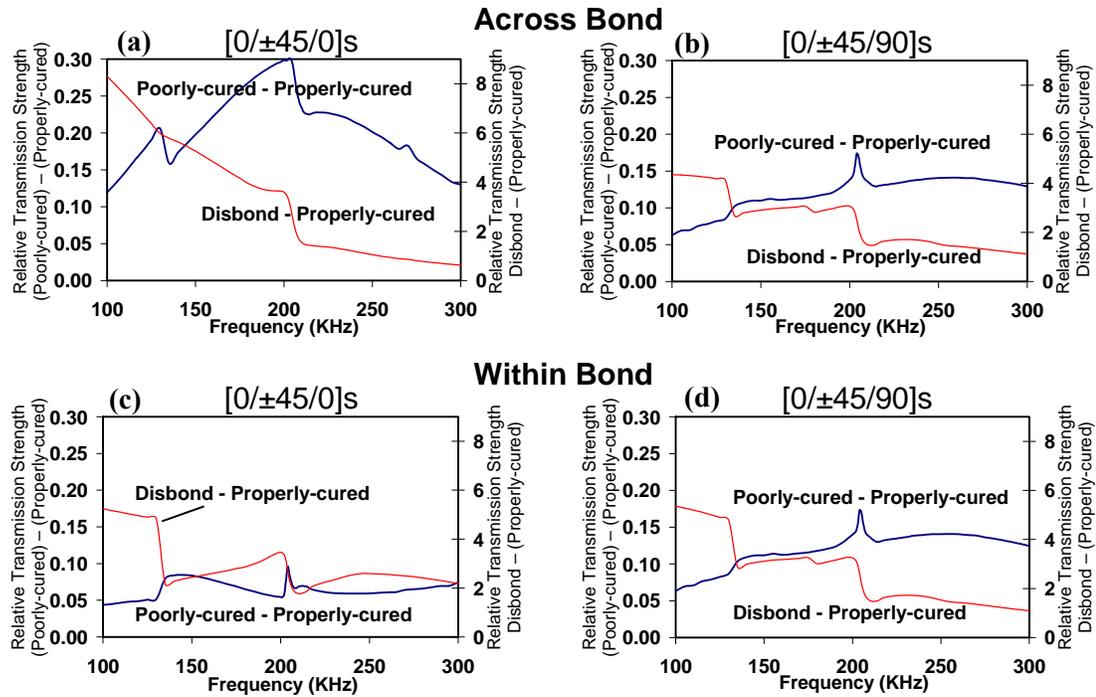
Fig. 5.9. Power flow differences in the "across the bond" testing of (c) the $[0/\pm45/0]_S$ skin, (d) the $[0/\pm45/90]_S$ skin, and for the "within the bond" testing of (e) the $[0/\pm45/0]_S$ skin and (f) the $[0/\pm45/90]_S$ skin.

5.6   Conclusions

SAFE analyses were performed upon models representing two bonded wing skin-to-spar joints. These results provided substantial insight into the guided wave behavior within pristine and damaged joints.

Assessment of the attenuation curves and guided wave mode shapes led to the conclusion that S_0 and A_1 would be the primary carriers of energy within the properly-cured and poorly-cured joint conditions while the $S_{0,plate}$ mode would be the dominant carrier across a disbonded joint. Both the S_0 and A_1 modes induce considerable strain within the bondline, making them sensitive to changes in the adhesive stiffness. In addition, distinguishable mode coupling between these two modes was observed in the dispersion curves near a frequency of 200 kHz. The through thickness power flow confirmed that this mode coupling region produces a large transfer of energy across the waveguide thickness. Therefore, it was anticipated that the mode coupling frequency range would provide maximum sensitivity to the bond monitoring strategy adopted in this thesis.

SAFE analyses were also used to predict the change in strength of transmission as a function of bond state. This damage feature was quantified based on the changes in the power flow (Poynting vector of carrier modes) along the wave propagation direction relative to the properly-cured bond. For all the cases considered the power flow results predicted that the strength of transmission would be larger for the defected joints compared to the properly-cured joint. Relative to the properly-cured bond, a maximum increase in the strength of transmission near 200 kHz was predicted for the poorly-cured bond, consistent with the observed mode coupling point. Experimental tests were conducted to validate the predicted changes in strength of transmission as a function of joint condition. These results are included in the following chapter.

Acknowledgement

"Ultrasonic guided wave monitoring of composite wing skin-to-spar bonded joints in aerospace structures". The dissertation author was the primary investigator and author of this paper.

Chapter 6

Active Interrogation of CFRP Plate-to-Spar Joints at Ambient Temperature

6.1. Test Specimens

This chapter discusses experimental tests which were conducted upon two of the representative wing skin-to-spar joints found within CFRP composite wing sections. The specimens matched closely the models analyzed numerically in chapter 5. Two composite plates were fabricated using T700/ p7263w-15 carbon epoxy prepreg with the two lay-ups of $[0/\pm45/0]_S$ and $[0/\pm45/90]_S$. Each plate had a total thickness of 1.067 mm. The plate dimensions were cut to 330 mm x 330 mm. The composite piece used to replicate the wing spar was a woven T800/924 carbon epoxy square tube with measured outer dimensions of 50.8 mm x 50.8 mm and a wall thickness of 5.23 mm. The composite tube was cut into two, 330 mm long sections to match the length of each plate. A two-part Hysol 9394 epoxy adhesive was used to bond the spar to the individual plates. Each of the two specimens was manufactured identically with the exception of the different plate lay-ups. Bonding of the plates was done such that the 0-deg fiber direction ran along the lengthwise direction of the spar. One of the fabricated joints is shown in Fig. 6.1.

The same type of bond conditions considered in the model were artificially created prior to assembling the joints (Fig. 6.1). The majority of the bond was comprised of a properly-mixed epoxy, representing the well-bonded region. In order to form a region of degraded bond stiffness, an improperly mixed sample of epoxy was prepared resulting in an approximate 50% stiffness degradation compared to the properly-cured case (the exact values from ultrasonic through-transmission testing of the mix were 42% degradation for the

Young's modulus and 44% degradation for the shear modulus as reflected by the velocity values in Table 5.2). Finally, two disbonded regions of different sizes were created by inserting Teflon release film with a thickness of .025 mm at the centerline of the bond. The release film was expected to severely degrade the shear stiffness of the bond while degrading its longitudinal stiffness to a smaller extent. The two simulated disbonds had dimensions of 12.7 mm x 12.7 mm and 25.4 mm x 25.4 mm, respectively. To maintain bondline thickness, fine glass beads were added to the epoxy mixture prior to application. The total bond thickness was measured to be 0.203 mm in both specimens. Before testing occured, ultrasonic A scans conducted along the joint confirmed the existence of simulated damage at the intended locations.
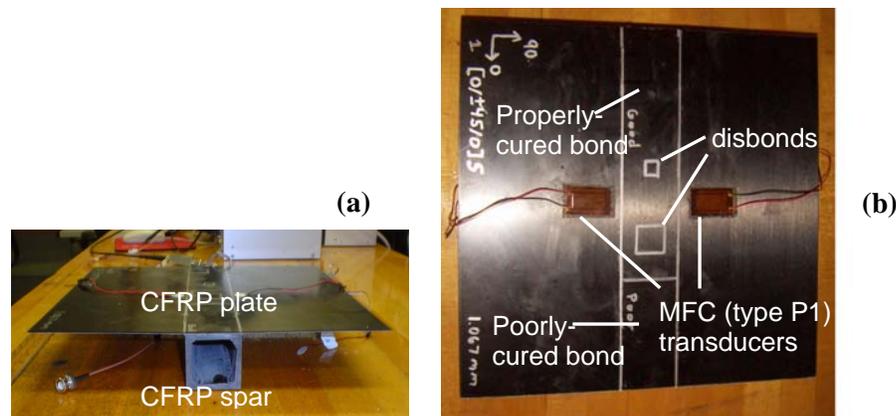
Fig. 6.1. (a) and (b) test specimens with attached MFC transducers and simulated damage.

6.2   Experimental Procedure and Feature Extraction

Testing was performed at ambient temperature on the two skin-to-spar joints described in section 6.1. Tests were conducted in both the "across the bond" and "within the bond" test configurations, however only the results for the "across the bond" configuration are

considered here. Tests for the other configuration produced similar results to that which will be discussed and are documented in Matt et al. [36].

The actuation/sensing efficiency of MFC (type P1) and MFC (type P2) is comparable. However, due to the increased flexibility and robustness for type P1, these MFC transducers were employed for active experimental tests.   A pair of MFC (type P1) transducers (dimensions of 40 mm × 25 mm × 0.3 mm) was used as wave actuator and sensor with a spacing of 115 mm as shown in Figure 6.1(b). The MFCs were bonded to the structure using a thermally-activated film adhesive. To assist in the normalization of the testing procedure, the same transducer pair was used throughout the tests. Tests run on the single skin plate confirmed that s_0 was the mode generated and detected by the MFCs with the greatest efficiency. This mode is ideal for the active guided wave diagnostics since its non-dispersive behavior within the frequency range of interest simplifies signal processing and feature extraction.

The signal generation and data acquisition system was a National Instruments PXI[©] platform running under LabVIEW that was assembled and programmed in-house. The system used an arbitrary function generator to allow for swept frequency tests using Hanning windowed tonebursts (20 V peak-to-peak) sent to the actuating MFC. The frequency sweeps were performed between 100 kHz and 300 kHz, at 1 kHz increments.

At each generation frequency, the signals detected by the MFC sensor were gated in time to isolate the predominant s_0 mode. The gated time signal was then processed through the Discrete Wavelet Transform (DWT) to extract the relevant wavelet coefficients. Greater detail on the DWT processing will be given in the following section. Based upon the results from the SAFE analyses, the ultrasonic transmission strength through the joints was selected as the damage sensitive feature. Quantification of the transmission strength was achieved by

taking the Root Mean Square (RMS) of both the time-domain signals and the corresponding

wavelet coefficients. The RMS is related to the energy of the signal and it was computed by

the well known relation:

$$\text{RMS} = \sqrt{\frac{\sum_{i=1}^{Z} x_i^2}{Z}} \qquad (6.1)$$

where x_i is a single data point within a collection of Z data points. The RMS spectra measured

for the different bond conditions and plate lay-ups were then compared.

6.2.1   Discrete Wavelet Analysis

Extracting damage-sensitive features from the Joint Time-Frequency (JTF) domain, in

addition to the conventional time domain, is becoming increasingly attractive in structural

monitoring applications. Among the various JTF analyses, the DWT has been used with the

most success in those monitoring applications based on guided waves and requiring real-time

data which is robust against noise [41,167,168]. Briefly, the wavelet decomposition of a

function $f(t)$ is calculated from the following inner product:

$$W_{j,n} = \int_{-\infty}^{+\infty} f(t)\, \psi_{j,n}(t)^* \, dt \qquad (6.2)$$

where $\psi_{j,n}(t)^*$ is the conjugate of the mother wavelet function, $\psi_{j,n}(t)$, and $W_{j,n}$ are the

wavelet coefficients. The parameter n^P (translation parameter) shifts the wavelet in time and

the parameter $s^P = 2^j$ (scale parameter) controls the wavelet frequency bandwidth, hence the

resulting joint time-frequency analysis.

Compared to its "continuous" version that cannot be performed in real-time, the DWT

is computationally efficient because of the existence of a fast orthogonal wavelet transform

algorithm based on a set of filter banks [169]. In Mallat's filter bank tree, the DWT

decomposition is done by pairs of low pass and high pass filters. Each level of decomposition, j, corresponds to a frequency band between $f_j + \Delta f_j / 2$ and $f_j - \Delta f_j / 4$ where Δf_j corresponds to the bandwidth. The central frequency, f_j, is a function of the mother wavelet central frequency, F_C, and the signal sampling rate, Δ, through:

$$f_j = \frac{\Delta \times F_C}{2^j} \tag{6.3}$$

The bandwidth, Δf_j, can be normally estimated as half of the distance between adjacent central frequencies f_{j+1} and f_{j-1}. Considering eq. (6.3), the bandwidth can thus be written as:

$$\Delta f_j = \left| \frac{f_{j+1} - f_{j-1}}{2} \right| = \frac{3}{4} f_j \tag{6.4}$$

The original signal can then be reconstructed from the wavelet coefficients as follows:

$$f(t) = \sum_j \sum_{n^P} W_{j,n^P} \psi_{j,n^P} \tag{6.5}$$

The selection of a proper mother wavelet is critical for a successful application of the DWT algorithm. It can be assumed that the most effective signal decomposition is achieved by a mother wavelet with greatest similarity to the original time signal [170]. An optimization routine was adopted to identify the mother wavelet providing high correlation with the signals detected in the joint specimens. The Daubechies wavelets of orders 2, 4, 10 and 40 (db 2, db 4, db 10 and db 40) were considered in this study because their shape resembles the narrowband character of the toneburst ultrasonic signals employed. The given mother wavelet was stretched in time such that its peak frequency matched that of the time-domain signals. Zero padding was added such that the frequency resolution was equal between the stretched wavelet, $\overline{\psi_{j,n^P}}(t)$, and the time-domain signal, $f(t)$. Finally, the cross-correlation was computed to quantify the similarity between these two functions at each frequency value:

$$X_{corr} = \left| \overline{\psi_{j,n^P}}(t) \otimes f(t) \right| \tag{6.6}$$

The maximum cross-correlation coefficient is plotted in Fig. 6.2 considering signals acquired across the properly-cured bond in the [0/±45/90]s joint. It can be seen that the db 10 wavelet provides the best correlation with the signals throughout the 100 kHz – 300 kHz frequency range. The low-order db 2 provides a comparable correlation only at around 200 kHz, whereas the high-order db 40 is comparable only at around 250 kHz. Hence the db 10 was chosen for the DWT decomposition of the ultrasonic signals measured in the joint specimens.
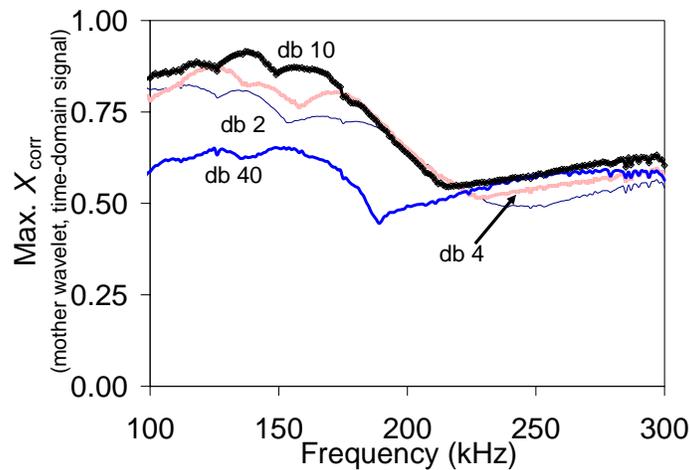
Fig. 6.2. Maximum cross-correlation coefficients between various mother wavelets and the s_0 time signal.

6.2.2   Wavelet Denoising and Compression

The DWT possesses superior de-noising and compression capabilities owing to the ability of selecting a few wavelet coefficients at given decomposition levels (pruning). Pruning, along with the ability to threshold the magnitude of the wavelet coefficients (thresholding), allows the compression of the essential signal information down to a very few number of data points.

An example is illustrated in Fig. 6.3, referring, again, to signals measured across the properly-cured bond of the [0/±45/90]s joint using the MFC actuator-sensor pair. Fig. 6.3(a) shows the raw signal detected by the MFC sensor at 200 kHz, which is completely embedded into noise. The same trace, after 50 averages, is shown in Fig. 6.3(b), where incoherent noise is reduced and the signals become clear. The early-arrival portion of the signal corresponds to actuator-sensor cross-talk, while the late-arrival, more meaningful portion is associated with the s_0 mode. Fig. 6.3(c) shows the DWT decomposition of the raw signal in Fig. 6.3(a) at level 6, which was centered at 214 kHz. The result of the thresholding step is shown in Fig. 6.3(d), where only the wavelet coefficients with amplitude above 70% of the maximum coefficient amplitude are retained and the remaining coefficients, related to noise, are discarded. By reconstructing the original signal from the thresholded, level 6 DWT coefficients of Fig. 6.3(d), the result of Fig. 6.3(e) is obtained. The excellent de-noising performance of this processing is clearly seen in this plot. In fact, the DWT result yields an even larger signal-to-noise ratio (SNR) than the 50-average result of Fig. 6.3(b), without compromising the speed of the analysis. The DWT compression abilities can be seen in Fig. 6.3(d) where as few as 5 coefficients are representative of the original, 3,000 point time-domain signal. In fact, the entire information on the s_0 mode resides exclusively in the latter two wavelet coefficients at around position 15. This level of data compression would be highly beneficial in an on-board monitoring system given the stringent requirements for data transmission (e.g. wireless) and storage.
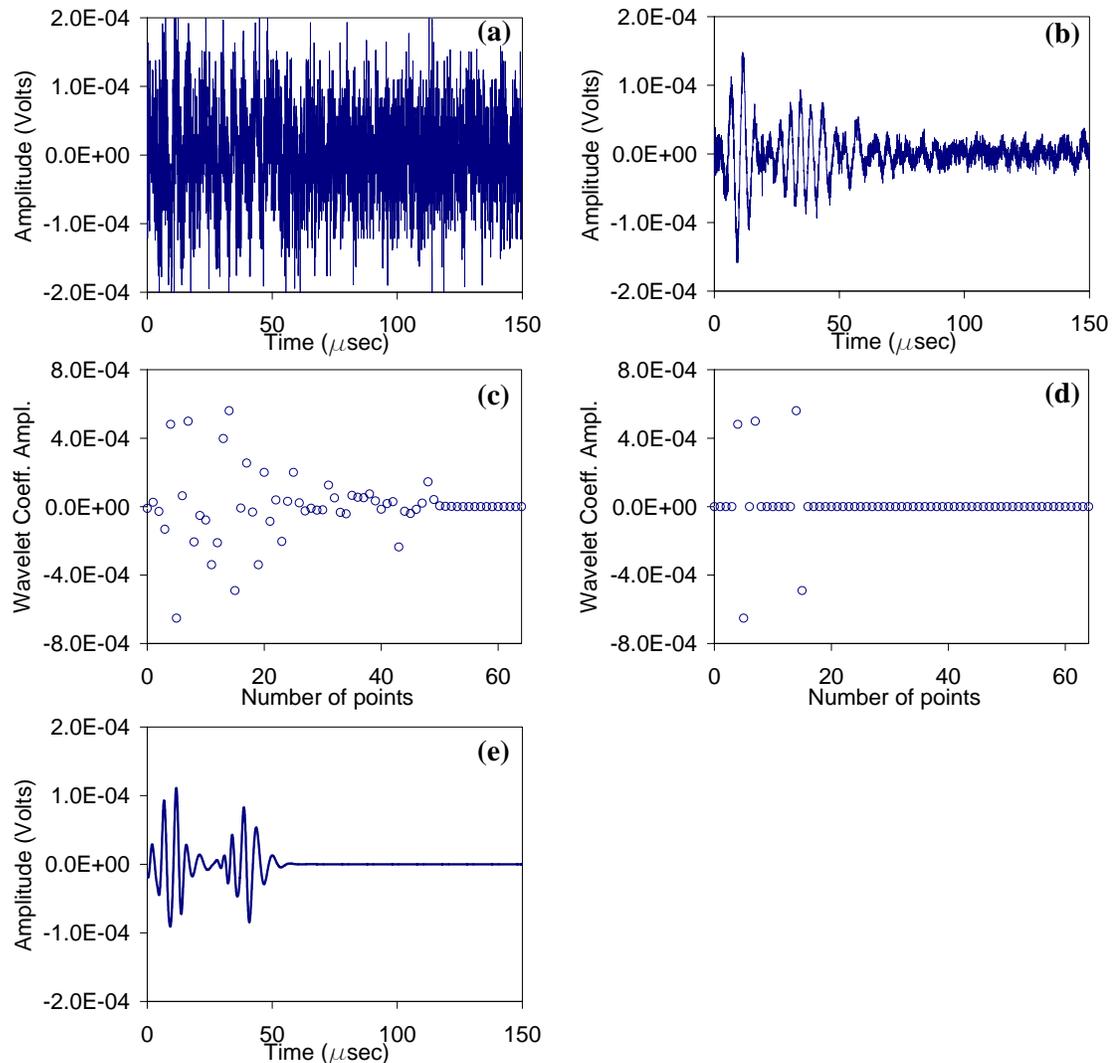
Fig. 6.3. DWT processing: (a) MFC raw signal at 200 kHz; (b) MFC signal after 50 averages; (c) wavelet coefficients of raw signal at decomposition level 6; (d) 70% thresholded wavelet coefficients of raw signal at decomposition level 6; (e) reconstructed signal from wavelet coefficients in (d).

The effectiveness of the DWT can be further observed in the curves of Fig. 6.4, representing the RMS values of the [0/±45/90]s joint signals acquired over the 100 kHz – 300 kHz range by using different numbers of averages, from 0 (raw signal) to 50. The use of a low number of averages results in an overestimation of the RMS values, although the error decays quickly once at least 5 averages are performed. Superimposed is the RMS of the

reconstructed signals after DWT processing. It can be seen that the general trend of the DWT result matches very well that of the 50-average result, which should be considered as closest to the "true" solution. The difference is that the DWT processing can be done in pseudo-real time. The larger scatter in the DWT result is due to the unavoidable variability of noise content between adjacent signals. In order to cover the entire frequency range of interest, the 6th, 7th, and 8th DWT decomposition levels were all accounted for in the reconstructions. These levels corresponded to central frequencies of 214 kHz, 107 kHz and 53.5 kHz, respectively.
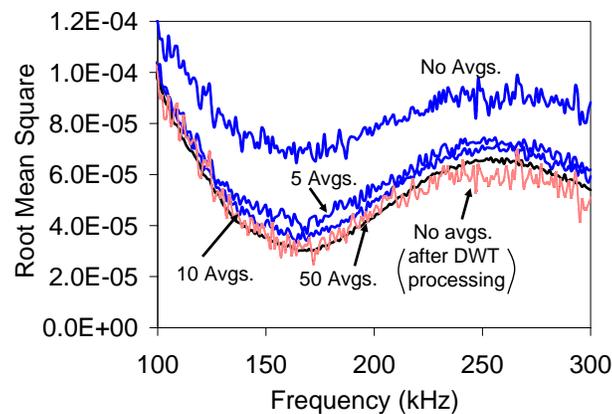
Fig. 6.4. Root mean square of s_0 time signals after performing various numbers of averages and after performing DWT analysis of the raw signals.

6.3   Bond Defect Detection

The RMS spectra for the four bond states examined (properly-cured bond, poorly-cured bond, 12.7 mm × 12.7 mm disbond and 25.4 mm × 25.4 mm disbond) are summarized in Fig. 6.5. The results are presented in terms of RMS differences from the properly-cured bond and normalized by the same quantity. Figs. 6.5(a) and 6.5(b) were obtained in the $[0/\pm45/90]_S$ lay-up from the time-domain signals and the corresponding DWT coefficients, respectively. Figs. 6.5(c) and 6.5(d) were obtained in the $[0/\pm45/0]_S$ lay-up. The time-domain signals were averaged 50 times. The DWT coefficients included levels 6, 7, and 8.
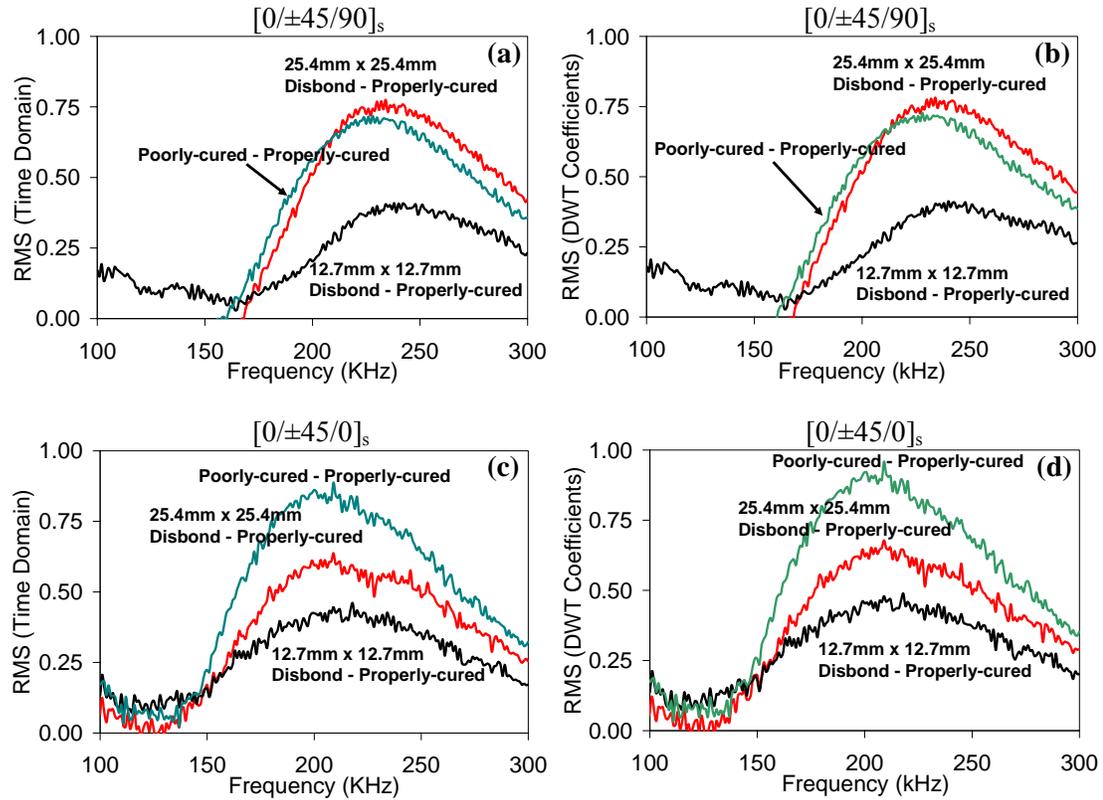
Fig. 6.5. Normalized root mean square differences of the defected bonds relative to the properly-cured bond: (a) time-domain signals for the $[0/\pm45/90]_S$ joint; (b) DWT-processed signals for the $[0/\pm45/90]_S$ joint; (c) same as (a) for the $[0/\pm45/0]_S$ joint; (d) same as (b) for the $[0/\pm45/0]_S$ joint.

The first observation from Fig. 6.5 is that the RMS spectra obtained from the time-domain signals are extremely close to those obtained from the DWT coefficients. This, again, reaffirms the robustness of the DWT processing for extracting bond-sensitive features.

It can also be seen that all of the RMS differences are generally positive, and thus the energy transmission is strengthened in the presence of any of the bond defects considered. This general observation is consistent with the predictions made from the power flow computed using the SAFE model. The peak RMS relative change occurs between 180 kHz and 220 kHz for the $[0/\pm45/0]_S$ lay-up. This frequency range is consistent with the mode coupling conditions predicted by the model, and it is thus confirmed as the most sensitive

range to detect the bond defects considered in this study. The most sensitive range is slightly shifted towards higher frequencies for the $[0/\pm45/90]_S$ lay-up, but it still partially overlaps with the predicted mode coupling conditions.

Other identifiable trends can be observed when comparing the results amongst each defect case. First, the strength of transmission of the poorly-cured bond is larger than that of the two disbonds across the entire frequency spectrum for the $[0/\pm45/0]_S$ lay-up. For the $[0/\pm45/90]_S$ lay-up, the difference between the poorly-cured bond and the large disbond is minimal. The SAFE power flow results predict that the strength of transmission should be larger for the disbond case compared to the poorly-cured bond, regardless of the skin lay-up. However, issues regarding the finite dimensions of the disbonds were not included in the model (that assumed a disbond extended for the entire width of the joint). Also, the degradation in disbond properties assumed in the model may have been too severe compared to the actual teflon inserts used in the specimens. Consequently, it can be reasonably expected that the model for the disbonded interfaces will somewhat overestimate the strength of transmission measured in the specimens.

In addition, each of the spectra in Fig. 6.5 shows that the strength of transmission associated with the large disbond is greater than that associated to the small disbond. This trend is due to the favorable P_{Vx} component of the Poynting vector of the $S_{0,plate}$ mode (Fig. 6.5) that isolates the majority of the wave energy within the same skin plate where the MFC actuator and sensor are located. Of the two specimens considered, the maximum discrimination among the different bond defects is measured in the $[0/\pm45/0]_S$ specimen, as seen in Figs. 6.5(c) and 6.5(d).

6.4   Conclusions

This chapter extended active ultrasonic guided wave methods to the detection of bond defects in composite-to-composite joints.   The specific bond defects considered include disbonds and regions where the stiffness of the adhesive is significantly reduced.   Consistent with SAFE analyses, the experimental results confirmed that the strength of transmission increases in the presence of the two types of bond defects compared to the properly-cured bond. A large sensitivity was measured corresponding to mode coupling conditions for the S_0 and A_1 carrier modes. Discrimination among the different bond defects was found maximum for the $[0/\pm45/0]_S$ lay-up. The result is encouraging, considering that the anisotropic lay-up is more representative of actual UAV wings.   In both lay-ups, the measured strength of transmission generally increased with increasing disbond size.

It was demonstrated that the damage sensitive feature based upon energy transmission can be extracted from a very small number of DWT coefficients of the raw ultrasonic signals, without compromising processing speed.   The DWT processing is likely to become even more useful in future wave-based health monitoring systems requiring small excitation powers to the actuators and large actuator-sensor distances for increased coverage.

Although the strength of transmission was shown to be sensitive to changes in the joint condition, this feature is also likely to be influenced by environmental factors such as temperature.   Variations in temperature during operation will also cause changes in the ultrasonic strength of transmission as a result of temperature-induced changes in the transducer-wing skin adherent, in the wing skin-to-spar epoxy adhesive, the electro-mechanical operation of the transducer and in the wing skin wave attenuation losses. Joint damage detection in a varying temperature environment is the subject of chapter 7.

Acknowledgement

Chapter 7

Damage Detection in a Varying Temperature Environment

7.1   Problem Statement

On-board application of an SHM system will require the ability to detect damage despite large variation in environmental and structural conditions. As opposed to global vibration based methods, boundary condition changes and ambient excitation of the structure are less detrimental to ultrasonic guided wave based diagnostics. However, temperature variation will lead to significant changes in the ultrasonic features used for damage detection. Therefore, field application of a guided wave based SHM system will require a robust statistical pattern process which is capable of discriminating between changes due to temperature and that due to damage.

This chapter initially addresses the effect of temperature on the guided wave signals acquired by MFC transducers. This is followed by experimental temperature tests conducted on the [0/±45/0]s representative wing skin-to-spar joint (Fig. 6.1). Statistically robust damage d0etection within the joint was successfully achieved under widely varying temperature conditions and transducer-structure coupling through the performance of multivariate outlier analysis.

7.2   Temperature Effects on Guided Wave Measurements

7.2.1   Qualitative Definition of Temperature Effects

Many mechanisms induce changes in guided wave signals as a result temperature variation. This section focuses upon the qualitative temperature effects on actuated and received ultrasonic signals through the use of PZT and MFC piezoelectric transducers. In the

following discussion, it is considered that the transducers are coupled to an isotropic substrate using a thin isotropic adhesive layer. It is also presumed that actuating frequencies are within the range where only the two fundamental symmetric and antisymmetric modes (s_0, a_0) propagate.

The most significant temperature induced effects on guided wave signals include changes in the elastic properties and thermal expansion of each layer in the transducer-structure system, as well as deviation in the electrical properties of the transducers. Let us first consider the effect of changes in elastic properties. For an isotropic substrate, the Young's modulus and shear modulus vary in a near linear fashion as a function of temperature [110]. As a consequence, the bulk wave velocities of the material will also change, resulting in a reduction in phase velocities and energy velocities for the two fundamental guided wave modes due to an increase in temperature. The change in wave velocity will naturally alter the arrival times of various wavepackets observed in the signal. In addition, the wavenumbers, which are proportional to the wavelength, are a function of the phase velocity and frequency. Therefore, according to the "wavelength tuning" effect described in chapter 3, the optimal response frequency of both transducers will shift toward lower frequencies due to an increase in temperature. The stiffness coefficients for the isotropic bonding agent used to couple the transducers and structure will also be influenced by temperature. For an increase in temperature, the effective area of the transducer will be reduced as a result of increasing shear lag. The shear lag effect coinciding with the transducer-structure coupling is discussed in Sirohi and Chopra [113]. Again, due to "wavelength tuning", a decrease in the transducer dimension shifts the peak response toward higher frequencies. The reduction in stiffness of the bonding agent will also reduce the shear coupling between in-plane strains within the transducer and that of the surface strain on the substrate. As a consequence, the actuation and

sensing efficiency will drop, causing a decrease in the signal amplitude. This effect can be minimized by selecting an adhesive which demonstrates stable behavior within the desired temperature range. Finally, changes in the elastic properties of the sensing transducer will scale its voltage response amplitude. This behavior can be observed from the PZT sensor response given in eq. (3.7) and MFC sensor responses shown in eqs. (3.16) and (3.17). From these equations, it can be observed that a decrease in the Young's modulus of the sensor as a result of increasing temperatures will yield a smaller voltage response. As supported in Konstantinidis *et al.* [110], the above effects are expected to influence the signal content corresponding to the first arrival of the a_0 mode more significantly than the s_0 mode due to the larger dispersion for a_0. This is further justification for the active damage identification approach adopted in thesis which is based upon feature extraction for the s_0 mode.

Temperature increase will induce thermal expansion along all directions of the substrate. A small expansion will occur along its thickness axis. Therefore, the dispersion curves will shift towards smaller values of the frequency×thickness product. As a consequence, the peak frequency response of both actuator and receiver is expected to shift toward higher frequencies. As demonstrated in Konstantinidis *et al.* [110], this effect is minor due to the finite thickness of the plate. The in-plane expansion of the substrate will increase the distance between actuation source and receiver, thereby causing deviation in the arrival time of incoming and reflected modes. Considering an increase in temperature, minor thermal expansion will also occur within the adhesive layer and transducers resulting in a slight shift in the peak frequency response of the transducers toward lower frequencies.

As reported in Hooker [171] and Lee and Saravanos [172], the dielectric permittivities, e_{ij}^{σ} and the piezoelectric charge constants, d_{ij} of piezoelectric ceramics increase with increasing temperature. From eqs. (3.7), (3.16) and (3.17), it can be found numerically

that an increasing dielectric permittivity reduces the sensor's voltage response; conversely, an increase in the piezoelectric charge constant increases the sensor's response.

Relative to other effects, changes in the piezoelectric properties of the PZT material will have the most dramatic influence on the transducer's response magnitude. This is a consequence of the relatively large change in these properties compared with the changes in the elastic constants of the transducer-structure system. For PZT-5A material which is used in MFC transducers, the rate of increase for the dielectric permittivity is much greater than that of the piezoelectric constant at temperatures in excess of 30 deg. C [172]. For this reason, the decrease in amplitude due to the first effect is expected to dominate the amplitude behavior in the guided wave signals above 30 deg. C.

7.2.2 Quantitative Effect of Temperature on Guided Wave Amplitude

Each of the effects discussed above will result in noticeable changes in guided wave signals due to variations in temperature. Mechanical, electrical and thermal properties of each layer in the transducer-structure system will ultimately dictate whether the combined effects result in increasing or decreasing signatures of the received waveforms.

For the proposed active damage detection method discussed in chapters 5 and 6, the effect of temperature on the wave amplitude is of utmost concern. The wave amplitude will be altered according to the mechanisms described above. In addition to these effects, it is also important to consider the hysteretic behavior of wave amplitude due to multiple temperature cycles. To study the behavior of guided wave amplitude in a varying temperature environment, experimental and theoretical analyses were performed on an aluminum plate and bonded MFC (type P1) transducers. Using this same specimen, experimental tests were also conducted to observe the hysteretic stability of the guided wave amplitude.

7.2.2.1 Theoretical Analysis

Initially, an analytical model was developed to predict the voltage response behavior, in the frequency domain, of MFC (type P1) transducers as a function of toneburst excitation frequency. These response curves were utilized to predict the change in response magnitude at a given toneburst frequency as a function of temperature.

From section 3.2.2, the voltage response of an MFC (type P1) sensor under plane stress conditions was described as:

$$V = \frac{\int_0^b \int_0^l \left[\left(d_{11}Y_1^E + d_{12}v_{12}Y_2^E \right)\varepsilon_{11} + \left(d_{11}v_{12}Y_2^E + d_{12}Y_2^E \right)\varepsilon_{22} \right] dxdy}{(2w)bp\left[\left(1 - v_{21}v_{12}\right)e_{11}^\sigma - \left(d_{11}^2 Y_1^E + 2d_{11}d_{12}v_{12}Y_2^E + d_{12}^2 Y_2^E \right) \right]} \tag{7.1}$$

Considering incident waves along the lengthwise axis of the transducer ($\theta = 0$) and assuming plane waves ($\varepsilon_{22} = 0$), the voltage response reduces to:

$$V = \frac{S_{MFC\,P1}}{(2w)p} \int_0^l \varepsilon_{11} dx \tag{7.2}$$

where the frequency independent constant $S_{MFC\,P1}$ for the MFC (type P1) becomes:

$$S_{MFC\,P1} = \frac{\left(d_{11}Y_1^E + d_{12}v_{12}Y_2^E \right)}{\left[\left(1 - v_{21}v_{12}\right)e_{11}^\sigma - \left(d_{11}^2 Y_1^E + 2d_{11}d_{12}v_{12}Y_2^E + d_{12}^2 Y_2^E \right) \right]} \tag{7.3}$$

The MFC (type P1) sensor response of an MFC (type P1) actuated toneburst is derived by coupling the transducer strain sensitivity described by eq. (7.2) with the harmonically-actuated surface strain field given in Giurgiutiu [114]. Only pure s_0 mode excitation is considered in the theoretical analysis and the generation and reception of the guided waves is taken to be along the lengthwise axis of the transducers as shown in Fig. 7.1. The host structure is taken to be an isotropic plate of thickness $2d$ and having a Young's modulus, Y^E and Poisson's ratio, v.
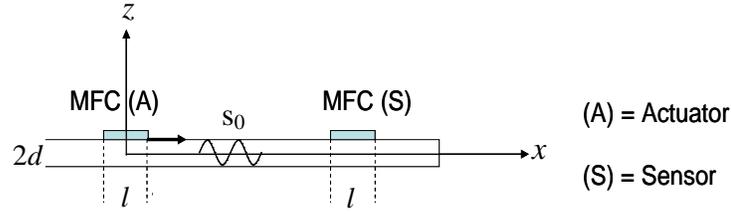
Fig. 7.1 MFC toneburst excitation and reception of s_0 guided waves in isotropic plate.

The total response, $\overline{U} = \overline{V} \times \overline{P}$, due a modulated toneburst excitation follows the procedure adopted in section 3.4.4 where $\overline{V}$ and $\overline{P}$ represent the harmonic response of the sensor due to the applied actuator pin force $l\tau_0$ of unit magnitude and the Fourier transform of the excitation, respectively. The frequency domain response magnitude of the MFC (type P1) sensor subject to an MFC (type P1) actuated toneburst excitation therefore becomes [148]:

$$\overline{U} = \frac{\overline{P}\, S_{MFC\ P1}\, A_{symm}}{(2w)\, pk} \left[\sin\left(\frac{kl}{2}\right) \right]^2$$

(7.4)

where $\overline{P}$ is the Fourier transform of a modulated toneburst signal of unit amplitude denoted as [118]:

$$\overline{P} = \frac{n}{4f_0} \left| \mathrm{sinc}\left(\frac{\pi n}{f_0}(f_0 - f)\right) + (-1)^{n+1} \mathrm{sinc}\left(\frac{\pi n}{f_0}(f_0 + f)\right) + \right.$$
$$+ \frac{1}{2}\left\{ \mathrm{sinc}\left(\frac{\pi n}{f_0}\left(f - \frac{n-1}{n}f_0\right)\right) + (-1)^{n+1} \mathrm{sinc}\left(\frac{\pi n}{f_0}\left(f + \frac{n-1}{n}f_0\right)\right) \right\} +$$
$$\left. + \frac{1}{2}\left\{ \mathrm{sinc}\left(\frac{\pi n}{f_0}\left(f - \frac{n+1}{n}f_0\right)\right) + (-1)^{n+1} \mathrm{sinc}\left(\frac{\pi n}{f_0}\left(f + \frac{n+1}{n}f_0\right)\right) \right\} \right|$$

(7.5)

The variables n and f_0 represent the number of half cycles and the central frequency of the toneburst signal, respectively. The temporal duration of the toneburst is therefore defined as $T = n/(2f_0)$. The actuated s_0 Lamb wave amplitude, A_{symm} is expressed as [114]:

$$A_{symm} = \frac{l\tau_0(1+\nu)}{Y^E}\left[\frac{kq(k^2+s^2)\cos rd \cos sd}{(k^2-s^2)\cos rd \sin sd + 4k^2 \cos sd \sin rd}\right] \tag{7.6}$$

In the following analysis, the response magnitude given in eq. (7.4) was evaluated at a given frequency f, by inputting the appropriate values for the transducer properties, the toneburst excitation, and the wavenumbers corresponding to an s_0 mode propagating within the isotropic plate. The wavenumbers k of the s_0 mode can be obtained numerically through the solutions of the Rayleigh-Lamb eq. (2.17) or by performing simple SAFE analyses. The geometric, elastic and piezoelectric properties of the MFC (type P1) transducer at ambient temperature (20 deg. C) were obtained from Smart Material© Corporation. The piezoelectric material for this particular transducer is PZT-5A and the values adopted in the analyses are summarized in table 1.

Table 7.1. Geometric, piezoelectric and elastic constants of MFC (type P1) transducer

Y_1^E (GPa)	Y_2^E (GPa)	d_{11} (pC/N)	d_{12} (pC/N)	ν_{12}	ν_{21}	e_{11}^σ (nF/m)
30.3	15.9	440	-185	0.31	0.16	16.37
l (m)	b (m)	a (mm)	g (mm)	w (mm)	p	
0.028	0.014	0.5	0.16	0.05	56	

Consistent with the experimental tests, it was presumed in the model that the MFC (type P1) transducers with active dimensions of 28mm × 14mm are bonded to a 1.524 mm-thick 1024-aluminum plate. Wave attenuation effects were not considered in the theoretical response due to the low level of damping associated with aluminum and close distance maintained between source and receiver during experimental testing. In the analyses, the temperature dependency of the following variables was accounted for:

- Elastic Modulus of aluminum plate (Y^E)
- Piezoelectric properties of MFC transducer ($e_{11}^\sigma, d_{11}, d_{12}$)
- Elastic Moduli of MFC transducer (Y_1^E, Y_2^E)

The MFC (type P1) was approximated as a single fiber reinforced lamina where the fibers are PZT-5A material, and the reinforcing matrix is epoxy. The temperature dependence of the Young's modulus of the epoxy was determined empirically using bulk epoxy samples and temperature chamber tests. The temperature dependence for the same quantity of the piezoelectric fibers was found in Sherrit et al. [173]. Therefore, for a given temperature, the elastic moduli for the MFC was found according to the mixture rule, where the volume fractions were initially evaluated using the known room temperature values of the MFC moduli. The piezoelectric properties as a function of temperature were adopted from experimentally determined values in [172]. The effect of thermal expansion, shear lag, and stiffness changes in the bonding agent were not considered in the model. However, these phenomenons are expected to have minimal influence on the guided wave response for the temperature range considered. All elastic and electric properties were assumed to be independent of frequency.

In the analyses, a modulated 3.5 cycle toneburst excitation frequency was varied between 1 kHz - 300 kHz at frequency intervals of 1 kHz. At each toneburst frequency, the peak response magnitude was extracted from the sensor response computed according to eq. (7.4) and considering an incident s_0 mode. The theoretically predicted peak response spectrum was generated for temperatures ranging from -40 deg. C to 60 deg. C in 10 deg. C increments. The normalized peak response spectrum curves are shown in Fig. 7.2 for toneburst excitation frequencies between 160 kHz to 300 kHz. This range is consistent with the frequencies used during active joint interrogation. The response curves are separated for the temperature range of -40 deg. C to 30 deg. C in Fig. 7.2(a) and 30 deg. C to 60 deg. C in Fig. 7.2(b). Examination of the results indicates a clear shift in the response curves toward lower frequency as the temperature rises. This trend is most evident at the peak frequency response

of the transducer near 260 kHz. As previously discussed, this phenomenon occurs as a result of the decrease in Young's modulus of the aluminum plate which alters the wavelength tuning effect. From Fig. 7.2(a), it is also observed that the response increases with increasing temperature. However, at temperatures above 30 deg. C, a decrease in the response magnitude is predicted by the models (Fig. 7.2(b)). This behavior is a consequence of the relative rate of increase for the dielectric permittivity of the PZT material than that of the piezoelectric constant at temperatures in excess of 30 deg. C [172]. The absolute difference in the response magnitudes, resulting from temperature changes, is a maximum near the wavelength tuning frequency of 260 kHz. However, if the effect of frequency shift is removed, the relative difference in magnitude will be equivalent over the entire frequency spectrum. This must be true because all elastic and electric properties were assumed to be frequency independent.
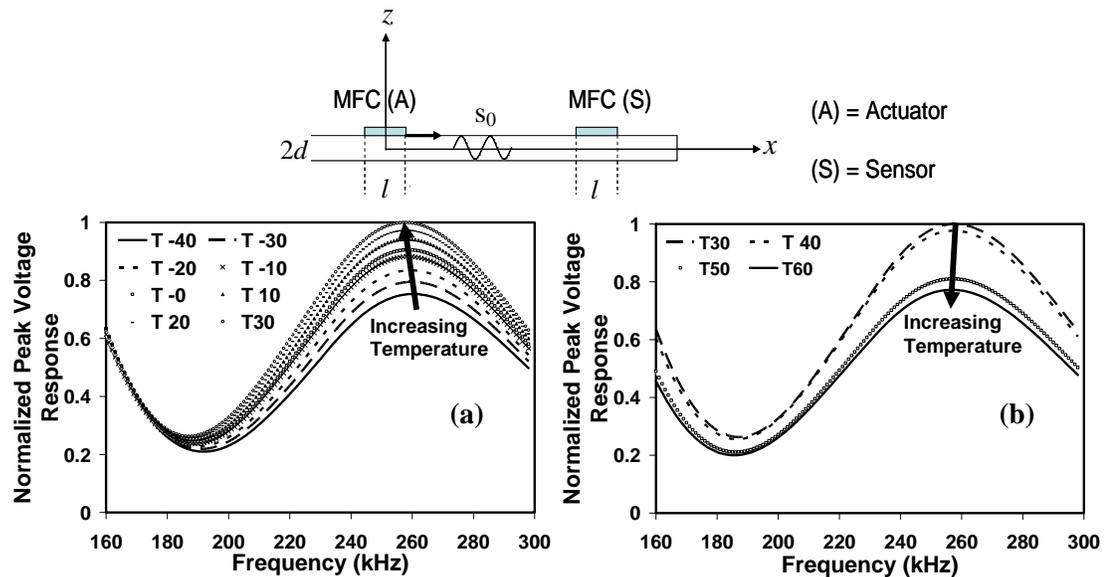
Fig. 7.2. Predicted peak response spectrum of MFC sensor subjected to MFC actuated tonebursts for temperatures ranging from (a) -40 deg. C to 30 deg. C and (b) 30 deg. C to 60 deg. C.

7.2.2.2 Experimental Analysis

Experimental tests were conducted on an aluminum plate with dimensions of 400 mm

× 350 mm × 1.524 mm. A pair of MFC transducers (type P1) was bonded using a thin layer of cyanoacrylate adhesive to perform pitch-catch guided wave tests. The distance between MFC actuator and MFC sensor was 110 mm. Using a controlled temperature chamber environment, the system was subjected to temperatures ranging from -40 deg. C to 60 deg. C in 10 deg. C intervals. At each interval, frequency sweeps were conducted within the range of 100 kHz to 300 kHz. A 3.5 cycle Hanning windowed toneburst was used as the actuating signal. A photograph of the test specimen and environmental chamber utilized during tests is shown in Fig. 7.3.
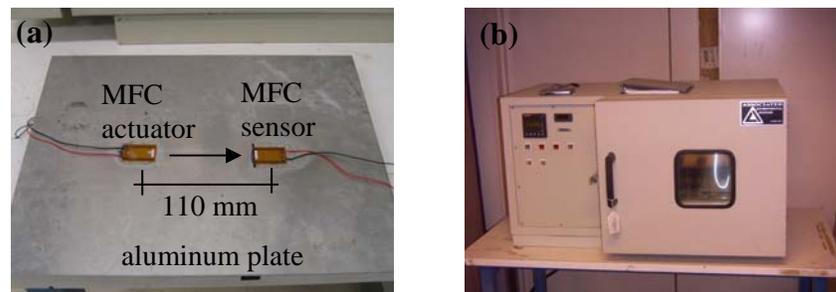
Fig. 7.3. (a) Test specimen with bonded transducers. (b) Environmental chamber used to perform temperature tests.

Each received waveform was gated in time to isolate the predominant s_0 mode from which the RMS was computed in order to quantify the response magnitude. Congruent with the theoretical analysis, the RMS, extracted at each frequency, was used evaluate the response spectra for each incremental temperature. The experimental response curves are shown in Fig. 7.4. In this figure, a frequency shift of the entire spectrum is observed, similar to that identified in the theoretical response curves (Fig. 7.2).
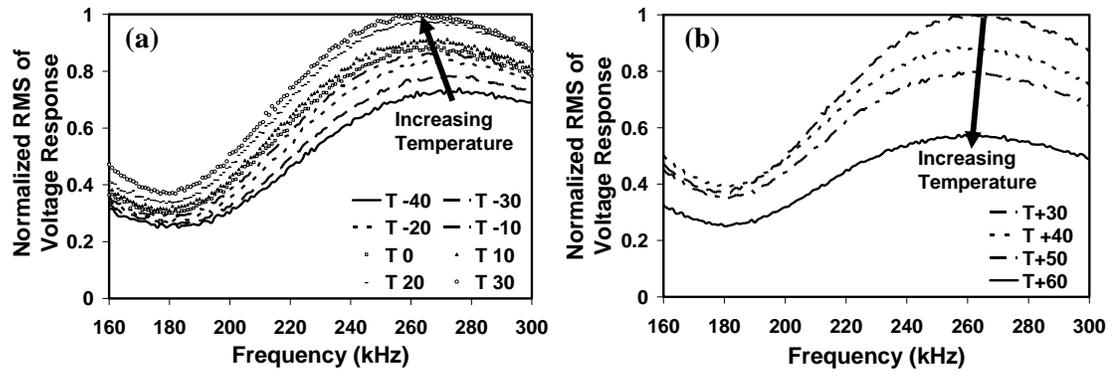
Fig. 7.4. Experimental response spectra of MFC transducer for temperatures ranging from (a) -40 deg. C to 30 deg. C and (b) 30 deg. C to 60 deg. C.

Fig. 7.5 presents the response magnitude, normalized to unity, at the wavelength tuning frequency of 260 kHz for the experimental and theoretical analyses as a function of temperature. The trend of increasing magnitude up to a temperature of 30 deg. C followed by a decreasing magnitude is easily observed within this figure. Good agreement in the relative response magnitude was achieved over the entire temperature range, with the exception of slight discrepancies existing at T=40 deg. C and T=60 deg. C.
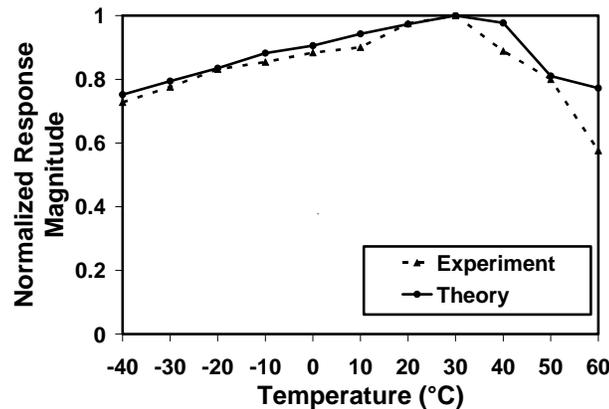
Fig. 7.5. Theoretical and experimental normalized MFC response magnitude for 260 kHz toneburst.

To demonstrate the hysteretic stability of the guided wave magnitude, the response of the MFC transducers to a complete thermal cycle (-40 deg. C to 60 deg. C to -40 deg. C) was

evaluated. The test procedure followed the same experimental procedure described above. Results, presented in Fig. 7.6, indicate good stability in the s_0 guided wave magnitude over the entire the temperature range considered. Therefore, it is expected that the variation in the amplitude based features extracted from the s_0 portion of a signal will be minimal due to temperature cycling.
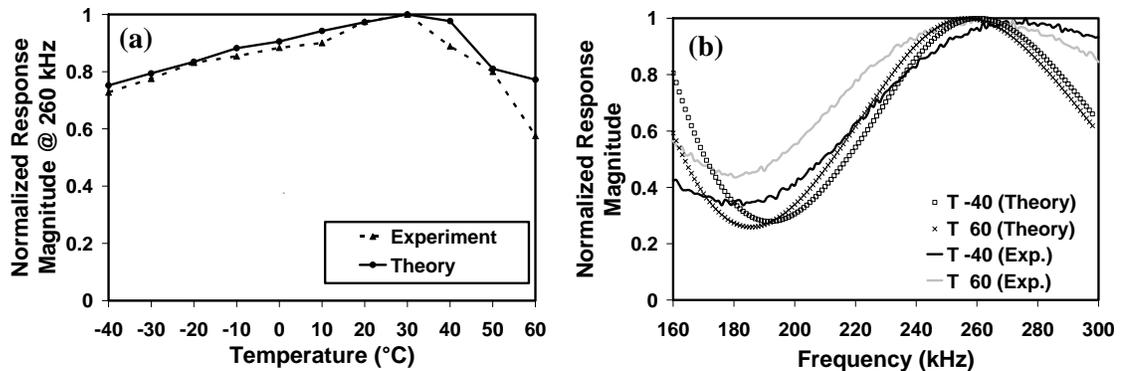
Fig. 7.6. (a) Theoretical and experimental normalized MFC response magnitude for 260 kHz toneburst. (b) Theoretical and experimental MFC response spectra for minimum and maximum temperatures of -40 deg. C and 60 deg. C.

7.2.3   Accounting for Temperature Effects in Damage Detection

The change in wave amplitude as a function of temperature will undoubtedly complicate damage detection based upon amplitude based features, such as that proposed within this thesis. Therefore, it is necessary to implement a statistical pattern process capable of distinguishing between normal operating conditions of the structure, including temperature variation, and changes in the system due to damage. The method proposed in this thesis is based upon the employment of an outlier analysis. A brief introduction of the outlier analysis is discussed next. Following this discussion are the results of a damage detection study performed in a varying temperature environment. These tests were conducted upon a representative wing skin-to-spar specimen by means of an outlier approach.

7.3   Background on Outlier Analysis

An outlier is a datum that appears inconsistent with a set of baseline data. The baseline data describes the normal condition of the structure under investigation. Ideally, the baseline data should include the statistical variation in damage sensitive features due to normal changes in environmental or operative conditions of the structure (e.g. temperature, humidity, loading).

7.3.1   Outlier Analysis for Univariate Data

In the analysis of univariate data, the detection of outliers is a straightforward process based upon the determination of the discordancy between a single observed datum and the baseline statistics. One of the most common discordancy tests is based on deviation statistics, defined as:

$$z_\zeta = \frac{|x_\zeta - \overline{x}|}{\sigma_B} \tag{7.7}$$

where x_ζ is the potential outlier, $\overline{x}$ and σ_B are the mean and the standard deviation of the baseline, respectively and z_ζ quantifies the extent of discordance. The mean and the standard deviation can be calculated with or without the potential outlier depending upon whether inclusive or exclusive measures are preferred. The value of z_ζ is then compared to a defined threshold value, in order to determine whether the datum x_ζ is an outlier (above the threshold) or not.

7.3.2   Outlier Analysis for Multivariate Data

A set of q-dimensional (multivariate) data consists of n observations in q variables.

The discordancy test equivalent to eq. (7.7) is expressed by the Mahalanobis Squared Distance (MSD), D_ς, which is a non-negative scalar defined as:

$$D_\varsigma = \left(\{x\} - \{\bar{x}\}\right)^T \left[S_{cov}\right]^{-1} \left(\{x\} - \{\bar{x}\}\right) \tag{7.8}$$

where $\{x\}$ is the potential outlier vector, $\{\bar{x}\}$ is the mean vector of the baseline data and $\left[S_{cov}\right]$ is the covariance matrix of the baseline data. Generally, the discriminatory power of a multivariate discordancy test increases with increasing dimension of the input vector. However, an excessive dimension of the problem can result in an unwanted sensitivity to spurious effects (e.g. noise) in addition to an increase in the computational complexity of the test. Thus, it is beneficial to select a low number of damage sensitive features in the input vector to increase the computational efficiency while ensuring high discriminatory power of the algorithm.

7.4   Outlier Analyses on CFRP Plate-to-Spar Joints

7.4.1   Test Description

The [0/±45/0]s composite bonded joint described in chapter 6 was subjected to a systematically varying temperature range of -40 deg. C to 60 deg. C in 10 deg. C steps. Controlled test conditions were achieved through the use a commercial environmental chamber and thermocouples measuring the interior chamber and joint temperatures. At each incremental temperature, signals were acquired over three pristine joint regions and each region of simulated joint damage. Separate pairs of permanently bonded MFC transducer pairs were utilized to test the various pristine and damaged regions of the joint (Fig. 7.7). Thus, a total of three transducer pairs were used for the three pristine regions, and another

three transducer pairs were used to interrogate the poorly-cured, 25.4mm × 25.4mm disbonded and 12.7mm × 12.7mm disbonded joint regions, respectively.
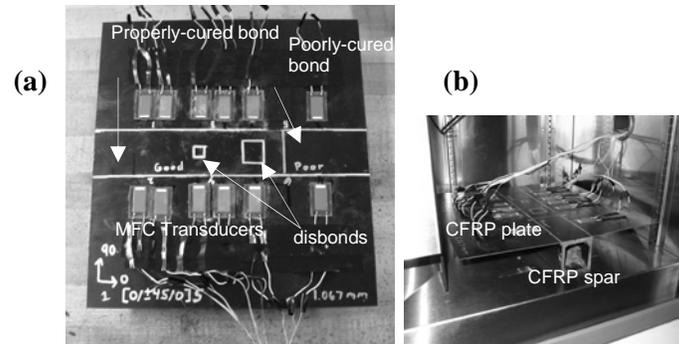
Fig. 7.7. Test specimen with attached MFC transducers and simulated damage: (a) plan view; (b) side view in environmental chamber.

7.4.2   Selection of Features for Multivariate Outlier Analysis

Guided wave tests were conducted in a complimentary manner as that described in chapter 6. Signals acquired at 205 kHz were gated in time to isolate the predominant s_0 mode. Based upon results from the SAFE analyses in chapter 5, eight damage sensitive features related to the energy transmission were extracted in both the time domain and frequency domain of the ultrasonic measurements. These features included the RMS, the variance, the kurtosis, the peak to peak and the peak of the time-domain signal, the peak and the area of the signal's FFT spectrum, and the area of the signal's Hilbert Transform. An eight-dimensional outlier analysis was then employed in order to discriminate bond degradation from temperature changes. Parametric analyses confirmed that the eight-dimensional pattern recognition algorithm satisfied the requirements of low dimensionality and high discriminatory power for damage detection.

7.4.3   Definition of Multivariate Baseline Statistics

For systems exposed to a changing environment, such as temperature variation, the statistics of the baseline data are undoubtedly altered. To compensate for this, Worden *et al.* [7] suggested that the mean vector and covariance matrix can be defined as a function of the known environmental parameter, in this case temperature. This technique is ideal for providing maximum discrimination amongst structural conditions. However, the complexity of the approach increases by requiring knowledge of the real-time environmental conditions as well storage of the statistical data for a large number of baseline measurements. As a result, this may not be suitable for computationally limited applications such as onboard monitoring systems. Instead, for this study the baseline set was defined in two slightly different manners. In one case, the baseline set incorporates the measurements taken for the pristine conditions over the entire temperature range investigated (-40 deg. C to 60 deg. C). Naturally, this "ambitious" baseline is expected to only yield a limited discriminatory power of the outlier analysis. However, defining a single baseline greatly simplifies the analysis for reasons described above. In a second analysis, the discordancy tests are conducted such that two separate baseline sets are defined. These correspond to measurements taken "above ambient" and "below ambient" where ambient is defined as 20 deg. C. Thus, the two temperature ranges considered were between -40 deg. C to 20 deg. C and 20 deg. C to 60 deg. C. It is worth highlighting that because separate transducer pairs were utilized during the data acquisition, the statistical variation in the features due to differences in transducer efficiency and bonding conditions, along with temperature effects, were accounted for in the tests.

7.4.4 Computation of Damage Threshold

For a given observation, the discordancy value is normally compared with a threshold value in order to classify the observation as an anomaly (outlier) or normal operating conditions of the system (inlier). A Monte Carlo simulation was employed for the computation of the threshold, which is associated with a given confidence interval. When baseline measurements are limited, a Monte Carlo simulation is an effective method for generating a large number of random data to populate the baseline distribution. For further detail on this approach, the reader is referred Worden *et al.* [7]. Definition of the threshold by the Monte Carlo method inherently assumes that the baseline data is normally distributed. To test the Gaussianity of the baseline distribution, probability plots of the baseline data were made. Results not shown here indicated that the baseline distribution followed a normal distribution with sufficient accuracy such that the threshold is acceptable and its associated confidence interval is reliable. Thresholds defined in the outlier analyses corresponded to a 99.9% confidence interval, suggesting that only 1 of every 1000 observations will result in a false-positive classification.

7.4.5 Bond State Discrimination Results

The results of the outlier analyses for the baselines established from the entire temperature range, below ambient and above ambient are presented in Figs. 7.8(a), 7.8(b), and 7.8(c), respectivelly. The plots show the discordancy level based upon the Mahalonobis squared distance on a logarithmic scale for a given observation. Each observation corresponds to a specific temperature and joint condition. For clarity, the observations in each figure are catagorized according to the structural condition of the joint. It is observed in Fig. 7.8(a) that a large number of damaged cases are classified as inliers, suggesting too large of a spread in

the baseline data. However, by splitting the baseline into the two separate temperature ranges (above and below ambient temperature), the proper classification of joint defects was greatly improved. In fact, for each discrete temperature examined, both disbonds and the poorly-cured bond were successfully classified as anomalies. As anticipated, the level of discordancy tended to increase with increasing severity of the simulated damage. In addition, the outlier anlayses properly classified all observations occuring over the well-cured regions as inliers, in other words, as normal operation conditions of the structure. Overall, these results demonstrate not only the sensitivity of the selected features to the bond state, but also the robustness of the outlier analysis for proper detection of bond defects despite these large variations in temperature.
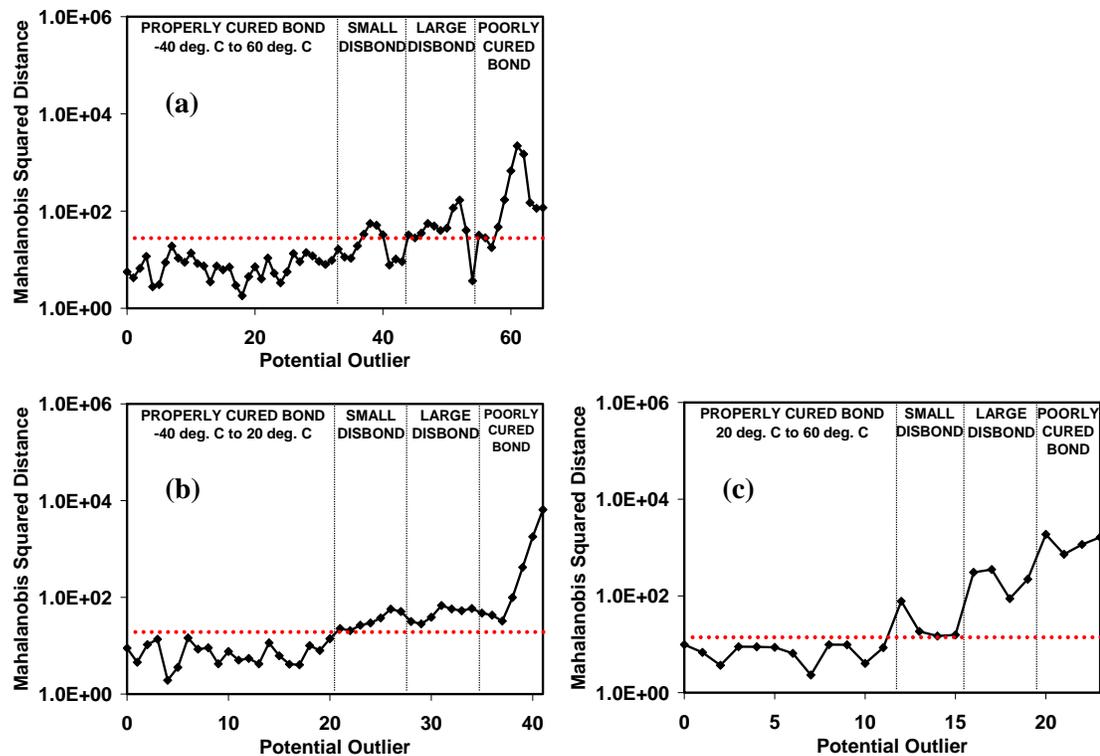
Fig. 7.8. Outlier analysis results of guided wave monitoring of composite joint subjected to varying temperatures. Baseline set incorporates data from (a) entire temperature range (-40 deg. C to 60 deg. C), (b) below ambient temperature (-40 deg. C to 20 deg. C), and (c) above ambient temperature (20 deg. C to 60 deg. C).

7.5   Conclusions

This chapter addressed the often neglected effects of temperature on guided wave damage detection.   Initially, the effects of temperature on the guided wave signals were discussed.   This chapter not only defined the various characteristics of guided waveforms that change as a function of temperature, but also justified each phenomenon according to the influence of temperature on the mechanical, electrical and thermal properties of each layer in the transducer-structure system.   Theoretical and experimental analyses were performed to validate some of the qualitatively described effects.

The influence of temperature on wave amplitude is most detrimental to the active bond diagnostic approach presented in chapter 6.   Despite this complication, statistically-robust detection of defects in a composite-to-composite adhesive joint was successfully achieved under varying temperature and varying transducer-structure coupling.   This was accomplished by a multivariate outlier analysis which used carefully selected features of guided wave measurements and only two baseline distributions corresponding to "above ambient" and "below ambient" temperature ranges.

7.6   Acknowledgement

Chapter 7, in part, has been submitted for publication in the *Journal of Intelligent Material Systems and Structures*, Salamone, Salvatore; Matt, Howard; Rizzo, Piervincenzo; Lanza di Scalea, Francesco. 2006. The current running title of this paper is "The influence of temperature on guided wave based MFC transduction and damage detection".   The dissertation author was a co-author of this paper.

Chapter 8

SAFE Analysis of Scaled UAV Wing Skin-to-Spar Joints

8.1   Model Definition

The test specimen considered in this analysis was a scaled representation of a UAV wing skin-to-spar joint.   The two wing skins were $[\pm45\,CFRP/honeycomb/\mp45\,CFRP]$ sandwich structures. Nomex honeycomb with a thickness of 3.2mm was used as the sandwich core. The top and bottom wing skins were bonded to a single CFRP tubular spar using Hysol 9394 epoxy. The spar cap had a $[\pm45/90/\overline{0}_4]_S$ layup, while the spar walls were comprised of a $[\pm45/90]_S$ layup. The 0 deg. fiber direction axis was parallel to the spar length. The sandwich skins tapered off near the joint due to the lack of honeycomb. The entire cross section of the joint thereby consisted of the following layers, $[\pm45/\mp45/epoxy/\pm45/90/0_4/90/\mp45]$. Photographs of the test specimen, upon which the models were based, are shown in Fig. 8.1.

The bond conditions that were examined in this analysis are regions with poorly-cured adhesive and disbonded regions, in addition to regions with properly-cured adhesive. For consistency with experiments, analyses considered guided waves propagating across the joint.

When modeling the guided wave propagation outside of the joint, the wing skin model only considered the CFRP portion of the skin. Preliminary experimental tests suggested that guided waves within the frequency range of interest did not propagate well through the entire cross section due to the presence of large voids existing within the honeycomb cells. Therefore guided waves are mainly confined to within the CFRP laminate upon which the transducer is bonded to.
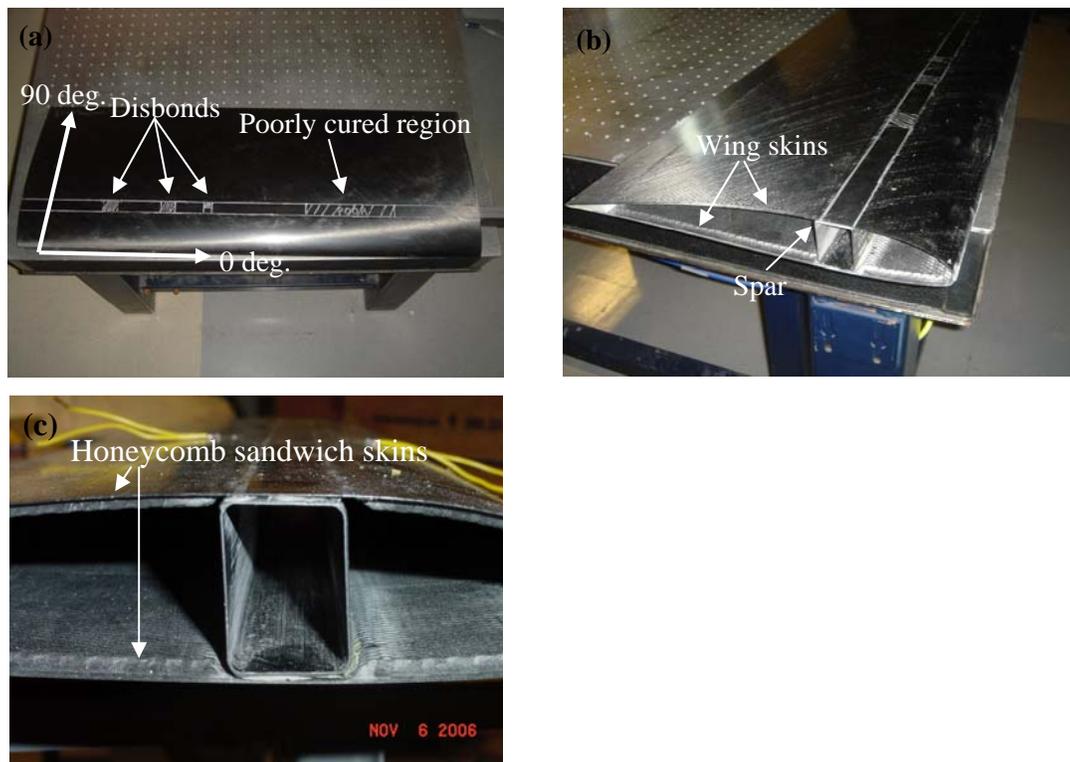
Fig. 8.1. Scaled representation of UAV partial wing section (a) Plan view with defected regions and fiber axes (b) isometric view and (c) elevation view.

Each ply of the CFRP wing skin and CFRP spar were modeled according to the approach described in chapter 5. In this analysis however, the spar was modeled according to its known layup instead of approximating it as a single homogenous layer. The values of the ultrasonic properties, thickness, density, real components, C_{ij}', and of the imaginary components, C_{ij}'', of the stiffness matrix adopted in the models were consistent with that prescribed in tables 5.1 and 5.2.

8.2   Dispersion Results for Different Bond States

Plots of the velocity and attenuation curves are shown for the well bonded joint in Fig. 8.2 considering wave propagation along the 90 deg. axis (across the joint). The frequency range shown is DC-300 kHz which corresponds to the operating range of the experimental tests. Within this frequency range, only three propagative modes exist. These modes are the zero-order symmetric, S_0, the zero- antisymmetric, A_0 and the zero-order shear horizontal, SH_0. As opposed to the SAFE results shown for the previously analyzed joints (chapter 5), the cut-on frequency of higher order modes occurs above 300 kHz due to the thinner joint cross section.

Fig. 8.2(c) clearly shows that the two modes with minimum attenuation losses are S_0 and SH_0. Thus these two modes are well-suited for transmission of energy across the joint. No mode coupling regions were observed in the frequency range considered.
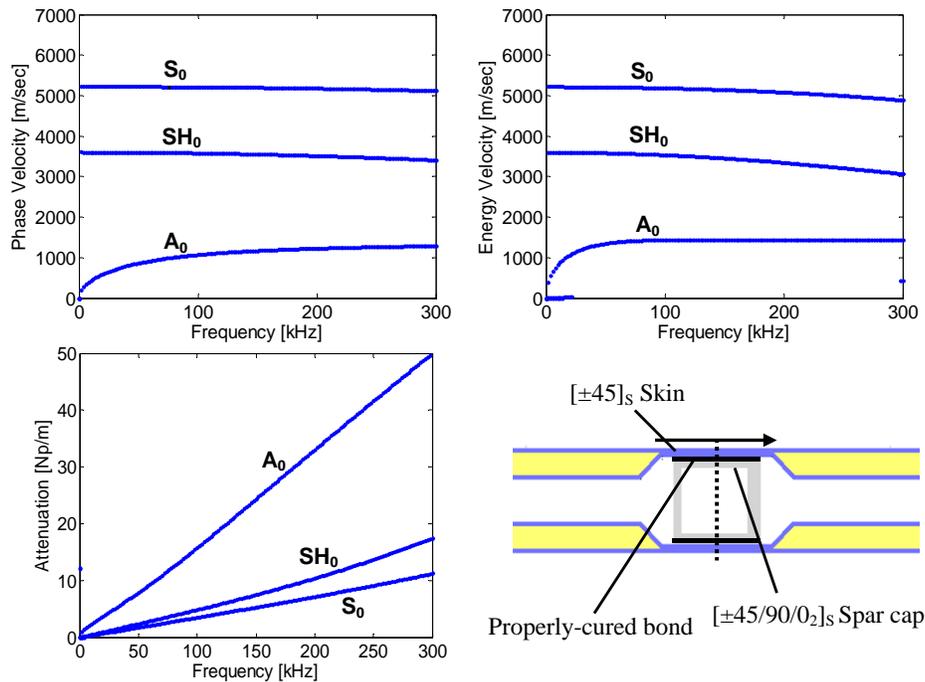
Fig. 8.2.   (a) Phase velocity, (b) energy velocity, (c) and attenuation curves for the well bonded $[\pm 45/\mp 45/\text{epoxy}/\pm 45/90/0_4/90/\mp 45]$ joint. Solutions correspond to wave propagation along 90 deg. fiber axis (across joint).

The dispersion curves for the case of the poorly-cured bond did not show any notable change from those of the properly-cured bond. This is because of the very small bond layer thickness compared to the thickness of the entire skin-to-spar assembly, which dominates the dispersion behavior. However, changes in the wave power flow between the two cases were predicted, as will be discussed in a following section.

Dramatic changes in the phase velocity, energy velocity and attenuation curves resulted from the disbond case. In this case, additional modes emerged. Similar to previous findings, the additional modes of the disbonded joint essentially coincide with the solutions of the individual wing skin laminate. Therefore, the introduction of a disbond allows for the propagation of two separate types of modes, namely those whose energy is mainly concentrated within the upper plate above the bondline (denoted by $S_{0,plate}$, $A_{0,plate}$, $SH_{0,plate}$), and those whose energy is mainly concentrated within the spar below the bondline (identified by $S_{0,spar}$, $A_{0,spar}$, $SH_{0,spar}$). Mode $S_{0,spar}$ of the disbonded joint corresponds to mode S_0 of the properly-cured joint. Under the testing conditions used in this study, the predominant carrier of energy through the disbonded joint is either the $S_{0,plate}$ or $SH_{0,plate}$. The dispersion curves of both of these modes in the disbonded joint are virtually coincident to those in the $[\pm45]_s$ laminate.

8.3 Identification of Carrier Modes

Consistent with the experimental tests, initial guided wave excitation upon the wing skin followed by wave propagation across the joint and along the global 90 deg. fiber axis was considered for the identification of carrier modes. As previously discussed, guided waves propagating in the sandwich skin will be primarily confined within the [±45] CFRP laminate. The velocity and attenuation curves for 90 deg. wave propagation in the [±45] CFRP laminate

are shown in Fig. 8.3. The two wing skin modes with significant in-plane displacement correspond to the zero order symmetric mode s_0, and shear horizontal mode sh_0. Therefore, due to predominant in-plane operation for piezoelectric transducers as well as the coupling of the in-plane motion parallel and perpendicular to the direction of propagation as a result of the ± 45 deg. fibers, both of these wing skin modes have the potential to be excited. The guided wave analysis of the "across the bond" test configuration was therefore based upon initial excitation of either the s_0 skin mode or the sh_0 skin mode and subsequent mode conversion in the bonded region. Mode conversion effects, as the wave travels across the joints, were evaluated on the basis of the similarity between the displacement mode shapes of an in incoming mode and those of a joint carrier mode. Similar conclusions were reached as that discussed in section 5.4. The only difference being that the A_1 mode is non-propagative at frequencies below 300 kHz for this particular joint. Therefore, the s_0/sh_0 skin mode is mode converted strictly to the S_0/SH_0 mode for the well-cured and poorly-cured bond conditions and to the $S_{0,plate}/ SH_{0,plate}$ mode in the case of the disbonded joint.

Due to the ambiguity of the incoming skin mode, experimental tests were performed in an attempt to identify which skin mode (s_0 or sh_0) was preferentially excited. However, test results were inconclusive as a result of the fact that both modes have similar phase and energy velocities (Figs. 8.3(a) and 8.3(b)). The following analyses thus considered either the S_0 or SH_0 multilayer joint mode being solely responsible for energy transmission across the joint.
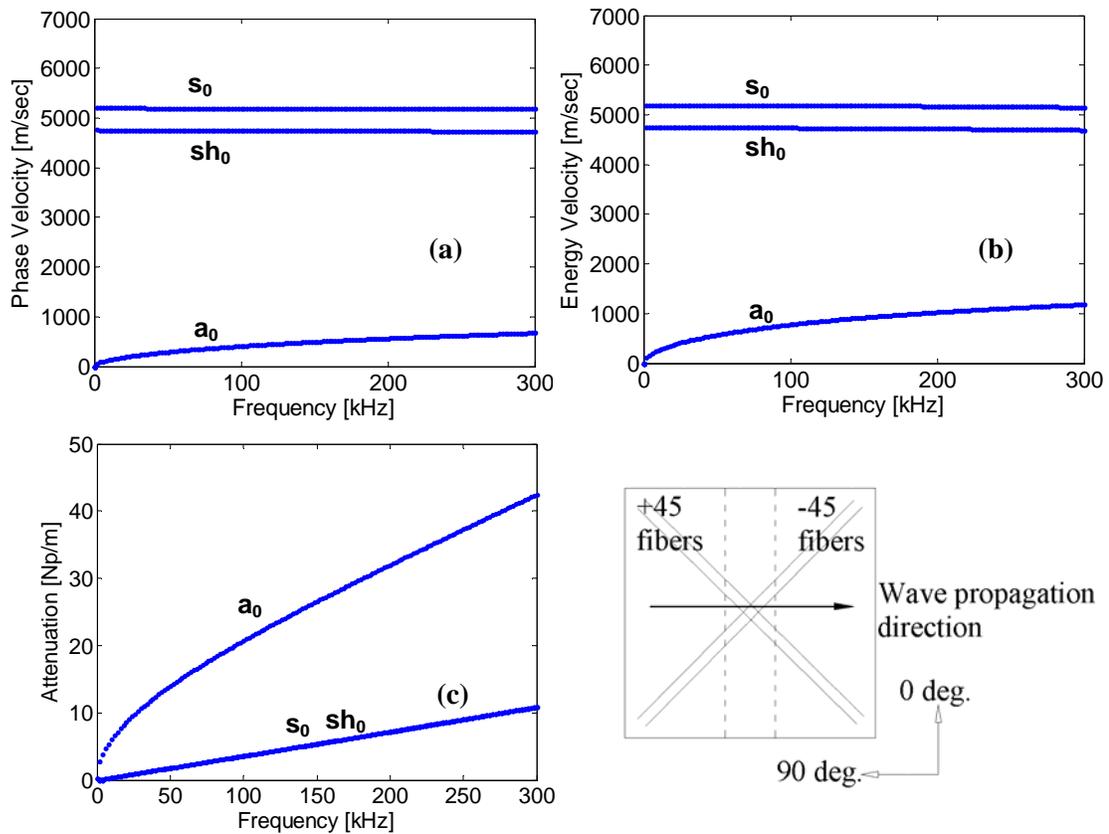
Fig. 8.3. (a) Phase velocity, (b) energy velocity, (c) and attenuation curves for [±45] CFRP laminate considering wave propagation along 0 deg. global axis.

The normalized cross-sectional strain components of both the S_0 and SH_0 joint carrier modes are shown at 200 kHz in Fig. 8.4. The two horizontal lines shown on each plot correspond to the bond layer, where above this is the wing skin laminate and below is the wing spar. It can be seen that a large concentration of both normal strain, ε_{xx}, and shear strain, γ_{xz}, within the adhesive layer exists for the S_0 joint mode. The SH_0 mode produces a very high concentration of shear strain, γ_{xy} within the bond line. Therefore, both carrier modes are expected to be suitable candidates for detecting changes in stiffness of the adhesive layer at or near 200 kHz.

(a) S$_0$ (200 kHz)   **(b) SH$_0$ (200 kHz)**

Depth [mm]

Normalized Strain (x10^{-6})

- - - - - - ε$_{xx}$
———— ε$_{zz}$
———— γ$_{xz}$

- - - - - - γ$_{yz}$
———— γ$_{xy}$
———— γ$_{xz}$
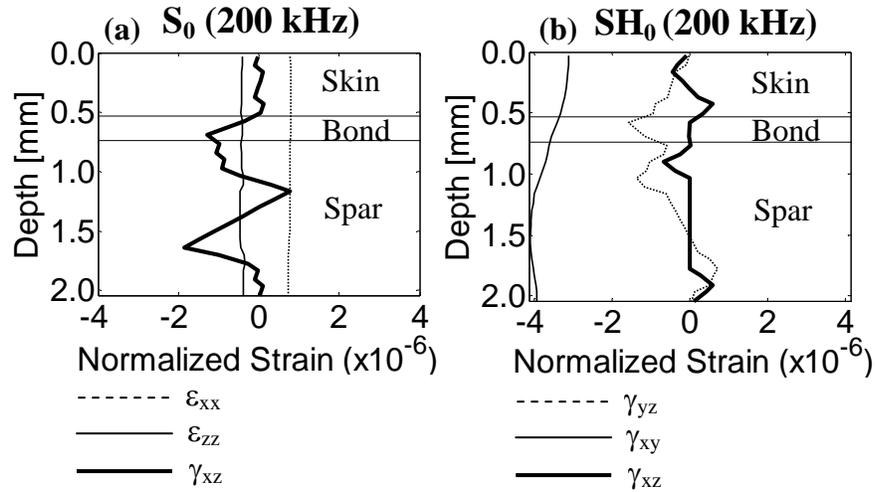
Fig. 8.4. Strain profiles for modes (a) S$_0$ and (b) SH$_0$ at 200 kHz in the properly-cured bond.

8.4   Strength of Transmission as a Function of Bond State

The change in strength of transmission as a function of bond condition was qualitatively predicted from the P$_{Vx}$ component of the Poynting vector. This quantity was divided by the normalization factor $\left(\int_H \mathbf{P_V} \cdot \hat{\mathbf{x}} dz \right)$ to enable direct comparisons between the various bond conditions and carrier modes. Fig. 8.4 illustrates the real normalized P$_{Vx}$ component profiles for the $[\pm 45/\mp 45/\text{epoxy}/\pm 45/90/0_4/90/\mp 45]$ CFRP joint for the different bond conditions. The properly-cured bond and the poorly-cured bond are compared in the top four plots for the two carrier modes S$_0$ and SH$_0$. Figs. 8.4(a) and 8.4(b) refer to S$_0$ propagating at 100 kHz and 200 kHz, respectively. Figs. 8.4(c) and 8.4(d) refer to the SH$_0$ mode propagating at the same respective frequencies.

It can be seen that at a frequency of 100 kHz, the powerflow within the wing skin does not significantly change between well bonded and poorly bonded conditions. However, at higher frequencies, the poorly-cured bond results in an increase in powerflow for S$_0$ and a corresponding decrease in powerflow for SH$_0$ above the bond line. It is therefore deduced that

at frequencies above 100 kHz, either an increase or decrease in energy transmission between the two bond conditions is expected, depending upon which mode the amplitude-based features are extracted from.
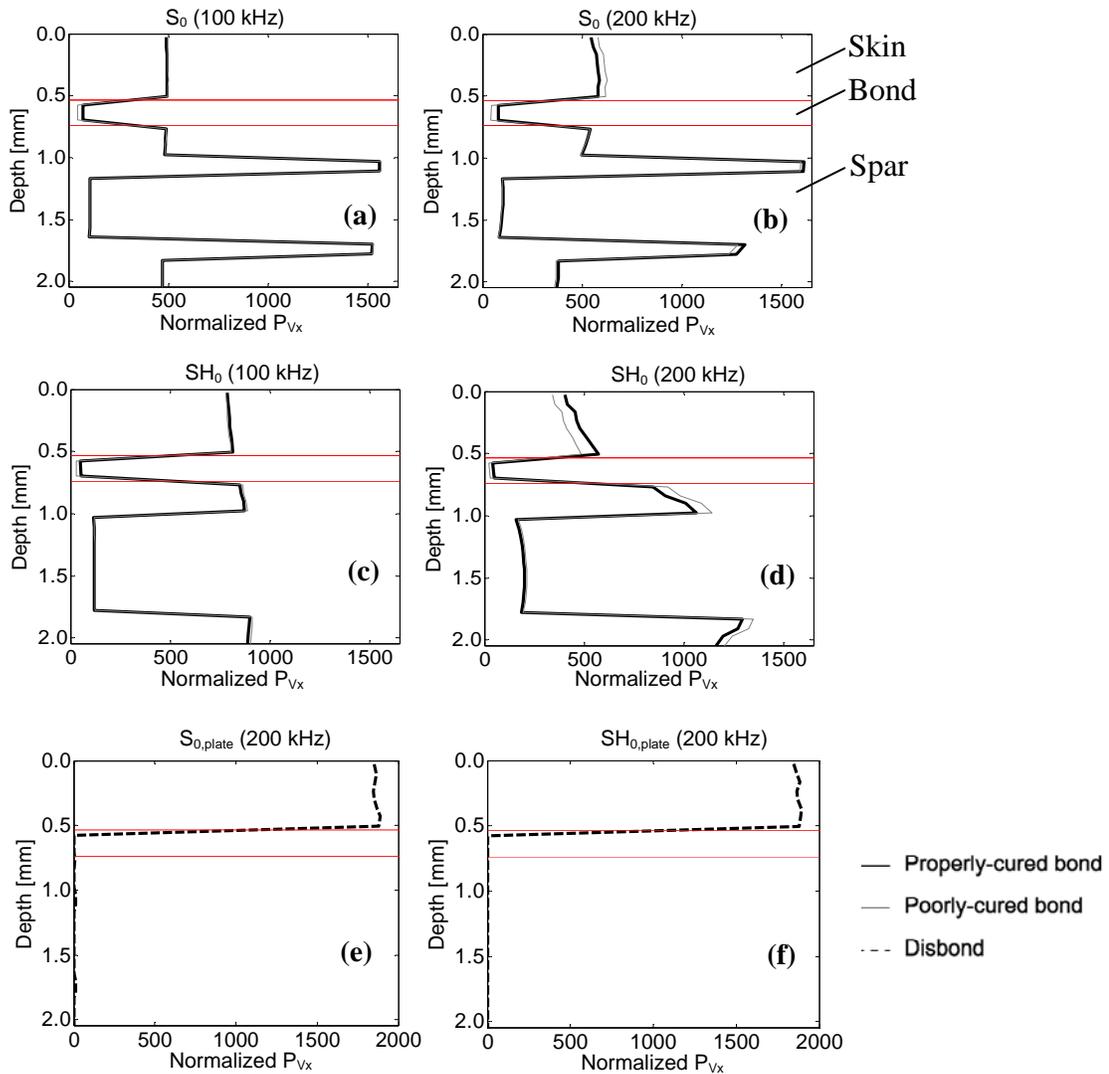
Fig. 8.5. P_{Vx} component of the Poynting vector in the properly-cured bond and in the poorly-cured bond for (a) S_0 at 100 kHz, (b) S_0 at 200 kHz, (c) SH_0 at 100 kHz, and (d) SH_0 at 200 kHz. Same quantity in the disbonded case for (e) $S_{0,plate}$ and (f) $SH_{0,plate}$ at 200 kHz.

As for the disbonded case, shown in Figs. 8.4(e) and 8.4(f) at 200 kHz, the power flow results confirm that $S_{0,plate}$ and $SH_{0,plate}$ are completely confined to the top plate. Note the difference in scales between plots (e) and (f) relative to (a)-(d). Due to the relative difference

in powerflow for the disbonded case, this joint condition is expected to produce larger changes in the energy transmission with respect to the properly-cured or poorly-cured bond conditions. This conclusion is consistent with those made for the other analyzed joints in chapter 5. Significant changes in the P_{V_x} component of the Poynting vector in the disbonded case were not observed over the frequency range of 100 kHz - 300 kHz.

8.5   Conclusions

This chapter discussed SAFE analyses performed on a scaled UAV wing skin-to-spar joint possessing well-bonded, poorly-bonded and disbonded condition. This specimen is considered to be a much more realistic representation of an actual UAV wing skin-to-spar joint than those specimens considered in chapters 5-7. Similar to chapter 5, the SAFE models were used to evaluate the frequency dependant guided wave velocities, attenuation, mode shapes, cross-sectional strain profiles and powerflow within the joint.

From the dispersion results for the pristine joint, only three modes (A_0, S_0 and SH_0) were found to propagate below a frequency range of 300 kHz. In addition, no mode phenomenon occurs. This in contrast to the specimens studied in chapter 5, where a higher number of modes were present and a predominant mode coupling effect was observed. It is concluded that the significant difference in joint thickness was the primary cause in disparity between the dispersion solutions. Indistinguishable difference existed in the velocity and attenuation curves found between the well-cured and poorly-cured joints. However, similar to the findings in chapter 5, the introduction of a disbond results in the emergence of two separate types of modes, namely those whose energy is mainly concentrated within the upper plate above the bondline, and those whose energy is mainly concentrated within the spar below the bondline.

Based upon the wave attenuation results and analysis of the mode conversion occurring at the entry point of the joint, the incoming s_0/sh_0 skin mode is expected to mode convert strictly to the S_0/SH_0 mode for the well-cured and poorly-cured bond conditions and to the $S_{0,plate}/ SH_{0,plate}$ mode in the case of the disbonded joint. Therefore, a different combination of modes is expected to transmit the energy across the joint in this specimen with respect to those specimen analyzed in chapter 5.

Evaluation of the strain profiles indicated a large concentration of both normal strain and or shear strain within the adhesive layer for the two carrier modes S_0 and SH_0 at a frequency of 200 kHz. Thus both carrier modes are expected to be suitable candidates for detecting changes in stiffness of the adhesive layer at or near 200 kHz.

To predict the change in strength of transmission as a function of bond state, the cross sectional powerflow profiles were compared for different joint mode-frequency combinations. At a frequency of 200 kHz, the poorly-cured bond resulted in an increase in powerflow for S_0 and a corresponding decrease in powerflow for SH_0 above the bond line. It was therefore concluded that either an increase or decrease in energy transmission between the two bond conditions is expected, depending upon which mode the amplitude based features are extracted from. When disbonding conditions occur, the power flow results confirm that the energy of $S_{0,plate}$ and $SH_{0,plate}$ is completely confined to the top plate. As a result, this defect is expected to produce larger changes in the energy transmission with respect to the poorly-cured bond conditions. This conclusion was consistent with those made for the joints analyzed in chapter 5.

The relative change in powerflow due to disbonding or poorly-cured joint conditions with respect to a properly-cured joint is comparable between the scaled wing skin-to-spar joint and less representative specimens described in chapter 5. Therefore, despite the lack of mode

coupling and variation in identified carrier modes, the strength of transmission within the scaled wing skin-to-spar joint will be a practical feature for detecting joint damage.

Chapter 9

Active Interrogation of Scaled UAV Wing Skin-to-Spar Joint at Ambient Temperature

9.1   Test Specimen

This chapter discusses additional experimental tests conducted upon the scaled representation of a UAV wing section. A general description of the layup and photographs of this specimen are given in section 8.1 and Fig. 8.1. The composite spar and laminates were fabricated using T700/p7263w-15 carbon epoxy prepreg. Nomex HRH-10-1/8-3.0 was utlized within the honeycomb sandwich skins with a thickness of 3.175 mm. The composite piece used to replicate the wing spar was a rectangular tube with a width, depth and length of 25.4 mm $\times$ 37 mm $\times$ 914.4 mm and respectively. The thickness of the spar cap and walls were 1.245 mm and .8 mm. A two-part Hysol 9394 epoxy adhesive was used to bond the spar to the upper and lower honeycomb sandwich wing skins. Bonding of the wing section was done such that the 0-deg fiber direction ran along the lengthwise direction of the spar. The planar dimensions of the wing section were approximately 312 mm $\times$ 812.8 mm. The leading and trailing edges of wing skin were adjoined, forming a curved wing cross section.

The same type of bond conditions considered in the models discussed in chapters 5 and 8 were artificially created prior to assembling the joints. The majority of the bond was comprised of a properly-mixed epoxy, representing the well-bonded region. A 25.5 mm $\times$ 152.4 mm region of degraded bond stiffness was also introduced along the wing skin-to-spar joint. The degraded bond was achieved by improperly mixing the ratios of resin and hardener. The properties of this bond are given in tables 5.1 and 5.2. Three disbonded regions of different sizes were created by inserting Teflon release film with a thickness of .025 mm. The release film was expected to severely degrade the shear stiffness of the bond while degrading

its longitudinal stiffness to a smaller extent. The two simulated disbonds have dimensions of 25.4 mm x 25.4 mm, thus they spanned across the entire width of the spar. A third disbond of dimension 12.7 mm x 12.7 mm was inserted near one edge of the joint. The thickess of the adhesive layer was estimated to be approximately 0.333 mm. A photograph of the wing section showing the simulated damage locations is shown in Fig. 8.1. Prior to testing, ultrasonic A scans conducted along the joint confirmed the existence of the simulated damage at the intended locations.

9.2   Experimental Analysis

Ultrasonic guided wave measurements were conducted across the scaled wing skin-to-spar joint at ambient temperature. Results from the SAFE analyses described in chapter 8 indicated that guided wave frequencies around 200 kHz should provide sufficient sensitivity to changes in the bond conditions. Recalling (eq. (7.4)) from chapter 7, the frequency domain response magnitude of an MFC sensor subject to an MFC actuated toneburst excitation with normal incidence was found to be proportional to $\left| \sin^2 \left(\pi l / \lambda \right) \right|$. Therefore, considering the phase velocity of either an s_0 or sh_0 mode to be approximately 5mm/μsec (Fig. 8.3) and a target frequency of 0.2 MHz, the ideal transducer length necessary to achieve maximum actuation/sensing capability is 12.5 mm. However, the peak transducer response does not take into consideration the increase in attenuation that occurs with increasing frequency. In fact, preliminary experimental tests indicated that significant wave attenuation occurred at high frequencies as a result of the honeycomb core which dissipated a large amount of wave energy. To compensate for this, the MFC (type P2) transducers used during testing had to be cut to a dimension smaller than the theoretically ideal length of 12.5 mm in order to excite and

detect frequencies near 200 kHz. A pair of MFC transducers was thereby cut to a lengthwise (PZT fiber axis) dimension of 9 mm. The MFCs were bonded to the structure using a thermally-activated film adhesive. The distance between actuator and receiver was maintained at 80 mm. A photograph of the MFCs attached to the scaled wing skin-to-spar joint can be seen in Fig. 9.1.
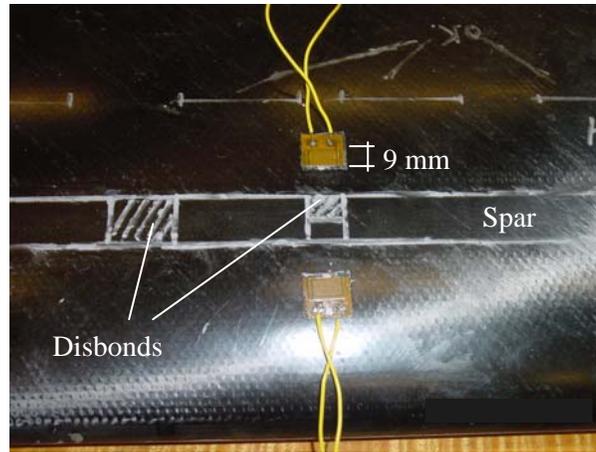
Fig. 9.1. MFCs attached to the scaled wing-skin-to-spar joint.

To assist in the normalization of the testing procedure, the same transducer pair was used throughout the tests. However, it is worth noting that the testing of various locations along the joint required re-bonding of the MFC actuator and sensor. The difference in transducer bonding conditions will inherently introduce some variability in the features characterizing the properly-cured joint. To compensate for this variability as well the variability in conditions along the joint, multiple tests were conducted at different locations of the properly-cured and poorly-cured adhesive regions. Two tests were conducted for each of the 12.7 mm $\times$ 12.7 mm and 25.4 mm $\times$ 25.4 mm disbonded regions. Three tests were performed over poorly-cured regions where as a total of four tests were done over different properly-cured regions.

The frequency sweeps were performed between 100 kHz to 300 kHz, with 1 kHz increments. At each generation frequency, the raw time signals (no signal averaging) acquired by the MFC sensor were gated in time to isolate the predominant s_0/sh_0 mode. The gated time signal was then processed through the discrete wavelet transform to extract the relevant wavelet coefficients. In the wavelet analysis, the db10 mother wavelet was utilized and the extracted DWT coefficients included levels 6, 7, and 8. Based upon the results from the SAFE analyses, the ultrasonic transmission strength through the joints was selected as the damage sensitive feature. Quantification of the transmission strength was achieved by taking the Root Mean Square (RMS) of both the raw time-domain signals and the corresponding wavelet coefficients. For each individual test, an RMS spectrum was evaluated. Using the multiple test data, the mean RMS spectrum was then computed for each individual joint condition (properly-cured bond, poorly-cured bond, 12.7 mm $\times$ 12.7 mm disbond and 25.4 mm $\times$ 25.4 mm disbond). The mean RMS spectra for the different joint conditions were then compared.

9.3 Bond State Discrimination Results

Results of the mean RMS spectra are compared in Fig. 9.2 in terms of absolute RMS differences from the properly-cured bond and normalized by the peak RMS of the properly-cured joint. Figs. 9.2(a) and 9.2(b) were obtained from the time-domain signals and the corresponding DWT coefficients, respectively.

The first observation from Fig. 9.2 is that the RMS spectra obtained from the time-domain signals are extremely different than that obtained from the DWT coefficients. This is a consequence of performing feature extraction upon the raw time signals (no signal averaging), which contained a large level of noise. In fact, the time domain feature is very difficult to interpret due to the large scatter in the results. On the other hand, feature

extraction from the DWT coefficients, computed again from the raw time signals (no signal averaging), provides a much cleaner distinction between the various bond conditions. This again demonstrates the effectiveness of DWT processing for robust feature extraction without the need for performing signal averaging.
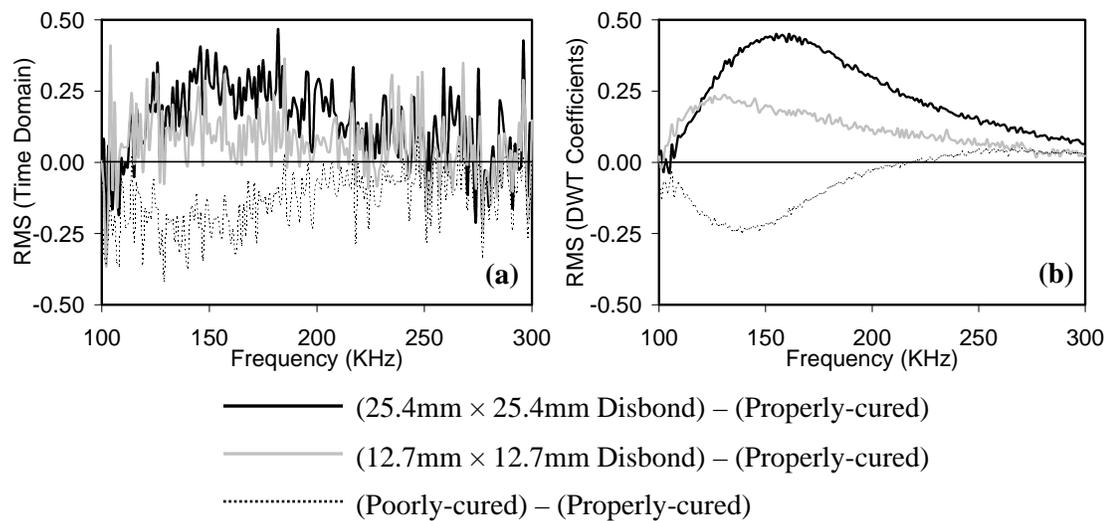
Fig. 9.2. Normalized root mean square differences of the defected bonds relative to the properly-cured bond: (a) feature extraction in raw time-domain; (b) feature extraction from DWT coefficients.

From Fig. 9.2(b), the RMS differences are seen to be positive for the disbonded cases. Thus, the energy transmission is strengthened in the presence of this defect. This general observation is consistent with the predictions made from the power flow computed using the SAFE model. In addition, the strength of transmission associated with the large disbond is larger than that associated to the small disbond. This occurrence results from the wave energy becoming confined within the same wing skin laminate where the MFC actuator and sensor are located.

Results of the poorly-cured bond show instead a loss in energy transmission when compared with the properly-cured bond. This observation indicates that the bulk energy of the analyzed waveform may correspond to the sh_0 mode as opposed to the s_0 mode. As discussed

in Fig. 8.5, the powerflow of the SH_0 joint mode above the bondline actually reduces when degradation of the epoxy stiffness occurs.

The peak RMS difference occurs near 150 kHz, mainly due to the competing effects of MFC transducer resonance and large wave attenuation at high frequencies. Similar to experimental results described in chapters 6 and 7, the frequency range of 125 kHz to 250 kHz appears to be the most sensitive zone for joint damage detection in this specimen.

9.4   Conclusions

The ultrasonic guided wave tests conducted upon a scaled representation of a UAV wing section confirmed that the strength of transmission increases in the presence of disbonds compared to the properly-cured bond. In the case of the poorly-cured bond, a decrease in energy transmission occurred. These results, which were produced on a much better representation of a typical UAV wing section, are complimentary to the damage detection tests performed on the two specimens described in chapters 6 and 7. For improved damage detection, it was also demonstrated that the damage sensitive features, based upon energy transmission, can be extracted from the DWT coefficients of ultrasonic signals containing a high level of noise.

Comparing the experimental results for this specimen with respect to those joints considered in chapters 6 and 7, several conclusions can be drawn. First, the wave attenuation was found to be much higher in the sandwich structure due to large amounts of energy being dissipated into the honeycomb core. As expected, this effect is more predominant at higher frequencies. The high wave attenuation therefore limits the transducer spacing as well as the probing frequencies to values below 300 kHz in such structures. Despite this, damage

detection is still easily achieved by exploiting DWT signal processing and the identified carrier mode sensitivity to bond defects within the frequency range of 125 kHz to 250 kHz.

As predicted by the powerflow profiles obtained from SAFE analyses, it is also observed that the difference in transmission strength occurring over properly-cured vs. disbonded joint is comparable for each of the test specimen considered. A noticeable reduction in the transmission strength difference occurs for the scaled wing skin-to-spar joint when considering the (properly-cured) – (poorly-cured) case. This result was also predicted by a comparison of the powerflow profiles for these two joint conditions and amongst the scaled wing skin-to-spar and CFRP plate-to-spar specimen. In addition, the two specimen studied in chapters 6 and 7 had a joint width twice that of the scaled wing skin-to-spar joint. Therefore, tests across the wider joints are expected to enhance changes in energy transmission due to the simulated poor bond conditions.

An environmental chamber large enough to host the scaled UAV wing skin-to-spar joint was not available. Consequently, temperature effects were not studied for this specimen. However, as discussed in chapter 7, the temperature effects on amplitude based features extracted from guided waves are mainly a result of changes in the electro-mechanical behavior of the transducers (piezoelectric and dielectric permittivity coefficients). Thermal effects within the host structure were shown to have much less influence than the transducer properties for these features. For this reason, along with the comparable defect-induced change in transmission strength, it is anticipated that the application of an outlier approach for damage detection in a widely varying temperature environment will yield similar success for the wing section studied within this chapter.

Chapter 10

Passive Damage/Impact Detection and Location by the Employment of Piezoelectric Rosettes

10.1 Novel Approach for Passive Damage/Impact Detection and Location

As discussed in section 1.5.1, time of flight based damage/impact location do not work particularly well in anisotropic or generally complex structures. In addition, neural networks require an extensive number of training observations while dynamic models must be uniquely and accurately developed for each particular system, making both methods of impact detection difficult to implement in full scale structures. In an attempt to circumvent these deficiencies, this chapter discusses the use of a unique unsupervised approach for damage or impact detection and location applicable to complex composite systems. Ideally, this technique could be adopted for both active and passive diagnostics. The method employs Macro Fiber Composite (MFC) piezoelectric transducers arranged in a rosette configuration. The rectangular geometry of these transducers can be exploited such that response characteristics exhibit predictable directivity behavior. When positioned in a rosette arrangement, the guided wave source location can be deduced without requiring the use of optimization routines, training observations or dynamic models. A conceptual illustration of the MFC rosette technique is shown in Fig. 10.1.

Rosette method for detection/location of existing damage
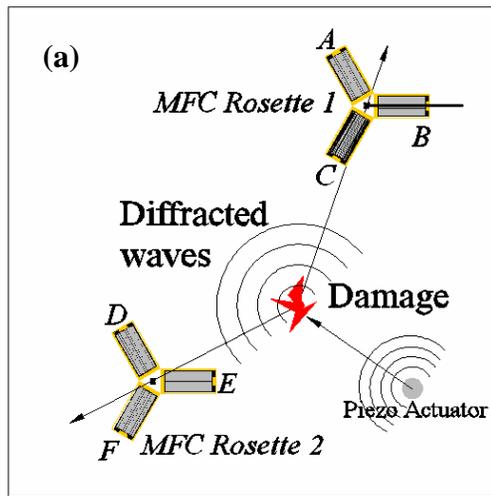
Rosette method for detection/location of active damage or impact
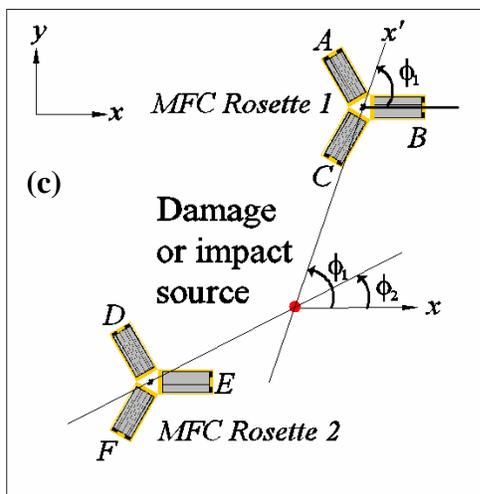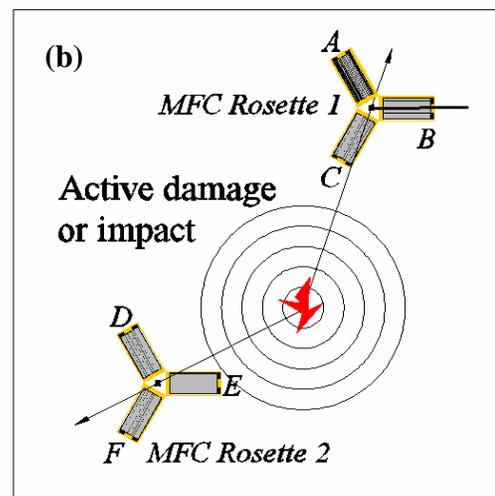
Fig. 10.1 Concept of MFC rosette approach for passive location of (a) existing damage and (b) active damage or impact. (c) Damage location according to evaluated directions of incoming elastic waves.

For the proposed method, existing damage location can be resolved by measuring piezo-actuated diffracted waves. The location of progressive, incipient or impact damage is made possible by detecting acoustic emission signals. This chapter will emphasize the use of MFC rosettes for passive detection and location of occurring damage or impacts. The MFC

rosette theory is based upon the derived response behavior of MFC transducers to broadband ultrasonic Lamb waves, developed in chapter 3. This theory enables the direction of incoming elastic waves to be evaluated. Finally, the application of this concept for the detection and location of simulated active damage or impacts on an aluminum plate, a composite plate, and a scaled CFRP sandwich wing specimen will be discussed.

10.2 Exploitation of the MFC Sensor's Response for Optimal Directivity

10.2.1 Definition of Broadband Sensitivity Factor

Let us recall the derived response behavior of a MFC (type P2) sensor subjected to oblique incident broadband Lamb wave excitation. From the formulation in section 3.5.2, the broadband response magnitude of the sensor was found to be:

$$\overline{U} = \frac{4 S_{MFC\ P2}\ \varepsilon^a_{x'x'}\big|_{z=0}}{lbk^2 \sin\theta\cos\theta} \sin\left(\frac{kb\sin\theta}{2}\right)\sin\left(\frac{kl\cos\theta}{2}\right) \tag{10.1}$$

where l and b are the active length and width of the transducer respectively, $S_{MFC\ P2}$ is the frequency independent term containing the piezoelectric and elastic constants of the MFC (type P2) transducer, as well as the wave propagation angle, and $\varepsilon^a_{x'x'}\big|_{z=0}(\omega)$ is the amplitude spectrum of the in-plane surface strain induced by the arbitrary source at the point of entry into the sensor. The terms θ and k represent the angle of wave incidence with respect to the transverse dimension of the transducer and the wavenumber, respectively.

By redefining the broadband sensor response for a given angular frequency ω_0 as the product of the strain magnitude and the transducer's broadband sensitivity factor (BSF) along the direction of incidence, eq. (10.1) can be re-written as:

$$\overline{U}(\omega_0) = \left|S(\theta,\omega_0)\right|\varepsilon^a_{x'x'}\big|_{z=0}(\omega_0) = \left|S\right|\overline{\varepsilon}_{x'x'} \tag{10.2}$$

In eq. (10.2), S and $\overline{\varepsilon}_{x'x'}$ denote the transducer sensitivity and strain magnitude in the direction of wave propagation, respectively. The transducer's BSF to ultrasonic waves can, in turn, be expressed as:

$$S = \frac{\overline{U}}{\varepsilon^a_{x'x'}\big|_{z=0}} = \frac{4S_{MFC\,P2}}{lbk^2 \sin\theta\cos\theta}\sin\left(\frac{kb\sin\theta}{2}\right)\sin\left(\frac{kl\cos\theta}{2}\right) \tag{10.3}$$

It can be demonstrated numerically that for frequencies at which $\lambda \geq l$, the BSF can be transformed in terms of the two sensitivities along each geometrical direction of the transducer. This therefore allows us to re-write eq. (10.3) as:

$$S \approx |S_1|\cos^2\theta + |S_2|\sin^2\theta \tag{10.4}$$

where S_1 and S_2 will be referred to as the longitudinal (lengthwise) and transverse (widthwise) sensitivity factors for a given frequency of the assumed wave field. It was also found numerically that the error associated with the approximation eq. (10.4) tends to zero for width to length transducer ratios equal to .577. Fig. 10.2 demonstrates the validity of the approximation eq. (10.4). The exact and approximate broadband sensitivity factors are plotted according to eqs. (10.3) and (10.4), respectively. The results in this figure considered an MFC (type P2) transducer bonded on an aluminum plate of thickness 1.54 mm subjected to an a_0 wave field at incident angles of $\theta = 30°, 45°,$ and $60°$. The dimensions of the transducer were chosen to be l= 25.5 mm and b= 12.2 mm, consistent with the measured active area of the transducers used to validate the MFC rosette concept. Therefore, the width to length transducer ratio for this sensor is 0.48. From this figure, it is apparent that eq. (10.4) is an accurate approximation for frequencies lower than the corresponding frequency of $\lambda \geq l$.
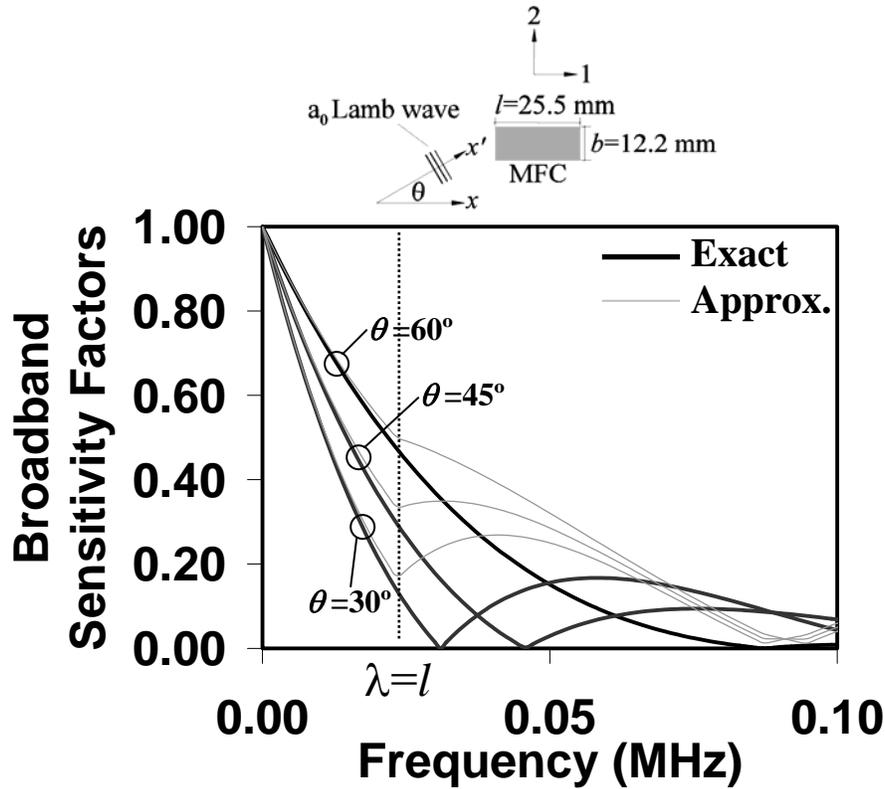
Fig. 10.2. Comparison of exact and approximate broadband sensitivity factors for an MFC sensor subjected to oblique incident a_0 waves at angles of $\theta = 30°, 45°,$ and $60°$.

The longitudinal and transverse sensitivity factors are frequency dependant and are defined by the exact eq. (10.3) after setting θ equal to 0 deg. and 90 deg. for S_1 and S_2, respectively. In doing so, we obtain:

$$S_1 = S\big|_{\theta=0°} = \frac{2t\left(d_{31}E_1 + d_{32}\nu_{12}E_2\right)\sin\left(\frac{kl}{2}\right)}{lk\left[\left(1-\nu_{21}\nu_{12}\right)e_{33}^{\sigma} - \left(d_{31}^2E_1 + 2d_{31}d_{32}\nu_{12}E_2 + d_{32}^2E_2\right)\right]}$$

$$S_2 = S\big|_{\theta=90°} = \frac{2t\left(d_{31}\nu_{12}E_2 + d_{32}E_2\right)\sin\left(\frac{kb}{2}\right)}{bk\left[\left(1-\nu_{21}\nu_{12}\right)e_{33}^{\sigma} - \left(d_{31}^2E_1 + 2d_{31}d_{32}\nu_{12}E_2 + d_{32}^2E_2\right)\right]}$$

(10.5)

From eqs. (10.2) and (10.4), the broadband MFC transducer response can be written as the following expression:

$$\overline{U}(\omega_0) \approx |S_1|\overline{\varepsilon}_{11} + |S_2|\overline{\varepsilon}_{22}$$

(10.6)

Therefore, the broadband response is approximated as the product of in-plane strain magnitudes along the 1 and 2 directions and the transducer sensitivity along each respective axis. By defining the response according to eq. (10.6), it was recognized that the transducer response is consistent with electrical resistance strain gage theory. As an example, for incident waves at an angle of 45 deg., the response corresponds to $\overline{U}\big|_{\theta=45°} = \frac{\overline{\varepsilon}_{x'x'}}{2}(|S_1| + |S_2|)$.

To further demonstrate this point, the longitudinal and transverse sensitivity factors are plotted in Fig. 10.3 according to eq. (10.5) for an MFC (type P2) transducer bonded on an aluminum plate of thickness 1.54 mm and considering a zero order antisymmetric wave field. Also shown in Fig. 10.3 is the exact broadband sensitivity factor (eq. (10.3)) for incident waves at 45 deg. It is recognized in Fig. 10.3 that significant directivity behavior of the transducer exists at certain frequencies. As an example, near the frequency at which $\lambda = l$, the transverse sensitivity, S_2 is large, where as the longitudinal sensitivity, S_1 is near zero due to wavelength tuning effects discussed in chapter 3. In addition, at frequencies lower than the corresponding frequency of $\lambda = l$, it is observed that the broadband sensitivity factor due to incident waves at 45 deg. is equal to $\frac{1}{2}(|S_1| + |S_2|)$. This directivity behavior, which is a consequence of the rectangular transducer geometry, enables the proposed MFC rosette approach to work.

In practice, the measured response magnitude is best captured over a small frequency band as opposed to a single frequency. The total response quantity between the frequency range of $\Delta\omega = \omega_2 - \omega_1$ can be expressed as:

$$\widetilde{U} = \sum_{\omega_1}^{\omega_2} \frac{\left[S_1(\omega)\overline{\varepsilon}_{11}(\omega) + S_2(\omega)\overline{\varepsilon}_{22}(\omega) \right]}{n_F} = \widetilde{S_1\overline{\varepsilon}_{11}} + \widetilde{S_2\overline{\varepsilon}_{22}} \tag{10.7}$$

where n_F is the number of discrete frequency responses captured within the summation. If the response is measured over a small frequency range, the in-plane strain magnitudes $\bar{\varepsilon}_{11}$ and $\bar{\varepsilon}_{22}$ are assumed to be constant within that range. Therefore, eq. (10.7) becomes:

$$\widetilde{U} = \widetilde{S}_1 \bar{\varepsilon}_{11} + \widetilde{S}_2 \bar{\varepsilon}_{22} \tag{10.8}$$

Where $\widetilde{S}_1$ and $\widetilde{S}_2$ represent the summation of each respective sensitivity factor magnitude in the frequency range $\Delta\omega$ and divided by n.
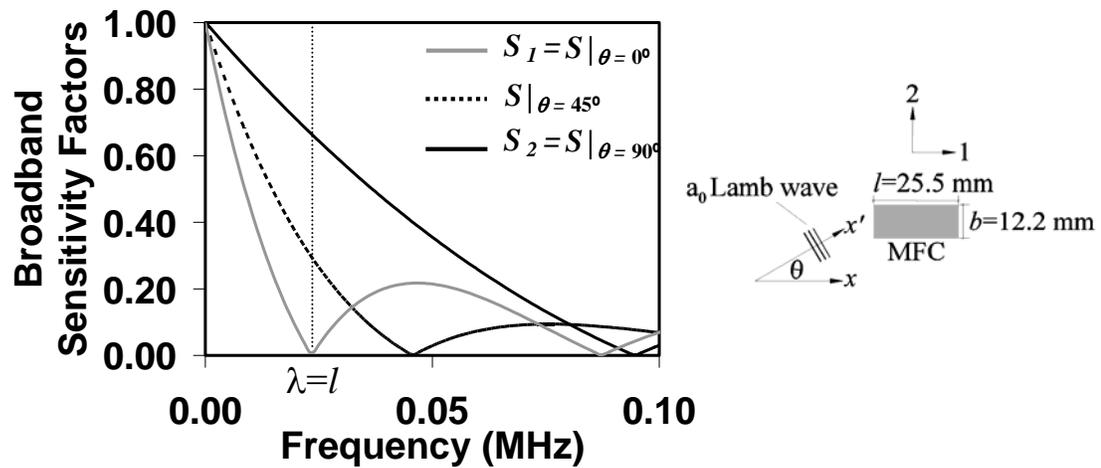
Fig. 10.3. Longitudinal, transverse and 45 deg. incident broadband sensitivity factors for a 12.2mm × 25.5mm MFC sensor bonded to aluminum plate.

10.3 Damage/Impact Detection and Location Theory for Piezoelectric Rosettes

10.3.1 Concept of Piezoelectric Rosettes

From eq. (10.8), it was observed that the total response magnitude of a rectangular transducer to oblique incident waves can be characterized by the product of the two orthogonal in-plane strains ($\bar{\varepsilon}_{11}, \bar{\varepsilon}_{22}$) and the primary and secondary sensitivities (S_1, S_2), respectively. In addition, due to the MFC transducer's rectangular geometry, the response magnitude can be isolated at specific frequencies such that it exhibits significant directivity

behavior. Both of these response characteristics present the capability to evaluate the principal strains existing within a 2 dimensional system when subjected to propagating stress waves such as acoustic emissions. This was achieved by employing rectangular transducers in a rosette configuration as shown in Fig. 10.4(a). After the principal strain magnitudes are computed, the principal strain angle can be evaluated. With two such angles, their intersection denotes the source location of the active damage or impact. This concept is illustrated in Fig. 10.4(b). Compared to conventional time-of-flight based methods, this source location technique does not require the knowledge of wave speed in the medium and it is easily applicable to anisotropic structures and/or structures possessing complex geometries.
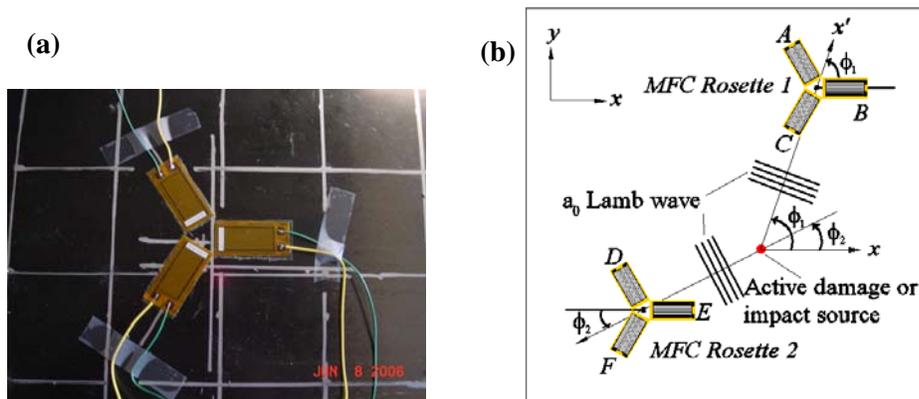
Fig. 10.4. (a) MFC Rosette attached to composite specimen. (b) Concept of MFC rosette approach for damage localization.

10.3.2 Evaluation of Principal Strains

Let us consider three rectangular MFC transducers A, B and C arranged in an arbitrary rosette configuration and subjected to a plane a_0 wave field as shown in Fig. 10.4(b). The longitudinal axes of the transducers A, B, and C are rotated at angles of β_A, β_B, and β_C from the global coordinate axis x. The principal angle ϕ of the ultrasonic wave is measured from

the global axis x and the line intersecting the centroid of the rosette (Fig. 10.4(b)). The responses of transducers A, B, and C are defined as:

$$\widetilde{U}^A = \widetilde{S}_1^A \overline{\varepsilon}_{11}^A + \widetilde{S}_2^A \overline{\varepsilon}_{22}^A$$
$$\widetilde{U}^B = \widetilde{S}_1^B \overline{\varepsilon}_{11}^B + \widetilde{S}_2^B \overline{\varepsilon}_{22}^B \qquad (10.9)$$
$$\widetilde{U}^C = \widetilde{S}_1^C \overline{\varepsilon}_{11}^C + \widetilde{S}_2^C \overline{\varepsilon}_{22}^C$$

By dividing eq. (10.9) by the sensor's longitudinal sensitivity factor we obtain:

$$\frac{\widetilde{U}^A}{\widetilde{S}_1^A} = \overline{\varepsilon}_{11}^A + K_T^A \overline{\varepsilon}_{22}^A$$

$$\frac{\widetilde{U}^B}{\widetilde{S}_1^B} = \overline{\varepsilon}_{11}^B + K_T^B \overline{\varepsilon}_{22}^B \qquad (10.10)$$

$$\frac{\widetilde{U}^C}{\widetilde{S}_1^C} = \overline{\varepsilon}_{11}^C + K_T^C \overline{\varepsilon}_{22}^C$$

where K_T is the transverse sensitivity ratio analytically defined as:

$$K_T = \frac{\widetilde{S}_2}{\widetilde{S}_1} = \left(\frac{l}{b}\right) \sum_{\omega_1}^{\omega_2} \frac{\sin\left(kb/2\right)}{\sin\left(kl/2\right)} \qquad (10.11)$$

The transverse sensitivity ratio is frequency dependant and can be quantified theoretically according to eqs. (10.5) and (10.11) or experimentally measured. It is important to note that the BSF's must be equivalent between transducers. However, eq. (10.3) does not consider the effect of bonding conditions, which will undoubtedly influence the transducer sensitivity. As a result, the quantities on the l.h.s. of eq. (10.10) will be affected by the variability in bonding conditions between transducers within the rosette. To correct for this variability, the total measured response in eq. (10.10) can be normalized by an experimentally derived BSF of each transducer.

Let us consider a transducer with its longitudinal and transverse axes rotated at an angle of β and $\beta + 90^\circ$ from the global axis x, respectively, as shown in Fig. 10.5. The strain

along any arbitrary rotation angle of a sensor, β can be expressed in terms of the global strains

by the following expression:

$$\overline{\varepsilon}_\beta = \overline{\varepsilon}_{xx} \cos^2 \beta + \overline{\varepsilon}_{yy} \sin^2 \beta + \overline{\gamma}_{xy} \sin \beta \cos \beta \qquad (10.12)$$

Therefore the response of the ith sensor can be re-written as:

$$\frac{\widetilde{U}^i}{\widetilde{S}_1^i} = \overline{\varepsilon}_{xx} \cos^2 \beta_i + \overline{\varepsilon}_y \sin^2 \beta_i + \overline{\gamma}_{xy} \sin \beta_i \cos \beta_i$$

$$+ K_T^i \left[\overline{\varepsilon}_{xx} \sin^2 \beta_i + \overline{\varepsilon}_{yy} \cos^2 \beta_i + \overline{\gamma}_{xy} \cos \beta_i \cos(\beta_i + 90) \right] \qquad (10.13)$$
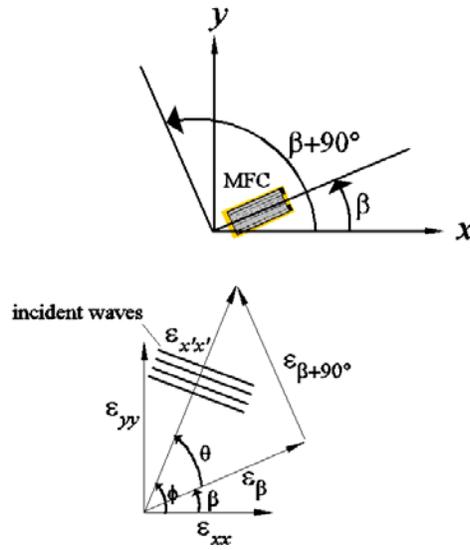
Fig. 10.5. Rotated sensor and strain transformation along its principal axes.

Defining the local strains in eq. (10.10) in terms of the global normal and shear strains yields a

linear system of equations:

$$\begin{bmatrix} \dfrac{\widetilde{U}^A}{\widetilde{S}_1^A} \\[2mm] \dfrac{\widetilde{U}^B}{\widetilde{S}_1^B} \\[2mm] \dfrac{\widetilde{U}^C}{\widetilde{S}_1^C} \end{bmatrix} = \left[\hat{T} \right] \begin{bmatrix} \overline{\varepsilon}_{xx} \\ \overline{\varepsilon}_{yy} \\ \overline{\gamma}_{xy} \end{bmatrix} \qquad (10.14)$$

where $\left[\hat{T}\right]$ is defined as:

$$
\left[\hat{T}\right]
$$
$$
= \begin{bmatrix} \cos^2 \beta_A + K_T^A \sin^2 \beta_A & \sin^2 \beta_A + K_T^A \cos^2 \beta_A & \cos \beta_A \left(\sin \beta_A + K_T^A \cos(\beta_A + 90) \right) \\ \cos^2 \beta_B + K_T^B \sin^2 \beta_B & \sin^2 \beta_B + K_T^B \cos^2 \beta_B & \cos \beta_B \left(\sin \beta_B + K_T^B \cos(\beta_B + 90) \right) \\ \cos^2 \beta_C + K_T^C \sin^2 \beta_C & \sin^2 \beta_C + K_T^C \cos^2 \beta_C & \cos \beta_C \left(\sin \beta_C + K_T^C \cos(\beta_C + 90) \right) \end{bmatrix} \quad (10.15)
$$

The global normal and shear strains can therefore be easily resolved from eq. (10.14) by inverting $\left[\hat{T}\right]$ and multiplying this by the measured response vector.

10.3.3 Evaluation of Principal Angle

The principal angle, ϕ, defining the wave propagation direction and measured from the global axis x to the line intersecting the centroid of a rosette (Fig. 10.4), can be computed from the following known relation:

$$
\tan 2\phi = \frac{\overline{\gamma}_{xy}}{\overline{\varepsilon}_{xx} - \overline{\varepsilon}_{yy}} = \frac{Num}{Den} \quad (10.16)
$$

As commonly done for electrical resistance strain gages, the ±90 deg. uncertainty affecting the angle ϕ due to the arctan function can be resolved based on the signs of the numerator (*Num*) and the denominator (*Den*) in eq. (10.16). Thus:

If *Num* > 0, $0° < \phi < 90°$;
If *Num* < 0, $-90° < \phi < 0°$;
If *Num* = 0 and
$\quad\quad$ *Den* > 0, $\phi = 0°$;
$\quad\quad$ *Den* < 0, $\phi = \pm90°$;
$\quad\quad$ *Den* = 0, ϕ is indeterminate.

10.3.4 Evaluation of Wave Source Location

Evaluation of the source location in a plane is readily achieved by the intersection of the principal directions determined by two rosettes. The principal angles calculated from the two rosettes through eq. (10.16), ϕ_1 and ϕ_2, define the equations of the straight lines connecting the wave source to each of the rosette centroids according to:

$$y_{SOURCE} = (x_{SOURCE} - x_1)\tan\phi_1 + y_1$$
$$y_{SOURCE} = (x_{SOURCE} - x_2)\tan\phi_2 + y_2$$

(10.17)

where (x_{SOURCE}, y_{SOURCE}) represent the coordinates of the wave source in the (x, y) cartesian system, and (x_1, y_1), (x_2, y_2) represent the coordinates of the centroids of the two rosettes, respectively. The linear system of equations can then be solved for the coordinates of the wave source as follows:

$$x_{SOURCE} = \frac{y_2 - y_1 + x_1 \tan\phi_1 - x_2 \tan\phi_2}{\tan\phi_1 - \tan\phi_2}$$
$$y_{SOURCE} = (x_{SOURCE} - x_1)\tan\phi_1 + y_1$$

(10.18)

10.4 Validation of MFC Rosette Method for Damage/Impact Detection and Location

10.4.1 Test Specimen and Experimental Procedure

Three test specimens were employed for the validation tests. The specimens, shown in Figs. 10.6(a-c), consisted of a 1.22m × 1.22m × 1.59 mm aluminum plate, .33m × .33m × 1.55mm $[0/\pm45]_{2s}$ CFRP plate, and .33m × .81m × 5.20mm curved $[0/\pm45/0_2/\mp45/0/honeycomb/0/\pm45/0_2/\mp45/0]$ CFRP sandwich panel. The latter specimen is a scaled representation of a honeycomb sandwich CFRP wing skin, similar to that studied in Chapter 9, but with a different lay-up. Two MFC rosettes with dimension l= 25.5 mm and b= 12.2 mm were surface bonded to each specimen.

Measurements were taken using a National Instruments data acquisition unit running under Labview software. The programs were developed according to the derived piezoelectric rosette theory in order to perform real-time damage/impact detection and location. A screen shot of the Labview program developed is shown in Fig. 10.6(d). Active damage was simulated by performing pencil lead breaks (Hsu-Neilsen source) at systematic grid locations over the majority of each specimen area. This out-of-plane excitation initiated a predominant zero order flexural wave and is similar in nature to delamination and impact sources [49]. A 5" (127 mm) and 2" (50.8 mm) test grid spacing was adopted for the aluminum and composite specimens respectively. For each transducer, the relative response magnitude was simultaneously quantified by measuring the signal energy within a narrow frequency band. For reasons previously discussed, this frequency band was selected such that significant directivity behavior existed in the MFC response while ensuring that the corresponding wavelengths were greater than or equal to the transducer length. Five lead breaks were conducted at each location in order to draw statistically significant conclusions.
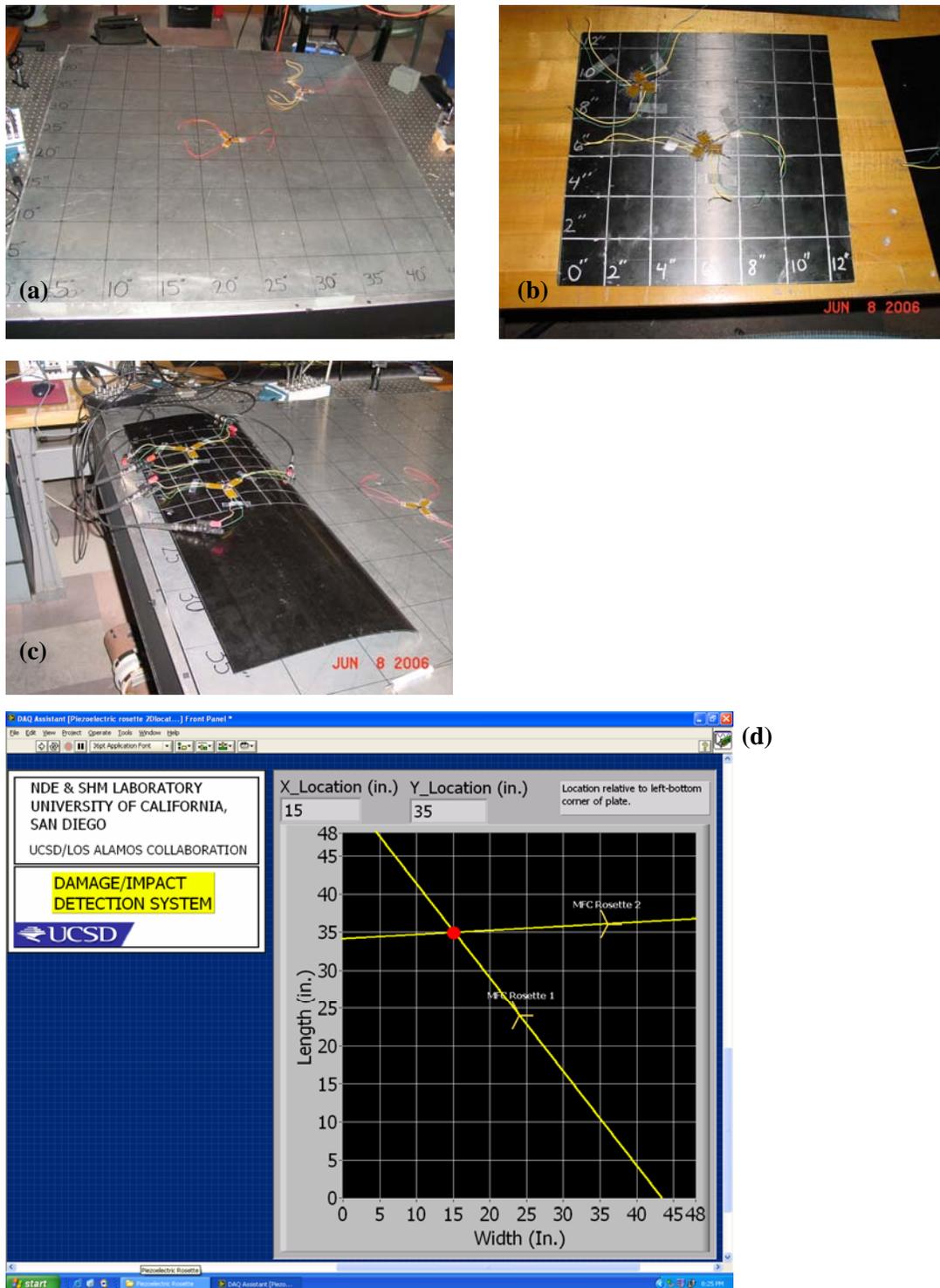
Fig. 10.6. Test specimen with attached MFC rosettes. (a) aluminum plate, (b) $[0/\pm45]_{2s}$ CFRP plate, and (c) $[0/\pm45/0_2/\mp45/0/honeycomb/0/\pm45/0_2/\mp45/0]$ representative wing skin. (d) Damage/impact detection Labview program based upon piezoelectric rosette theory.

10.4.2 Simulated Damage/Impact Location Results

The results of the location tests are shown in Figs. 10.7(a-c). The mean evaluated location for the five lead breaks is represented on each figure by an X, and the actual simulated damage location is shown as an open circle. An interconnecting line between the actual and predicted location is also shown for clarity. Note that the scales are different between Figs. 10.7(a) and 10.7(b-c).
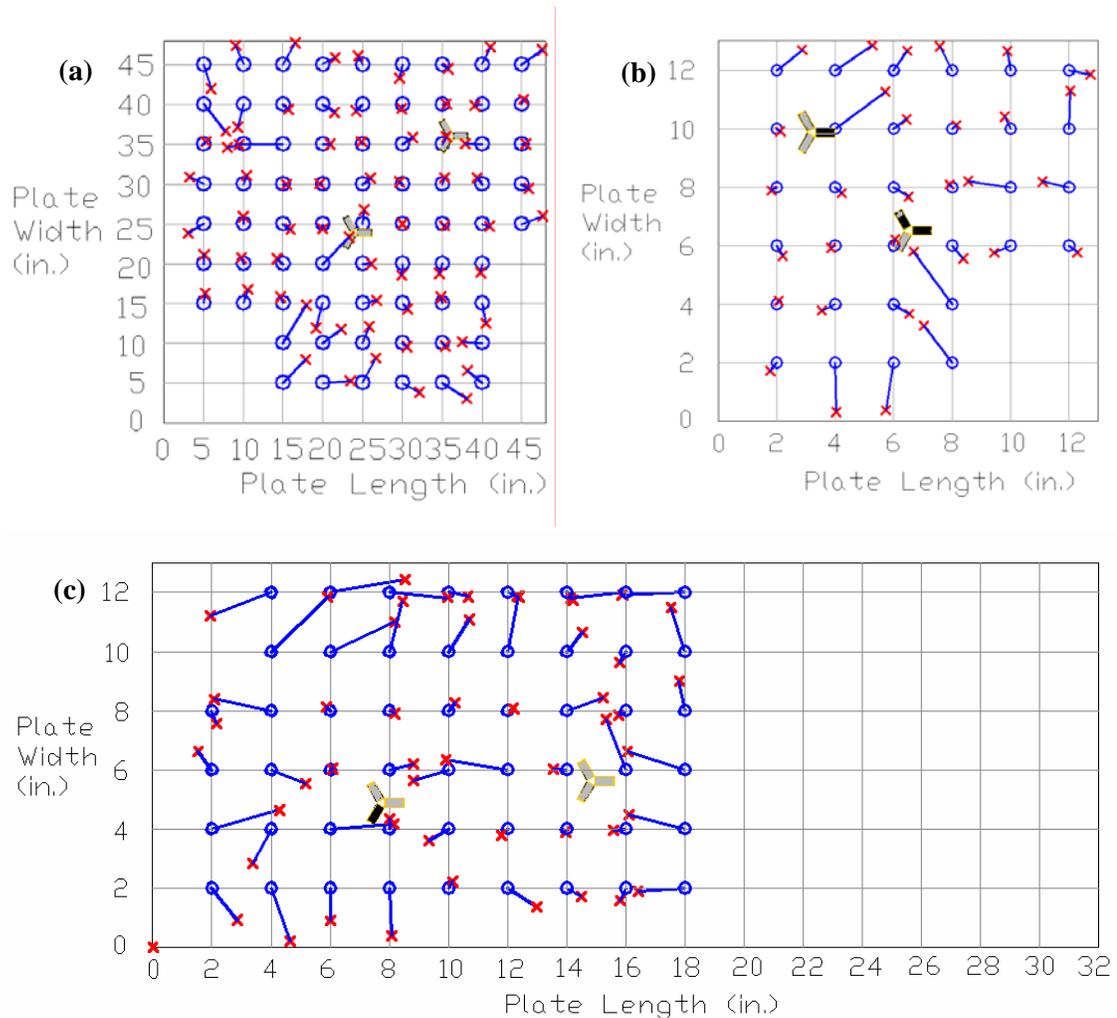
Fig. 10.7. Simulated damage/impact location results for (a) aluminum plate, (b) $[0/\pm45]_{2s}$ CFRP plate, and (c) $[0/\pm 45/0_2/\mp 45/0/honeycomb/0/\pm 45/0_2/\mp 45/0]$ representative wing skin.

The test results are summarized in tables 10.1 through 10.3 for the aluminum plate, CFRP plate and CFRP sandwich skin. The Cartesian coordinates x and y run parallel to the length and width of each specimen, respectively. For the aluminum plate, the maximum and minimum standard deviations of the location results were x_{stdev}=7.9 mm, y_{stdev}=200.1 mm and x_{stdev}=0.5 mm, y_{stdev}=1.8 mm observed at (x=381 mm (15"), y=127 mm (5")) and (x=889 mm (35"), y=762 mm (30")) respectively. The maximum mean error was observed at (x=381 mm (15"), y=254 mm (10")) with an error of x_{delta}=76.2 mm, y_{delta}=121.9 mm. Tests conducted on the $[0/\pm45]_{2s}$ CFRP plate resulted in maximum and minimum standard deviations of x_{stdev}=20.3 mm, y_{stdev}=27.9 mm and x_{stdev}=1.3 mm, y_{stdev}=0.7 mm observed at (x=304.8 mm (12"), y=254 mm (10")) and (x=101.6 mm (4"), y=152.4 mm (6")), respectively. The maximum mean error was found to be x_{delta}=38.1 mm, y_{delta}=48.3 mm at location (x=203.2 mm (8"), y=101.6 mm (4")). The maximum and minimum standard deviations resulting from tests on the representative wing skin were x_{stdev}=78.7 mm, y_{stdev}=200.7 mm and x_{stdev}=0.5 mm, y_{stdev}=1.8 mm observed at (x=381 mm (15"), y=127 mm (5")) and (x=889 mm (35"), y=762 mm (30"), respectively. The maximum mean error was observed at location (x=381 mm (15"), y=254 mm (10")) with an error of x_{delta}=76.2 mm, y_{delta}=121.9 mm.

For all specimens, significant errors are generally observed in the regions around the line connecting the two rosette positions. In these "shadow" regions, the two principal directions are close to parallel and the determination of their intersection point is inevitably unstable. This problem could be corrected by the use of a third rosette providing a redundant location node. Other regions with significant errors are seen at the edges of the specimens due to end reflections or attenuation losses. Careful design of the time gate used to isolate the first flexural arrival would be required in practice if edge regions are to be covered. As in

traditional damage/impact location, attenuation losses will remain a problem, particularly for waves generated far from the rosette detection point in highly-damped materials. In this case, a denser array of rosette nodes will be required.

Table 10.1. Results of simulated damage/impact location tests on aluminum plate

x_{stdev} max. (mm)	y_{stdev} max. (mm)	x_{stdev} min. (mm)	y_{stdev} min. (mm)	x_{delta} max (mm)	x_{delta} max (mm)
7.9	200.1	0.5	1.8	76.2	121.9
stdev max. x loc. (mm)	stdev max. y loc. (mm)	stdev min. x loc.(mm)	stdev min. y loc.(mm)	delta max. x loc. (mm)	delta max. y loc. (mm)
381.0	127.0	889.0	762.0	381.0	254.0

Table 10.2. Results of simulated damage/impact location tests on CFRP plate

x_{stdev} max. (mm)	y_{stdev} max. (mm)	x_{stdev} min. (mm)	y_{stdev} min. (mm)	x_{delta} max (mm)	x_{delta} max (mm)
20.3	27.9	1.3	0.7	38.1	48.3
stdev max. x loc. (mm)	stdev max. y loc. (mm)	stdev min. x loc.(mm)	stdev min. y loc.(mm)	delta max. x loc. (mm)	delta max. y loc. (mm)
304.8	254.0	101.6	152.4	203.2	101.6

Table 10.3. Results of simulated damage/impact location tests on CFRP sandwich skin

x_{stdev} max. (mm)	y_{stdev} max. (mm)	x_{stdev} min. (mm)	y_{stdev} min. (mm)	x_{delta} max (mm)	x_{delta} max (mm)
78.7	200.7	0.5	1.8	76.2	121.9
stdev max. x loc. (mm)	stdev max. y loc. (mm)	stdev min. x loc.(mm)	stdev min. y loc.(mm)	delta max. x loc. (mm)	delta max. y loc. (mm)
381.0	127.0	889.0	762.0	381.0	254.0

10.5   Conclusions

This chapter proposed a new method for detection and location of both "active" damage and impacts based upon the use of piezoelectric transducer rosettes. With this technique, common complications associated with the measurement and storage of baseline features or training data, complex modeling, and dense sensor arrays are alleviated. In

addition, because the rosette concept is not based on time-of-flight information, it does not require knowledge of the wave speed, thereby eliminating the need for optimization routines to determine damage location in highly anisotropic or geometrically-complex structures.

It was initially shown that the MFC response to broadband sources can be decomposed according to the longitudinal and transverse sensitivities and the two in-plane strain magnitudes. Therefore, by arranging the MFC transducers in a rosette configuration and isolating the response at selected frequencies, the principal directions of strain resulting from propagating stress waves can be computed. By employing two MFC rosettes, the source location of these waves can be readily evaluated using known strain transformation equations.

The experimental results demonstrate that the piezoelectric rosette technique is quite accurate in predicting the simulated damage location even in the highly anisotropic, non-prismatic sandwich structures with significant curvature. The coverage area for two rosettes was found to be at least 1.5 m^2 and .3 m^2 for the aluminum and the CFRP composite specimens, respectively. Although no formal results are discussed here, the MFC rosette technique was able to accurately detect and locate low velocity impacts resulting from dropped objects of varying shape and mass.

10.6 Acknowledgement

Chapter 11

Conclusions and Recommendations for Future Studies

11.1   Conclusions

Interest is shifting toward the implementation of a condition based monitoring methodology for aircraft structures. In this methodology, maintenance is only performed when the system has undergone damage beyond a tolerable level. Routinely scheduled inspection would be replaced by the integration of a built-in Structural Health Monitoring (SHM) system that can perform continuous on-line diagnostics. Ideally, a properly designed SHM system will increase the operational availability, extend the lifespan of the aircraft, enhance life-safety and dramatically reduce life-cycle costs. This thesis investigates a local SHM approach, based upon ultrasonic guided wave measurements, in order to perform damage identification of critical components of CFRP composite aircraft wings, mainly the wing skin-to-spar joints.

Guided wave transduction was achieved using piezoelectric Macro Fiber Composite (MFC) transducers which are ideal for on-board applications due to their robust, unobtrusive, and geometrically flexible characteristics. In an extension to previous studies, this work examined the fundamental response of surface-mounted, piezoceramic (PZT) and piezocomposite (MFC type P1 and type P2) sensors subjected to oblique incident harmonic, broadband and narrowband wave fields, as well as piezo-actuated tonebursts. The problem was studied by coupling the essential behavior of the sensor as a strain integrator to the strain field associated to the particular excitation. The models developed are useful for predicting the response characteristics of the sensor over a given frequency range to arbitrary wave fields

in both isotropic and anisotropic plate systems. The theoretical models were validated through simple experimental tests.

The ultrasonic guided wave approach for structural diagnostics was demonstrated by the dual application of active and passive monitoring techniques. For active interrogation, the wave propagation problem was studied numerically by a Semi-Analytical Finite Element (SAFE) method. The SAFE models were used to evaluate dispersion solutions as well as to identify certain mode-frequency combinations sensitive to disbonding and a loss of adhesive stiffness within the joint. Results from the SAFE analyses indicated that for modes preferentially excited by surface-mounted piezoelectric transducers, the strength of transmission across the joint can be used as a damage indicator. To maximize the sensitivity of this wave feature, frequencies corresponding to mode-coupling points were found desirable.

This work also extended active ultrasonic guided wave methods to the specific case of composite-to-composite bonded joints. Guided wave tests were conducted at ambient temperature across three simulated wing skin-to-spar joints using attached MFC transducers. For each specimen studied, careful wave-feature extraction, based upon the Discrete Wavelet Transform (DWT), allowed for successful discrimination between pristine and damaged joint conditions even for signals with large noise contamination. Consistent with the SAFE results, the general conclusions of these tests were an increased strength of transmission of the waves in the presence of bond defects and a large sensitivity at mode coupling points.

As opposed to global-vibration based methods, boundary condition changes and ambient excitation of the structure are less detrimental to ultrasonic guided wave SHM. However, temperature variation will undoubtedly lead to significant changes in the guided wave features used for damage detection. Very few published papers discuss the effects of temperature upon guided wave signals acquired by piezoelectric transducers. In this work, the

various characteristics of guided waveforms that change as a function of temperature were identified. Each signal feature change is associated to the influence of temperature on the mechanical, electrical and thermal properties of each layer comprising the transducer-structure system. Theoretical and experimental analyses were performed to validate the identified effects of temperature on the guided wave measurements considering a range consistent with grounded and operational conditions of an aircraft (-40 deg. C to 60 deg. C or -40 deg. F to 140 deg. F). These analyses led to the conclusion that temperature deviation primarily results in a scaling of the sensor response magnitude, mainly due to changes in the piezoelectric charge and dielectric permittivity coefficients of the PZT material, as well as a slight shift in the frequency response due to changes in the elastic properties of the host structure.

To study the effectiveness of guided wave damage detection in a changing temperature environment, a multivariate statistical analysis was employed. The objective of this study was to discriminate the bond defects considered in the simulated wing skin-to-spar joints from the temperature variation in the range -40 deg. C to 60 deg. C. A critical step in the statistical analysis was the selection of as few as eight features related to the strength of transmission of the wave through the joint. While the number of features was kept low to alleviate computational efforts, this number was large enough to ensure a satisfactory discriminatory power of the multivariate deviation statistics. Experimental tests conducted in an environmental chamber confirmed that all of the bond defects examined could be detected, despite the temperature changes, once only two baseline (undamaged) data distributions were considered. These two baseline distributions were established from undamaged measurements taken below ambient temperature (-40 deg. C to 20 deg. C) and above ambient temperature (20 deg. C to 60 deg. C).

Based upon the derived sensor response characteristics, this thesis also proposed a novel method for passive-only damage/impact detection and location by utilizing piezoelectric transducers, specifically MFCs, arranged in a rosette configuration. This technique can be used for detecting and localizing both existing damage (through measurements of diffracted waves) and "active" damage or impacts (through measurements of acoustic emissions). Compared to conventional time-of-flight based damage location in acoustic emission methods, the proposed piezoelectric rosette technique does not require knowledge of the wave speed and it is thus applicable to anisotropic or geometrically-complex structures. In addition, relative to model or artificial intelligence-based damage/impact location in other wave-based methods, the piezoelectric rosette technique does not require large sets of training data or accurate modeling of the wave propagation properties of the structure.

The piezoelectric rosette technique was demonstrated for the detection and location of simulated "active" damage or impact on multiple specimens, including an aluminum plate, a CFRP plate and a honeycomb sandwich representative wing skin. The accuracy of the technique was found to be quite high for all three specimens; however the coverage area for the honeycomb sandwich specimen was limited due to the high wave attenuation.

11.2 Applicability to Full-Scale Aircraft Structures and Recommendations for Future Studies

The use of ultrasonic guided waves for the performance of SHM of CFRP composite components shows considerable promise. However, additional research is necessary in order to make the transition from the laboratory to within a full-scale, operational aircraft.

Specific to the research considered within thesis, the theoretical models and experimental analyses could be extended to more accurately characterize realistic systems and the true physical parameters governing the system behavior. The analytical models used to

predict the piezoelectric transducer response behavior could be enhanced by considering closed form solutions to the amplitude spectrum of the surface strain induced by transient sources. SAFE analyses used to ascertain information on the guided wave behavior should also be extended to harmonic and transient forced excitation as well as to models representative of the entire honeycomb sandwich system. The SAFE and experimental results presented within this thesis are strictly applicable to the specific joints examined. However, the general conclusions of an increased strength of transmission in the presence of bond defects and a large sensitivity at mode coupling points can be extended to other geometries or materials. For systems which do not exhibit mode-coupling frequencies in the hundreds of kilohertz range, the probing frequency should be chosen according to guided wave parameters such as wavelength and attenuation. Higher frequencies provide increased sensitivity to small damage while, at the same time, reducing the SNR of the measurements due to attenuation (damping) losses. Therefore, a compromise must be found between defect detectability and monitoring range requirements. This issue is particularly relevant for applications in honeycomb sandwich structures which cause high levels of wave attenuation as a result of the interlayer wave leakage into the honeycomb core.

Signal processing is an important component of the damage identification process. In particular, the DWT algorithm may prove essential for built-in SHM systems due to its de-noising and data compression capabilities. Aero-elastic and aero-acoustic excitations will have a predominant role in the vibration response of an aircraft wing. However, these sources of excitation are expected to occur at frequencies lower than the guided wave bond probing frequency above 100 kHz, and it should thus be possible to filter them out by the DWT de-noising algorithm. In addition, the de-noising capability of the DWT is highly applicable to future wave-based health monitoring systems because they will require small excitation

powers to the actuators and large actuator-sensor distances for increased coverage. The DWT was also shown to be useful during the feature extraction process. The damage sensitive feature based upon energy transmission can be extracted from a very small number of DWT coefficients of the raw ultrasonic signals, without compromising processing speed. This level of data compression would be vital in an on-board monitoring system given the stringent requirements for data transmission (e.g. wireless) and storage.

Although the guided wave-based damage detection approach proved successful in the laboratory, its effectiveness for online bond monitoring still remains to be demonstrated. The effect of temperature on the damage detection reliability is a primary issue which must be addressed. The field application of a guided wave based SHM system will require a robust statistical pattern process which is capable of discriminating between changes due to temperature and that due to damage. Through intelligent feature extraction and the use of a multivariate statistical outlier approach, reliable damage detection was shown to be possible in the laboratory for simulated components subjected to typical grounded and or operational temperatures of an aircraft. Additional research is still needed to demonstrate this approach on a realistic CFRP wing structure.

The joint damage considered within this research was simulated and introduced prior to the establishment of baseline (undamaged) conditions. Therefore, the active damage identification was done such that baseline measurements and damaged measurements were acquired over different locations along the wing skin-to-spar joint. To better validate the proposed method of active damage detection, further experimental tests should be conducted upon specimens prior to and after the introduction of realistic damage sources, e.g. overloaded structural conditions.

The effects of temperature on the amplitude based features extracted from guided waves were found to be mainly a result of changes in the electro-mechanical behavior of the transducers and less the result of thermal effects within the host structure. These conclusions were drawn for an isotropic plate. Thus, further research is needed to examine any disparity when considering the thermal effects on piezoelectric transducers bonded to a composite structure.

The proposed piezoelectric rosette approach for damage/impact detection and location could be improved. For the validation tests presented in this thesis, the dimensions of the transducer were restricted. However, the customization of the MFC rosette dimensions and the introduction of additional rosettes are expected to yield even higher accuracy in the damage localization, particularly for highly-attenuative structures. In addition, by exploiting the wavelength-tuning behavior, the customization of the MFC dimensions would allow for the isolation of certain frequency ranges known to be excited by specific damage sources. Therefore, the system could target particular types of damage. Only passive applications of this piezoelectric rosette method were demonstrated. Yet, through the addition of a separate actuation source, this approach could conceptually be extended to actively locate existing damage based upon the measurement of diffracted signals.

Bibliography

[1]   Staszewski, W., Boller C., and G. Tomlinson. (2004). Health monitoring of aerospace structures. *John Wiley & Sons*, West Sussex, England.

[2]   Hall S.R. and T.J. Conquest. (1999). "The total data initiative-structural health monitoring, the next generation," *Proc. of the USAF ASIP*, 2nd *ed*.

[3]   Sohn H., Farrar C.R., Hemez F.M., Shunk D.D., Stinemates D.W. and B.R. Nadler. (2003). "A review of structural health monitoring literature: 1996-2001," *Technical Report LA-3976-MS*, Los Alamos National Laboratory, Los Alamos, NM.

[4]   Worden K. and J.M. Dulieu-Barton. (2005). "An overview of intelligent fault detection in systems and structures," *Struct. Health Mon*. **3**(1), pp. 85-98.

[5]   Zapico, J., Worden, K., and F. Molina. (2001). "Vibration-based damage assessment in steel frames using neural networks," *Smart Mater. Struct.* **10**, pp. 553-559.

[6]   McNamara, J., Lanza di Scalea, F. and M. Fateh. (2004). "Automatic defect classification in long-range ultrasonic rail inspection using a support vector machine-based smart system," *Insight* **46**, pp. 331-337.

[7]   Worden, K., Sohn, H. and C.R. Farrar. (2002). "Novelty Detection in a Changing Environment: Regression and Interpolation Approaches," *J. Sound Vibr.*, **258**(4), pp. 741-761.

[8]   Manson, G., Pierce, G., Worden, K., Monnier, T., Guy, P. and K. Atherton. (2000). "Long-Term Stability of Normal Condition Data for Novelty Detection," *Proc. of 7th International Symposium on Smart Structures and Materials*, San Diego, CA.

[9]   Worden, K. (1997) "Structural fault detection using a novelty measure," *J. Sound Vibr.* **201**(1), pp. 85-101.

[10]   Worden K., Manson G. and N.R.J. Fieller. (2000). "Damage detection using outlier analysis," *J. Sound Vibr.* **229**(3), pp. 647-667.

[11]   Salawu O.S. (1997). "Detection of structural damage through changes in frequency: A review," *Engineering Structures* **19**(9), pp. 718-723.

[12]   Berger H., Chaquin J.P. and R. Ohayon. (1984). "Finite element model adjustment using experimental data," *Proc. 2nd International Modal Analysis Conference*, pp. 638-642.

[13]   West W.M. (1984). "Illustration of the use of madal assurance criterion to detect structural changes in an orbiter test specimen," *Proc. Air Force Conference on Aircraft Structural Integrity*, pp. 496-501.

[14] Doebling S.W., Farrar C.R., Prime M.B. and D.W. Shevitz. (1996). "Damage identification and health monitoring of structural and mechanical systems from changes in their vibration characteristics: A literature review*," Technical Report LA-13070-MS*, Los Alamos National Laboratory, Los Alamos, NM.

[15] Zhang H., Schulz M.J. and F. Feruson. (1999). "Structural health monitoring using transmittance functions," *Mechanical Systems and Signal Processing* **5**, pp. 765-787.

[16] Valdez S.H.D. and C. Soutis. (1999). "Delamination detection in composite laminates from variations of their modal characteristics," *J. Sound Vibr.* **1**, pp. 1-9.

[17] Park G., Sohn H., Farrar, C.R. and D.J. Inman. (2003). "Overview of piezoelectric impedance-based health monitoring and path forward," *The Shock and Vib. Dig. J.* **35**(6), pp. 451-463.

[18] Wang C.S. and F-K. Chang. (2000). "Diagnosis of impact damage in composite structures with built-in piezoelectrics network," *Proc. of SPIE* **3990**, pp. 13-19.

[19] Kessler S.S., Spearing S.M. and C. Soutis. (2002). "Damage detection in composite materials using Lamb wave methods," *Smart Mat. and Struc.* **11,** pp. 269-278.

[20] Maseras-Gutierrez M.A., Staszewski W.J., Found M.S. and K. Worden. (1998). "Detection of impacts in composite materials using piezoceramic sensors and neural networks," *Proc. of SPIE* **3329**, pp. 491-497.

[21] Mal A.K., Banerjee S. and F. Ricci. (2004). "Automated structural health monitoring system using acoustic emission and modal data," *Proc. of SPIE* **5394,** pp. 1-10.

[22] Richardson, M.O.W. and M.J. Wisheart. (1996). "Review of low-velocity velocity impact properties of composite materials," *Applied Science and Manufacturing*, **27A** (12), pp. 1123-1131.

[23] Lestari W. and P. Qiao. (2005). "Damage detection of fiber-reinforced polymer honeycomb sandwich beams," *Composite Structures* **67**, pp. 365-373.

[24] Monnier T. (2006). "Lamb waves-based impact damage monitoring of a stiffened aircraft panel using piezoelectric transducers," *J. of Intell. Mat. Sys. Struc.* **17**, pp. 411-421.

[25] Adams R.D. and B.W. Drinkwater. (1999). "Non-destructive testing of adhesively bonded joints," *Int. J. of Materials and Product Technology* **14**(5/6), pp. 385-398.

[26] Guyott C.C.H., Cawley P. and R.D. Adams. (1986). "The non-destructive testing of adhesively bonded structure: A review," *J. Adhesion* **20**, pp. 129-159.

[27] Rokhlin S. I. and Wang Y. J. (1991). "Analysis of boundary conditions for elastic wave interaction with an interface between two solids," *J. Acoust. Soc. Am.* **89**, 503-515.

[28]   Guyott C.C.H and P. Cawley. (1988a). "The ultrasonic vibration characteristics of adhesive joints," *J. Acoust. Soc. of Am.***83**, pp. 632-640.

[29]   Guyott C.C.H. and P. Cawley. (1988). "Evaluation of the cohesive properties of adhesive joints using ultrasonic spectroscopy," *NDT&E Int.* **21**, 233-240.

[30]   Chaudhry Z., Lalande F., Ganino A. and C. Rogers. (1996). "Monitoring the integrity of composite patch structural repair via piezoelectric actuators/sensors," *AIAA-1996-1074-CP*.

[31]   Koh Y.L., Rajic N., Chiu W.K. and S. Galea. (1999). "Smart structures for composite repair," *Composite Structures* **47**(1), pp. 745-752.

[32]   Xu Y.G. and G.R. Liu. (2002). "A modified electro-mechanical impedance model of piezoelectric actuator-sensors for debonding detection of composite repair patches," *J. of Intell. Mat. Sys. Struc.* **13**(6), pp. 389-405.

[33]   Raju V., Park G. and H. Cudney. (1998). "Impedance-based health monitoring technique of composite reinforced structures," *Proceedings of 9th International Conference on Adaptive Structures and Technologies*, Oct. 14-16, Cambridge, MA, pp. 448-457.

[34]   Pohl J., Herold S., Mook G. and F. Michel. (2001). "Damage detection in smart CFRP composites using impedance spectroscopy," *Smart Mater. Struct.* **10**, pp. 834-842.

[35]   Bois C. and C. Hochard. (2002). "Measurement and modeling for the monitoring of damaged laminate composite structures," *Proc. of 1st European Workshop on Structural Health Monitoring*, Cachan, France, pp. 425-432.

[36]   Matt H M, Bartoli I., and F. Lanza di Scalea. (2005). "Ultrasonic guided wave monitoring of composite wing skin-to-spar bonded joints in aerospace structures," *J. Acoust. Soc. of Am.* **118**, pp. 2240-2252.

[37]   Ogisu T., Shimanuki M., Yoneda H., Okabe Y., Takeda N. and T. Sakurai. (2006). "Damage growth detection of aircraft bonding structure under cyclic loading using FBG/PZT hybrid sensor system," *Proc. of 3rd European   Workshop   on Structural Health Monitoring*, Granada, Spain.

[38]   Qing X.P., Wu Z., Chang F-K., Ghosh K., Karbhari V. and C. Sikorsky. "Monitoring the disbond of externally bonded CFRP composite strips for rehabilitation of bridges," *Proc. of 3rd European Workshop on Structural Health Monitoring*, Granada, Spain.

[39]   Wang X., Foliente G., Su Z. and L. Ye. (2006). "Multilevel decision fusion in a distributed active sensor network for structural damage detection," *Struct. Health Mon.* **5**(1), pp. 45-58.

[40]   Lichtenwalner P.F. and D. Sofge. (1998). "A local area damage detection in composite structures using piezoelectric transducers," *Proc. of SPIE* **3326**, pp. 509-515.

[41]   Paget C.A., Grondel S., Levin K. and C. Delebarre. (2003). "Damage assessment in composites by Lamb waves and wavelet coefficients," *Smart Mat. Struc.* **12,** pp. 393-402.

[42]   Ip K-H and Y-W Mai. (2004). "Delamination detection in smart composite beams using Lamb waves," *Smart Mat. and Struc.* **13,** pp. 544-551.

[43]   Sohn H., Park G., Wait J., Limback N., and C.R. Farrar. (2003). "Wavelet-based active sensing for delamination detection in composite structures," *Smart Mater. Struct.* **13**, pp. 153-160.

[44]   Lanza di Scalea F., Matt H.M., Bartoli I., Coccia S, Park G., and C.R. Farrar. (2006). "Health monitoring of UAV wing skin-to-spar joints using guided waves and macro fiber composite transducers," *in print J. of Intell. Mat. Sys. Struc.*.

[45]   Valdes S.D. and C. Soutis. (2002). "Real-time nondestructive evaluation of fiber composite laminates using low-frequency Lamb waves," *J. Acoust. Soc. of Am.* **111**(5), pp. 226-2033.

[46]   Diamanti K., Hodgkinson J.M. and C. Soutis. (2004). "Detection of low-velocity impact damage in composite plates using Lamb waves," *Struct. Health Mon.* **3**(1), pp. 33-41.

[47]   Su Z. and L. Ye. (2004). "Fundamental Lamb mode-based delamination detection for CF/EP composite laminates using distributed piezoelectrics," *Struct. Health Mon.* **3**(1), pp. 43-68.

[48]   Yuan S., Lei W. and L. Shi. (2003). "Active monitoring for on-line damage detection in composite structures," *J. Sound Vibr.* **125**, pp. 178-186.

[49]   Gubbala, R. and V.S. Rao. (2003). "Health monitoring of adhesively bonded composite patch repair of aircraft structures using wavelet transforms of Lamb wave signals," *Proc. of SPIE* **5056**, pp. 33-40.

[50]   Farrar C.R., Park G., Hemez F.M, Tippetts T.B., Sohn H., Wait J., Allen D.W. and B.R. Nadler. (2004). "Damage detection and prediction for composite plates," *Proc. of Material Science and Technology(MST), Symp. on Materials Damage Prognosis*, New Orleans, LA.

[51]   Prasad S.M., Balasubramaniam K. and C.V. Krishnamurthy. (2004). "Structural health monitoring of composite structures using Lamb wave tomography," *Smart Mat. and Struc.* **13**, pp. 73-79.

[52] Lemistre M. and Balageas D. (2001). "Structural health monitoring system based on diffracted Lamb wave analysis by multiresolution processing," *Smart Mat. Struc.* **10**, pp. 504-511.

[53] Blaise E. and F-K. Chang. (2002). "Built-in damage detection system for sandwich structures under cryogenic temperatures," *Proc. of SPIE* **4701**, pp. 97-107.

[54] Sohn H., Park H., Law K.H. and C.R. Farrar. (2005). "Instantaneous online monitoring of unmanned aerial vehicles without baseline signals," *Proceedings of 23rd International Modal Analysis Conference*, Orlando, FL, Jan. 30th – Feb.3rd, pp. 105-114.

[55] Kim S.D., In C.W., Cronin, K.E., Sohn H. and K. Harris. (2006). "Application of outlier analysis for baseline-free damage diagnosis," *Proc. of SPIE* **6174**, pp. 13-19.

[56] Gupta N., Kamath G.M., Sundaram R. and M. Subba Rao. (2005). "Neural network based damage detection algorithm for structural health monitoring of aerospace composite structures," *Proc. of ISSS*, Bangalore, India, pp. 179-186.

[57] Jones R. and S. Galea. (2002). "Health monitoring of composite repairs and joints using optical fibers," *Composite Structures* **58**, pp. 397-403.

[58] Li H.C.H., Herszberg I. and A.P. Mouritz. (2006). "Automated characterization of structural disbonds by statistical examination of bond-line strain distribution," *Struct. Health Mon*. **5**(1), pp. 83-94.

[59] Hou L. and S.A. Hayes. (2002). "A resistance-based damage location sensor for carbon-fibre composites," *Smart Mat. and Struc.* **11**, pp. 966-969.

[60] Lemistre M.B. and D.L. Balageas. (2002). "Health monitoring system for composite material using electromagnetic field measurement," *Proc. of SPIE* **4702**, pp. 272-281.

[61] Kabeya K., Jiang Z. and H. Cudney. (1998). "Structural health monitoring by impedance and wave propagation measurements," *Proc. of International Motion and Vibration Control*, Aug. 25-28, Switzerland, pp. 207-212.

[62] Koh Y.L., Chiu W.K., Marshall I.H., Rajic N. and S.C. Galea. (2001). "Detection of disbonding in a repair patch by means of an array of lead zirconate titanate and polyvinylidene fluoride sensors and actuators," *Smart Mat. and Struc.* **10**, pp. 946-962.

[63] Lowe M.J.S. (1995). "Matrix techniques for modeling ultrasonic waves in multilayered media," *IEEE Transactions on Ultrasonics, Ferroelectrics, and Frequency Control* **42**, pp. 525-542.

[64] Aalami B. (1973). "Waves in prismatic guides of arbitrary cross section", *J. of Applied Mechanics* **40**, 1067-1072.

[65]   Nelson R.B., Dong S.B. and R.D. Kalra. (1971). "Vibrations and waves in laminated orthotropic circular cylinders," *J. Sound Vibr.* **18**, pp. 429-444.

[66]   Huang K.H. and S.B. Dong. (1984). "Propagating waves and edge vibrations in anisotropic composite cylinders," *J. Sound Vibr.* **96**, 363-379.

[67]   Taweel H., Dong S.G. and M. Kazic. "Wave reflection from the free end of a cylinder with an arbitrary cross-section," *Int. J. of Solids and Structures* **37**, pp. 1701-1726.

[68]   Hladky-Hennion A.C. (1996) "Finite element analysis of the propagation of acoustic waves   in waveguides," *J. Sound Vibr.* **194**, 119-136.

[69]   Gavrić L. (1995). "Computation of propagating waves in free rail using a finite element technique," *J. Sound Vibr.* **185**, 531-543.

[70]   Hayashi T., Song W.J. and J.L. Rose. (2003). "Guided wave dispersion curves for a bar with an arbitrary cross-section, a rod and rail example," *Ultrasonics* **41**, 175-183.

[71]   Wilcox P., Evans M., Diligent O., Lowe M.J.S. and P. Cawley. (2002). "Dispersion and excitability of guided acoustic waves in isotropic beams with arbitrary cross section," *Rev. of Progress in Quantitative NDE* **21**, 203-210.

[72]   Dong S.B. and K.H. Huang. (1985). "Edge vibrations in laminated composite plates," *J. of Applied Mechanics* **52**, 433-438.

[73]   Mukdadi O.M., Desai Y.M., Datta S.K., Shah A.H. and A.J. Niklasson. (2002). "Elastic guided waves in a layered plate with rectangular cross section," *J. Acoust. Soc. of Am.* **112**, 1766-1779.

[74]   Kohl T., Datta S.K. and A.H. Shah. (1992). "Axially symmetric pulse propagation in semi-infinite hollow cylinders," *AIAA J.* **30**, 1617-1624.

[75]   Han X.,. Liu G.R, Xi Z.C. and K.Y. Lam. (2002). "Characteristics of waves in a functionally graded cylinder," *Int. J. for numerical methods in engineering* **53**, 653-676.

[76]   Shorter P. J. (2004). "Wave propagation and damping in linear viscoelastic laminates," *J. Acoust. Soc. of Am.* **115**, 1917-1925.

[77]   Mal A.K. (1988). "Guided waves in layered solids with interface zones," *Int. J. Engr. Sci.* **26**, 873-881.

[78]   Nagy P.B., and L. Adler. (1989). "Nondestructive evaluation of adhesive joints by guided waves," *J. Appl. Phys.* **66**, pp. 4658-4663.

[79]   Mal A.K., Xu P., and Y. Bar-Cohen. (1990). "Leaky Lamb waves for the ultrasonic nondestructive evaluation of adhesive bonds," *ASME J. Eng. Mat. Tech.* **112**, pp. 255-259.

[80]   Xu P.C., Mal A.K., and Y. Bar-Cohen. (1990). "Inversion of leaky Lamb wave data to determine cohesive properties of bonds," *Int. J. Eng. Sci.* **28**, pp. 331-346.

[81]   Pilarski A. and J.L. Rose. (1992). "Lamb wave mode selection concepts for interfacial weakness analysis*," J. Nondestr. Eval.* **11**, pp. 237-249.

[82]   Lowe M.J.S. and P. Cawley. (1994). "Applicability of plate wave techniques for the inspection of adhesive and diffusion bonded joints," *J. Nondestr. Eval.* **13**, pp. 185-200.

[83]   Kundu T. and K. Maslov. (1997). "Material interface inspection by Lamb waves," *Int. J. Sol. Struct.* **34**, pp. 3885-3901.

[84]   Chimenti D.E. (1997). "Guided waves in plates and their use in materials characterization," *Appl. Mech. Rev.* **50**, pp. 247-284.

[85]   Kundu T., Maji A., Ghosh T., and K. Maslov. (1998). "Detection of kissing disbonds by Lamb waves," *Ultrasonics* **35**, pp. 573-580.

[86]   Rose J.L., Zhu W., and M. Zaidi. (1998). "Ultrasonic NDT of titanium diffusion bonding with guided waves," *Mat. Eval.* **56**, pp. 535-539.

[87]   Heller K., Jacobs L.J., and J. Qu. (2000). "Characterization of adhesive bond properties using Lamb waves," *NDT&E Int.* **33**, pp. 555-563.

[88]   Cheng A., Murray T.W., and J.D. Achenbach. (2001). "Simulation of laser-generated ultrasonic waves in layered plates," *J. Acoust. Soc. of Am.* **110,** pp. 848-855.

[89]   Seifried R., Jacobs L.J., and J. Qu. (2002). "Propagation of guided waves in adhesive bonded components," *NDT&E Int.* **35**, pp. 317-328.

[90]   Castaings M. and B. Hosten. (2003). "Guided waves propagating in sandwich structures made of anisotropic, viscoelastic, composite materials," *J. Acoust. Soc. of Am.* **113**, pp. 2622-2634.

[91]   Hay T.R., Wei L., and J.L. Rose. (2003). "Rapid inspection of composite skin-honeycomb core structures with ultrasonic guided waves," *J. Comp. Mat.* **37**, pp. 929-939.

[92]   Rokhlin S.I. (1991). "Lamb wave interaction with lap-shear adhesive joints: theory and experiment," *J. Acoust. Soc. of Am.* **89**, pp. 2758-2765.

[93]   Rose J.L., Rajana K.M., and M.K.T. Hansch. (1995). "Ultrasonic guided waves for NDE of adhesively bonded structures," *J. Adhesion* **50**, pp. 71-82.

[94]   Chang Z. and A.K. Mal. (1995). "A global-local method for wave propagation across a lap joint," *Num. Meth. Struct. Mech.* **204**, pp. 1-11.

[95]   Mal A.K., Chang Z., and D. Guo. (1996). "Lap joint inspection using plate waves," *Proc. SPIE* **2945**, pp. 128-137.

[96]   Lowe M.J.S., Challis R.E., and C.W. Chan. (2000). "The transmission of Lamb waves across adhesively bonded lap joints," *J. Acoust. Soc. of Am.* **107**, pp. 1333-1345.

[97]   Lanza di Scalea F., Bonomo M., and D. Tuzzeo. (2001). "Ultrasonic guided wave inspection of bonded lap joints: noncontact method and photoelastic visualization," *Res. Nondestr. Eval.* **13**, pp. 153-171.

[98]   Sun Z., Rose J.L., and M. Zaidi. (2002). "A phased array guided wave approach to adhesive bonding structural integrity analysis," *Mat. Eval.* **61**, pp. 941-946.

[99]   Lanza di Scalea F., Rizzo P., and A. Marzani. (2004). "Propagation of ultrasonic guided waves in lap-shear adhesive joints: case of incident a_0 Lamb wave," *J. Acoust. Soc. of Am.* **115**, pp. 146-156.

[100]   Lakshmanan K.A. and D.J. Pipes. (1997). "Modeling damage in composite rotocraft flexbeams using wave mechanics," *Smart Mater. Struct.* **6**, pp. 383-392.

[101]   Wang C.S. and F-K. Chang. (1999). "Built-in diagnostics for impact damage identification in composite structures," *Proc. 2nd Intl. Workshop on Structural Health Monitoring*, Stanford, pp. 612-621.

[102]   Ihn J., Chang F.K., and H. Speckmann (2001). "Built-in diagnostics for monitoring crack growth in aircraft structures," *Proc. 4th Intl. Conf. on Damage Assessment on Structures*, Cardiff, **204-205**, pp. 299-308.

[103]   Giurgiutiu V. and A. Zagrai. (2002). "Embedded self-sensing piezoelectric active sensors for on-line structural identification," *ASME J. Vib. Acoust.* **124,** pp. 116-125.

[104]   Giurgiutiu V., Bao J., and W. Zhao. (2003). "Piezoelectric wafer active sensor embedded ultrasonics in beams and plates," *Exp. Mech.* **43**, pp. 428-44.

[105]   Kim S.D., In C.W., Cronin K.E., Sohn H. and K. Harries. (2006). "Active sensing for disbond detection in CFRP strengthened RC beam," *Proc. of 3rd European Workshop on Structural Health Monitoring*, Granada, Spain.

[106]   Surace C. and K. Worden. (1998). "A novelty detection approach to diagnose damage in structures: an application to an offshore platform," *Proc. of the 8th ISOPE*, Canada, pp. 64-70.

[107]   Sohn H., Farrar C.R., Hunter N.F. and K. Worden. (2001). "Structural Health Monitoring Using Statistical Pattern Recognition Techniques," *J. of Dynamic Sys., Meas., and Control*, **123**, pp. 706-711.

[108]   Lee B.C., Manson G. and W.J. Staszewski. (2003). "Environmental effects on Lamb wave responses from piezoceramic sensors," *Materials Science Forum* **440-441**, pp. 195-202.

[109]   Michaels J.E. and T.E. Michaels. (2005). "Detection of structural damage from the local temporal coherence of diffuse ultrasonic signals," *IEEE Transactions on Ultrasonics, Ferroelectrics, and Frequency Control* **52**(10), pp. 1769-1782.

[110]   Konstantinidis G., Drinkwater B.W. and P.D. Wilcox. (2006). "The temperature stability of guided wave structural health monitoring systems," *Smart Mater. Struct.* **15**, pp. 967-976.

[111]   Wojcik G.L., Vaughan A.N., and J. Mould Jr. (1993). "Electromechanical modeling using explicit time-domain finite elements," *Proc. of IEEE Ultrasonics Symp.*, pp. 1107-1112.

[112]   Lichtenwalner P.F. and D. Sofge. (1998). "A local area damage detection in composite structures using piezoelectric transducers," *Proc. SPIE* **3326**, pp. 509-515.

[113]   Sirohi J. and I. Chopra. (2000). "Fundamental understanding of piezoelectric strain sensors," *J. of Intell. Mat. Sys. Struc*. **11**, pp. 246-257.

[114]   Giurgiutiu V. (2005). "Tuned Lamb wave excitation and detection with piezoelectric wafer active sensors for structural health monitoring," *J. of Intell. Mat. Sys. Struc*. **16**, pp. 291-305.

[115]   Monkhouse R.S.C., Wilcox P., and P. Cawley. (1997). "Flexible interdigitated PVDF transducers for the generation of Lamb Waves in Structures," *Ultrasonics* **35**, pp. 489-498.

[116]   Moulin E., Assaad J., and C. Delebarre. (2000). "Modeling of Lamb waves generated by integrated transducers in composite plates using a coupled finite element-normal modes expansion method*," J. Acoust. Soc. of Am.* **107**, pp. 87-94.

[117]   Lin X. and F.G. Yuan. (2001). "Diagnostic Lamb waves in an integrated piezoelectric sensor/actuator plate: analytical and experimental studies," *Smart Mater. Struct.* **10**, pp. 907-913.

[118]   Raghavan A. and C.E. Cesnik. (2004). "Modeling of piezoelectric-based Lamb-wave generation and sensing for structural health monitoring," *Proc. SPIE* **5391**, pp. 419-430.

[119]   Greve D.W., Neumann J.J., Nieuwenhuis J.H., Oppenheim I.J. and N.L. Tyson. (2005). "Use of Lamb waves to monitor plates: experiments and simulations," *Proc.*

SPIE **5765,** pp. 281-292.

[120]   Nieuwenhuis J.H., Newumann J. J., Greve D.W., and I.J. Oppenheim. (2005). "Generation and detection of guided waves using PZT wafer transducers,*" IEEE Trans. Ultrason., Ferroelectr., Freq. Control* **52**, pp. 2103-2111.

[121]   Coverly P.T. and W.J. Staszewski. (2003). "Impact damage location in composite structures using optimized sensor triangulation procedure," *Smart Mat. and Struct.* **12**, pp. 795-803.

[122]   Prosser W.H., Jackson K.E., Kellas S., Smith B.T. McKeon J. and A. Friedman. (1995). "Advanced waveform based acoustic emission detection of matrix cracking in composites," *Materials Eval.* **53**(9), pp. 1052-1058.

[123]   Staszewski W.J., Worden K., Wardle R. and G.R. Tomlinson. (2000). "Fail-safe sensor distribution for impact detection in composite materials," *Smart Mat. and Struct.* **9**, pp. 298-303.

[124]   Seydel R. and F-K. Chang. (2001). "Impact identification of stiffened composite panels: I. System development," *Smart Mat. and Struc.* **10**, pp. 354-369.

[125]   Thursby G., Sorazu B., Betz D., and B. Culshaw. (2005). "Novel methods of Lamb wave detection for material damage detection and location," *Proc. SPIE* **5768**, pp. 313-322.

[126]   Kawiecki G. and S. Jesse. (2002) "Rosette piezotransducers for damage detection," *Smart Mat. and Struc.* **11**, pp. 196-201.

[127]   Auld B.A. (1990). Acoustic fields and waves in solids, 2nd edition. *R.E. Krieger Publishing*, Malabar, Fl.

[128]   Achenbach J.D. (1987). Wave Propagation in Elastic Solids. *North Holland Publishing*, Amsterdam, Holland.

[129]   Thomas W.T. (1950). "Transmission of elastic waves through a stratified solid medium," *J. of Applied Physics* **21**, pp. 89-93.

[130]   Nayfeh A.H. (1990). "The general problem of elastic wave propagation in multilayered anisotropic media," *J. Acoust. Soc. Am.* **89**(4), pp. 1521-1531.

[131]   Hosten B. and M. Castaings. (1993). "Transfer matrix of multilayered absorbing and anisotropic media. Measurements and simulations of ultrasonic wave propagation through composite materials," *J. Acoust. Soc. of Am.* **94**(3), pp. 1488-1495.

[132]   Hosten B. (1991). "Bulk heterogeneous plane waves propagation through viscoelastic plates and stratified media with large values of frequency domain," *Ultrasonics* **29**, pp. 445-450.

[133] Knopoff L. (1964). "A matrix method for elastic wave problems," *Bull. Seism. Soc. Am.* **54**, pp. 431-438.

[134] Yang P.C., Norris C.H. and Y. Stavsky. (1966). "Elastic wave propagation in heterogeneous plates," *Int. J. of Solids and Structures*, **2**, pp. 665-684,

[135] Whitney J.M. and N. J. Pagano. (1970). "Shear deformation in heterogeneous anisotropic plates," *J. of Applied Mechanics*, **37**, pp. 1031-1036,

[136] Joeng H. (2001). "Analysis of plate wave propagation in anisotropic laminates using wavelet transform," *NDT&E Intl.* **34**, pp. 185-190.

[137] Williams R.B. and D.J. Inman. (2002). "An Overview of Composite Actuators with Piezoceramic Fibers," *Proc. 20th International Modal Analysis Conference*, Los Angeles, CA.

[138] Wilkie W.K., Bryant R.G., High J.W., Fox R.L., Hellbaum R.F., Jalink A., Little B.D. and P.H. Mirick. (2000). "Low-cost Piezocomposite Actuator for Structural Control Applications," *Proc. SPIE's 7th Annual International Symposium on Smart Structures and Materials*, Newport Beach, CA, pp. 323-334.

[139] Barbezat M., Brunner A.J., Flüeler P., Huber C. and X. Kornmann. (2004). "Acoustic Emission Sensor Properties of Active Fibre Composite Elements Compared with Commercial Acoustic Emission Sensors," *Sensors and Actuators A: Physical*, **114**, pp. 13-20.

[140] Brunner A.J., Barbezat M., Flüeler P. and C. Huber. (2004). "Composites from Piezoelectric Fibers as Sensors and Emitters for Acoustic Applications," *J. of Acoustic Emission*, **22**, pp. 127-137.

[141] Bevan J.S. and C. Mei. (2001). "Piezoceramic Actuator Placement for Structural Acoustic and Vibration Control of Flat and Curved Panels," *Proc. SPIE* **4327**, pp. 698-708.

[142] Schoenecker A.J., Gebhardt S.E., Rödig T., Keitel U., Bruckner B., Schnetter J. and T. Daue. (2005). "Piezocomposite Transducers for Smart Structures Applications," *Proc. SPIE* **5764**, pp. 34-41.

[143] Thien A.B., Chiamori H.C., Ching J.T., Wait J.R. and G. Park. (2005). "Piezoelectric Active Sensing for Damage Detection in Pipeline Structures," *Proceedings 23rd International Modal Analysis Conference*, Orlando, FL, pp. 323-336.

[144] IEEE. (1978). Piezoelectricity IEEE Standard 176, *IEEE*, New York, NY.

[145] Azzouz M.S., Mei C., Bevan J.S. and J.J. Ro. (2001). Finite element modeling of MFC/AFC actuators and performance of MFC *J. of Intell. Mat. Sys. Struc.* **12**, pp. 601-612

[146]   Tzou H.S. (1993). Piezoelectric Shells:Distrubuted Sensing and Control of Continua, *Kluwer Academic Publishers*, Dordrecht, Netherlands.

[147]   Wang X.D. and S.A. Meguid. (2000). "On the electroelastic behaviour of a thin piezoelectric actuator attached to an infinite host structure," *Inter. J. of Solids and Structures* **37**, pp. 3231-3251.

[148]   Salamone S., Matt H.M., Lanza di Scalea F. and P. Rizzo. (2006). "The influence of temperature on guided wave based MFC transduction and damage detection," *to be submitted to J. of Intell. Mat. Sys. Struc.*

[149]   Matt H.M. and F. Lanza di Scalea. (2006). "New method for damage location in complex CFRP structures based upon the use of piezoelectric transducer rosettes," *to be submitted to Smart Mater. Struct.*.

[150]   Wang X.D. and G.L. Huang. (2006). "The coupled dynamic behavior of piezoelectric sensors bonded to elastic media," *J. of Intell. Mat. Sys. Struc.* **17**, pp. 883-894.

[151]   Rose J.L. (1999). Ultrasonic Waves in Solid Media, *Cambridge University Press*, Cambridge, UK.

[152]   Crawley E.F. and J. de Luis. (1987). "Use of piezoelectric actuators as elements of intelligent structures," *AIAA J.* **25**, pp. 1373-1385 .

[153]   Chopra A.K. (2001). Dynamics of Structures, *Prentice-Hall*, Englewood Cliffs, New Jersey.

[154]   Lanza di Scalea F., Matt H.M. and I. Bartoli. (2006). "Response of piezoceramic sensors to Rayleigh and Lamb ultrasonic waves," *J. Acoust. Soc. of Am, (in print).*

[155]   *Abaqus User's Manual* Version 6.5.

[156]   Alleyne D. and P. Cawley. (1991). "A two-dimensional Fourier transform method for the measurement of propagating multimode signals," *J. Acoust. Soc. of Am.* **89**, pp. 1159-1168.

[157]   Moser F., Jacobs L.J., and J. Qu. (1999). "Modeling elastic wave propagation in waveguides with the finite element method," *NDT&E Int.* **32**, pp. 225-234.

[158]   Poularikas A.D. (1996). The Transforms and Applications Handbook, *CRC Press*, Boca Raton, FL.

[159]   Viktorov I.A. (1967). Rayleigh and Lamb Waves, *Plenum Press*, New York, NY.

[160]   Shorter P.J. (2004). „Wave propagation and damping in linear viscoelastic laminates," *J. Acoust. Soc. of Am.***115**, pp. 1917-1925.

[161]   Bartoli I., Marzani A., Lanza di Scalea F.L. and E. Viola. (2006). "Modeling wave propagation in damped waveguides of arbitrary cross-section," *in print in J. Acoust. Soc. of Am.*

[162]   Neau G. (2003). "Lamb waves in anisotropic viscoelastic plates. Study of the wave fronts and attenuation," Ph.D Thesis, L'Université Bordeux I.

[163]   Bernard A., Lowe M.J.S. and M. Deschamps. (2001). "Guided waves energy velocity in absorbing and non-absorbing plates", *J. Acoust. Soc. of Am.* **110**, pp. 186-196.

[164]   Jones R.M. (1975). Mechanics of composite materials, *Taylor & Francis*, Philadelphia, PA.

[165]   Neau G., Lowe M.J.S. and M. Deschamps. (2002). "Propagation of lamb waves in anisotropic and absorbing plates: theoretical derivation and experiments," *Review of Progress in Quantitative NDE* **21**, pp. 1062-1068.

[166]   Karunasena W., Shah A.H., and S.K. Datta. (1991). ''Wave propagation in a multilayered cross-ply composite plate,'' *J. Appl. Mech.* **58**, pp. 1028–1032.

[1167]   Staszewski W. (2002). "Intelligent Signal Processing for Damage Detection in Composite Materials," *Composites Science and Technology* **62**, pp. 941-950.

[168]   Rizzo P. and F. Lanza di Scalea. (2005). "Ultrasonic Inspection of Multi-wire Steel Strands with the Aid of the Wavelet Transform," *Smart Mater. Struct.* **14**, pp. 1-11.

[169]   Mallat S.G. (1999). A Wavelet Tour of Signal Processing, *Academic Press*, New York, NY.

[170]   Abbate A., Koay J., Frankel J., Schroeder S.C. and P. Das. (1994). "Application of Wavelet Transform Signal Processor to Ultrasound," *Proc. Ultrasonic Symposium,* 94CH3468-6, pp. 1147-1152.

[171]   Hooker M.W. (1998). "Properties of PZT-Based piezoelectric ceramics between –150 and 250º C," *Technical report NASA/CR-1998-208708.*

[172]   Lee H-J. and D.A. Saravanos. (1997). "The effect of temperature dependent material nonlinearities on the response of piezoelectric composite plates," *Technical report NASA/TM—97-206216.*

[173]   Sherrit S., Yang G., Wiederick H.D. and B.K. Mukherjee. (1971). "Temperature dependence of the dielectric, elastic and piezoelectric material constants of lead zirconate titanate ceramics," *J.of Applied Physics* **42**(6,) pp. 2219-2230.